可编程非刚性 Square-twist 折纸超材料的设计与分析

Design and Analysis of Programmable Non-rigid Square-twist Origami Metamaterials

一级学科：机械工程

研究方向：折纸结构

作者姓名：臧世玺

指导教师：陈焱　　教授

马家耀　副教授

天津大学机械工程学院

二〇二二年五月

摘要

超材料是在不违背基本物理学规律的前提下，通过设计其微结构上的拓扑与变形，来获得超常的物理性能。如今，超材料已成为跨学科、高度交叉的前沿研究领域。折纸作为经典结构设计方法已被广泛用于设计超材料，且刚性和非刚性折纸结构均表现出独特的机械性能。本文研究了刚性和非刚性混合折纸超材料的几何设计准则和性能编程方法。其中刚性折纸结构已经建立了基于运动学的理论模型，并可用于分析其机械性能。因此，本文关注非刚性单元的研究，以及混合折纸超材料的编程。本文的研究重点如下：

首先，基于单轴拉伸的实验结果，通过添加虚拟折痕创造等效刚性折纸单元的方式，建立了非刚性 Square-twist Type 2 单元的理论模型。计算结果表明，Type 2 单元有两条变形路径，且存在分岔点。而理论与实验结果的对比则证明了，Type 2 单元趋向于沿低能量路径折叠。本文揭示了 Type 2 单元的几何和材料参数与其机械性能的对应关系，为其性能编程提供了理论依据。

其次，基于双轴拉伸的实验结果，非刚性 Square-twist Type 1 单元表现出复杂的变形行为，因此，本文通过实验和有限元相结合的方法，建立了 Type 1 单元的经验模型。对此模型的详细分析表明，该单元的变形过程中存在收紧、解锁和压扁 3 个阶段。本文提出的经验模型将该折纸结构的几何、材料参数与其机械性能进行了关联，并进一步基于具体工程要求，实现了对机械性能的准确预测和编程。

最后，根据已知的单元行为的分析结果，本文进一步研究了拓扑构型不同、几何参数不同的单元的空间排布方式，构造了混合与渐变折纸超材料。研究证明，该折纸超材料的机械性能可由构成单元的相应性能叠加得到。通过建立超材料单元类型、几何参数、基础材料与其整体机械性能的定量关系，实现了超材料的可编程设计。

本文显著改进了折纸超材料的设计原理和性能可编程性。混合刚性和非刚性折纸设计方法启发了一类新的可编程折纸超材料，可以满足各个工程领域的复杂需求。

关键词：运动学，非刚性折纸，山谷折痕排布，图案镶嵌，机械超材料，可编程性，可预测性

ABSTRACT

Metamaterials have unusual physical properties that are produced by designing topology and deformation of their microstructures based on the basic physical laws. The previous studies have allowed metamaterials at the forefront of an interdisciplinary research field. Origami, a famous design method, has been used in creating metamaterials, where both rigid and non-rigid structures show unique mechanical properties. This dissertation investigates metamaterials created by a mixture of rigid and non-rigid origami units and proposes geometric design rules and property programming approaches. Notice that the rigid units have received kinematic analysis, which contributes to the available theoretical model for mechanical research. Thus, this dissertation focuses on the study of non-rigid units and the programmability of mixture metamaterials. The highlights of this dissertation are listed as follows.

First, based on the uniaxial tension experimental results, a theoretical model of the non-rigid square-twist type 2 unit is proposed by building an equivalent rigid pattern with an additional virtual crease. Two deformation paths with a bifurcation are found by the theoretical calculation of the type 2 unit. The comparison between theoretical and experimental results proves that square-twist type 2 unit tends to follow a low-energy deformation path. The research reveals successfully programmable mechanical properties by tuning geometrical parameters and material stiffness.

Next, due to the complex deformation and unavailable equivalent model method, an empirical model is presented to study the non-rigid square-twist type 1 unit by combining biaxial tension experiments and finite element modeling. A three-stage deformation process, including tightening, unlocking, and flattening, is unveiled in the type 1 unit through a detailed analysis. The empirical model correlates geometric/material parameters of the origami structure and its mechanical behaviors and further offers accurately predicting and programmable mechanical properties based on specific engineering requirements.

Finally, a design method is proposed to create tessellated and graded metamaterials by rationally arranging units with different types and geometric parameters according to the analysis of units' mechanical behaviors. The energy, initial peak force, and maximum stiffness of metamaterials are proved to be the summation of the

corresponding properties of the component units. The programmability of metamaterials can be achieved by establishing the relationship between the mechanical properties and the types, proportions, geometric and material parameters of the units.

This dissertation significantly improves the design principle and property programmability of origami-based metamaterials. The design method of mixing rigid and non-rigid origami units inspires a new class of programmable origami metasheets for complex engineering applications.

KEY WORDS: Kinematics, Non-rigid origami, Mountain-valley crease assignment, Tessellation, Mechanical metamaterials, Programmability, Predictability

Contents

List of Figures

List of Tables

Notation

Parameters

a	Length of the common side between trapezoidal and rectangular facets in the square-twist pattern
a_i^j	The j-th side length of the i-th unit in a metasheet
A, B, C, D	Vertices of the square-twist pattern
D_x, D_y, D_z	Dimensions of an origami tessellation
D_D	Diagonal length in the empirical model of type 1 structure
D_t, $D_{4\times4}$	Diagonal length of unit and 4×4 metasheet, respectively
d_i	Length coefficients of crease i
d_{Fi}	Coefficient corresponding to d_i in the equation of initial peak force of type 1 structure
d_{Ki}	Coefficient corresponding to d_i in the equation of maximum stiffness of type 1 structure
$\boldsymbol{e}_i$	Normalized vectors represent the i-th creases in the pattern
$\tilde{e}_i$	The quaternion corresponding to vector $\boldsymbol{e}_i$
E	Young's modulus
$f_i(x)$	Best-fit polynomial of the bending central square facet along diagonal A–C
$f_{ci}(\varphi)$	Rotation function with a variable φ in the empirical model of type 1 structure
$f_f(\varphi)$	Function with a variable φ of facet deformation in the empirical model of type 1 structure
$f_{i,j}(\cos\delta)$, $f_{i,j}^{-1}(\cos\delta)$	Function of $\cos\delta$
$f_S(\varphi)$, $f_R(\varphi)$, $f_T(\varphi)$	Deformation functions of the square, rectangular, and trapezoidal facets in the empirical model of type 1 structure
$f_{di}(\varphi)$	Deformation functions corresponding to d_i
F	Tension force
F_t^i, $F_{4\times4}$	Tension force of the i-th unit and 4×4 metasheet, respectively
F_x, F_y, F_z	Tension force of an origami structure in x, y, z directions
$\overline{F}_x$, $\overline{F}_y$, $\overline{F}_z$	Tension force of an origami structure in x, y, z directions under uniaxial loading
F_{min}	Minimum of the tension force

$F_{\max}$	Initial peak force of the square-twist structure
$F_{2\times2\text{-max}}$	Initial peak force of the 2×2 square-twist metasheet
g^i	Parameter of the sign in the equation of ψ_4^j for the j-th vertex in kinematic analysis of the square-twist pattern
g	Parameter of the sign in the equation of φ_6 in the mechanical study of the square-twist structure
H_{D}	Height of type 1 structure
H_{D0}	Natural height of type 1 structure
ΔH	Compression displacement of a unit in H direction
H_{u0}	Initial height of an origami unit
$\mathbf{I}_i$	Identity matrix of order i
I	Moment of inertia
(i), (ii), (iii), (iv), (v)	Representative DIC reconfigurations
I_i, II_i, III_i, IV_i, V_i, VI_i	Representative configurations of different kinematic paths
I, II, III, IV, V, VI	Representative configurations of numerical results
$k_{s,i}$, $k_{r,i}$	Stiffness of stretched and rotated creases
$k_{\mathrm{c}i}$, k_{c}	Torsional elastic constant per unit length along the i-th crease of a unit or tessellated metasheet
k_{f}	Torsional elastic constant per unit length of the virtual crease or bending facets of a unit or tessellated metasheet
K	Stiffness of the square-twist structure
K_{t}^i, $K_{4\times4}$	Stiffness of the i-th unit and 4×4 metasheet, respectively
$\widetilde{K}_i$	Components in the equation of the stiffness K in the empirical model of type 1 structure
$K_{\max}$	Maximum stiffness of the square-twist structure or metasheet
$K_{2\times2\text{-max}}$	Maximum stiffness of the 2×2 square-twist metasheet
l	Length of the side for the central square facet in the square-twist pattern
l_i	Side length of the i-th unit in a metasheet
$l_{s,i}$, $l_{r,i}$	Length of stretched and rotated creases
l_i^j	Length of the i-th vector of the j-th vertex in diagram method
L_i	Length of the i-th crease in the mechanical study of the square-twist structure
$L_{\mathrm{c}i}$ (i=1, 2, 3, …, 12)	Crease length in the empirical model of type 1 structure

L_f	Length of facet deformation in the empirical model of type 1 structure
L_s	Length of the virtual crease in the mechanical study of the type 2 structure
L_{D0}	Natural diagonal length of type 1 structure
L_S, L_R, L_T	Diagonal length of the central square, rectangular, and trapezoidal facets in the type 1 structure
L_{S0}, L_{R0}, L_{T0}	Natural diagonal length of the square, rectangular, and trapezoidal facets in the type 1 structure
m	The number of units in a row or column of a metasheet
M	Bending moment per unit length of the creases
$\boldsymbol{n}_i$	Normalized vectors perpendicular to the i-th surface
$\tilde{n}_i$	The quaternion corresponding to vector $\boldsymbol{n}_i$
N_c, N_{c1}, N_{c2}	The number of creases
N_m	The number of possible tessellations for an $m\times m$ metasheet,
P_j	The j-th vertex of type 1 square-twist unit
q	Positive integer in the calculation of N_m
$\tilde{q}$	Quaternion of a vector
$\tilde{q}^{e_i}$, $\tilde{q}^{n_i}$	Quaternion of vector $\boldsymbol{e}_i$ or $\boldsymbol{n}_i$
q_i^j, p_i^j	The i-th parameter in the equation of ψ_4^j and ψ_5^j for the j-th vertex in kinematic analysis of the square-twist pattern
q_i, p_i	The i-th parameter in the equation of φ_6 and φ_5 in the mechanical study of the square-twist structure
$\mathbf{Q}_{i(i+1)}$	3×3 transformation matrix between the coordinate system of link $(i\text{-}1)i$ and that of link $i(i+1)$ for spherical linkages
Q_i^j, P_i^j	The i-th parameter in the equation of θ_4^j and θ_5^j for the j-th vertex in kinematic analysis of the square-twist pattern
s	Bending arc length of the central square measured from the reconstructed geometry based on digital image correlation
S_i	The i-th surface
S_f	Deformed area of the facet in the empirical model of type 1 structure
S_e, S_p	Elastic and plastic regions of the facet in the empirical model of type 1 structure
$S_{S\text{-}j}$, $S_{R\text{-}j}$, $S_{T\text{-}j}$ (j=e, p)	Elastic and plastic regions of the square, rectangular, and trapezoidal facets in the empirical model of type 1 structure

t	Thickness of the material
T^j, T_i^j (i=1, 1R, 2, 3, and j=L, R)	Building units in the square-twist metasheet
$T_{1\text{-i}}$, $T_{1\text{-ii}}$, $T_{1\text{-iii}}$, $T_{1\text{-iv}}$	The type 1 units with different locations in the 4×4 metasheets
T_{i}, T_{ii}, T_{iii}, T_{iv}, $T_{2\times2\text{-i}}$, $T_{2\times2\text{-ii}}$, $T_{2\times2\text{-iii}}$, $T_{2\times2\text{-iv}}$	The unit and metasheet, respectively, with four different boundary conditions
u_{ci} (i=1, 2, 3, …, 12)	Constant coefficient of crease energy in the empirical model of type 1 structure
u_{f}	Constant coefficient of facet energy in the empirical model of type 1 structure
$u_{\text{S-}j}$, $u_{\text{R-}j}$, $u_{\text{T-}j}$ (j=e, p)	Elastic and plastic energy coefficients of the square, rectangular, and trapezoidal facets in the empirical model of type 1 structure
$u_{\text{U}i}$, $u_{\text{F}i}$, $u_{\text{K}i}$	The i-th coefficient in the equation of energy at unfolded configuration, initial peak force, and maximum stiffness of type 1 structure
U	Energy
U_{t}^i, $U_{4\times4}$	Energy of the i-th unit and 4×4 metasheet, respectively
U_{bar}, U_{spr}	Strain energy stored in the bar elements and the rotational springs
U_i	Energy of the i-th crease
U_{c}, U_{f}	Energy of the original creases and facets in an origami unit
U_{s}	Energy of the virtual crease on the central square of an origami unit
U_{t}	Total energy of an origami unit
U_{S}, U_{R}, U_{T}	Energy of the central square, rectangular, and trapezoidal facets in an origami unit
$U_{2\times2}$	Energy of the 2×2 square-twist metasheet at unfolded configuration
u, v, w	Components of the equation for x_{d}
$\vec{u}_i$, $\vec{v}_i$, $\vec{w}_i$	The vectors to describe the pattern with a single crease neighbored by two rigid panels
W_{ext}	External work
Δx	Tension displacement in the mechanical experiment
x_{d}	Deformed diagonal length of the type 2 specimen
$x_{\text{d,0}}$	Natural diagonal length in the undeformed state of the type 2 specimen
Δx_{max}	Maximum displacement in the mechanical experiment

x_i, z_i	x, z coordinate axis of system i
x, y, z	Coordinate axis of the loading system in the mechanical experiment and finite element model

Symbolic Variables

α	Twist angle of the central square facet in the square-twist pattern
$\alpha_{i(i+1)}$	Twist angle of link $i(i+1)$ between joints i and $i+1$ or sector angle of a multi-crease vertex pattern
$\alpha_{i(i+1)}^{j}$	Sector angle between the i-th and $(i+1)$-th creases for the j-th vertex in the square-twist pattern
ψ_i^j	Dihedral angle of the i-th crease for the j-th vertex in kinematic analysis
δ_i, δ, $\delta_{i,j}$	Folding angles of a single-vertex
φ_{4g}, ψ_{1g}	Value of the dihedral angles φ_4 and ψ_1^j at the bifurcation point of type 2 and 2M patterns
φ_i	Dihedral angle for the i-th crease in the mechanical study
$d\varphi'$	Infinitesimal element of dihedral angle φ
$\varphi_{i,0}$	Natural dihedral angle in the undeformed state for the i-th crease in the mechanical study
φ_s	Dihedral angle for the virtual crease in the mechanical study
$\varphi_{s,0}$	Natural dihedral angle in the undeformed state for the virtual crease in the mechanical study
$\Delta\varphi$	The change in the dihedral angle of the creases in the mechanical study
$\Delta\varphi_y$	Angle of $\Delta\varphi$ which illustrates the two stages of the nonlinear elastic torsional constant of the creases
φ	Angle variable in the empirical model of type 1 structure
φ_U, φ_F, φ_K	Variable φ corresponding to the energy at the end of loading, the initial peak force, and the maximum stiffness
γ_{i1}, γ_{i2}, γ_{i3} (i=S, R, T)	Constant coefficients of the plastic regions for the square, rectangular, and trapezoidal facets in the empirical model of type 1 structure
Π	Potential energy of an origami structure
θ_i	Angle of rotation from x_i to x_{i+1} about axis z_i in joint i
θ_i^j	Rotation angle along the i-th crease of the j-th vertex in kinematic analysis of the square-twist pattern

Abbreviations

DoF	Degree of freedom

DIC	Digital image correlation
PET	Polyethylene terephthalate
PEEQ	Equivalent plastic strain
Type 1M, Type 2M	Modified type 1 and type 2
MPC	Multiple point constraint
S4R	Four-node quadrilateral shell elements with reduced integration

Chapter 1 Introduction

1.1 Background and Significance

Metamaterials, man-made architected materials with extraordinary and customizable physical properties that are unavailable in the traditional materials, lead to a wide range of potential applications including seismic surveillance, space crafts, and renewable energy. The behaviors, such as negative index of refraction in the electromagnetic field[1], controlled and redirected propagation in the acoustic field[2], and negative Poisson's ratio in the mechanical field[3], are dictated by both engineered repeating microstructures or units and material constituents[4-7]. Unlike the exotic properties of some metamaterials obtained by the simple permanent 3D constructions, those of mechanical metamaterials are more sensitive to the kinematic motion, structural deformation, or equilibrium state transition of the microstructures. This phenomenon introduces more programmable and tunable properties to mechanical metamaterials and attracts the attention of many researchers.

The unusual and desirable properties of mechanical metamaterials are enabled by relying on the large deformation of their structures and controlled by the deformation of the unit[8-11] or the relative motion between the combined units[12-14]. In previous studies, elastic materials are used in fabricating metamaterial structures to provide motion behaviors similar to compliant mechanisms[15]. And the structural design contributes to the reconfigurable behavior in metamaterials[16-20]. By purposely managing the connections between the neighboring units or rational designing the building block and hinges, programmable/controllable mechanical behaviors can be created[21, 22]. In general, structural characteristics play a key role in achieving various counterintuitive mechanical properties. It means the rational design of the deformed or deployed structures is required in metamaterials. The existing structural design methods of mechanical metamaterials includes elastic bars[23-29], arrays of grids[30-33], structural network[34-40], topological framework[41], lattice structures[42], kirigami[21, 22, 43-45] and origami[46, 47] methods.

As one of the famous design strategies of deployed structures, origami has a superior capability of generating complex 3D structures by folding 2D sheets following

patterns with a set of mountain and valley creases[48]. This folding behavior supports the tunable and deployable frameworks of origami structures, while the patterns offer systematically variable design parameters to carry out the programming on them. The existing researches show that folding behaviors perform in two ways: folding along the creases and folding through the deformed facets. The patterns folded through the former way are called rigid-foldable origami[46]. Due to the folding process controlled by individual creases, the rigid-foldable origami structure usually shows a simplified mechanical response. Those folded by the mixture of the two ways are named non-rigid-foldable origami[47]. Contribution from facet deformation can extensively increase the overall stiffness and enlarge the energy landscape of the metamaterials, leading to an upper band of mechanical properties as opposed to the rigid metamaterials. Previous origami metamaterials are predominantly developed from rigid-foldable origami patterns, represented by the well-known Miura-ori[46, 49-54] and its derivatives[55-60]. To widen the properties in origami metamaterials, non-rigid origami patterns, represented by the Kresling[47, 61-64] and square-twist patterns[65, 66], have been of increasing interest to researchers. Both rigid and non-rigid origami patterns have advantages in different aspects of creating metamaterials, respectively. However, past studies usually consider the metamaterial formed by a single type of either rigid or non-rigid pattern. And the research of non-rigid-foldable origami usually has difficulty predicting the motion or deformation of the structure caused by complicated patterns.

In addition, previous studies have proved that both the material components and the shape of the structure demand programmability to widen the application range of the mechanical metamaterials. For varying geometry or shape of the programmable metamaterial, the methods usually include altering the type of unit cells[67], tuning the density of the tessellation block in the assembly structure[68], or switching the zero-energy configuration of the metamaterial consisting of several zero-energy modes[69]. But the programming approaches based on modifying material parameters vary by the design and fabricated principle of the metamaterial. For example, in the auxetic metamaterial designed by square lattice structures, the temperature depending materials were introduced to the material components to create programmable stiffness by altering the buckling behavior of the lattice structure with temperature[42]. Moreover, studies on origami metamaterials discovered that different material sheets used to fabricate facets and creases produce programmable thermal expansion coefficients by

offering varied motion behaviors using the materials' stiffness[49, 70]. Noticing that programmability is the significant feature of metamaterials, the effects of changes in both geometric and material parameters have to be investigated in this dissertation.

Therefore, for creating a new series of mechanical metamaterials with improved properties, it is necessary to establish mobile structures by combining rigid and non-rigid origami patterns. To reach this aim, two problems demand solutions. One is how to join two or more types of origami patterns together. In this combination, both the mountain-valley crease assignment and the geometric parameters of different types of units have to be compatible, which is the foundation of a mobile tessellated structure. The other is how to achieve the predicted and programmable properties of the mechanical metamaterial. Since the mechanical metamaterial is structural sensitive, their properties can be easily programmed by tuning the proportion or geometric characteristics of each type of unit. Meanwhile, the different material properties of the facets and creases also provide programmable incompatible or complex deformation of the origami units. In conclusion, the solutions to both the compatibility of tessellations and the programmability of metamaterials will create a systematically constructional process of novel mechanical metamaterials and contribute to their further engineering applications.

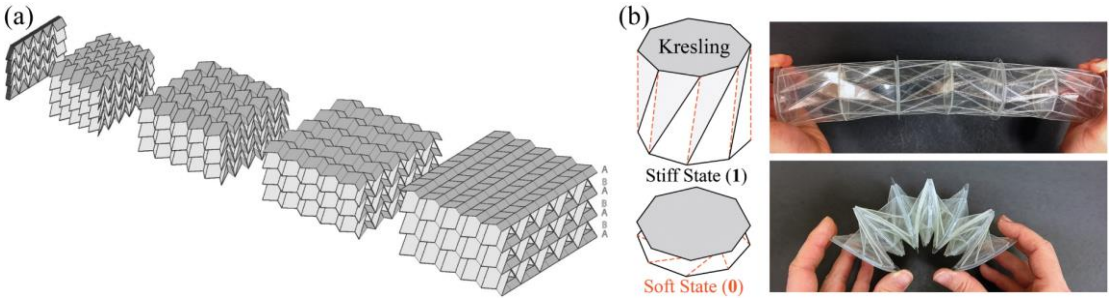

Fig. 1-1 (a) Rigid[46] and (b) non-rigid[71] origami mechanical metamaterial.

1.2 Literature Review

1.2.1 Rigid Origami Mechanical Metamaterials

The rigid foldability gives these origami structures stiff facets and flexible creases, which allows them to be analyzed by kinematic methods[46]. Many previous studies of

the rigid origami metamaterials focus on the design strategy of the Miura-ori pattern, which has simple geometric parameters. The Miura-ori metamaterial has been proved to have a single degree of freedom (DoF) and a negative in-plane Poisson's ratio (Fig. 1-2(a))[46, 53, 54]. The units of a Miura-ori structure always fold synchronously according to the rigidity, which results in only one peak and a flat plateau in the force vs. displacement curve[52]. In further investigations, the rigid foldable behavior is found to retain in some Miura-ori derivatives. For example, the Tachi-Miura pattern (Fig. 1-2(b)) in Ref. [72] can also form a rigid origami metamaterial. Because of the stiff facets and one DoF behavior, dynamic features of the rigid-foldable origami structure can be analyzed by the multi-bar linkage model, where the facets and creases are modeled as bars and hinges, respectively. Moreover, some defect design methods help the Miura-ori pattern to keep rigid foldability and add properties. As shown in Fig. 1-2(c), a new origami pattern named Basic unit Cell with Hole[59, 60] is designed based on the Miura-ori pattern in two ways. One is to create an offset between two adjacent strips with original geometric parameters[60], and the other is created by combining two zigzag strips with different scales[59]. The kinematic methods and the calculation of Poisson's ratio used in the Miura-ori structure have been proved to apply to this new origami pattern. And the additional variables of the holes' dimensions provide the defective pattern with a way to program the in-plane Poisson's ratio. In the above origami metamaterials, the rigid foldability is active in the whole folding process. However, some origami patterns only offer rigid foldability in a partial folding process.

The partially rigid foldability has been found in some Miura-ori derivatives[55, 73-75] and other traditional origami patterns, such as waterbomb[76-82]. The origami pattern in Fig. 1-2(d) is designed by modifying the sector angles of each parallelogram facet in the original Miura-ori pattern, which also changes the folding angle or configuration of different facets[55]. The kinematic calculation of this generalized Miura pattern indicates that the rigid foldability only occurs before the minimum folding angle equals zero. Furthermore, the multilayer metamaterial designed by stacking units also shows partially rigid foldability because the layers with lower height always finish the folding process before others. This type of rigid foldability expands the negative Poisson's ratio in the original Miura-ori metamaterial to the tunable one and creates infinite stretching and bulk moduli[55]. Another Miura-ori derivative is a tube shown in Fig. 1-2(e)[73] assembled by two rows of Miura-ori units. Several Miura-ori tubes can be connected in

different directions to form an anisotropic metamaterial. The interaction between multiple origami tubes generates an incomplete folding or unfolding process. Folding behaviors of the anisotropic metamaterial varied in different directions contribute to the reconfigurability. Combined with the 3D printing technique, the anisotropic construction helps microscaled origami metamaterials to tunable anisotropic stiffness[74, 75]. In addition, the partially rigid foldability in waterbomb and Ron Resch patterns also results from some parts of the structure folding more quickly than others. As shown in Fig. 1-2(f), in the rigid folding process, the diameter of the waterbomb tube is continuously decreased[76]. For some geometric parameters, facet interference happens at the ends of the tube when the diameter of the middle row of units does not reach the minimum, which means the rigid motion cannot finish in the practical metamaterial. Meanwhile, for some situations where all rows of units synchronously achieve the minimum diameter, twisted performance appears in the origami tube from the middle rows of units after the rigid motion process, forming a non-rigid folding process[77]. These non-rigid deformations result in a significant increase in stiffness in the waterbomb tube. The partially rigid-foldable origami metamaterials show that the non-rigid deformation process leads to more exotic properties than the rigid one.

In general, the above references show that though the rigid origami can be easily analyzed and programmed, it is difficultly used to produce novel metamaterials to satisfy the increasingly demanding engineering requirements.

1.2.2 Study Methods of Rigid Origami Metamaterials

1.2.2.1 Rigid Foldability and Relationship between Rotation Angles

Folding of rigid-foldable patterns is characterized by pure rotation about the creases without deformation from the facets, which is the foundation of the analytical derivation of the folded configuration. Thus, judging the rigid foldability of an origami pattern is the first step in calculating its folding process and associated rotation of creases. A simple judging method called the diagram method is proposed in Ref. [83] and validated by a matrix treatment. In a single-vertex patten, the mountain and valley creases (marked by solid and dotted lines in Fig. 1-3) are represented by vectors with direction away from or towards the vertex and numbered in anticlockwise order. With adjusted length, the vectors are connected head-to-tail. The rigid-foldable vertex has a closed loop of vectors while the vectors' oriented area has both positive and negative

signed parts. The opposite is non-rigid foldable. In a multi-vertex pattern, After determining the rigidity of each vertex, the rigidity of the pattern can be judged by comparing the vector length of the common creases. For the vector length, l_i^j (i=1, 2, 3, 4, and j=a, b, c, d), the compatible condition $l_1^a = l_1^b$, $l_2^b = l_2^c$, $l_3^c = l_3^d$, and $l_4^d = l_4^a$ appears in a rigid-foldable pattern (the left picture in Fig. 1-3), while the opposite incompatible condition appears in a non-rigid-foldable pattern (the right one in Fig. 1-3).

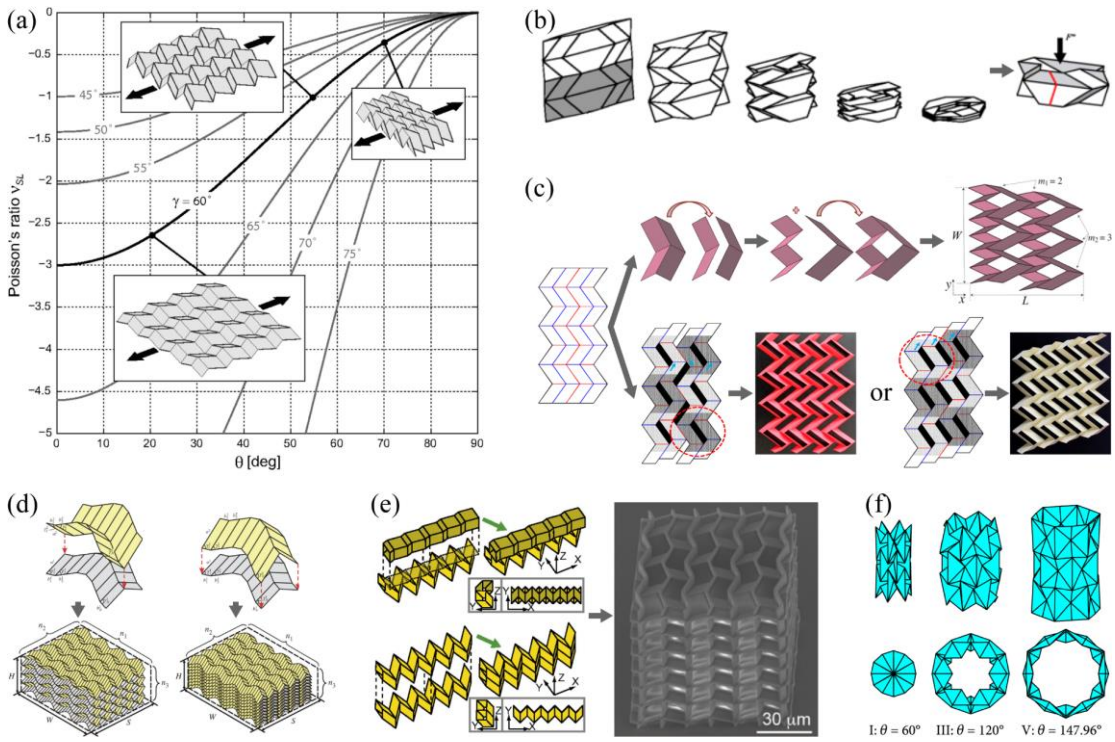

Fig. 1-2 Mechanical metamaterials designed by rigid origami including (a) Miura-ori[46], (b) Tachi-Miura polyhedron[72], (c) Basic unit Cell with Hole (BCH)[59, 60], (d) generalized Miura[55], (e) Miura-ori tube[73, 75], and (f) waterbomb[76].

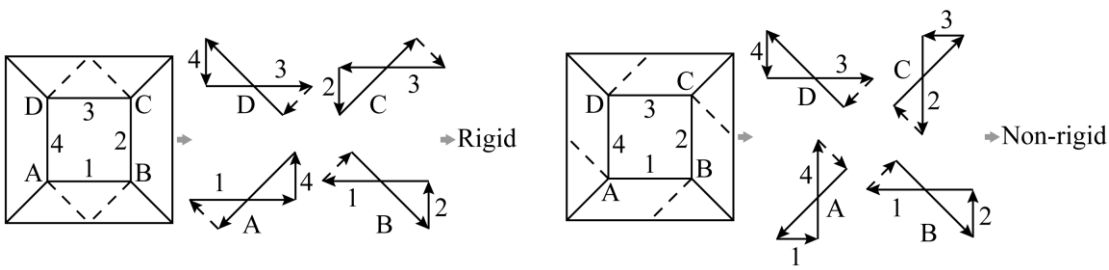

Fig. 1-3 Illustration of judging the rigid foldability of origami patterns.

There are also some analytical methods to judge the rigidity of the origami pattern and give the 3D state or the relationship between rotation/dihedral angles at the same time, such as numerical algorithms[84], kinematic theory[85-88], and quaternions and dual quaternions[89].

In the numerical algorithms method[84] (Fig. 1-4(a)), the relationship between folding angles, δ_i, of a single-vertex pattern is given by $\cos\delta_i = f(\cos\delta_{i+1})$ or $\cos\delta_{i+1} = f^{-1}(\cos\delta_i)$. When the inner facets of a pattern are formed by four vertices, see the lower picture in Fig. 1-4(a), the pattern is rigid-foldable when the equations, $f_{i,j+1}\left(f_{i+1,j+1}^{-1}\left(f_{i+1,j}\left(f_{i,j}^{-1}(\cos\delta)\right)\right)\right) \equiv$ Identity or $f_{i+1,j}\left(f_{i,j}^{-1}(\cos\delta)\right) \equiv f_{i+1,j+1}\left(f_{i,j+1}^{-1}(\cos\delta)\right)$, are always workable for arbitrary folding angle δ[84].

In kinematic theory[85-88], the vertex surrounded by multiple creases can be modeled as a spherical linkage. To explain this method, the example of a combination of the four-crease vertex and its corresponding spherical 4R linkage is shown in Fig. 1-4(b). The crease in the pattern is modeled by joint z_i in the linkage, the sector angle $\alpha_{i(i+1)}$ is equivalent to the angle of rotation from revolute joints z_i to z_{i+1}, and the dihedral angle ψ_i^j can be calculated by the rotation angle θ_i[87, 88]. For computing the kinematic motion of a spherical 4R linkage, the closure equation based on Denavit-Hartenberg (D-H) notation is given as

$$\boldsymbol{Q}_{21} \cdot \boldsymbol{Q}_{32} \cdot \boldsymbol{Q}_{43} \cdot \boldsymbol{Q}_{14} = \boldsymbol{I}_3, \tag{1-1}$$

where $\boldsymbol{Q}_{(i+1)i}$ (i=1, 2, 3, 4), the matrix that transforms the expression form (i+1)-th coordinate system to i-th coordinate system, is expressed as

$$\boldsymbol{Q}_{(i+1)i} = \begin{bmatrix} \cos\theta_i & -\cos\alpha_{i(i+1)} \cdot \sin\theta_i & \sin\alpha_{i(i+1)} \cdot \sin\theta_i \\ \sin\theta_i & \cos\alpha_{i(i+1)} \cdot \cos\theta_i & -\sin\alpha_{i(i+1)} \cdot \cos\theta_i \\ 0 & \sin\alpha_{i(i+1)} & \cos\alpha_{i(i+1)} \end{bmatrix}, \tag{1-2}$$

and i+1 is replaced by 1 when it is equal to 5[87]. Substituting Eq. (1-2) to Eq. (1-1), the relationship between rotation angles, θ_i, are obtained. For a mountain crease, the dihedral angles, ψ_i, are calculated by $\psi_i=\pi-\theta_i$. For a valley crease, the equation is given as $\psi_i=\theta_i-\pi$[87]. Then, the relationship between dihedral angles is established from that between the rotation angles. When the dihedral angles of each vertex have been obtained, the compatible condition of combining these vertices becomes the key point to judge the rigid foldability and solve the folding process of the given pattern. In Fig. 1-4(b), the three vertices share three common creases, which means an equivalence relationship, $\psi_4^a = \psi_1^b, \psi_4^b = \psi_1^c, \psi_4^c = \psi_1^a$, can be established between the dihedral

angles of the adjacent vertices around these creases[87]. Thus, the compatible condition is established:

$$\frac{\tan\frac{\psi_4^a}{2}}{\tan\frac{\psi_1^a}{2}}\cdot\frac{\tan\frac{\psi_4^b}{2}}{\tan\frac{\psi_1^b}{2}}\cdot\frac{\tan\frac{\psi_4^c}{2}}{\tan\frac{\psi_1^c}{2}}=1, \tag{1-3}$$

An origami pattern can be rigidly folded if its sector angles satisfy Eq. (1-3).

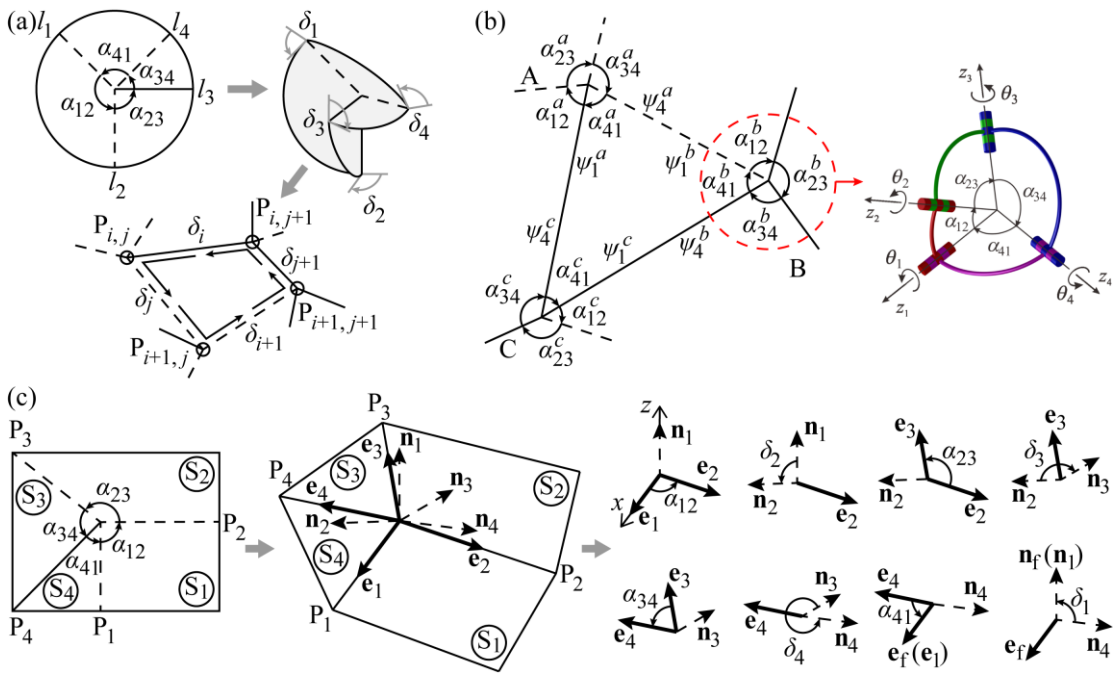

Fig. 1-4 Explanation of (a) numerical algorithms, (b) kinematic theory[87], and (c) quaternions and dual quaternions.

The example of the quaternions and dual quaternions[89] method is shown in Fig. 1-4(c), where the normalized vectors $\boldsymbol{e}_i$ represent the i-th creases in the pattern, and the normalized vectors $\boldsymbol{n}_i$ are perpendicular to the i-th surface S_i. This method is based on the rotating vector model. The right picture in Fig. 1-4(c) shows that the sector angle $\alpha_{i(i+1)}$ is the rotating angle from $\boldsymbol{e}_i$ to $\boldsymbol{e}_{i+1}$ and the folding angle δ_i is the rotating angle from $\boldsymbol{n}_{i-1}$ to $\boldsymbol{n}_i$. In Ref. [89], the rotation of the vector is represented by a quaternion $\tilde{q}$ that is a combination of a scalar part and a vector part. Then, the relationship between the normalized vectors of creases is calculated by $\tilde{e}_{i+1}=\tilde{q}^{n_i}\cdot\tilde{e}_i\cdot\left(\tilde{q}^{n_i}\right)'$, where $\tilde{q}^{n_i}$ and $\left(\tilde{q}^{n_i}\right)'$ are corresponding to the sector angles and the normalized vectors of surfaces. Similarly, the relationship between the normalized vectors of surfaces is calculated by

$\tilde{n}_{i+1} = \tilde{q}^{e_{i+1}} \cdot \tilde{n}_i \cdot \left(\tilde{q}^{e_{i+1}}\right)'$. Thus, if the pattern is rigid-foldable, the loop-closure equations of this system are $\boldsymbol{n}_{\mathrm{f}} = \boldsymbol{n}_1$ and $\boldsymbol{e}_{\mathrm{f}} = \boldsymbol{e}_1$, where $\boldsymbol{n}_{\mathrm{f}}$ and $\boldsymbol{e}_{\mathrm{f}}$ are the final vectors in calculating the rotation of the vectors[89].

Based on the relationship between dihedral angles given by the above methods, the 3D configuration of the origami pattern in the folding process is constructed. Combining the 3D configuration with other analysis methods, the exotic properties of the corresponding metamaterial can be studied.

1.2.2.2 Mechanical Behaviors

In the rigid-foldable Miura-ori and its derivations, the facets rotate only around the creases, which implies that the configuration and mechanical behaviors of the unit or tessellation structure can be all determined by the side lengths and the rotation angles[46, 53-55]. When creases of an origami pattern are modeled as rotational hinges with a hinge spring constant, the energy calculation of the i-th crease is $U_i = k_i \cdot l_i \cdot \left(\varphi_i - \varphi_{i,0}\right)^2 / 2$ [54, 55, 90], where k_i, l_i, φ_i, and $\varphi_{i,0}$ are the rotation stiffness, length, dihedral angle and natural dihedral angle of the i-th crease. In this crease energy calculation, the dihedral angles can be obtained by the kinematic or matrix methods reviewed in Section 1.2.2.1. For the general origami pattern with no kinematic analysis, a vector method is introduced to the crease energy calculation. In this method, the definition of creases and facets are all described by vectors as shown in Fig. 1-5, and the crease energy for the i-th crease is given as $U_i = l_i \cdot \left(-k_i \cos\varphi_{i,0} \cdot \vec{u}_i \cdot \vec{v}_i - k_i \sin\varphi_{i,0} \cdot \left(\vec{u}_i \times \vec{v}_i\right) \cdot \vec{w}_i\right)$[91]. Then, the elastic energy of an origami unit or tessellation structure with N_c creases is shown as the summation of all crease energy.

$$U = \sum_{i=1}^{N_c} U_i \,. \tag{1-4}$$

For the rigid origami structure, the work of external forces is satisfied with the minimum total potential energy principle[54, 55], which offers the calculation method of external force and stiffness. In the tessellation structure with external forces shown in Fig. 1-6, the elastic energy is obtained by Eq. (1-4). The potential energy is calculated by the elastic energy and the work of the external forces, F_x, F_y, and F_z, applied in the three directions.

$$\Pi = U - \int_{\varphi_0}^{\varphi} F_x \cdot \frac{dD_x}{d\varphi'} d\varphi' - \int_{\varphi_0}^{\varphi} F_y \cdot \frac{dD_y}{d\varphi'} d\varphi' - \int_{\varphi_0}^{\varphi} F_z \cdot \frac{dD_z}{d\varphi'} d\varphi' \,. \tag{1-5}$$

Due to the principle, the condition of the equilibrium state when the structure is subjected to external forces is expressed as $d\Pi/d\varphi = 0$ [54, 55]. The external forces are calculated by

$$F_x \cdot \frac{dD_x}{d\varphi} + F_y \cdot \frac{dD_y}{d\varphi} + F_z \cdot \frac{dD_z}{d\varphi} = \frac{dU}{d\varphi}. \tag{1-6}$$

When the experiment is conducted by a uniaxial load, Eq. (1-6) is rewritten as

$$\overline{F}_x = \frac{dU}{d\varphi}\Big/\frac{dD_x}{d\varphi} = \frac{dU}{dD_x},\quad \overline{F}_y = \frac{dU}{d\varphi}\Big/\frac{dD_y}{d\varphi} = \frac{dU}{dD_y},\quad \overline{F}_z = \frac{dU}{d\varphi}\Big/\frac{dD_z}{d\varphi} = \frac{dU}{dD_z}. \tag{1-7}$$

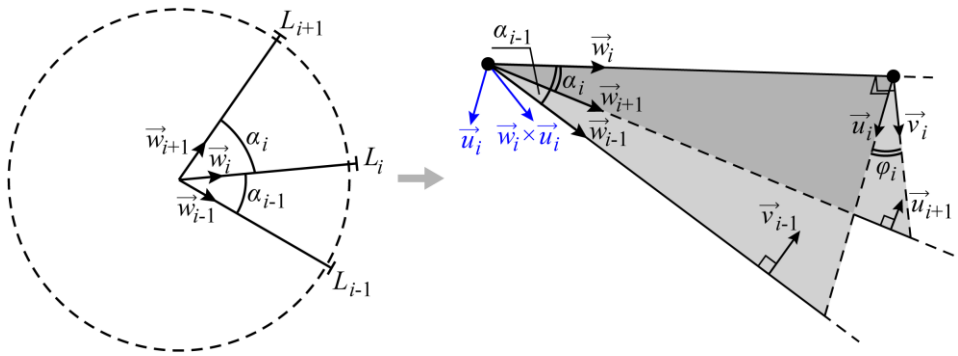

Fig. 1-5 Illustration of the calculation for general origami pattern established from an *n*-crease vertex.

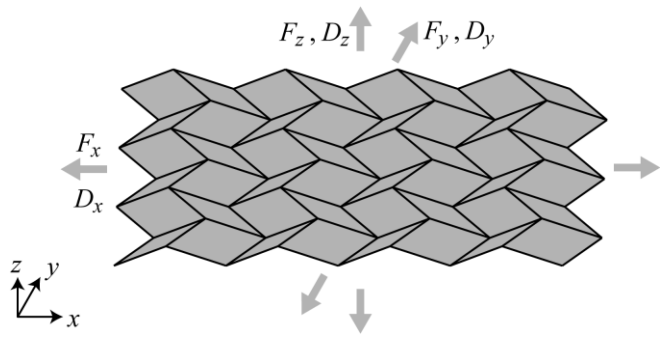

Fig. 1-6 Illustration of calculating the mechanical properties of rigid origami tessellation metamaterials.

Besides these analytical methods, the property of origami structure can be investigated by the finite element method[92], which has been validated in both quasi-static and impact test analysis on rigid origami structures[93]. To obtain an accurate analysis method, researchers also presented the combination of finite element method and theoretical analysis to study the mechanical properties of rigid origami structure[52]. The finite element method is sensitive to mesh, so the analysis of the optimal element

size has to be conducted before the simulation of the structure. In a practical origami structure, the length and width of the facets are much larger than their thickness. Many numerical simulations of the origami structure are quasi-static analyses, where the ratio of kinetic to internal energy is kept below 5% to ensure that the dynamic effect is insignificant.

This section reviews the investigations on the mechanical properties of rigid origami metamaterial. Some of the research methods have become the basis of the study on non-rigid origami metamaterials. Thus, the approaches to studying the mechanical properties of non-rigid origami metamaterials are explained in the next section.

1.2.3 Non-rigid Origami Mechanical Metamaterials

The unusual properties of non-rigid origami mechanical metamaterials are caused by their structural deformation that focuses on facet bending or stretching. The existing non-rigid folding behaviors are produced by two methods: (1) transition from rigid-foldable origami patterns to non-rigid ones by changing their material or geometric parameters, (2) the original pattern design shows a non-rigid folding process. Thus, the review of non-rigid origami metamaterials is presented in these aspects.

1.2.3.1 Non-rigid Origami Structures Created from Rigid-foldable Patterns

In the non-rigid-foldable structures transitioned from the rigid origami patterns, there are three established transition methods, including introducing material/geometric defects to rigid-foldable origami patterns, rationally changing pattern features of several component units, and modifying the construction of origami units.

In previous studies, most defective origami structures are established depending on the Miura-ori one and always show non-rigid foldability. Tuning the number and dimensions of imperfections is an effective way to program the mechanical properties of the corresponding metamaterials. For example, different materials of the facets can change the deformation mode of the original Miura-ori structure from rigid to non-rigid[94] (Fig. 1-7(a)). Compared with the high Young's modulus, the material with the lower one can be regarded as a defect. The stiff facets have the same motion as the original origami structures, while the soft ones contribute facet-bending behavior to the structure. The folded behaviors added by soft facets lead to programmable DoF of the non-rigid origami structure. Moreover, the example in Fig. 1-7(b) shows a method to

create pop-through defects on an original Miura-ori metasheet[95]. The defects break the rigid folding process of the Miura-ori structure due to their neighboring bending facets. Thus, the new bending behaviors affect the structure‘s responses to the compression load. The experiments in Ref. [95] established a relationship between the compression modulus of the defect Miura-ori structure and the number and location of the defects, which validate the programmable modulus of the defect origami structures. Besides, the imperfections appear not only on the 3D folded configuration but also in the 2D crease pattern. Literature [96] shows a perturbed crease pattern that is created by introducing a small perturbation on the vertices of a Miura-ori pattern, which changes the pattern from a flat-foldable one to a non-flat-foldable one (Fig. 1-7(c)). The non-flat folded configuration of the modified pattern affects its folded process and mechanical behaviors. The experimental and numerical analyses proved that the linear modulus and plateau stress of perturbed origami metamaterial are significantly affected by the degree of perturbation on the vertices[96].

Rational changes in pattern feature usually lead to graded origami patterns, which have regularly varied characteristics on one or several dimensions. For example, in the Miura-ori derivatives with graded mechanical behaviors, the changeable features include mountain-valley crease assignments and geometric parameters. Based on the regular switch between mountain and valley creases, various configurations are designed by Miura-ori pattern and result in different deformed and mechanical behaviors[97]. Further analyses show that the parameters of the metamaterials fabricated by stacking origami units can be graded both in and out of layers. The example in Fig. 1-8(a) shows a stacked Miura-ori metamaterial with two different sets of geometric parameters, which results in nested-in and bulged-out configurations[98-101]. The switch between two configurations is a non-rigid folding process and causes bistability in a two-layer construction. Then, the metamaterial assembled by multiple two-layer structures can achieve multi-stability and program its modulus by controlling the switch of nested-in and bulged-out configurations[98]. On the other hand, the example in Fig. 1-8(c) shows a metamaterial designed by identical layers of origami units with graded in-layer parameters[102]. Each layer of the structure is modeled by parallelogram facets at intervals of rectangular ones. In a compression test, the rectangular facets collapse after the parallelogram ones. The folding process of the parallelogram facets is a mechanism motion, and that of the rectangular one is a structural deformation. The two

different deformation behavior processes cause a two-stage graded peak force and stiffness. The above references express that the graded geometric parameters introduce a mechanism motion process followed by several structural deformed ones to the metamaterial. Since the structural deformation offers higher mechanical properties than the mechanism motion, the graded metamaterial structure designed by appropriate geometric parameters shows a progressive increase in the peaks of stress/force curves. Thus, a novel design method of graded geometric parameters has been presented to improve the force response and achieve superior energy absorption[56-58]. As shown in Fig. 1-8(b) and (d), the side lengths or sector angels decrease/increase progressively in the neighboring units and then influence the dimensions and shapes of the multi-layer metamaterial in height and width directions[56, 57]. Both types of graded metamaterial collapsed layer by layer or column by column, leading to multiple peaks in the stress or force curves and further high energy absorption.

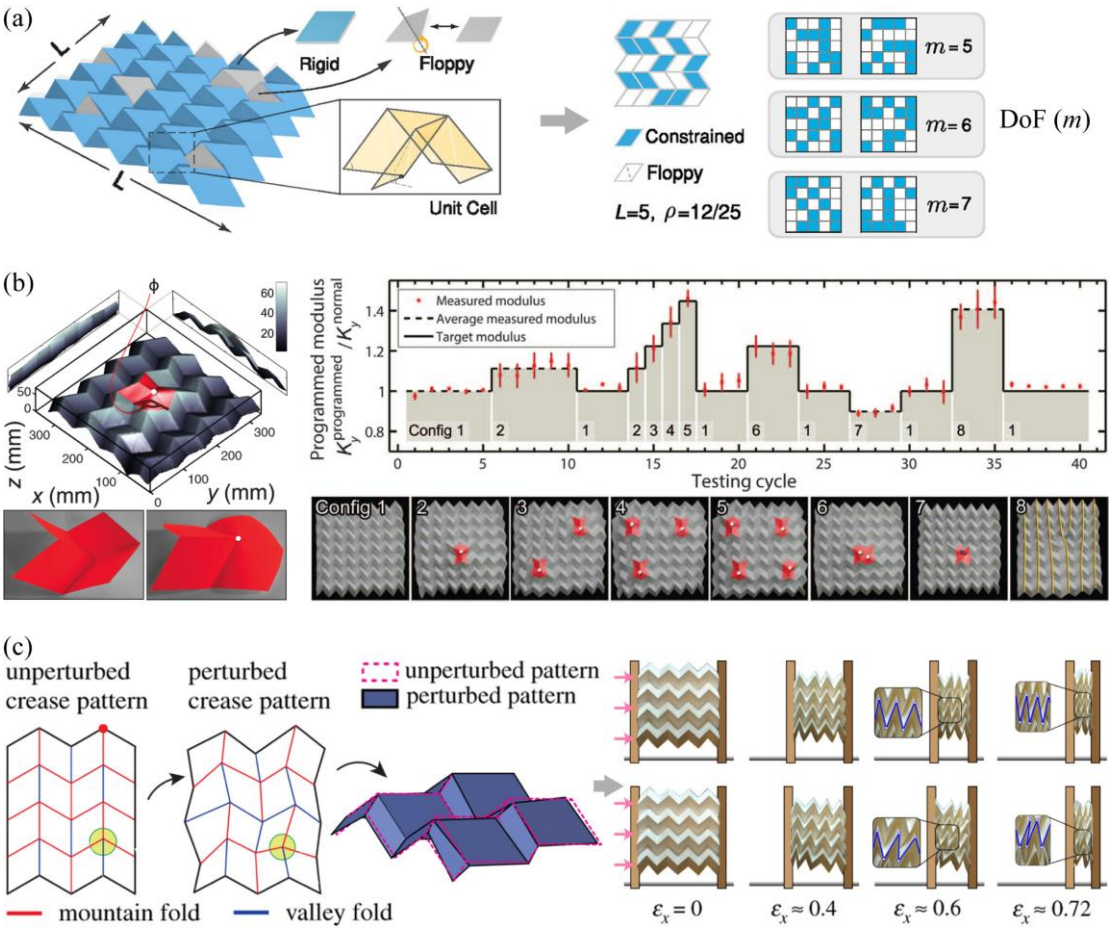

Fig. 1-7 Metamaterials designed by defective origami structures, such as (a) different materials on facets[94], (b) pop-through defects[95], and (c) perturbation of vertices[96].

Modifying the construction of origami units creates new building blocks in mechanical metamaterials, such as origami loops[103, 104] and modular units[105, 106]. The novel mechanical metamaterial designed by origami loops has programmable foldability and stability due to its tunable geometric parameters and formed methods. As shown in Fig. 1-9(a), identical rigid Miura-ori units can be used to produce origami loops through different assemble ways[107]. Both rigid and non-rigid foldability can be achieved in the origami loops because the compatible condition in the original Miura-ori structure is not always available in the looped origami structures in the folding process. Each non-rigid foldable origami loop shows a bistable behavior. This design principle allows the metamaterials fabricated by Miura-ori loops to retain the negative Poisson's ratio of Miura-ori units while producing multiple stable states. Moreover, a special class of closed loops, named star-shaped units, was proposed[108] (Fig. 1-9(b)). The results show that tuning the geometric parameters of the pattern can program the stability of the star-shaped unit from single to double. In the structure fabricated by several *n*-pointed star-shaped units, the discrete configurations that are satisfied the compatible condition introduces the multi-stable states to these star-shaped structures. Further analysis proves that a cubic metamaterial formed by lots of independent star-shaped origami loops can be programmed to have multi-stability and single-stability in different directions. In contrast to origami loops, modular origami structures usually have unique configurations that introduce reconfigurable and reprogrammable behaviors to the corresponding non-rigid origami metamaterials. A modular unit shown in Fig. 1-9(c) has two rigid-foldable paths distinguished by a non-rigid-foldable gap, which results in bistability[109]. The theoretical calculation in Ref. [109] proved that the bistability of the modular unit is controlled by the width of the non-rigid-foldable gap and programmed by geometric parameters. For modular origami metamaterials, the reprogrammable mechanical responses are produced by connecting the units with varied geometric parameters or in different stable states. Another modular origami metamaterial is designed by extruded polyhedrons that are assembled by folded ribbons[110-112], as shown in Fig. 1-9(d). The folded ribbons affect both the foldability[110] and DoFs (i.e. the number of the deformed path)[111] of the extruded polyhedron unit. The origami unit with multiple DoFs has various pre-folded states with different behaviors, which achieves reprogrammable mechanical responses[110] and reconfigurable acoustic waveguides[112] in the corresponding modular metamaterials.

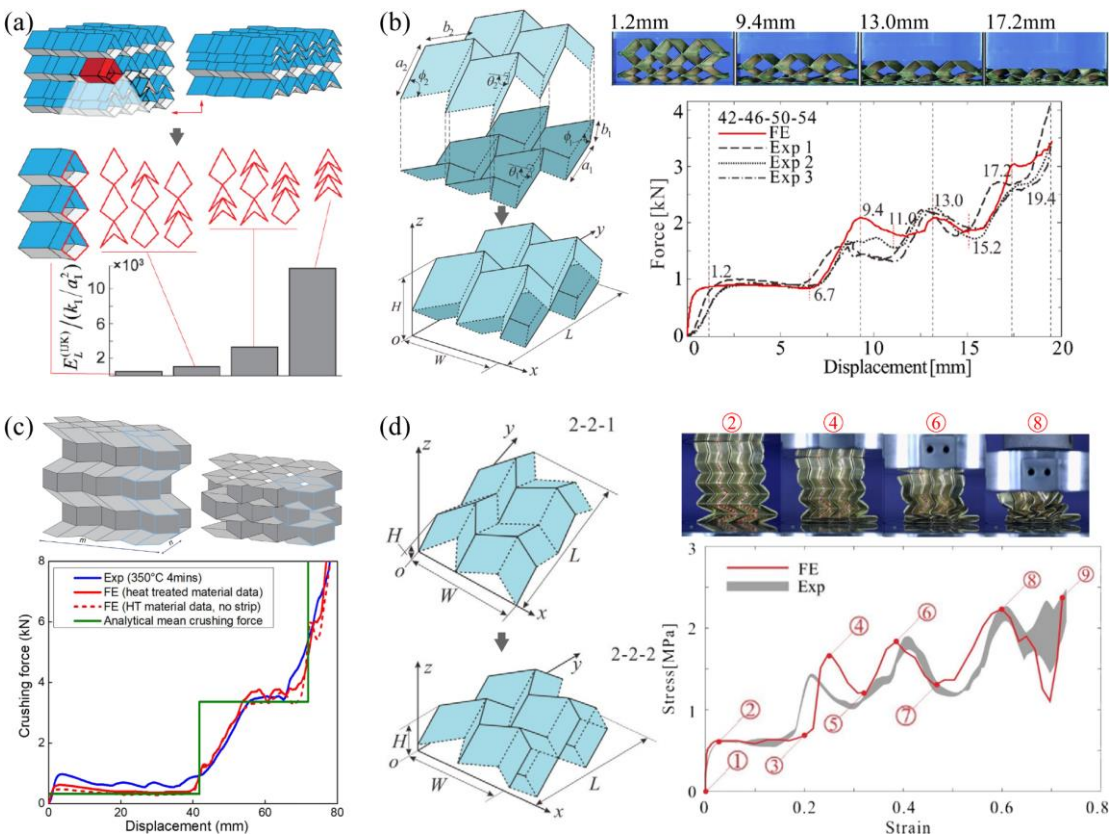

Fig. 1-8 Metamaterials designed by graded origami patterns, including graded geometric parameters (a and b) among different layers[56, 98], or (c and d) within identical ones[57, 102].

However, these non-rigid structures transitioned from rigid-foldable ones have their limitation in designing mechanical metamaterials. For the metamaterial fabricated by defective origami structure, defects reduce local stiffness and furtherly produce unexpected failure and fracture in their construction, which affects the mechanical properties controlled by deformations. In graded origami metamaterials, the design of geometric parameters significantly affects their mechanical properties, but the existing investigations mainly focus on the Miura-ori pattern. The effects of this method on other potential origami patterns need to be analyzed. For the metamaterial designed by origami loops, its programmability is only controlled by geometric configuration, such as the sector angles and side lengths. Once geometric parameters of the origami loop are determined, mechanical properties of the corresponding metamaterial cannot be tuned by other methods, such as switching some mountain creases to valley ones. Moreover, the disadvantage of modular origami metamaterials is that the original foldability and mechanical properties of the individual unit may not appear in the whole structure because of the connected behavior between neighboring units. Thus, many

researchers prefer to study the mechanical metamaterials created by the original non-rigid-foldable origami patterns.

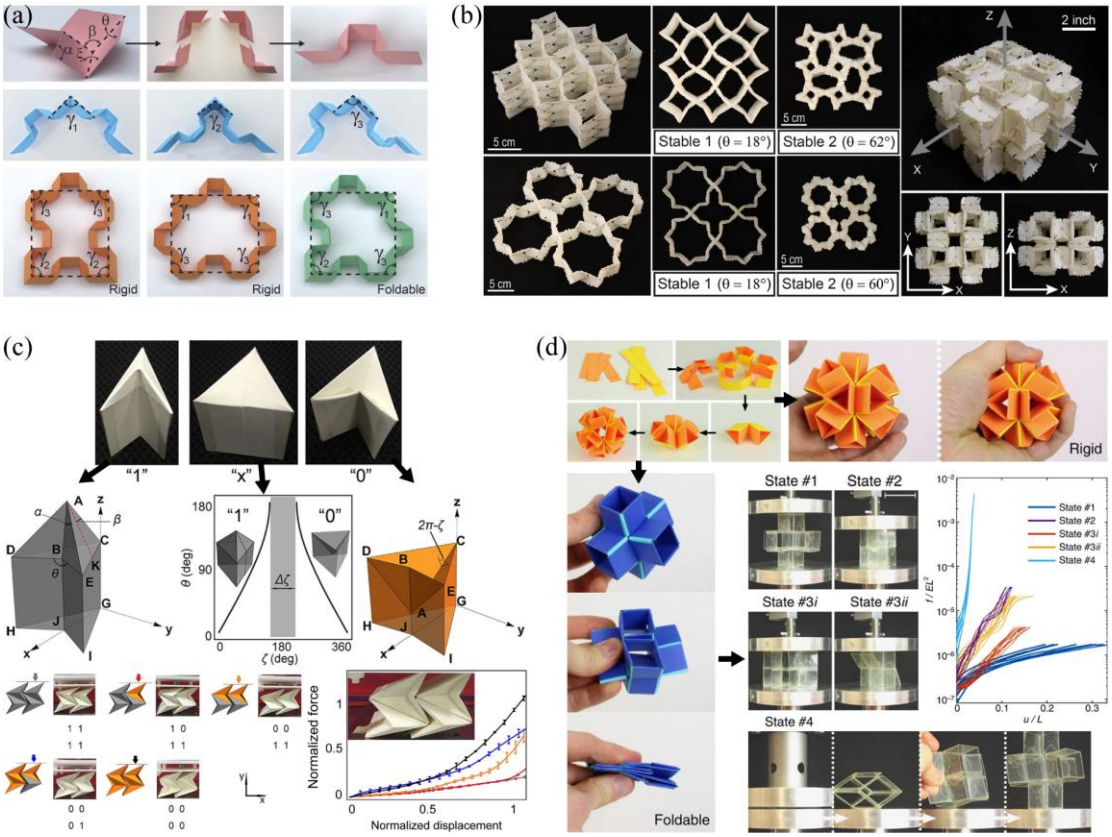

Fig. 1-9 Mechanical metamaterials designed by (a) origami loops[107], (b) star-shaped loops[108], (c) origami cube[109], and (d) extruded polyhedron with assembled folded ribbons[110].

1.2.3.2 Non-rigid Origami Structures Designed by Original Non-rigid-foldable Patterns

In addition to the non-rigid origami metamaterials created by modifying rigid-foldable patterns, the design principle of non-rigid-foldable ones is one of the most effective ways. Its unique configuration and deformation have an advantage in designing metamaterials that are satisfied with complex conditions. According to the facet's shape of the folded configuration, the original non-rigid-foldable structures can be divided into two groups: the planar origami and the curved one.

The planar origami patterns can form both planar and tubular metamaterials. For the planar metamaterials, a traditional origami pattern named Ron Resch pattern[53, 113] has a complete non-rigid folding process except for the configuration where the dihedral angles of valley creases equal zero[113]. The compression on the zero-angle construction

causes a further deformation of the vertical facets and valley creases, which offers a high energy absorption. In the tubular metamaterials, one of the famous non-rigid origami patterns is triangulated cylinder pattern, also called Kresling pattern[47, 114-121]. The significant behavior of Kresling unit is that the number of equilibrium states can be tuned by sector angles of the pattern[47, 119]. As shown in Fig. 1-10(a), the Kresling structure with small sector angles has two equilibrium states, which results in easy deployability and collapsibility. But that with large sector angles has only one equilibrium state, which implies high load-bearing capability. Another special behavior of the cylinder structure with large sector angles (see Ref. [119]) is collapsing along two different paths because the height of the completely deployed state is lower than the maximum one. The cylinder structure that is stretched to the maximum height before compression is easy to reach the collapsed state while that along direct compression path is hard. It indicates that two different mechanical responses can be achieved in the same Kresling structure and can be tuned by an external load. Then, a metamaterial that can both be deployed and carry load are able to be created based on this origami design method. In a further study, the Kresling pattern with easily collapsible units was used to fabricate a metamaterial mechanism that can form rarefaction solitary waves[120] (Fig. 1-10(b)). When the metamaterial was under an impact load, the analysis results in Ref. [120] showed that the former part of the origami structure feels compression while the latter part feels tension first. This special phenomenon allows the metamaterial to create an impact mitigating system independent of the material properties. Meanwhile, the two equilibrium states result in chaotic dynamics of the Kresling pattern, where the energy absorption performance[121], the nonlinear spring behavior[122] and the prediction of nonlinear dynamic behavior[123, 124] have been received attention. The special deployed and folded configurations of Kresling pattern also enable itself to combine with magnetic actuation[125, 126] (Fig. 1-10(c)) or motor-driven tendons[71], and further achieve origami robot with highly integrated motion and multi-stability[127-129]. In the engineering field, the bistable resonator created by Kresling structure can efficiently tune the torsional bandgaps to solute the torsional vibrations[130]. Moreover, the Kresling pattern can be combined with the 4D printed method, in which the shape memory materials help to produce the tunable compression twist behavior[131]. Changing the arrangement and sector angles of the triangular facets, the twisting triangulated cylinders with spring behavior were produced[132, 133]. The spring behavior

is produced by the combination of collapsible twisting unit and the elastic material, where the former is for energy storage and the latter is for shape recovery. These characteristics contribute to building a soft robot with highly reversible compressibility. When the crease assignment and sector angles are modified in another way, a diamond pattern is created and shows similar mechanical behavior as the Kresling pattern. The load-carrying behavior allows the structure of diamond pattern to be used to improve energy absorption devices[134].

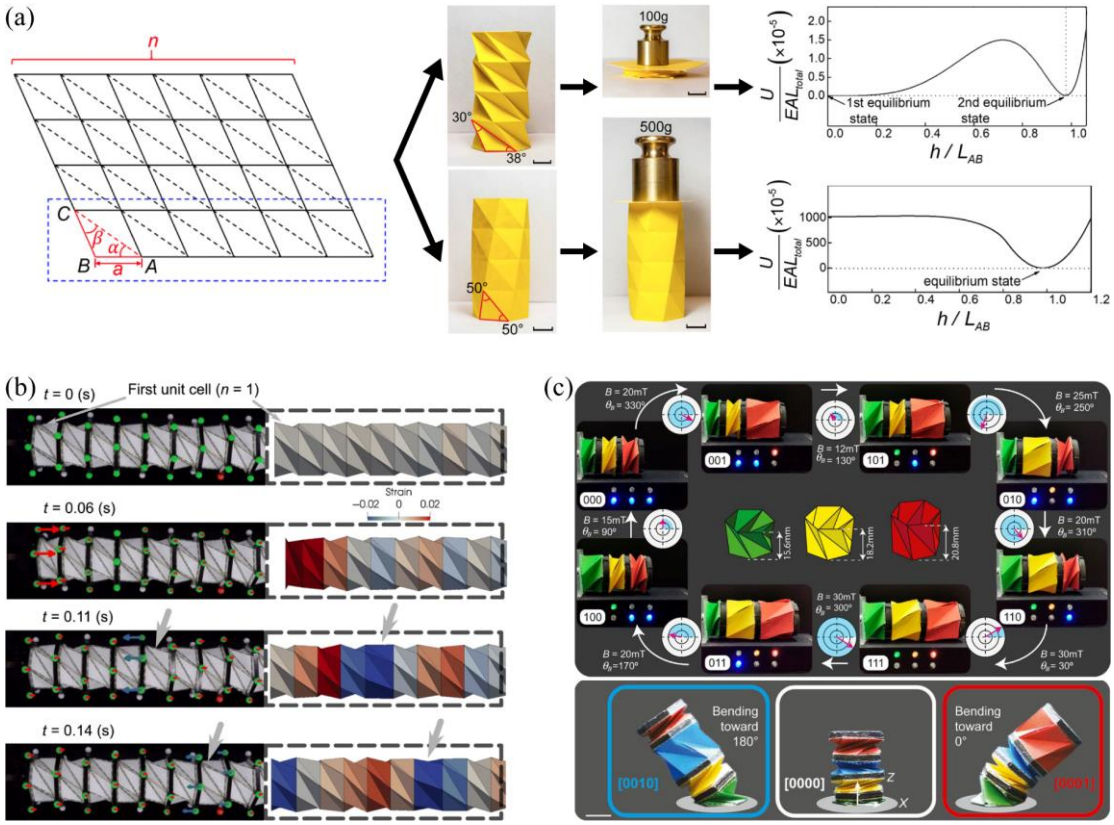

Fig. 1-10 Metamaterial based on Kresling origami pattern, which creates (a) programmable equilibrium states[119], (b) impact mitigation[120], and (c) origami robot[125, 126].

Besides the origami patterns consisting of planar facets and straight creases, the curved origami patterns can also form non-rigid origami metamaterial because of the deformation caused by buckling or bending surface. The existing design principles of curved origami patterns include curved-crease[135-138] and curved surfaces[139-141] (Fig. 1-11). All curved origami structures show deformed motion and configurations caused by the bending behavior of facets combined with the bending and folding behavior of the creases. To establish an analytical model of curved origami structure, the elastica

surface generation method[142, 143] is introduced to the design of curved origami construction, where the novel mechanical response and structure's developability can be both accomplished. Further work proved that the mechanical properties of a curve origami metamaterial can be tuned by the curvature of the creases[135].

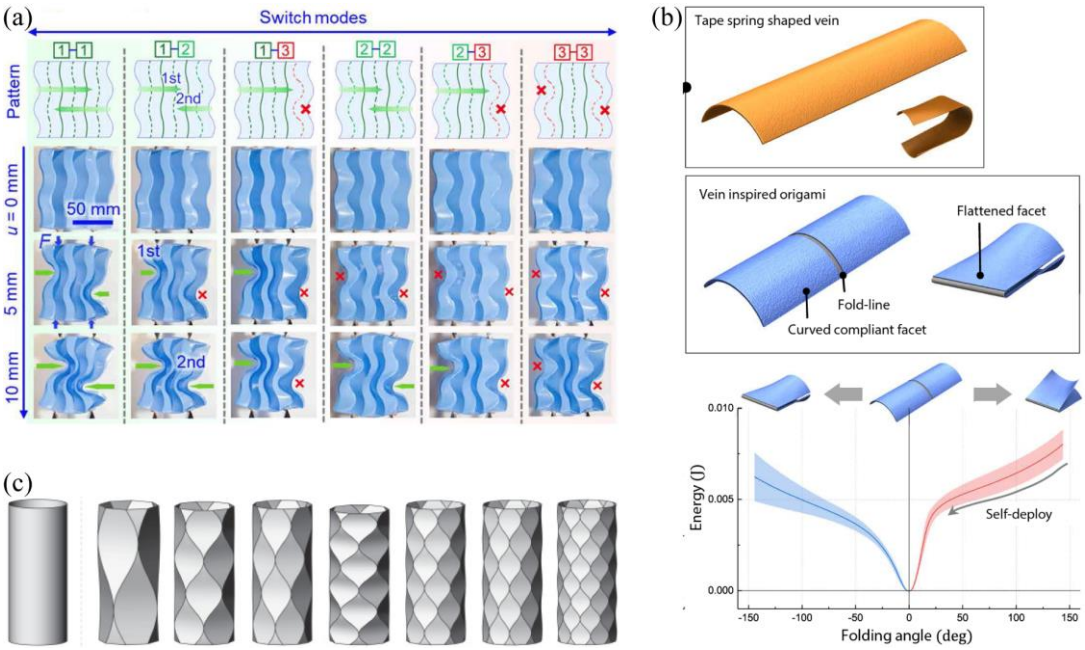

Fig. 1-11 Metamaterials inspired by curved origami pattern including (a) curved-crease on planar surface[135], (b) straight crease on curved surface[139], and (c) curved-crease on curved surface[140]。

There are also some unsolved problems in the metamaterials produced by non-rigid-foldable origami patterns. The curved origami pattern usually has difficulty fabricating practical models because the material sheet on the boundary of the curved structure cannot meet the curvature of the design principle. It limits the experiments and practical applications of curved origami structures. For other non-rigid-foldable origami patterns, the configuration cannot generally be accurately calculated by analytical methods. So, the difficulty of studying the corresponding metamaterials is quantifying their mechanical properties.

The references in Section 1.2.2 present that contribution from structural deformation can extensively increase the overall stiffness and enlarge the energy landscape of the origami-inspired metamaterials. The facet bending and stretching in the non-rigid structures lead to a wider range of mechanical properties as opposed to rigid ones. However, past researches mainly focus on metamaterials formed by a single

type of rigid or non-rigid origami structure/pattern. The possible mixture of origami units with different rigidities requires more attention because it can cover a wide range of mechanical properties.

1.2.4 Study Methods of Non-rigid Origami Metamaterials

The non-rigid-foldable patterns give significant facet deformation during folding to the corresponding origami structures and metamaterials[65]. And they offer a much larger collection of crease patterns and hence could lead to wider and more versatile potential applications compared with rigid origami patterns. However, it is very difficult to predict the motion of non-rigid-foldable origami analytically due to the simultaneous deformation along creases and within facets. Thus, developing a better and more predictive understanding of non-rigid-foldable origami remains a challenge. Overcoming this hurdle will result in novel mechanical metamaterials with programmable properties.

1.2.4.1 Mechanical Analysis of Triangular Pattern

In general non-rigid triangular patterns, the deformation of the facets is illustrated by the stretching and rotation of the creases, which gives assumed conditions for calculating the structure's elastic energy. For example, when an origami structure has N_{c1} creases stretched and N_{c2} creases rotated in the folding process, the elastic energy can be given by

$$U = \sum_{i=1}^{N_{c1}} \frac{1}{2} k_{s,i} \cdot \left(l_{s,i} - l_{s,i,0}\right)^2 + \sum_{i=1}^{N_{c2}} \frac{1}{2} k_{r,i} \cdot l_{r,i} \cdot \left(\varphi_i - \varphi_{i,0}\right)^2 , \tag{1-8}$$

where $l_{s,i}$, $l_{r,i}$, $k_{s,i}$, $k_{r,i}$ are the length and stiffness of the stretched and rotated creases, φ_i is the rotation angles of the rotated creases, and subscript 0 represents the initial state[120]. In this method, the length of the stretched creases and the rotation of the rotated creases are all calculated by the deformed configuration of the origami structure. Thus, it is only available for non-rigid origami with a known analytical model at arbitrary configuration. The configuration of non-rigid origami structure usually includes stable and instable modes. For non-rigid triangular patterns, the stable or instable states can be determined by introducing bar, cable-rod, or cable-rod-membrane models with vertices defined as finite particles to analyze the non-rigid structure[144].

Furthermore, the numerical simulations were also introduced to the nonlinear study of non-rigid origami structures with triangular facets, where the creases are all

modeled as bars and simulated by truss elements[145, 146]. The Young's moduli of the three types of creases are different, where the stiff ones are used for keeping the constant length of the crease and the soft ones enable the structure to fold. However, when the Kresling structure is fabricated by engineering plastic, the stiff assumption is not applicable for the triangular facets. The solution to this situation is that the four-node shell elements are used to model the triangular facets while the nodes on all sides of one polygon are fixed at a reference point[147]. All finite element models that are used in further study need to be validated by analytical or experimental results.

Noting that the above research methods only contain the crease deformation while ignoring the effect of the facets, this theoretical modeling method cannot accurately describe the configuration of the whole non-rigid origami family. The non-rigid origami with other shaped facets demands new approaches.

1.2.4.2 Mechanical Analysis of Non-triangular Pattern

The challenge for property characterization and programming the mechanical behaviors of non-rigid patterns is caused by their complicated deformation modes. For non-rigid origami structures with non-triangular patterns, a commonly used approach is to triangulate the pattern by adding extra virtual creases in non-triangular facets[65]. The non-rigid origami structure usually has a few compatible configurations and a series of incompatible ones[148]. The former can be determined by crease rotations as those used in rigid origami structures, while the latter can be modeled by simplifying the facet bending as a rotation of the virtual crease on the diagonal of the facet. This usually will turn a non-rigid pattern into a rigid one[149], but not necessarily with one degree of freedom. Then by assigning different rotational stiffness to the original and virtual creases, the deformation of the pattern can be solved analytically in certain cases[150]. Based on these analytical crease rotations, the energy of the non-rigid origami structure can be obtained by the rotation energy of both original and virtual creases. Moreover, several computational approaches based on the same triangulation principle have also been developed for non-rigid patterns, such as bar-and-hinge models[151] or pin-jointed bar framework models[152]. In these computational models, the creases are modeled by bar elements with rotational springs, where the former shows the deformation of the creases and the latter explains the folding behavior around the creases. And the facets are triangulated by a bar element on the diagonal, where the

rotation of the bar element represents the bending behavior of the facet. Thus, the vertices in the pattern become the joint between these connected bar elements. The potential energy of the system can be expressed as $\Pi = U_{\text{bar}} + U_{\text{spr}} - W_{\text{ext}}$, where the strain energy stored in both the bar elements, U_{bar}, and the rotational springs, U_{spr}, and W_{ext} is the external work. Those models enable an analysis of complicated patterns very efficiently in comparison with standard finite element models, but also inevitably preserve the limitation of pattern triangulation.

The essence of this facet triangulated approach is using the rotation of virtual creases to simulate the bending of facets, when the main deformation of the facets is bending with a single curvature, this approach will yield quite accurate results. However, when the facet distortion is more complex with non-zero Gauss curvature or the non-rigid pattern is already formed by only triangular facets and cannot be further triangulated, it would be difficult to obtain realistic results out of this approach. When only one or a few facets in a non-rigid pattern are noticeably bent with a single curvature, it is possible to add virtual creases only to those facets and obtain an equivalent rigid pattern with a single degree of freedom. Yet, there is no ready solution for every non-rigid pattern. As the complexity of the pattern increases, an analytical solution cannot always be obtained. In response to this difficulty, finite element models of the pattern have been developed for specific applications[153, 154]. In modeling the deformation process, one method uses the eight-node linear brick elements to form a continuous model where the differences between creases and facets are caused by the thickness of the element[154], while the other one uses four-node shell elements in the model where the rotation stiffness of the creases can be quantified as a spring constant of hinges[65]. However, most finite element analyses of non-rigid origami structures only offer qualitative study of the deformed modes and mechanical properties[153]. The validation by comparison with experiments or analytical results is required in using the finite element method to quantitively research and furtherly predict or program the mechanical behavior of non-rigid origami structures[56].

The references reviewed in Section 1.2 show that origami-inspired mechanical metamaterials have the potential for many applications, such as soft robots, energy absorptions, and adaptive systems. The rigid and non-rigid origami structures both offer novel and exotic properties to mechanical metamaterials. But previous studies are conducted on a single type of rigid or non-rigid origami structure. A possible mixture

of rigid and non-rigid origami structures is required to widen the range of mechanical metamaterials' properties. Thus, the potential design approach combining rigid and non-rigid origami units in a single metamaterial demands more attention. Meanwhile, the validated theoretical or experimental analysis corresponding to each type of unit contributes to the accurate prediction and programming of mechanical responses of the whole metamaterial.

1.2.5 Square-twist Origami Mechanical Metamaterials

In the traditional origami patterns, 'square-twist' origami, first proposed by Kawasaki and Yoshida[66], is remarkable because it has both rigid- and non-rigid-foldable types controlled by the assignment of mountain and valley creases. The assignment characteristics confirm that the square-twist pattern has four unique types[155, 156], named type 1-4 (Fig. 1-12(a)). The illustration in Fig. 1-12(a) shows that each type of square-twist origami pattern contains four identical 4-crease vertices. Meanwhile, the kinematic analysis of 4-crease vertices indicates that different relationships between rotation angles occur on the vertices with varied mountain-valley assignments[149]. Thus, based on the motion transmission path, the compatible condition established on the close-loop of four vertices implies that there are two non-rigid-foldable (type 1 and 2) and two rigid-foldable (type 3 and 4) square-twist origami patterns [149, 157] (Fig. 1-12(b)).

The rigid type 3 and 4 square-twist patterns have simple mechanical behaviors due to the deformation of rigid origami configuration concentrating on the creases, which leads to few studies existing in these two origami units. The non-rigid type 1 and 2 square-twist patterns have rotationally symmetric behavior in both mountain-valley crease assignment and folding process, which results in complex deformation and further produces numerous mechanical properties. Thus, more researchers focus on the two non-rigid origami units, especially the type 1 square-twist unit. Previous studies have used the type 1 square-twist origami pattern to design an origami-equivalent compliant mechanism[153], frequency reconfigurable origami antenna[154], and mechanical energy storage[158] (Fig. 1-13). Most of them ignore the facet distortions by replacing the facets with flexible linkages or fabricating the creases with lower material stiffness than the facets. However, the facet deformation plays a key role in providing the non-rigid origami units with widened mechanical behaviors, such as the strong self-

locking behavior resulting from the interaction between facets in type 1 square-twist unit. So, both crease and facet deformation need to be analyzed before using the square-twist units to design mechanical metamaterials.

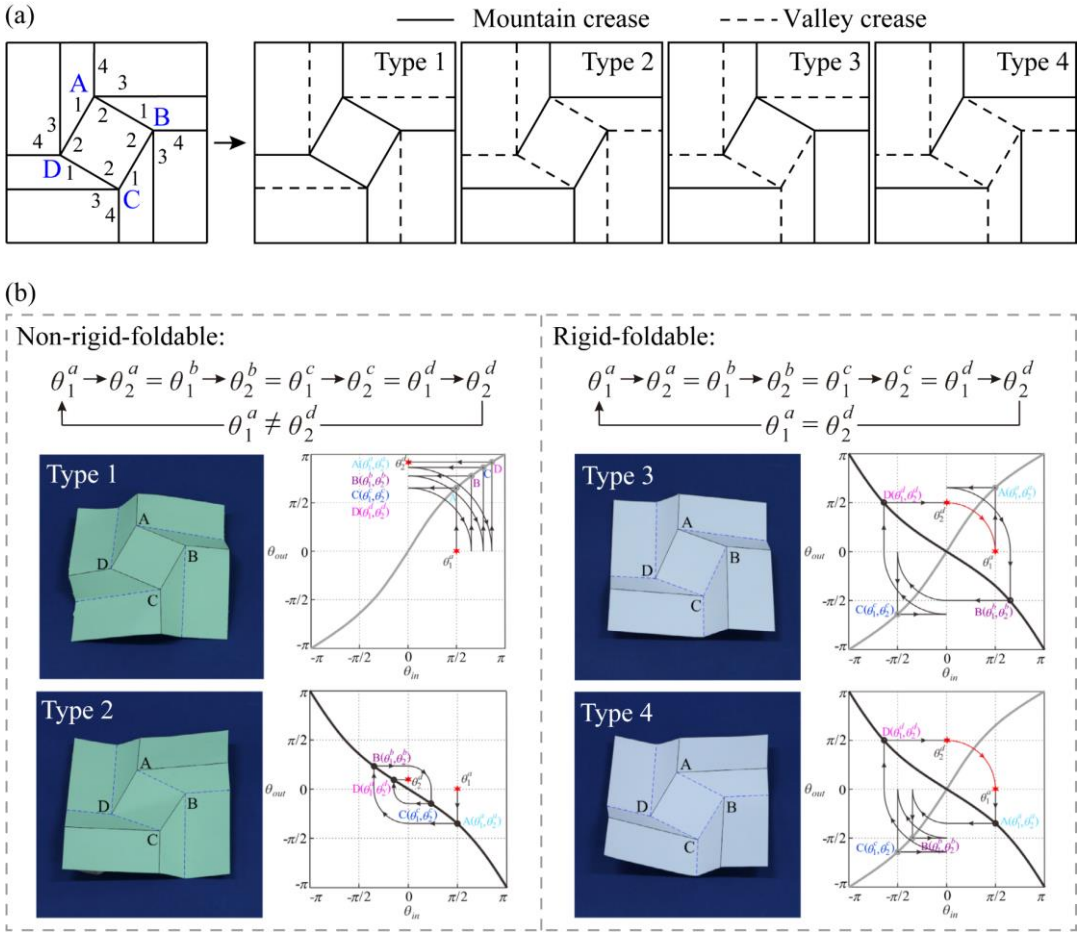

Fig. 1-12 (a) Square-twist origami pattern and four different mountain-valley assignments. (b) The rigidity of type 1-4 square-twist patterns[149].

Designing metamaterials with a wide range of tunable properties needs to solve two problems. First of all, it is important to propose a potential design approach that combines rigid and non-rigid origami units in a single metamaterial. It should be noted that incorporating origami units of different types is in general not trivial because they commonly have different crease numbers and mountain-valley assignments, and thus, may not be compatible with each other. However, the four types of square-twist patterns possess an identical crease layout, which makes it possible to tessellate different units together while maintaining geometrical compatibility in the flat and fully folded states. Folding a pattern with such a mixture of units with different rigidities opens up ample

opportunities to program the mechanical properties. By varying the proportion of each type of unit, the mechanical properties can be tuned between an upper limit posed by the non-rigid pattern and a lower limit set by the rigid one. The second problem is to find out the quantitative relationship between the mechanical properties of the pattern and the geometric and material design parameters. Previous efforts on mechanical characterization of the non-rigid square-twist pattern include triangulating the entire pattern and analyzing it as a system of bars and hinges[65]. Alternatively, a virtual diagonal crease was introduced in the central square facet to turn it into a rigid pattern with a single degree of freedom[159] so that it can be analyzed using an established mathematical[160] or kinematic approach[149]. Nevertheless, those two approaches could not capture the complex facet deformation in the pattern. Thus, the equivalent theoretical model has attracted researchers' attention and expressed the constitutive relation and stability of the square-twist units[161]. Moreover, finite element models of the pattern have also been developed for specific applications[154, 158], but little information is given about the detailed deformation process or validation with experiments.

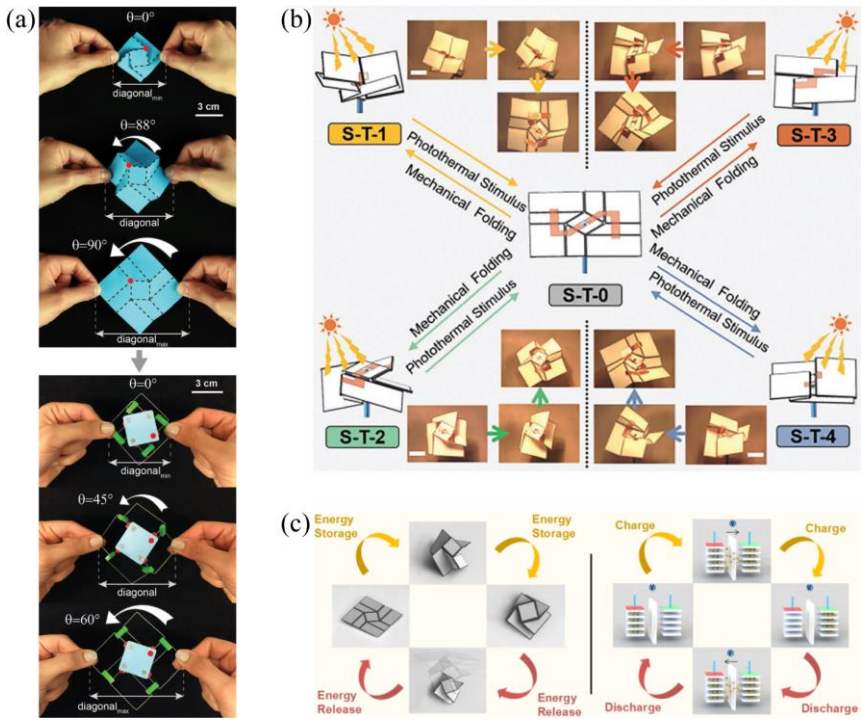

Fig. 1-13 Metamaterials inspired by non-rigid-foldable square-twist origami pattern, which have applications in (a) origami-equivalent compliant mechanism[153], (b) frequency reconfigurable origami antenna[154], and (c) mechanical energy storage[158].

In conclusion, due to the varied rigidity of different square-twist units, the origami pattern can be used to design metamaterials to cover a wide range of mechanical properties. Section 1.2.5 indicates that the unresolved issues are the construction principle of different units and programming methods of mechanical properties.

1.3 Aim and Scope

This dissertation aims to establish the validated mechanical model of non-rigid-foldable square-twist origami patterns, find a general tessellated method for a variety of square-twist units, and propose an approach to program and predict the mechanical properties of the corresponding tessellated metasheets.

In this process, the theoretical model of the mechanical property of rigid foldable units has been obtained by the known relationship between the rotation angles. Thus, the predicted or programmable model of mechanical properties of the non-rigid square-twist origami units is firstly investigated. For the non-rigid type 2 unit, a theoretical model is presented according to the kinematic analysis that converts the foldability of the unit. For the complex non-rigid type 1 unit, an empirical model is proposed using the combination of finite element model and experimental analysis. Depending on the theoretical or empirical models of the non-rigid units, their mechanical properties can be programmed by the geometric and material parameters. Then, a tessellation rule for the square-twist metasheets is explored using the rigid and non-rigid unit patterns. The metasheets with the compatible crease assignments and the gradient geometric parameters are both designed in this research. Finally, the approach for predicting the mechanical behaviors of the square-twist metasheets is introduced. Based on the relationship between the mechanical behavior and geometric or material parameters discovered in the study of units, the programmability of properties of the metasheets can be achieved by increasing/reducing the proportion of one type of unit or changing their designed parameters. As the evaluation of the metasheet, this study focuses on widening the range of the tunable properties and creating superior mechanical behaviors.

1.4 Outline of Thesis

This dissertation consists of five chapters, which are outlined as follows.

Chapter 1 presents a review of the previous works on mechanical metamaterials and mechanical modeling methods of rigid- and non-rigid-foldable origami structures.

Chapter 2 proposes a method to create the theoretical model of the non-rigid type 2 pattern based on the kinematic analysis of the rigid modified type 2 pattern that has an additional crease compared with the non-rigid one. The axial tension experiment introduced to the type 2 and modified type 2 pattern validates the theoretical model and explains an important bifurcation behavior of the pattern. The mechanical properties of the type 2 pattern can be programmed by the theoretical model, which becomes the foundation for predicting the behaviors of the corresponding uniform tessellation.

Chapter 3 is to build an empirical model of the non-rigid type 1 pattern using the combination of biaxial tension experiment and numerical simulation after the kinematic analysis method proves to be unavailable for its deformed behaviors. The correlation between the geometric and material parameters of the structure and its mechanical properties can be obtained by the empirical model. Then, the programmable mechanical properties of the pattern depending on the empirical model are discussed, where its possibility of use in a uniform tessellation is illustrated.

Chapter 4 is devoted to seeking a validated approach to creating a series of square-twist metasheets with programmable mechanical properties. First, the tessellation rule of the metasheets formed by different types of units or different geometric parameters is presented. Then, the quasi-static tension experiments are conducted to establish the relationship between the metasheets with different constructions and their deformation process and mechanical properties. Finally, the global mechanical properties predicting and programming of the square-twist metasheets are achieved by calculating and tuning their constitutional unit behaviors, respectively.

As a conclusion of this dissertation, Chapter 5 summarizes the main achievements of the research and the suggestions for future works.

Chapter 2 The Non-rigid Square-twist Type 2 Unit

2.1 Introduction

The type 2 square-twist pattern is composed of a central square facet, four trapezoidal ones, and four rectangular ones, with the mountain-valley crease arrangement and folded configuration shown in Fig. 2-1. It is parameterized by two side lengths, l and a, and a twist angle, α. For theoretical characterization of the non-rigid-foldable pattern, determination of the deformation mode is a prerequisite. Folding and unfolding of a cardboard model indicated that besides rotation of the creases, the central square seemed to be noticeably bent whereas all the other facets were nearly flat. In rigid-foldable patterns, the deformation of origami structures comes only from the rotation of creases, the dihedral angles of which can be theoretically derived. Consequently, the elastic energy of the structure can be easily calculated by adding up the energy in each crease[54].

For theoretical characterization of the non-rigid-foldable type 2 pattern, however, two major challenges arise, i.e., how to obtain the dihedral angles of the creases and how to calculate the bending energy of the deformed central square. Here, the approach of adding a virtual diagonal crease between vertices B and D is adopted on the central square so as to derive the dihedral angles of all the creases from the kinematic model of the modified type 2 pattern, and to quantify the bending energy of the central square as rotation energy of the virtual crease.

The outline of this chapter is as follows. In section 2.2, an axial tension experiment is introduced to the type 2 pattern. Section 2.3 presents the kinematic analysis of the type 2 pattern modified by adding a crease on the central square. The theoretical model of type 2 and modified type 2 pattern is built based on the kinematic analysis result in Section 2.4. In Section 2.5, the validation of the theoretical model and the stability analysis are presented by experiments. An important bifurcation behavior of the pattern is also discussed in this section. In Section 2.6, the theoretical model is utilized to program the mechanical properties of the pattern. Furthermore, a 2×2 type 2 metasheet is tested to demonstrate the feasibility of the proposed theoretical model. Finally, a conclusion is given in Section 2.7.

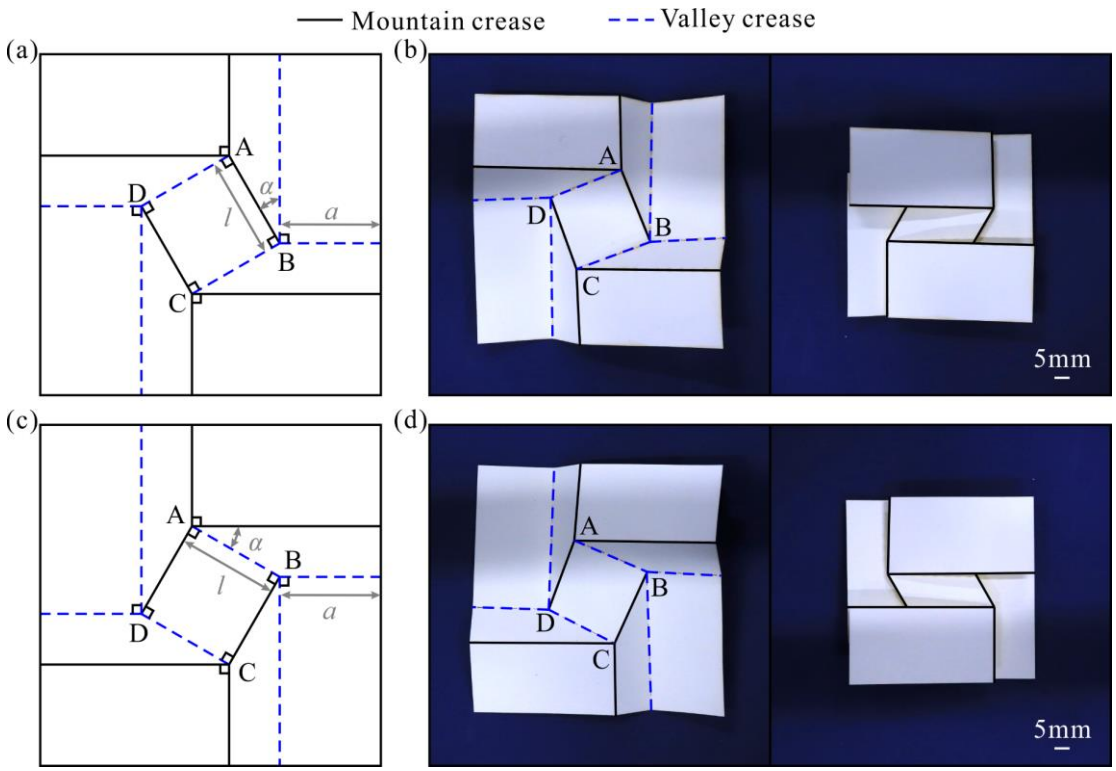

Fig. 2-1 (a and c) Pattern, geometric parameters, and crease mountain-valley assignment of type 2 square-twist pattern with left-handed and right-handed versions, (b and d) unfolded and folded configurations of a paper model with left-handed and right-handed versions.

2.2 Uniaxial Tension Experiment

2.2.1 Digital Image Correlation (DIC) Test

Considering the two-fold rotational symmetry of the type 2 unit, a uniaxial tension experiment in the diagonal direction was established to quantify the deformation of the central square. As shown in Fig. 2-2. The experiment was conducted on a horizontal testing machine developed in house to avoid the influence of gravity. The machine had a load cell of 50N with an accuracy of 0.5% and a stroke of 800mm. The specimen was tensioned by a displacement of 32.96mm at the loading rate of 0.2mm/s to eliminate dynamic effects. The deformation process of the experiments was recorded using a standard digital camera (Canon 70D) at 25 frames per second. The exact deformed configuration of the central square facet was captured by a digital image correlation (DIC) system CSI Vic-3D9M with a camera resolution of 2704×3384 pixels at a frame time interval of 500ms.

The specimen shown in Fig. 2-3 was fabricated from polyethylene terephthalate (PET) of thickness t=0.5mm using a Trotec Speedy 300 laser cutter. The geometry of the specimen was selected as a=25mm, l=25mm, and α=30º. The creases were cut as dotted lines of 2mm×0.3mm perforations at 1mm intervals in Fig. 2-3(a). To decrease the stress concentration and avoid the crack initiation and propagation, a circle perforation was produced on the vertices of the patterned material sheet. Then, it was folded by hand to form the origami structure. The specimen was attached to the machine using two fixtures as shown in Fig. 2-3(b). The left one was fixed on the load cell, whereas the right one on the support had a rotational degree of freedom to allow the specimen to rotate about the x-axis. Moreover, a hinge was connected to each fixture to enable rotation of the specimen about the y axis. The central square marked by red lines was painted with black speckles, which was the measured area for DIC capture of the type 2 specimen.

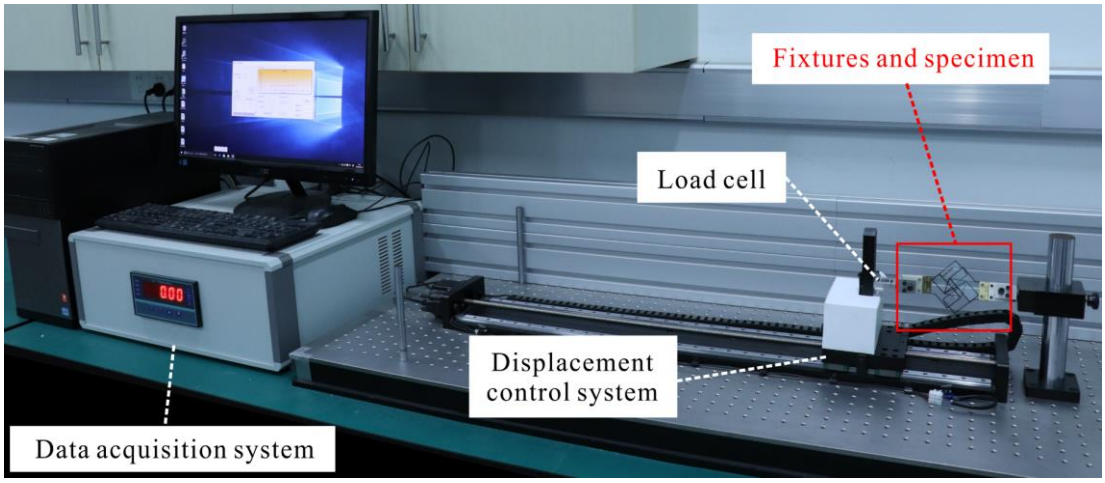

Fig. 2-2 Experimental setup, where the horizontal testing machine consists of a load cell, displacement control, and data acquisition systems.

2.2.2 Geometrical Reconstruction

The experimental result of the type 2 specimen is shown in Fig. 2-4. Four configurations of the specimen with tension displacement Δx=0mm, 4.84mm, 15.48mm, and 21.12mm, are shown in Fig. 2-4(a) as representatives. It is observed that during tension, facet rotation about the creases dominates, whilst the central square facet always bends and unbends along diagonal A–C. Then the exposed areas of the

square enclosed in the red quadrilateral regions are geometrically reconstructed using DIC and subsequently fit with single-curved surfaces with the following polynomial governing equations

$$f_{\mathrm{i}}(x)=0 \tag{2-1a}$$

$$f_{\mathrm{ii}}(x)=-1.61\times10^{-6}x^4-3.23\times10^{-5}x^3+1.11\times10^{-2}x^2+1.76\times10^{-2}x-3.72\times10^{-2} \tag{2-1b}$$

$$f_{\mathrm{iii}}(x)=2.26\times10^{-6}x^4-3.16\times10^{-5}x^3+1.36\times10^{-2}x^2-1.47\times10^{-2}x-3.61\times10^{-1} \tag{2-1c}$$

$$f_{\mathrm{iv}}(x)=5.36\times10^{-6}x^4-2.00\times10^{-5}x^3+1.17\times10^{-2}x^2-8.10\times10^{-3}x-3.06\times10^{-1} \tag{2-1d}$$

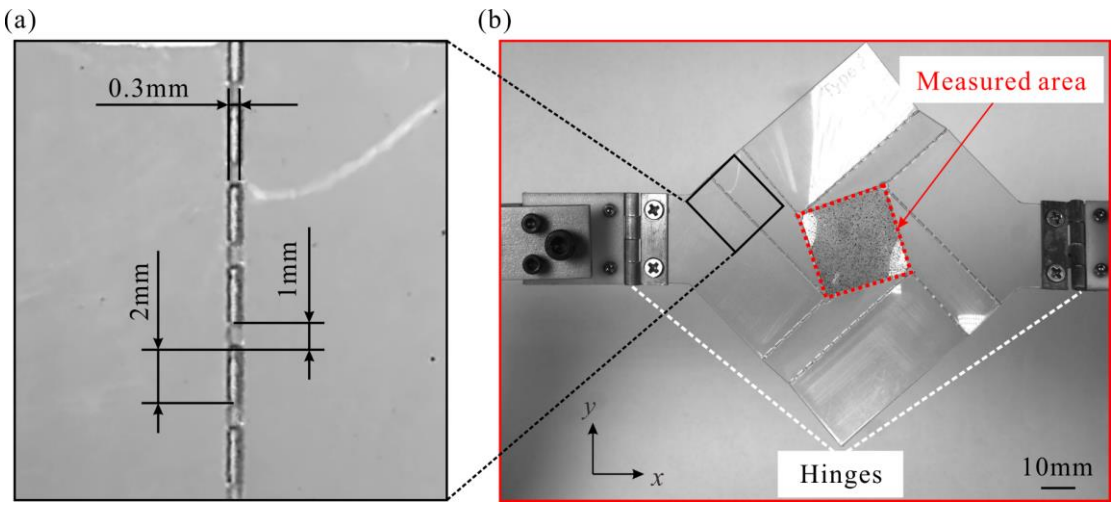

Fig. 2-3 Details of (a) the specimen and (b) fixtures.

As shown in Fig. 2-4(b), geometrically reconstructed central squares (measured area) were established using DIC (colored points) and best-fit polynomial single-curved surfaces (yellow surfaces) in Eq. (2-1). A good match between the experimental result and the fitting surface is obtained in all four configurations, with the fitting error calculated in Fig. 2-4(c) being within half of the material thickness (the green and yellow areas in pie graphs) in over 90% of the measured area. Hence, it has been proven experimentally that the central square of the type 2 pattern is subjected to bending with a single curvature, based on which a theoretical model will be built to characterize its mechanical behavior. Noting that the bending behavior of the central square in Fig. 2-4 is similar to the folding behavior of the central square with an additional crease. Here, the approach of adding a virtual diagonal crease between vertices B and D is adopted on the central square so as to derive the dihedral angles of all the creases from the kinematic model of the type 2M pattern (see Section 2.3), and to quantify the bending energy of the central square as rotation energy of the virtual crease.

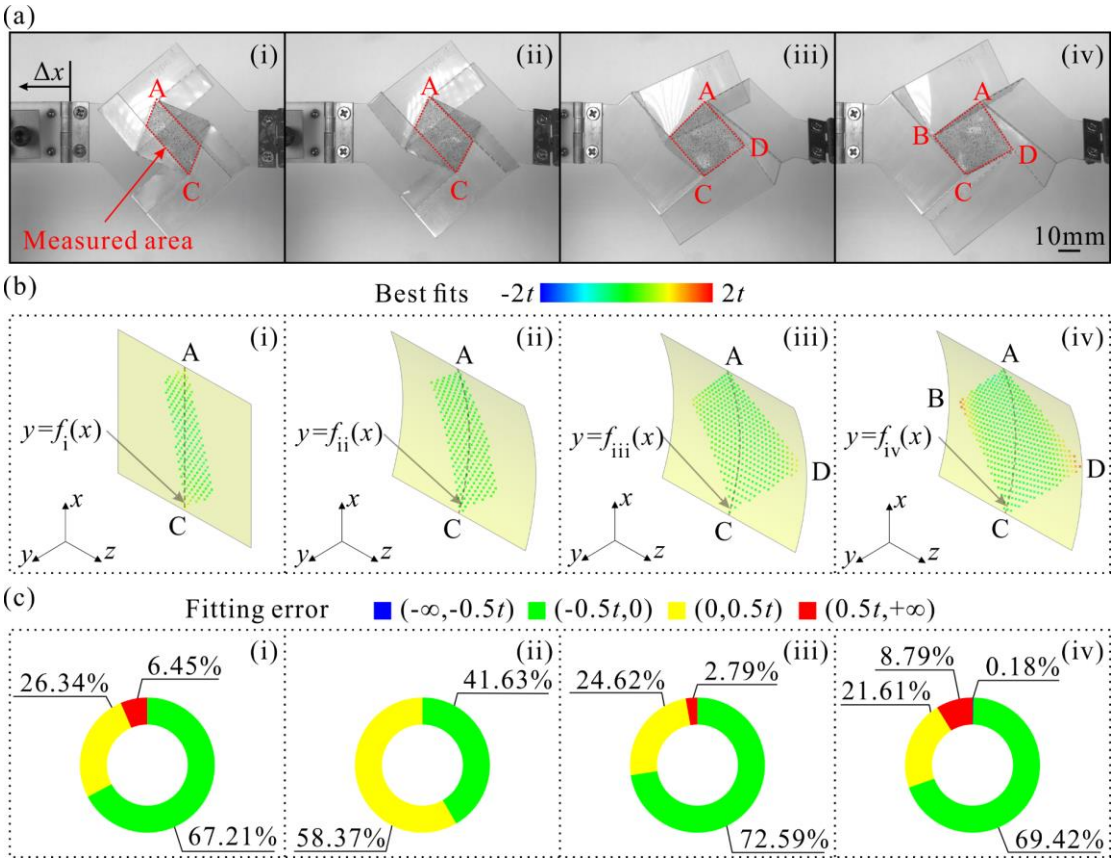

Fig. 2-4 (a) Configuration, (b) geometrically reconstructed central squares, and (c) the pie graphs of the errors between the experimental results and fitting surfaces of the specimen at four representative tension displacements.

2.3 Kinematic Analysis

The square-twist pattern in Fig. 2-1 has four identical 4-crease vertices, noted as vertices A, B, C, and D. In kinematic analysis, the vertex can be modeled by a spherical 4*R* linkage as shown in Fig. 2-5, where the axes of the revolute joints intersect at one point. For the coordinate frames on the links and joints presented in this figure, z_i is along the revolute axis of joint *i*, and x_i is normal to both z_{i-1} and z_i. $\alpha_{i(i+1)}$, the twist of link $i(i+1)$, is the angle of rotation from z_i to z_{i+1} about x_{i+1}. θ_i, the revolute variable of joint *i*, is the angle of rotation from x_i to x_{i+1} about z_i. Then, for type 2 square-twist unit, the equivalent kinematic model is a closed loop of four spherical 4*R* linkages as shown in Fig. 2-6. Based on the matrix method of the Denavit–Hartenberg notations[162], the closure equation of the spherical 4*R* linkage is

$$\mathbf{Q}_{12}\cdot\mathbf{Q}_{23}\cdot\mathbf{Q}_{34}\cdot\mathbf{Q}_{41}=\mathbf{I}_3 \tag{2-2}$$

where

$$\mathbf{Q}_{i(i+1)}=\begin{bmatrix}\cos\theta_i & -\cos\alpha_{i(i+1)}\cdot\sin\theta_i & \sin\alpha_{i(i+1)}\cdot\sin\theta_i\\ \sin\theta_i & \cos\alpha_{i(i+1)}\cdot\cos\theta_i & -\sin\alpha_{i(i+1)}\cdot\cos\theta_i\\ 0 & \sin\alpha_{i(i+1)} & \cos\alpha_{i(i+1)}\end{bmatrix} \tag{2-3}$$

when i=4, (i+1) is equal to 1. By calculating Eq. (2-2), the relationship between revolute variables θ_i and θ_{i+1} (i=1, 2, 3, 4) can be expressed as

$$\begin{aligned}&\cos\alpha_{(i+1)(i+2)}\cdot\sin\alpha_{(i-1)i}\cdot\sin\alpha_{i(i+1)}\cdot\cos\theta_i\\&+\cos\alpha_{(i-1)i}\cdot\sin\alpha_{i(i+1)}\cdot\sin\alpha_{(i+1)(i+2)}\cdot\cos\theta_{i+1}\\&+\cos\alpha_{i(i+1)}\cdot\sin\alpha_{(i+1)(i+2)}\cdot\sin\alpha_{(i-1)i}\cdot\cos\theta_i\cdot\cos\theta_{i+1}\\&-\sin\alpha_{(i+1)(i+2)}\cdot\sin\alpha_{(i-1)i}\cdot\sin\theta_i\cdot\sin\theta_{i+1}\\&+\cos\alpha_{(i+2)(i+3)}-\cos\alpha_{i(i+1)}\cdot\cos\alpha_{(i+1)(i+2)}\cdot\cos\alpha_{(i-1)i}=0.\end{aligned} \tag{2-4}$$

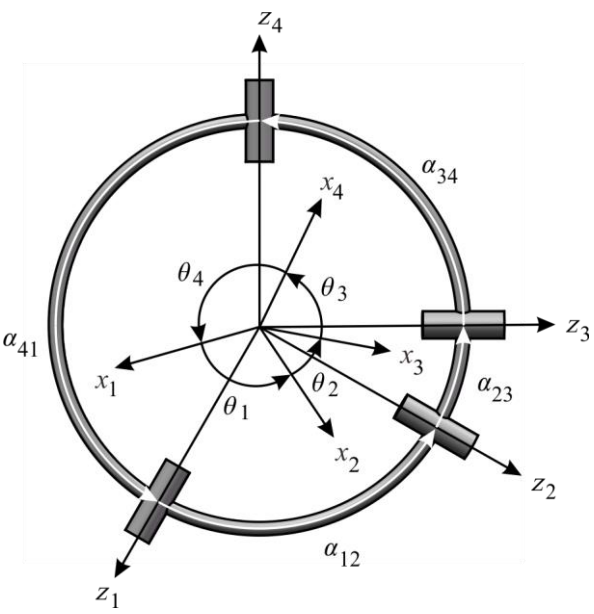

Fig. 2-5 A spherical 4*R* linkage.

In general, the rotation angle from joint i to joint (i+1) in linkage j, $\alpha^j_{i(i+1)}$ (i=1, 2, 3, 4, and j=a, b, c, d), is the sector angle between the i-th and (i+1)-th creases for the j-th vertex. The revolute variable of joint i in linkage j, θ^j_i (i=1, 2, 3, 4, and j=a, b, c, d), is the rotation angle along the i-th crease of the j-th vertex in the origami pattern. According to the definition in Fig. 2-1, the sector angles can be given by

$$\alpha^j_{12}=\frac{\pi}{2},\alpha^j_{23}=\alpha,\alpha^j_{34}=\frac{\pi}{2},\alpha^j_{41}=\pi-\alpha \tag{2-5}$$

Substituting Eq. (2-5) to Eq. (2-4) and noting the mountain-valley assignment of type 2 pattern, the relationship between the rotation angles θ_i^j and θ_{i+1}^j can be solved as

$$\frac{\tan\frac{\theta_2^j}{2}}{\tan\frac{\theta_1^j}{2}}=\frac{-\cos\alpha}{\sin\alpha+1},\ \frac{\tan\frac{\theta_3^j}{2}}{\tan\frac{\theta_2^j}{2}}=\frac{-\cos\alpha}{1-\sin\alpha},\ \frac{\tan\frac{\theta_4^j}{2}}{\tan\frac{\theta_3^j}{2}}=\frac{\cos\alpha}{\sin\alpha+1},\ \frac{\tan\frac{\theta_1^j}{2}}{\tan\frac{\theta_4^j}{2}}=\frac{\cos\alpha}{1-\sin\alpha}. \quad (2\text{-}6)$$

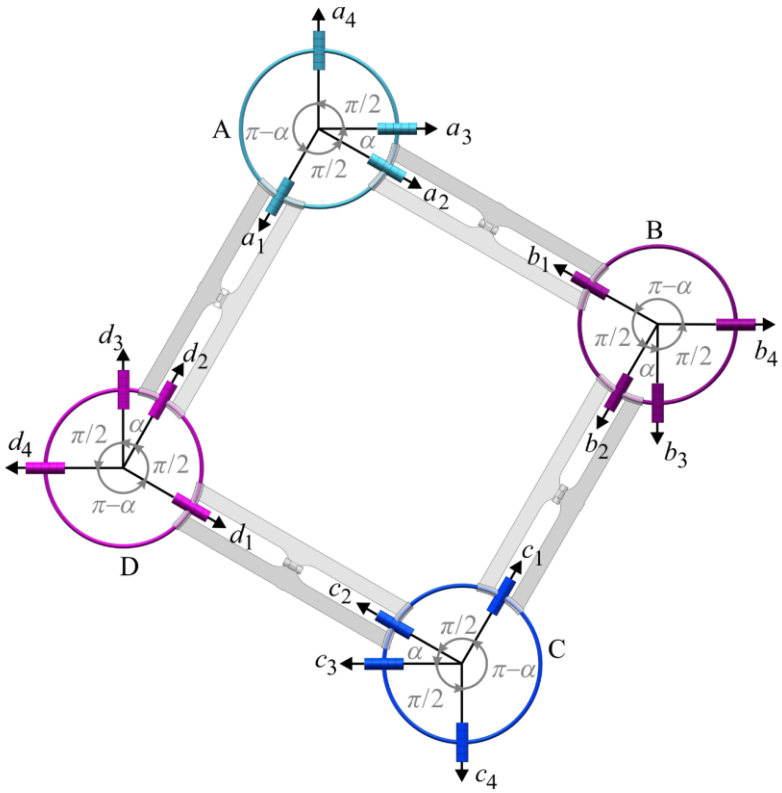

Fig. 2-6 The equivalent kinematic model of the type 2 unit, which is a closed loop of four spherical 4*R* linkages.

A single spherical 4*R* linkage is kinematically of one degree of freedom. For the linkage loop in Fig. 2-6, each pair of adjacent linkages shares a common joint (or creases), i.e., AB, BC, CD, and DA should have an identical rotation angle for the vertices on both ends,

$$\theta_2^a=\theta_1^b,\ \theta_2^b=\theta_1^c,\ \theta_2^c=\theta_1^d,\ \theta_2^d=\theta_1^a \quad (2\text{-}7)$$

In each linkage (or vertex), the kinematic transmission between θ_1^j and θ_2^j (j=a, b, c, d) can be described by Eq. (2-6). Substituting Eq. (2-7) into Eq. (2-6), the input-output relationship can be described as

$$\theta_2^d=\frac{\cos^4\alpha}{(1+\sin\alpha)^4}\theta_1^a \quad (2\text{-}8)$$

The relationship, $\theta_2^d \neq \theta_1^a$ when $\alpha \in (0, \pi/2)$, indicates that the four spherical 4*R* linkages in Fig. 2-6 with the crease arrangement of the type 2 pattern cannot form a complete loop. To create a compatible closed loop with retaining the original crease arrangement of the type 2 pattern, I proposed a method that adds a diagonal crease in the central square between vertices B and D according to the experimental result in Section 2.2, as shown in Fig. 2-7(a).

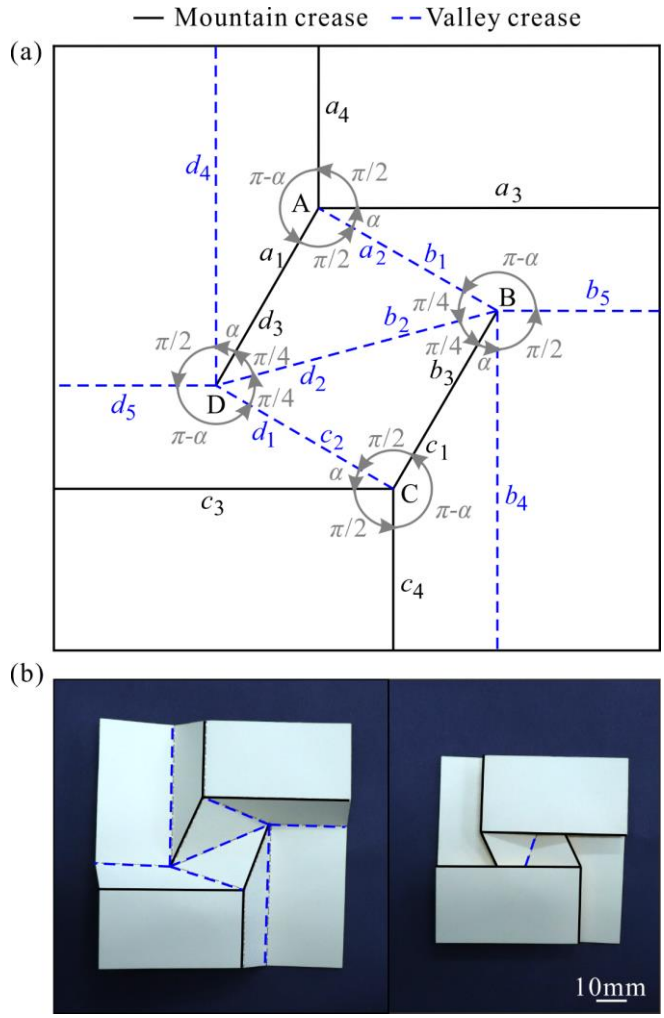

Fig. 2-7 (a) Pattern, geometric parameters, definition of creases and vertices, (b) unfolding and folding configurations of modified type 2 (2M) unit.

This method modifies the relationship between the kinematic variables θ_1^j and θ_2^j (j=b, d) and converts the foldability of the type 2 unit from non-rigid to rigid. The modified type 2 (2M) unit consists of two 4-crease vertices (A and C), which can be modeled as spherical 4*R* linkages with the same geometric parameters and kinematics

as Eq. (2-5) and (2-6), and two 5-crease vertices (B and D), which can be modeled as spherical 5*R* linkages, see Fig. 2-8. The closure equation of the spherical 5*R* linkage can be given as

$$\mathbf{Q}_{12}\cdot\mathbf{Q}_{23}\cdot\mathbf{Q}_{34}\cdot\mathbf{Q}_{45}\cdot\mathbf{Q}_{51}=\mathbf{I}_3 \tag{2-9}$$

where $\mathbf{Q}_{i(i+1)}$ is defined by Eq. (2-3), and when i=5, (i+1) is equal to 1. By setting up the geometric parameters of the type 2M unit in Fig. 2-7(a), the sector angle $\alpha^j_{i(i+1)}$ (i=1, 2, 3, 4, 5, and j=b, d) of the two 5-crease vertices can be defined as

$$\alpha^j_{12}=\frac{\pi}{4},\alpha^j_{23}=\frac{\pi}{4},\alpha^j_{34}=\alpha,\alpha^j_{45}=\frac{\pi}{2},\alpha^j_{51}=\pi-\alpha \tag{2-10}$$

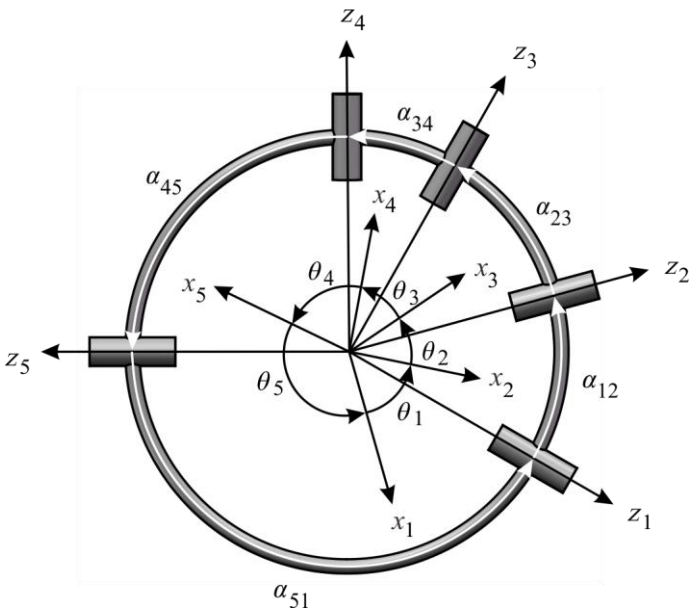

Fig. 2-8 A spherical 5*R* linkage.

Because the spherical 5*R* linkage is of two degrees of freedom, θ^j_1 and θ^j_3 are defined as the input angles to obtain the output angles θ^j_2, θ^j_4 and θ^j_5 (j=b, d). Substituting Eq. (2-10) into Eq. (2-9), the relationship between the kinematic variables is expressed as

$$\tan\frac{\theta^j_4}{2}=\frac{Q^j_2\pm\sqrt{Q^j_3}}{Q^j_1}, \tag{2-11}$$

$$\tan\frac{\theta^j_5}{2}=\frac{-P^j_2+\sqrt{P^{j\,2}_2-4P^j_1\cdot P^j_3}}{2P^j_1}, \tag{2-12}$$

$$\cos\theta^j_2=2\sin\alpha\cdot\left(-\cos\alpha\cdot\cos\theta^j_4+\cos\alpha\cdot\cos\theta^j_5-\sin\alpha\cdot\sin\theta^j_4\cdot\sin\theta^j_5\right)+1, \tag{2-13}$$

where

$$\begin{aligned}
Q_1^j &= \sin\alpha + \cos\alpha + \sin\alpha\cdot\cos\theta_1^j + \cos\alpha\cdot\cos\theta_3^j \\
Q_2^j &= -\sin\theta_3^j \\
Q_3^j &= \sin^2\alpha\cdot\left(\sin^2\theta_1^j + \sin^2\theta_3^j\right) - 2\sin\alpha\cdot\cos\alpha\cdot\left(\cos\theta_1^j - \cos\theta_3^j\right)
\end{aligned}, \tag{2-14a}$$

$$\begin{aligned}
P_1^j &= \left(\cos\alpha\cdot\sin\theta_3^j\cdot\sin\theta_4^j - \cos^2\alpha\cdot\cos\theta_3^j\cdot\cos\theta_4^j - \sin\alpha\cdot\cos\alpha\cdot\cos\theta_4^j + 1\right) \\
&\quad + \left(\sin^2\alpha\cdot\cos\theta_3^j - \sin\alpha\cdot\cos\alpha\right) \\
P_2^j &= 2\left(-\sin\alpha\cdot\sin\theta_3^j\cdot\cos\theta_4^j - \sin\alpha\cdot\cos\alpha\cdot\cos\theta_3^j\cdot\sin\theta_4^j - \sin^2\alpha\cdot\sin\theta_4^j\right) \\
P_3^j &= \left(\cos\alpha\cdot\sin\theta_3^j\cdot\sin\theta_4^j - \cos^2\alpha\cdot\cos\theta_3^j\cdot\cos\theta_4^j - \sin\alpha\cdot\cos\alpha\cdot\cos\theta_4^j + 1\right) \\
&\quad - \left(\sin^2\alpha\cdot\cos\theta_3^j - \sin\alpha\cdot\cos\alpha\right)
\end{aligned}. \tag{2-14b}$$

The kinematics of vertices A and C in Eq. (2-6), can be simplified as

$$\tan\frac{\theta_2^j}{2} = \frac{-\cos\alpha}{\sin\alpha+1}\tan\frac{\theta_1^j}{2}, \theta_4^j = -\theta_2^j, \theta_3^j = \theta_1^j. \tag{2-15}$$

To illustrate the folding more clearly, the dihedral angles ψ_i^j (i=1, 2, 3, 4, j=a, c, and i=1, 2, 3, 4, 5, j=b, d) of each vertex, instead of θ_i^j (i=1, 2, 3, 4, j=a, c, and i=1, 2, 3, 4, 5, j=b, d), are used to analyse the configuration and kinematic paths of the type 2M unit. Their relationships are

$$\theta_1^j = \pi - \psi_1^j, \theta_2^j = \psi_2^j - \pi, \theta_3^j = \pi - \psi_3^j, \theta_4^j = \pi - \psi_4^j. \tag{2-16}$$

where j=a, c. Substituting Eq. (2-16) into Eq. (2-15), the relationship between dihedral angles of vertices A and C is given by

$$\tan\frac{\psi_2^j}{2} = \frac{\cos\alpha}{1-\sin\alpha}\tan\frac{\psi_1^j}{2}, \psi_4^j = \psi_2^j, \psi_3^j = \psi_1^j \tag{2-17}$$

Similarly, the geometric relationships of the kinematic rotation angles and the dihedral angles for vertices B and D are

$$\theta_1^j = \psi_1^j - \pi, \theta_2^j = \psi_2^j - \pi, \theta_3^j = \pi - \psi_3^j, \theta_4^j = \psi_4^j - \pi, \theta_5^j = \psi_5^j - \pi. \tag{2-18}$$

where j=b, d. Substituting Eq. (2-18) into Eq. (2-11)-(2-14), the dihedral angles of vertices B and D can be calculated by

$$\tan\frac{\psi_4^j}{2} = \frac{q_1^j}{q_2^j \mp \operatorname{sgn}\left(g^j\right)\sqrt{q_3^j}}, \tag{2-19}$$

$$\tan\frac{\psi_5^j}{2} = \frac{p_1^j}{-p_2^j + \sqrt{p_2^{j\,2} - p_1^j\cdot p_3^j}}, \tag{2-20}$$

$$\cos\psi_2^j = 2\sin\alpha\cdot\left(-\cos\alpha\cdot\cos\psi_4^j + \cos\alpha\cdot\cos\psi_5^j + \sin\alpha\cdot\sin\psi_4^j\cdot\sin\psi_5^j\right) - 1. \tag{2-21}$$

where

$$\begin{aligned}
q_1^j &= \sin\alpha + \cos\alpha - \sin\alpha\cdot\cos\psi_1^j - \cos\alpha\cdot\cos\psi_3^j \\
q_2^j &= \sin\psi_3^j \\
q_3^j &= \sin^2\alpha\cdot\left(\sin^2\psi_1^j + \sin^2\psi_3^j\right) + 2\sin\alpha\cdot\cos\alpha\cdot\left(\cos\psi_1^j - \cos\psi_3^j\right)
\end{aligned}, \tag{2-22a}$$

$$p_1^j = \left(\cos\alpha \cdot \sin\psi_3^j \cdot \sin\psi_4^j + \cos^2\alpha \cdot \cos\psi_3^j \cdot \cos\psi_4^j - \sin\alpha \cdot \cos\alpha \cdot \cos\psi_4^j - 1\right) + \left(\sin^2\alpha \cdot \cos\psi_3^j + \sin\alpha \cdot \cos\alpha\right)$$

$$p_2^j = \sin\alpha \cdot \sin\psi_3^j \cdot \cos\psi_4^j - \sin\alpha \cdot \cos\alpha \cdot \cos\psi_3^j \cdot \sin\psi_4^j + \sin^2\alpha \cdot \sin\psi_4^j$$

$$p_3^j = \left(\cos\alpha \cdot \sin\psi_3^j \cdot \sin\psi_4^j + \cos^2\alpha \cdot \cos\psi_3^j \cdot \cos\psi_4^j - \sin\alpha \cdot \cos\alpha \cdot \cos\psi_4^j - 1\right) - \left(\sin^2\alpha \cdot \cos\psi_3^j + \sin\alpha \cdot \cos\alpha\right) \tag{2-22b}$$

$$g^j = \psi_1^j - \psi_{1g}, \tag{2-22c}$$

$$\psi_{1g} = 2\arctan\sqrt{\cos\alpha/(1-\sin\alpha)}. \tag{2-22d}$$

Joining the four vertices together can form a closed loop of two 4-crease vertices and two 5-crease vertices, see Fig. 2-7(a). The common creases of adjacent vertices have the same kinematic rotation angles,

$$\psi_1^a = \psi_3^d, \psi_2^a = \psi_1^b, \psi_1^c = \psi_3^b, \psi_2^c = \psi_1^d, \psi_2^b = \psi_2^d, \tag{2-23}$$

which leads to the compatibility condition to determine the rigid foldability of the pattern

$$\begin{tikzcd}
 & \psi_1^b = \psi_2^a \arrow[dl] & \psi_1^a = \psi_3^d \arrow[l] \arrow[dr] & \\
\psi_2^b & & & \psi_2^d \\
 & \psi_3^b = \psi_1^c \arrow[ul] \arrow[r] & \psi_2^c = \psi_1^d \arrow[ur] & \\
 & \psi_2^b = \psi_2^d \arrow[uul] \arrow[urr] & &
\end{tikzcd} \tag{2-24}$$

Here, a spherical 4*R* linkage is with one degree of freedom, so in linkage A, ψ_1^a is taken as input and ψ_2^a as output; in linkage C, ψ_1^c is taken as input and ψ_2^c as output. Meanwhile, a spherical 5*R* linkage is with two degrees of freedom, so in linkage B, $\psi_2^a = \psi_1^b$ and $\psi_1^c = \psi_3^b$ are taken as two inputs to determine the output ψ_2^b; in linkage D, $\psi_2^c = \psi_1^d$ and $\psi_1^a = \psi_3^d$ are taken as two inputs to determine the output ψ_2^d. Eventually, $\psi_2^b = \psi_2^d$ is the additional condition to setup the relationship between the initial inputs, ψ_1^a and ψ_1^c. Therefore, the whole system is of only one degree of freedom.

Substituting Eq. (2-17), (2-19)-(2-23) into Eq. (2-24), two sets of kinematic equations of the type 2M pattern can be obtained, which means there are two folding paths for the pattern. The equations for path 1 are

$$\tan\frac{\psi_2^a}{2} = \frac{\sin\alpha + 1}{\cos\alpha}\tan\frac{\psi_1^a}{2}, \tag{2-25a}$$

$$\psi_2^a = \psi_4^a = \psi_2^c = \psi_4^c = \psi_1^b = \psi_1^d, \tag{2-25b}$$

$$\psi_1^a = \psi_3^a = \psi_1^c = \psi_3^c = \psi_3^b = \psi_3^d, \tag{2-25c}$$

$$\tan\frac{\psi_4^d}{2} = \frac{q_1^d}{q_2^d - \mathrm{sgn}(g^d)\sqrt{q_3^d}}, \tag{2-25d}$$

$$\tan\frac{\psi_5^d}{2}=\frac{p_1^d}{-p_2^d+\sqrt{p_2^{d\,2}-p_1^d\cdot p_3^d}},\tag{2-25e}$$

$$\cos\psi_2^d=2\sin\alpha\cdot\left(-\cos\alpha\cdot\cos\psi_4^d+\cos\alpha\cdot\cos\psi_5^d+\sin\alpha\cdot\sin\psi_4^d\cdot\sin\psi_5^d\right)-1,\tag{2-25f}$$

$$\psi_2^b=\psi_2^d,\tag{2-25g}$$

$$\psi_4^b=\psi_4^d,\tag{2-25h}$$

$$\psi_5^b=\psi_5^d,\tag{2-25i}$$

and the equations of path 2 are

$$\tan\frac{\psi_2^a}{2}=\frac{\sin\alpha+1}{\cos\alpha}\tan\frac{\psi_1^a}{2},\tag{2-26a}$$

$$\psi_2^a=\psi_4^a=\psi_2^c=\psi_4^c=\psi_1^b=\psi_1^d,\tag{2-26b}$$

$$\psi_1^a=\psi_3^a=\psi_1^c=\psi_3^c=\psi_3^b=\psi_3^d,\tag{2-26c}$$

$$\tan\frac{\psi_4^d}{2}=\frac{q_1^d}{q_2^d+\mathrm{sgn}\left(g^d\right)\sqrt{q_3^d}},\tag{2-26d}$$

$$\tan\frac{\psi_5^d}{2}=\frac{p_1^d}{-p_2^d+\sqrt{p_2^{d\,2}-p_1^d\cdot p_3^d}},\tag{2-26e}$$

$$\cos\psi_2^d=2\sin\alpha\cdot\left(-\cos\alpha\cdot\cos\psi_4^d+\cos\alpha\cdot\cos\psi_5^d+\sin\alpha\cdot\sin\psi_4^d\cdot\sin\psi_5^d\right)-1,\tag{2-26f}$$

$$\psi_2^b=\psi_2^d,\tag{2-26g}$$

$$\psi_4^b=\psi_4^d,\tag{2-26h}$$

$$\psi_5^b=\psi_5^d,\tag{2-26i}$$

where

$$g^d=\psi_1^d-\psi_{1g},\tag{2-27a}$$

$$\psi_{1g}=2\arctan\sqrt{\cos\alpha/\left(1-\sin\alpha\right)},\tag{2-27b}$$

$$\begin{aligned}q_1^d&=\sin\alpha+\cos\alpha-\sin\alpha\cdot\cos\psi_1^d-\cos\alpha\cdot\cos\psi_3^d\\q_2^d&=\sin\psi_3^d\\q_3^d&=\sin^2\alpha\cdot\left(\sin^2\psi_1^d+\sin^2\psi_3^d\right)+2\sin\alpha\cdot\cos\alpha\cdot\left(\cos\psi_1^d-\cos\psi_3^d\right)\end{aligned},\tag{2-27c}$$

$$\begin{aligned}p_1^d&=\left(\cos\alpha\cdot\sin\psi_3^d\cdot\sin\psi_4^d+\cos^2\alpha\cdot\cos\psi_3^d\cdot\cos\psi_4^d-\sin\alpha\cdot\cos\alpha\cdot\cos\psi_4^d-1\right)\\&\quad+\left(\sin^2\alpha\cdot\cos\psi_3^d+\sin\alpha\cdot\cos\alpha\right)\\p_2^d&=\sin\alpha\cdot\sin\psi_3^d\cdot\cos\psi_4^d-\sin\alpha\cdot\cos\alpha\cdot\cos\psi_3^d\cdot\sin\psi_4^d+\sin^2\alpha\cdot\sin\psi_4^d\\p_3^d&=\left(\cos\alpha\cdot\sin\psi_3^d\cdot\sin\psi_4^d+\cos^2\alpha\cdot\cos\psi_3^d\cdot\cos\psi_4^d-\sin\alpha\cdot\cos\alpha\cdot\cos\psi_4^d-1\right)\\&\quad-\left(\sin^2\alpha\cdot\cos\psi_3^d+\sin\alpha\cdot\cos\alpha\right)\end{aligned}.\tag{2-27d}$$

To illustrate the kinematic characteristics, two kinematic paths of the type 2M pattern together with six representative configurations on each path are shown in Fig. 2-9. The configurations (I_1 II_1 III_1 IV_1 V_1 VI_1) represent the unfolding sequence on path 1; (I_2 II_2 III_2 IV_2 V_2 VI_2) represent the unfolding motion on path 2. Rectangular facets

in the same colour (dark or light blue) are parallel during motion. These paths intersect at three points that correspond to fully folded (I_1 and I_2), fully deployed (VI_1 and VI_2), and bifurcation configurations (IV_1 and IV_2). In each kinematic path, there are two pairs of parallel rectangular facets, and all four facets become parallel in the bifurcation configuration. In addition, penetration of the facets into each other occurs on kinematic path 2 between the fully folded and bifurcation configurations, which is exemplified by configuration II_2 in Fig. 2-9. This is an important observation, as it implies that when a type 2M unit is unfolded, it may not be able to follow kinematic path 2 because of physical interference. Hence, there are two possible paths to unfold the unit: one is path 1 throughout, and the other is path 1 first, followed by a switch to path 2 at the point where the paths bifurcate. The bifurcation on configurations IV_1 and IV_2 in Fig. 2-9 only holds when α=30°.

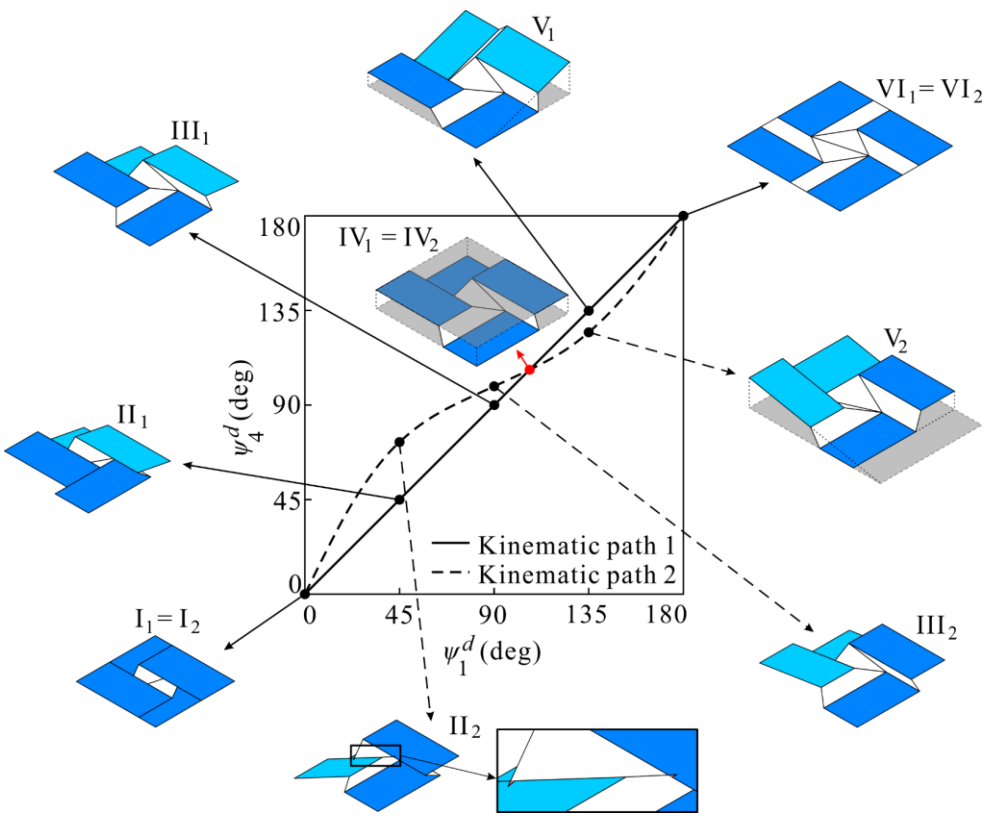

Fig. 2-9 Two different kinematic paths of the type 2M pattern together with six representative configurations on each path, where α=30° and the bifurcation is $\psi_1^d = 105.54°$.

The comparison between Eq. (2-25) and (2-26) reveals that the relationship between the dihedral angles in both kinematic paths, which can be described with five

different angular variables, ψ_1^d, ψ_2^d, ψ_3^d, ψ_4^d, and ψ_5^d, are all related to α. The variation in the two kinematic paths with varied α presented in Fig. 2-10 shows that the bifurcation point with $\psi_1^d = 2\arctan\sqrt{\cos\alpha/(1-\sin\alpha)}$ is always found in the kinematic curves of the type 2M pattern. The larger α is, the later the bifurcation happens (Fig. 2-10(a)).

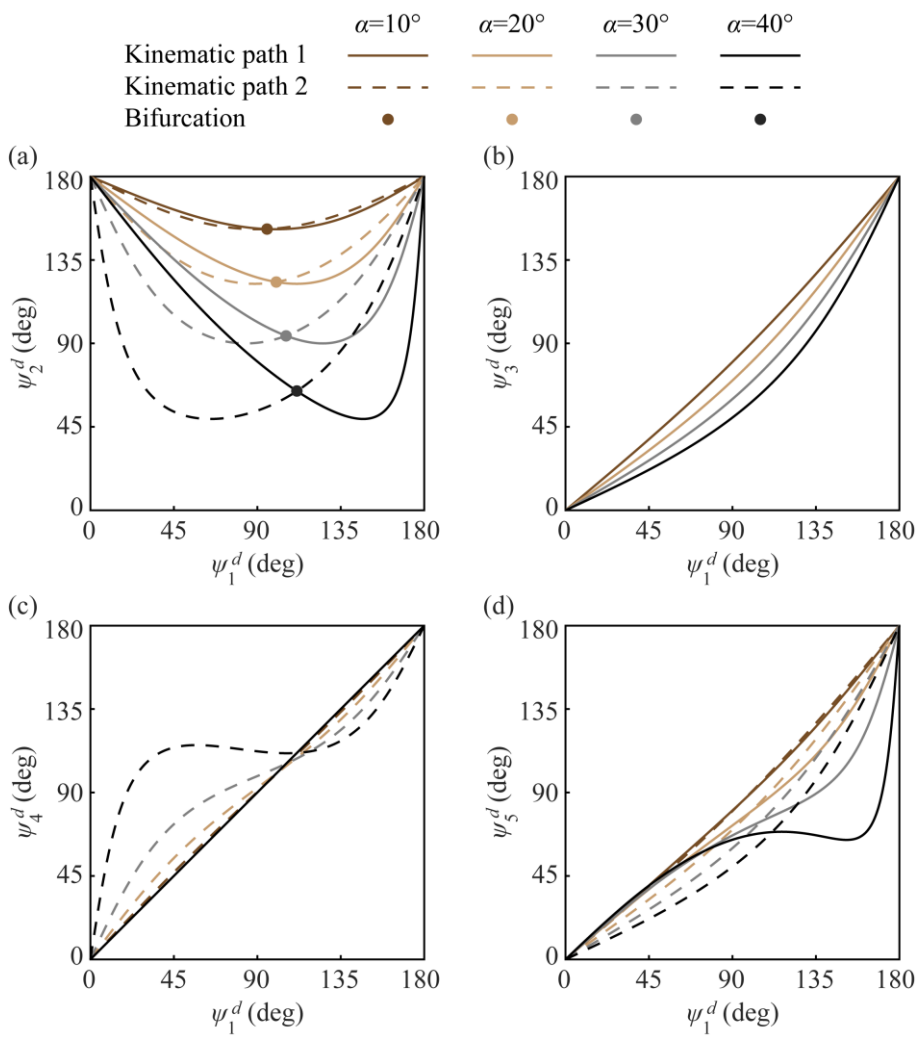

Fig. 2-10 Kinematic curves of the dihedral angles (a) ψ_2^d, (b) ψ_3^d, (c) ψ_4^d, and (d) ψ_5^d vs. ψ_1^d for kinematic paths 1 and 2 of the type 2M unit with varied α.

Furthermore, the facet penetration appeared in configuration II2 is caused by the difference between ψ_4^a and ψ_4^d, where $\psi_4^a = \psi_1^d$ is always in both kinematic paths by Eq. (2-25b) and (2-26b). The relationship between ψ_4^d and ψ_1^d in Fig. 2-10(c) indicates that the larger α is, the larger difference between the two dihedral angles exists in path 2 before the bifurcation point, i.e. the more serious the penetration of the facet

is. Notice that the two kinematic paths have an identical relationship between ψ_3^d and ψ_1^d in Fig. 2-10(b), which is not affected by varied α. It is because ψ_3^d and ψ_1^d are controlled by the two 4-crease vertices A and C in Eq. (2-25a)-(2-25c) and (2-26a)-(2-26c), and each 4-crease vertex with determined crease assignment has a unique solution as shown in Eq. (2-2)-(2-6). In other words, the two different kinematic paths of the type 2M pattern is only depending on the 5-crease vertices B and D.

2.4 Theoretical Model

Before calculating the theoretical energy, the definition of dihedral angles for the crease of a type 2 unit is simplified as shown in Fig. 2-11. Then, the elastic energy, U_t, of the type 2 pattern during unfolding along either kinematic path can be calculated as the summation of the energy of the twelve original creases, U_c, and that of the virtual crease on the central square, U_s.

$$U_t = U_c + U_s = \frac{1}{2}\sum_{i=1}^{12} k_{ci} \cdot L_i\left(\varphi_i - \varphi_{i,0}\right)^2 + \frac{1}{2} k_f \cdot L_s\left(\varphi_s - \varphi_{s,0}\right)^2. \tag{2-28}$$

In which k_{ci}, L_i, φ_i, and $\varphi_{i,0}$ are, respectively, the torsional elastic constant per unit length along the crease, length of the crease, dihedral angle, and natural dihedral angle in the undeformed state for the i-th crease, whilst k_f, L_s, φ_s and $\varphi_{s,0}$ are the corresponding parameters of the virtual crease.

According to the kinematic analysis in Section 2.3, the relationship of the dihedral angles in Fig. 2-11 is as follows when φ_4 is set as the input angle.

$$\tan\frac{\varphi_1}{2} = \frac{1-\sin\alpha}{\cos\alpha}\tan\frac{\varphi_4}{2}, \tag{2-29a}$$

$$\tan\frac{\varphi_6}{2} = \begin{cases} \dfrac{q_1}{q_2 - \operatorname{sgn}(g)\sqrt{q_3}} \\ \dfrac{q_1}{q_2 + \operatorname{sgn}(g)\sqrt{q_3}} \end{cases}, \tag{2-29b}$$

$$\tan\frac{\varphi_5}{2} = \frac{p_1}{-p_2 + \sqrt{(p_2)^2 - p_1 \cdot p_3}}, \tag{2-29c}$$

$$\cos\varphi_{13} = 2\sin\alpha \cdot \left(-\cos\alpha \cdot \cos\varphi_6 + \cos\alpha \cdot \cos\varphi_5 + \sin\alpha \cdot \sin\varphi_6 \cdot \sin\varphi_5\right) - 1, \tag{2-29d}$$

$$\varphi_2 = \varphi_8 = \varphi_{10} = \varphi_4,\ \ \varphi_9 = \varphi_7 = \varphi_3 = \varphi_1,\ \ \varphi_{12} = \varphi_6,\ \ \varphi_{11} = \varphi_5, \tag{2-29e}$$

where

$$g = \varphi_4 - \varphi_{4g}, \tag{2-29f}$$

$$\varphi_{4g} = 2\arctan\sqrt{\cos\alpha/(1-\sin\alpha)}, \tag{2-29g}$$

$$\begin{aligned} q_1 &= \sin\alpha + \cos\alpha - \sin\alpha \cdot \cos\varphi_4 - \cos\alpha \cdot \cos\varphi_1 \\ q_2 &= \sin\varphi_1 \\ q_3 &= \sin^2\alpha \cdot \left(\sin^2\varphi_4 + \sin^2\varphi_1\right) + 2\sin\alpha \cdot \cos\alpha \cdot \left(\cos\varphi_4 - \cos\varphi_1\right) \end{aligned} , \tag{2-29h}$$

$$\begin{aligned} p_1 &= \left(\cos\alpha \cdot \sin\varphi_1 \cdot \sin\varphi_6 + \cos^2\alpha \cdot \cos\varphi_1 \cdot \cos\varphi_6 - \sin\alpha \cdot \cos\alpha \cdot \cos\varphi_6 - 1\right) \\ &\quad + \left(\sin^2\alpha \cdot \cos\varphi_1 + \sin\alpha \cdot \cos\alpha\right) \\ p_2 &= \sin\alpha \cdot \sin\varphi_1 \cdot \cos\varphi_6 - \sin\alpha \cdot \cos\alpha \cdot \cos\varphi_1 \cdot \sin\varphi_6 + \sin^2\alpha \cdot \sin\varphi_6 \\ p_3 &= \left(\cos\alpha \cdot \sin\varphi_1 \cdot \sin\varphi_6 + \cos^2\alpha \cdot \cos\varphi_1 \cdot \cos\varphi_6 - \sin\alpha \cdot \cos\alpha \cdot \cos\varphi_6 - 1\right) \\ &\quad - \left(\sin^2\alpha \cdot \cos\varphi_1 + \sin\alpha \cdot \cos\alpha\right) \end{aligned} . \tag{2-29i}$$

Here, the relationships, $\varphi_2 = \varphi_8$, $\varphi_{10} = \varphi_4$, $\varphi_9 = \varphi_3$, $\varphi_7 = \varphi_1$, $\varphi_{12} = \varphi_6$, and $\varphi_{11} = \varphi_5$, are caused by the two-fold rotational symmetry of type 2 unit, while $\varphi_2 = \varphi_4$, $\varphi_8 = \varphi_{10}$, $\varphi_9 = \varphi_7$, and $\varphi_3 = \varphi_1$ result from Eq. (2-17) of vertices A and C.

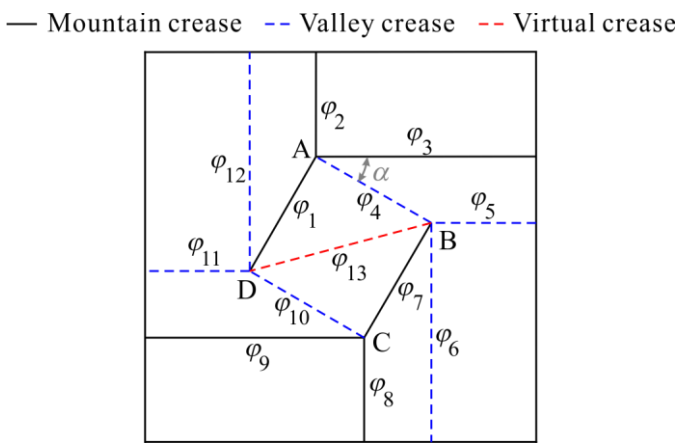

Fig. 2-11 Definition of the dihedral angles.

Using the dihedral angles in Eq. (2-29), the energy of each crease can be calculated by

$$U_7 = U_1 = \frac{1}{2} k_c \cdot l\left(\varphi_1 - \varphi_{1,0}\right)^2, \tag{2-30a}$$

$$U_8 = U_2 = \frac{a}{l} U_4 = \frac{1}{2} k_c \cdot a\left(\varphi_4 - \varphi_{4,0}\right)^2, \tag{2-30b}$$

$$U_9 = U_3 = \frac{\left(a + l \cdot \cos\alpha\right)}{l} U_1 = \frac{1}{2} k_c \left(a + l \cdot \cos\alpha\right)\left(\varphi_1 - \varphi_{1,0}\right)^2, \tag{2-30c}$$

$$U_{10} = U_4 = \frac{1}{2} k_c \cdot l\left(\varphi_4 - \varphi_{4,0}\right)^2, \tag{2-30d}$$

$$U_{11} = U_5 = \frac{1}{2} k_c \cdot a\left(\varphi_5 - \varphi_{5,0}\right)^2, \tag{2-30e}$$

$$U_{12} = U_6 = \frac{1}{2} k_c \left(a + l \cdot \cos\alpha\right)\left(\varphi_6 - \varphi_{6,0}\right)^2, \tag{2-30f}$$

$$U_{13} = \frac{\sqrt{2}}{2} k_{\mathrm{f}} \cdot l\left(\varphi_{13} - \varphi_{13,0}\right)^2, \tag{2-30g}$$

where k_c and k_f are the torsional elastic constants of the original creases and the virtual crease, respectively, l and a are two side lengths of the type 2 pattern (Fig. 2-1(a)).

Then, the energy of the original creases, U_c, is

$$\begin{aligned} U_{\mathrm{c}} &= \sum_{i=1}^{12} U_i \\ &= k_{\mathrm{c}}\left(a + l \cdot \cos\alpha + l\right)\left(\varphi_1 - \varphi_{1,0}\right)^2 + k_{\mathrm{c}}\left(a + l\right)\left(\varphi_4 - \varphi_{4,0}\right)^2, \\ &\quad + k_{\mathrm{c}} \cdot a\left(\varphi_5 - \varphi_{5,0}\right)^2 + k_{\mathrm{c}}\left(a + l \cdot \cos\alpha\right)\left(\varphi_6 - \varphi_{6,0}\right)^2 \end{aligned} \tag{2-31}$$

and that of the virtual crease on the central square, U_s, is

$$U_{\mathrm{s}} = \frac{\sqrt{2}}{2} k_{\mathrm{f}} \cdot l\left(\varphi_{13} - \varphi_{13,0}\right)^2. \tag{2-32}$$

Finally, substituting Eq. (2-31) and (2-32) to Eq. (2-28), the total energy of the type 2 pattern, U_t, is

$$\begin{aligned} U_{\mathrm{t}} &= U_{\mathrm{c}} + U_{\mathrm{s}} \\ &= k_{\mathrm{c}}\left(a + l \cdot \cos\alpha + l\right)\left(\varphi_1 - \varphi_{1,0}\right)^2 + k_{\mathrm{c}}\left(a + l\right)\left(\varphi_4 - \varphi_{4,0}\right)^2 + k_{\mathrm{c}} \cdot a\left(\varphi_5 - \varphi_{5,0}\right)^2 \cdot \\ &\quad + k_{\mathrm{c}}\left(a + l \cdot \cos\alpha\right)\left(\varphi_6 - \varphi_{6,0}\right)^2 + \frac{\sqrt{2}}{2} k_{\mathrm{f}} \cdot l\left(\varphi_{13} - \varphi_{13,0}\right)^2 \end{aligned} \tag{2-33}$$

As shown in Fig. 2-3(b), the tension loading on the specimen is in the diagonal direction. The deformed diagonal length and the natural diagonal length in the undeformed state of the type 2 specimen is defined as x_d and $x_{d,0}$, respectively. The diagonal length, x_d, can be described using the dihedral angles in Eq. (2-29).

$$x_{\mathrm{d}} = \sqrt{u^2 + v^2 + w^2}, \tag{2-34a}$$

where

$$\begin{aligned} u &= \left(a + l \cdot \cos\alpha\right) - l \cdot \sin\alpha \cdot \cos\varphi_5 + a \cdot \cos\left(\varphi_3 - \varphi_5\right) \\ v &= -a + l \cdot \sin\alpha \cdot \cos\varphi_6 - \left(a + l \cdot \cos\alpha\right)\cos\left(\varphi_8 - \varphi_6\right) \\ w &= \left[l \cdot \sin\alpha \cdot \sin\varphi_5 + a \cdot \sin\left(\varphi_3 - \varphi_5\right)\right] \\ &\quad - \left[l \cdot \sin\alpha \cdot \sin\varphi_6 + \left(a + l \cdot \cos\alpha\right)\sin\left(\varphi_8 - \varphi_6\right)\right] \end{aligned}. \tag{2-34b}$$

And the natural diagonal length, $x_{d,0}$, can be calculated by Eq. (2-34) when the dihedral angles, φ_i, is equal to the natural dihedral angles, $\varphi_{i,0}$. Then, the displacement, Δx, which is the deformation of the type 2 specimen in the diagonal direction, can be defined by

$$\Delta x = x_{\mathrm{d}} - x_{\mathrm{d},0} \tag{2-35}$$

The elastic energy of a type 2 pattern and the creases following each kinematic path is, respectively, calculated, normalized by $k_c l$, and drawn against normalized tension displacement $\Delta x/l$ in Fig. 2-12 and Fig. 2-13. The geometry of the pattern is

selected as α=30º, a=l, $\varphi_{4,0}$=0º, and the ratio k_f/k_c is set to 8 in order to exemplify the difference between the two paths. It can be seen that the elastic energy of kinematic path 2 is higher than that of path 1 prior to the bifurcation point and becomes lower than that of path 1 afterward. Theoretically, when a structure is loaded, the low-energy deformation path will be followed. Therefore, the theoretical model predicts that the type 2 pattern will initially follow path 1 and then bifurcate to follow path 2, which has not been reported in origami structures of its kind.

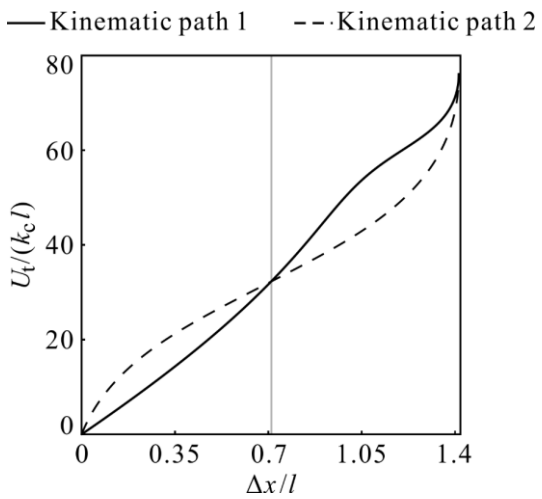

Fig. 2-12 Normalized theoretical elastic energy $U_t/(k_c l)$ vs. displacement $\Delta x/l$ of the type 2M pattern.

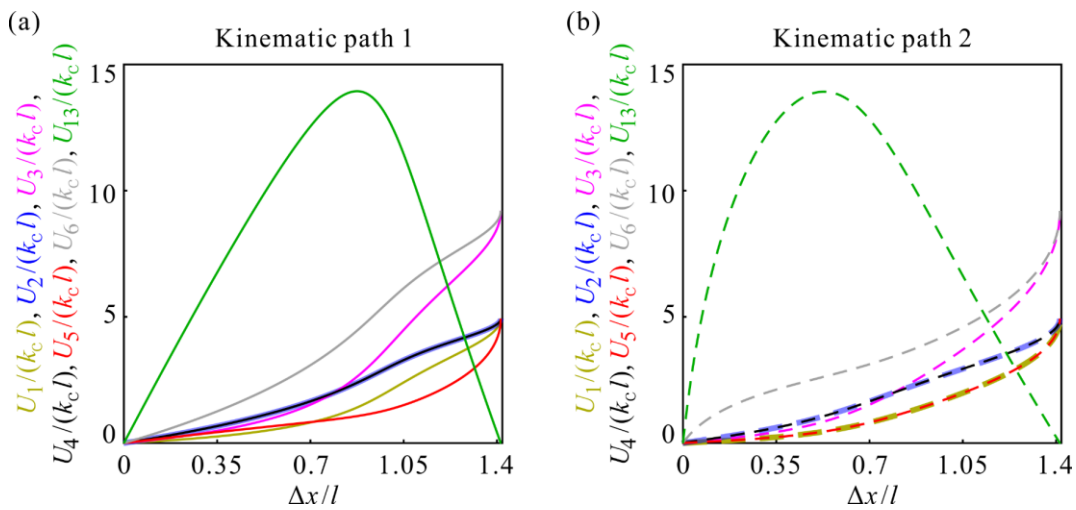

Fig. 2-13 Normalized theoretical elastic energy $U_1/(k_c l)$, $U_2/(k_c l)$, $U_3/(k_c l)$, $U_4/(k_c l)$, $U_5/(k_c l)$, $U_6/(k_c l)$, and $U_{13}/(k_c l)$ vs. displacement $\Delta x/l$ of (a) kinematic path 1 and (b) kinematic path 2 of the type 2M pattern.

It is worth mentioning that Eq. (2-28) is valid only when the creases have a linear elastic torque versus rotation angle relationship, and modifications are required should a different constitutive relationship be adopted.

2.5 Mechanical Behaviors of Type 2 Unit

2.5.1 Validation of Theoretical Model

To validate the theoretical model derived in Section 2.4, a rigid-foldable type 2M specimen was first built and tested. The specimen had identical geometric parameters with the type 2 one in Fig. 2-4(a) except for the additional crease at the central square, and was manufactured and tensioned in the same manner. In the theoretical calculation of the elastic energies of the type 2M and type 2 specimens, the torsional stiffness of the original creases was determined through experiments and curve fitting. A preliminary crease rotation experiment indicated an elastic followed by a mild hardening relationship between the bending moment per unit length, M, and the change in the dihedral angle, $\Delta\varphi$. Thus a nonlinear elastic relationship with two stages as shown in Fig. 2-14 is used to characterize the torsional behaviour of the original creases for simplicity in theoretical calculation. Then, two parameters were determined: the dihedral angle (for illustrating the range of the first branch of the curve), $\Delta\varphi_y$, and the torsional elastic constant per unit length (slope of the first branch of the curve), k_c. In this model, the slop of the second branch of the curve was set by zero (see Fig. 2-14). As expressed by the experimental results of the type 2M unit, the first-stage linear elastic response occurred when $40^o \leq \varphi_4 \leq 55.23^o$ (Fig. 2-15(a)). Thus, the dihedral angle was set as $\Delta\varphi_y = 55.23^o - 40^o = 15.23^o$. The torsional elastic constant per unit length of the creases, k_c, was obtained through the best fit of the experimental curve in Fig. 2-15, to be $0.76 N \cdot rad^{-1}$.

Then the theoretical total energy of the specimen following the two kinematic paths is calculated and differentiated with respect to tension displacement to obtain force. In the calculation, the natural dihedral angle $\varphi_{4,0}=40^o$ is measured from the specimen, whereas the others are derived based on the kinematic model. A nonlinear elastic model is found to be able to realistically model the relationship between crease torque and rotation angle. This model indicates that when the rotation of the dihedral angle is less than $\Delta\varphi_y$, the creases perform elastic deformation with torsional elastic

constant, k_c, and result in linear elastic energy. While for the dihedral angle that rotates more than $\Delta\varphi_y$, the beyond part is elastic deformation with a zero torsional constant and leads to nonlinear elastic energy. Here, the torsional elastic constant and rotation angle are determined as $k_c=k_f=0.76\text{N}\cdot\text{rad}^{-1}$ and $\Delta\varphi_y=15.23^\circ$ based on experiment and curve fitting. Correspondingly, Eq. (2-28) is modified as follows to calculate the total energy of the type 2M specimen.

$$U_t=\begin{cases}\sum_{i=1}^{13}\frac{1}{2}k_c\cdot L_i\left(\varphi_i-\varphi_{i,0}\right)^2,\ \varphi_{i,0}<\varphi_i\le\varphi_{i,0}+\Delta\varphi_y,\\ \sum_{i=1}^{13}\left[\frac{1}{2}k_c\cdot L_i\cdot\Delta\varphi_y{}^2+k_c\cdot L_i\cdot\Delta\varphi_y\left(\varphi_i-\varphi_{i,0}-\Delta\varphi_y\right)\right],\ \varphi_i>\varphi_{i,0}+\Delta\varphi_y.\end{cases}\tag{2-36}$$

In which, $k_c\cdot L_i\left(\varphi_i-\varphi_{i,0}\right)^2/2$ and $k_c\cdot L_i\cdot\Delta\varphi_y{}^2/2$ represent the first stage of the nonlinear elastic energy while $k_c\cdot L_i\cdot\Delta\varphi_y\left(\varphi_i-\varphi_{i,0}-\Delta\varphi_y\right)$ represents the second one.

In the tension experiments, the force is measured directly from the experiment and the energy is obtained by integration of the force over the displacement. The theoretically derived normalized total energy, $U_t/(k_c l)$, and normalized force, F/k_c, of type 2M are drawn against normalized displacement $\Delta x/l$ together with the experimental ones in Fig. 2-15(a) and (b). Note that before the bifurcation point, only the energy and force on kinematic path 1 are calculated, because kinematic path 2 in this range is inaccessible in experiments owing to physical interference. As expected, the experimental curves bifurcate and follow the low-energy deformation path throughout loading. One discrepancy, however, is that the tiny force drops at the bifurcation point in the theoretical curve is not observed in the experimental curve, possibly because the magnitude of the force drop is too small.

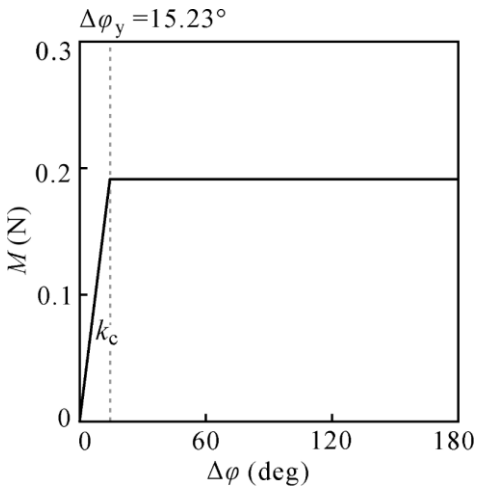

Fig. 2-14 Nonlinear elastic model for the original creases.

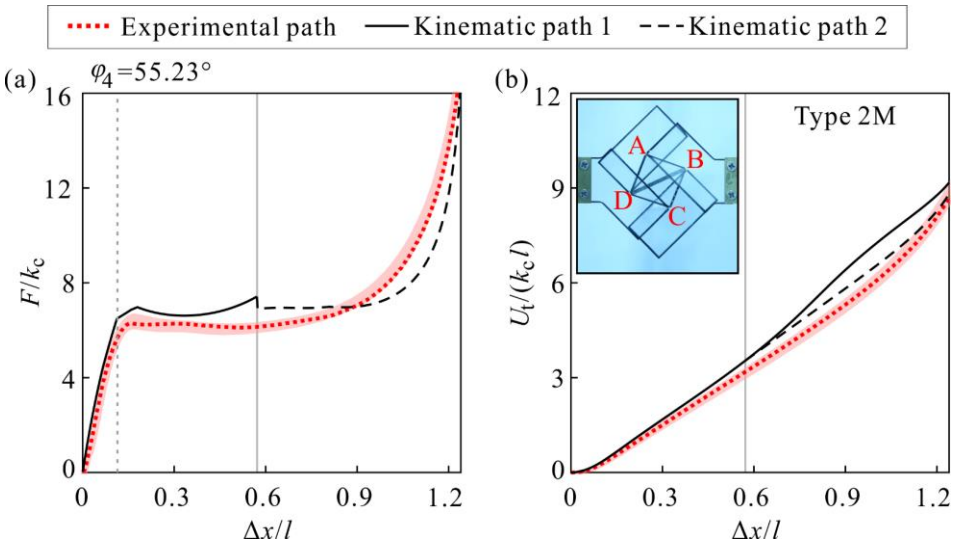

Fig. 2-15 Theoretical and experimental (a) normalized force F/k_c and (b) normalized energy $U_t/(k_c l)$ versus normalized displacement $\Delta x/l$ for the type 2M specimen with the natural dihedral angle $\varphi_{4,0}$=40º. (Bifurcation of the theoretical curves occurs at φ_{13}=94.12º.)

Regarding the virtual crease on the central square of the type 2 unit, I determined from the digital image correlation result that the maximum strain in the central square during loading, 0.67%, was lower than the yield strain of the material, 0.72%, indicating that the material was in the elastic range during deformation. Therefore the virtual crease was assumed to be linear elastic. The torsional elastic constant per unit length, k_f, was calculated based on the bending stiffness of the facet[65],

$$k_f = \frac{E \cdot I}{s} = \frac{E \cdot t^3}{12s} \tag{2-37}$$

where E=2299.18MPa was the Young's modulus of the polyethylene terephthalate sheet, which was determined from tension experiments, t=0.5mm was the thickness of the sheet, and s=21.50mm was the bending arc length of the central square measured from the reconstructed geometry based on digital image correlation (arc from vertices A to C in Fig. 2-16(a) and (b)). Substituting the values into Eq. (2-37), the torsional elastic constant per unit length of the virtual crease was determined to be k_f=1.11N·rad^{-1}.

Subsequently, the model is validated by comparing the experimental and theoretical results for the non-rigid-foldable type 2 specimen in Fig. 2-4(a) with a natural dihedral angle of $\varphi_{4,0}$=30º. The same procedure as in the case of the type 2M pattern is followed expect for that the torsional stiffness of the virtual crease needs to be determined. Here, the energy of the virtual crease is $k_f \cdot L_s(\varphi_s - \varphi_{s,0})^2/2$ in the whole folding process because of the linear elastic bending deformation existing in the

central square facet. Consequently, the theoretical total energy can be calculated by modification of Eq. (2-28) as follows

$$U_{\mathrm{t}}=\begin{cases}\sum_{i=1}^{12}\frac{1}{2}k_{\mathrm{c}}\cdot L_i\left(\varphi_i-\varphi_{i,0}\right)^2+\frac{1}{2}k_{\mathrm{f}}\cdot L_{\mathrm{s}}\left(\varphi_{\mathrm{s}}-\varphi_{\mathrm{s},0}\right)^2, & \varphi_{i,0}<\varphi_i\le\varphi_{i,0}+\Delta\varphi_y,\\ \left(\begin{array}{l}\sum_{i=1}^{12}\left[\frac{1}{2}k_{\mathrm{c}}\cdot L_i\cdot\Delta\varphi_y{}^2+k_{\mathrm{c}}\cdot L_i\cdot\Delta\varphi_y\left(\varphi_i-\varphi_{i,0}-\Delta\varphi_y\right)\right]\\ +\frac{1}{2}k_{\mathrm{f}}\cdot L_{\mathrm{s}}\left(\varphi_{\mathrm{s}}-\varphi_{\mathrm{s},0}\right)^2\end{array}\right), & \varphi_i>\varphi_{i,0}+\Delta\varphi_y.\end{cases}\tag{2-38}$$

Then the force can also be derived by differentiation of the energy against displacement.

The theoretical and experimental results are presented in Fig. 2-17(a) and (b). Again a reasonable agreement is achieved, especially with respect to the four feature points I–IV on the force curve. In addition, the theoretical force reaches a local maximum (point III) at the bifurcation point and then drops. This is because the virtual diagonal crease starts to unbend when the structure reaches its bifurcation configuration, which releases elastic energy and causes a drop in the force. Notice that the drop is not as dramatic in the experiment due to that the limited rigidity of the facets makes them deform simultaneously with the creases.

The repeatability of the experimental results proved by several specimens is described as the red shade in Fig. 2-15(a) and (b) as well as Fig. 2-17(a) and (b). Therefore, a conclusion can be obtained that the two challenges for theoretical characterization of the non-rigid-foldable pattern have been solved. The analytical model, which combines kinematics and mechanics, can accurately predict the mechanical behaviors of type 2 square-twist pattern.

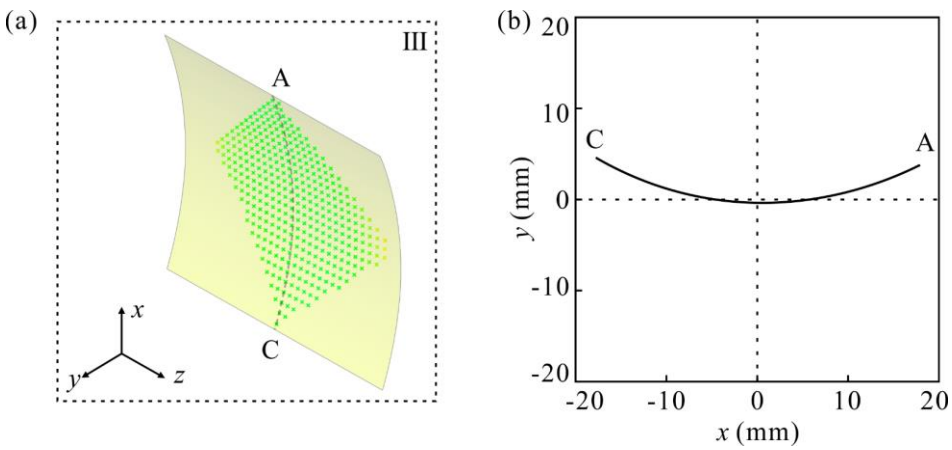

Fig. 2-16 (a) Bending arc length and (b) the fitting curve using polynomial functions between vertices A and C of the central square of the type 2 unit.

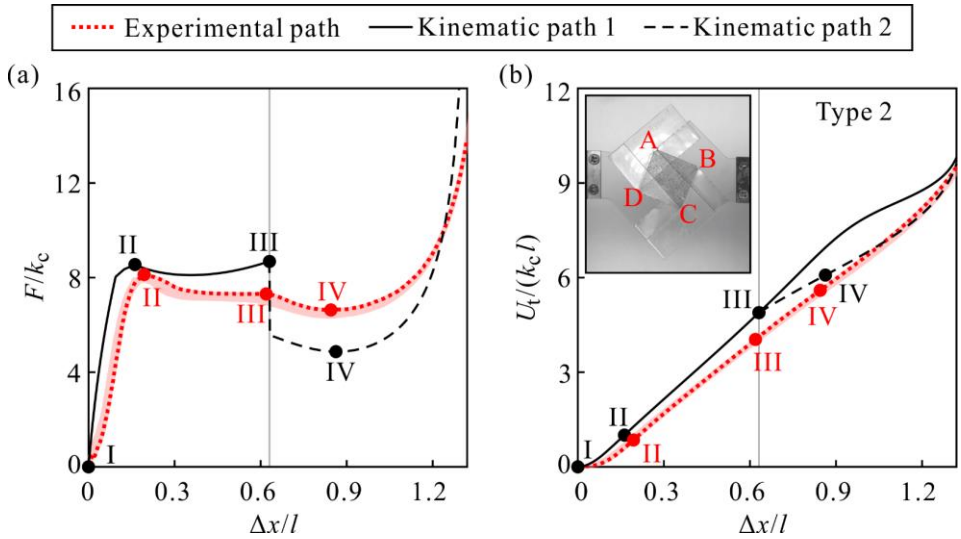

Fig. 2-17 Theoretical and experimental (a) normalized force F/k_c and (b) normalized energy $U_t/(k_c l)$ versus normalized displacement $\Delta x/l$ for the type 2 specimen with the natural dihedral angle $\varphi_{4,0}$=30º. (Bifurcation of the theoretical curves occurs at φ_{13}=94.12º.)

2.5.2 Stability of Deformation Path

It has been shown that if undisturbed during loading, both type 2M and type 2 patterns will follow the low-energy path. However, it would be interesting to know if initially placed on the high-energy path, whether it will follow it or drop to the low-energy one. To investigate this, a type 2M specimen was fabricated with two voids of 9.50mm by 16.50mm (inset of Fig. 2-18) to eliminate physical interferences. This made the branch of kinematic path 2 before the bifurcation point physically reachable, leading to four possible deformation modes: path 1 throughout deformation; path 1 followed by path 2; path 2 followed by path 1, and path 2 throughout. Then four experiments were conducted on the specimen, and the experimental paths in terms of φ_6 versus φ_4 were measured and presented in Fig. 2-18.

Specifically, in experiment 1, the specimen was set initially on kinematic path 1 and tensioned without disturbance. It moved on path 1 up to the bifurcation point and then dropped to kinematic path 2. In experiment 2, the specimen was also on kinematic path 1 initially. Immediately after bifurcating to path 2, it was manually adjusted back to kinematic path 1 and then applied further tension. However, the specimen did not stay on kinematic path 1 and quickly dropped to kinematic path 2. Experiments 3 and

4 respectively followed the procedures of experiments 1 and 2, but started from a configuration on kinematic path 2. In both cases, the specimen quickly dropped to the low-energy path (i.e., path 1 prior to and path 2 after the bifurcation point). Those experimental findings agree with theoretical analysis. Moreover, the results imply that the origami structure will follow a stable deformation path that is insensitive to perturbation, which makes it better adaptive to various work conditions.

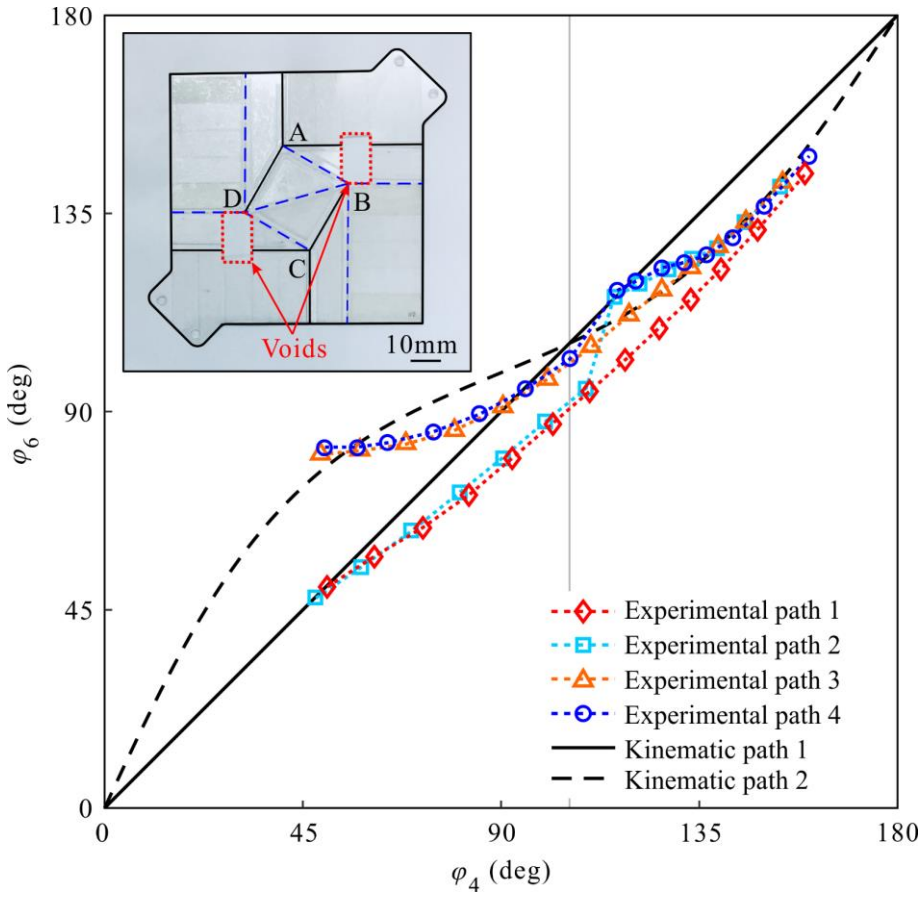

Fig. 2-18 Two kinematic paths and four experimental paths of a type 2M specimen with two voids. In the experiments, the initial dihedral angle $\varphi_{4,0}$=45°.

2.6 Programmability of Mechanical Properties

2.6.1 Effects of Geometric and Material Parameters

Using the theoretical model, the mechanical response of the type 2 pattern can be readily programmed by simply changing the material and geometrical parameters. This

is demonstrated by calculating and comparing the energy and force of a series of structures with varying parameters (see Fig. 2-19 for material parameters and Fig. 2-20 and Fig. 2-21 for geometric parameters). In the calculation, the same nonlinear elastic original creases, linear elastic virtual crease, and natural dihedral angle $\varphi_{4,0}$=30º as those for the type 2 specimen in Fig. 2-4(a) are adopted. And the displacement is normalized by the maximum displacement, Δx_{max}, in all the curves for convenient comparison.

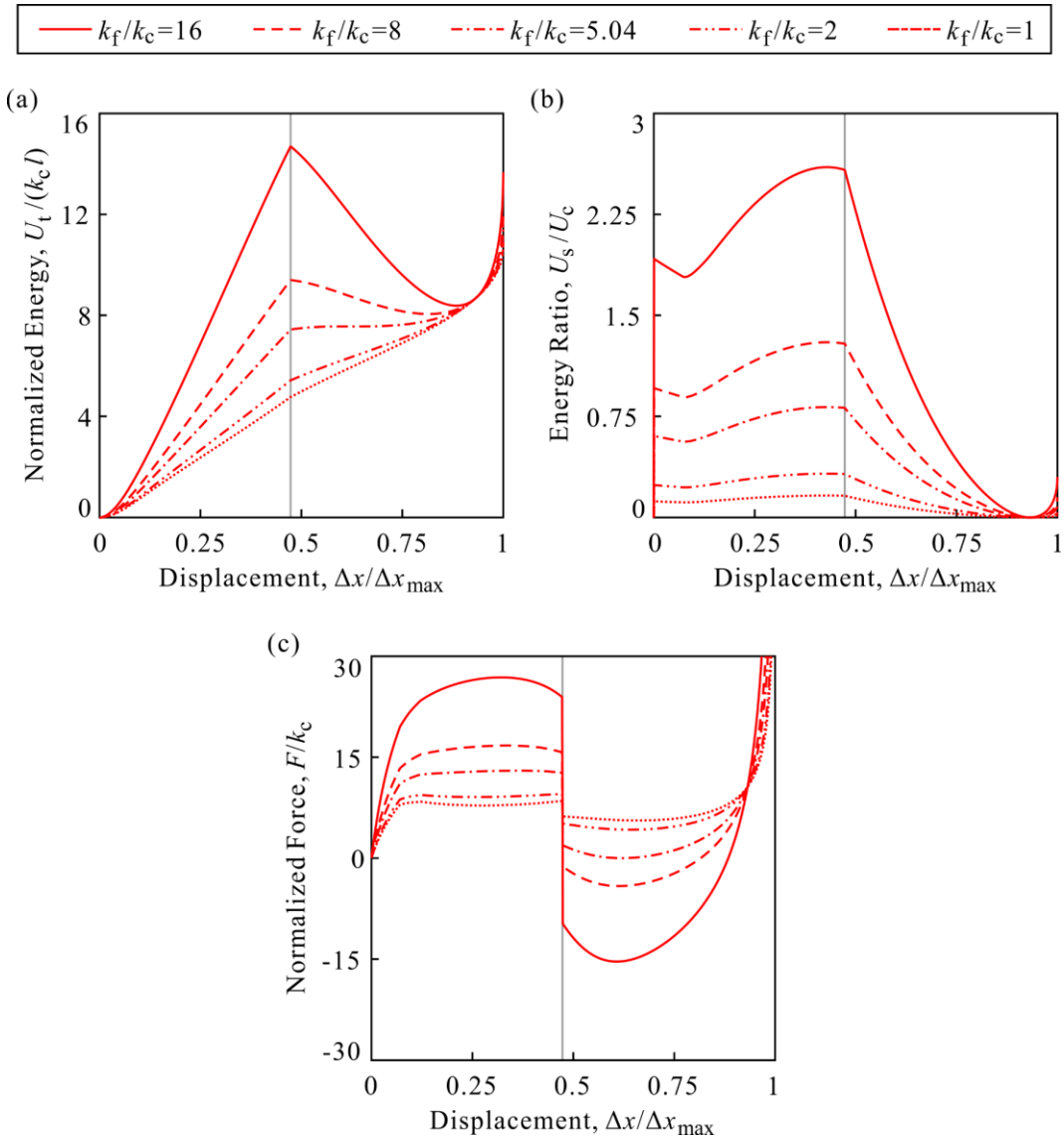

Fig. 2-19 The effects of the stiffness ratio k_f/k_c. (a) The normalized energy, $U_t/(k_c l)$, (b) ratio of the central square bending energy to the crease energy, U_s/U_c, and (c) normalized force, F/k_c, of the type 2 pattern derived from the theoretical model.

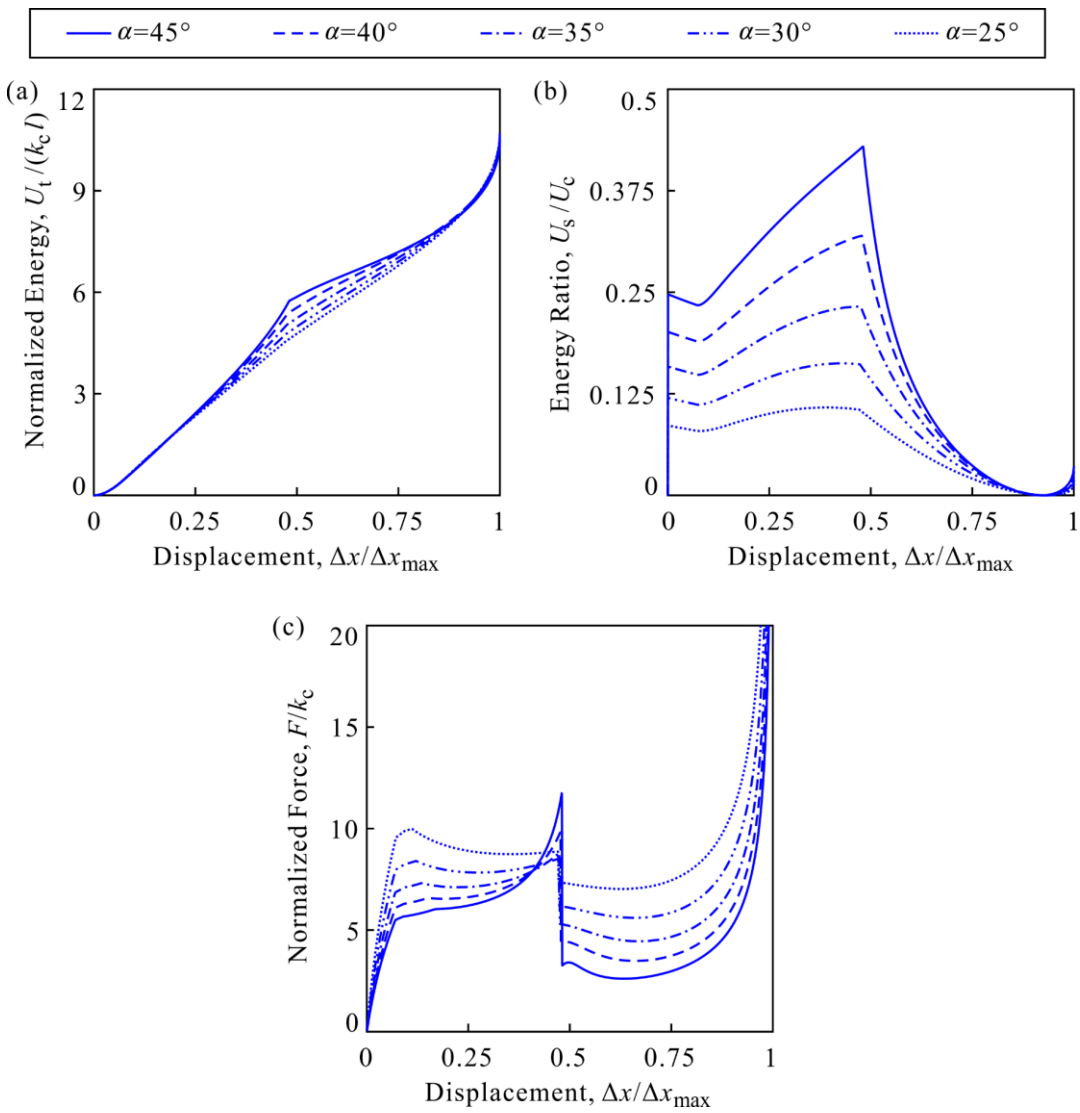

Fig. 2-20 The effects of the twist angle α. (a) The normalized energy, $U_t/(k_c l)$, (b) ratio of the central square bending energy to the crease energy, U_s/U_c, and (c) normalized force, F/k_c, of the type 2 pattern derived from the theoretical model.

The investigated material parameter is the ratio of the torsional stiffness of the virtual crease, which is essentially the bending stiffness of the central square, to that of the original creases. The energy and force curves of five models with identical α=30º and a/l=1, but different k_f/k_c values ranging from 1 to 16, are presented in Fig. 2-19. It can be seen that as the ratio increases, both the energy and force increase. This is because at higher torsional stiffness, more energy is required to deform the central square, thereby lifting the force barrier to reach bifurcation. Furthermore, the decrease in force at the bifurcation point becomes larger, and a negative force occurs when k_f/k_c surpasses 5.04. The condition for the existence of a negative force is analyzed in Section

2.6.2. Briefly, this phenomenon is best explained by the variation in the bending energy of the central square. It has been shown in Fig. 2-17(a) and (b) that the unbending of the central square after bifurcation releases elastic energy and leads to a drop in the force. As shown in Fig. 2-19(b), the ratio of the central square bending energy to the crease energy, U_s/U_c, increases with k_f/k_c. When k_f/k_c>5.04, the energy release in the central square is greater than the energy increase in the original creases, leading to a reduction in the total energy of the structure and a corresponding negative force. Therefore, the mechanical properties and behavior of the structure can be programmed simply by tuning the bending stiffness of the central square facet.

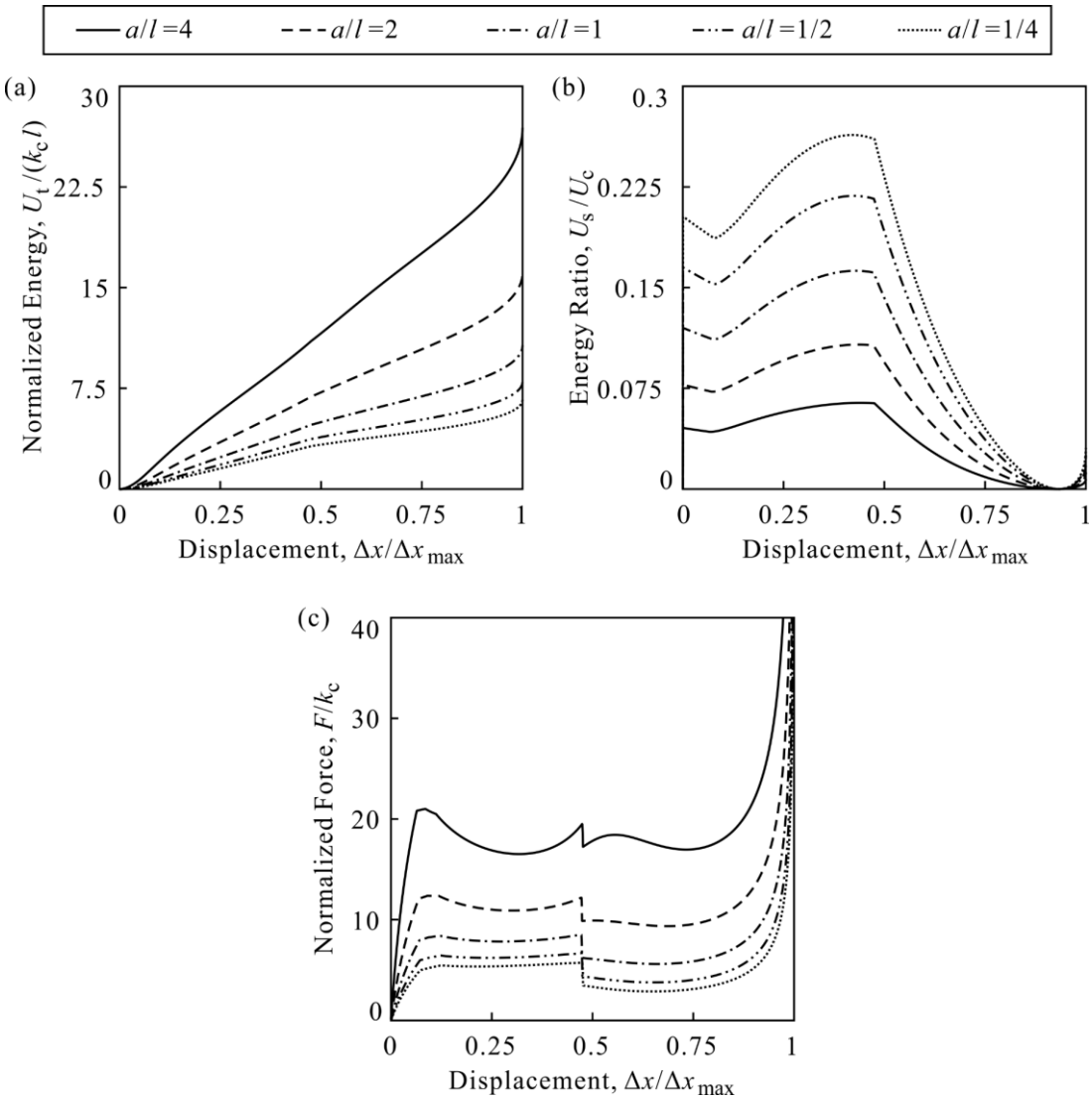

Fig. 2-21 The effects of the side length ratio a/l. (a) The normalized energy, $U_t/(k_c l)$, (b) ratio of the central square bending energy to the crease energy, U_s/U_c, and (c) normalized force, F/k_c, of the type 2 pattern derived from the theoretical model.

The geometric parameters also influence the behavior of the structure. A comparison of five models with α in the range of 25º–45º, k_f/k_c=1 and a/l=1 indicates that increasing the twist angle lowers the initial peak force but raises the force barrier to the bifurcation point (Fig. 2-20). Decreasing a/l, which means keeping the size of the central square constant while shortening the facets around it, reduces the entire force level owing to the decrease in the crease lengths, see the results in Fig. 2-21 from five models with a/l ranging from 1/4 to 4 while α=30º and k_f/k_c=1. The force drop in the bifurcation point becomes more pronounced with decreasing a/l because of the higher bending energy of the central square facet.

2.6.2 Negative Force

As shown in Fig. 2-19(c), the force curve can be negative after the bifurcation point when the stiffness ratio, k_f/k_c, surpasses a critical value. To analyse this critical stiffness ratio, the force is calculated using the following equation.

$$F = \frac{dU_t}{d(\Delta x)}. \tag{2-39}$$

Substituting Eq. (2-33) into Eq. (2-39), a rewritten equation is expressed as

$$\begin{aligned} F &= \frac{d\begin{pmatrix} k_c(a+l\cdot\cos\alpha+l)(\varphi_1-\varphi_{1,0})^2 + k_c(a+l)(\varphi_4-\varphi_{4,0})^2 + k_c\cdot a(\varphi_5-\varphi_{5,0})^2 \\ + k_c(a+l\cdot\cos\alpha)(\varphi_6-\varphi_{6,0})^2 + \frac{\sqrt{2}}{2}k_f\cdot l(\varphi_{13}-\varphi_{13,0})^2 \end{pmatrix}}{d(\Delta x)} \\ &= \frac{d\begin{pmatrix} k_c(a+l\cdot\cos\alpha+l)(\varphi_1-\varphi_{1,0})^2 \\ + k_c(a+l)(\varphi_4-\varphi_{4,0})^2 + k_c\cdot a(\varphi_5-\varphi_{5,0})^2 \\ + k_c(a+l\cdot\cos\alpha)(\varphi_6-\varphi_{6,0})^2 \end{pmatrix} + d\left(\frac{\sqrt{2}}{2}k_f\cdot l(\varphi_{13}-\varphi_{13,0})^2\right)}{d(\Delta x)} \\ &= k_c\cdot\frac{d\begin{pmatrix} (a+l\cdot\cos\alpha+l)(\varphi_1-\varphi_{1,0})^2 \\ + (a+l)(\varphi_4-\varphi_{4,0})^2 + a(\varphi_5-\varphi_{5,0})^2 \\ + (a+l\cdot\cos\alpha)(\varphi_6-\varphi_{6,0})^2 \end{pmatrix} + \frac{k_f}{k_c}d\left(\frac{\sqrt{2}}{2}l(\varphi_{13}-\varphi_{13,0})^2\right)}{d(\Delta x)} \end{aligned}. \tag{2-40}$$

Generally, the force can be positive or negative depending on the geometric and material parameters. Considering the models in Fig. 2-19 with α=30º, a/l=1, and $\varphi_{4,0}$=30º, Eq. (2-29) and (2-40) can be used to work out that the minimum force F_{min}<0, i.e., a negative force occurs when

$$\frac{k_{\mathrm{f}}}{k_{\mathrm{c}}} > -\left(\left. \frac{d\begin{pmatrix} (a+l\cdot\cos\alpha+l)(\varphi_1-\varphi_{1,0})^2+(a+l)(\varphi_4-\varphi_{4,0})^2 \\ +a(\varphi_5-\varphi_{5,0})^2+(a+l\cdot\cos\alpha)(\varphi_6-\varphi_{6,0})^2 \end{pmatrix}}{d\left(\frac{\sqrt{2}}{2}l(\varphi_{13}-\varphi_{13,0})^2\right)} \right|_{\min} \right) = 5.04\,. \tag{2-41}$$

Physically, this means that when k_f/k_c surpasses the critical value, the energy release in the central square is greater than the energy increase in the original creases, thereby leading to a negative value in the force curve.

2.6.3 Tension Experiment of 2×2 Type 2 Metasheet

Here, it is validated that the mechanical properties of type 2 metasheet can be predicted by the theoretical model of unit as mentioned above. A 2×2 tessellation of the type 2 unit (Fig. 2-22) was designed, manufactured using the same material and technique for the type 2 unit in Fig. 2-4, and tested to demonstrate the feasibility of the proposed design approach. Therefore, the same torsional stiffness for the original and virtual creases were also utilized to calculate the theoretical energy and force curves. Based on the programmability analysis, the angle α=40º is chosen for the tessellation so as to manifest its bifurcation behaviour. The theoretical energy and force curves are also calculated from Eq. (2-38) and drawn together with the experimental results in Fig. 2-23. Six points of interest are marked in red on the curve in Fig. 2-23(a) and (b), which correspond to the six configurations in Fig. 2-24. It can be seen from Fig. 2-24 that a simultaneous unfolding of the four units was obtained. The natural dihedral angle $\varphi_4 = 20°$. Bifurcation occurs at $\Delta x/\Delta x_{\max}$=0.7 ($\varphi_{13} = 64.29°$).

The theoretical curves still capture the main features of the structure, including the force plateau region (points II, III, and IV) and the force drop (point V) due to bifurcation. The reasonably good matches between theoretical and experimental data are achieved in both normalized energy and force. The drop (point V) in the normalized force results from the virtual diagonal crease on the central square starting to unbend when the structure reaches its bifurcation configuration, which releases elastic energy. Notice that the drop is not as dramatic in the experiment, which is also discovered in the unit experiment. That is because the facets in the theoretical calculation are perfectly stiff, but those in the experiment have limited rigidity that makes them deform simultaneously with the creases. In brief, the results in Fig. 2-23 indicate that the

theoretical model developed based on the unit can be readily employed to predict and program the mechanical properties of the tessellated metamaterials.

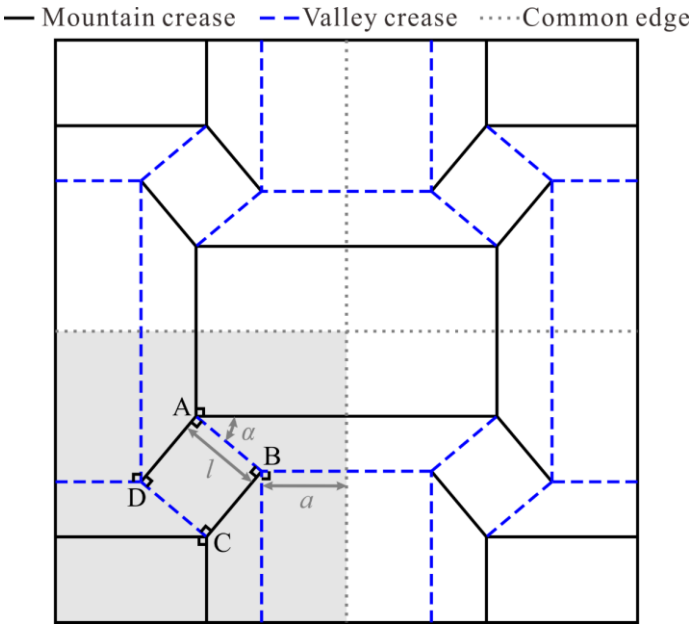

Fig. 2-22 A 2×2 tessellation of the type 2 unit defined by a=25mm, l=25mm, and α=40º.

2.7 Conclusions

In this chapter, a theoretical model for the non-rigid-foldable type 2 pattern has been developed to achieve predictable programmable mechanical behavior, based on the kinematic analysis results of its rigid-foldable counterpart. It has been demonstrated theoretically and experimentally that the non-rigid-foldable pattern bifurcates during tension so as to always follow the low-energy path. This feature has not been reported previously for origami structures. The model enables us to accurately program the mechanical properties of the origami structure by tuning the geometry of the pattern and/or mechanical properties of the creases and the central square facet. This programmability through the pattern geometry and material allows various mechanical functions to be achieved in the origami structure. For example, to design an ideal impact energy absorption device, which requires a long and flat plateau[163], smaller values of k_f/k_c and α, and a larger value of a/l should be selected to minimize the force drop at the bifurcation point. The diagram shown in Fig. 2-21c shows nearly perfect force plateaus when k_f/k_c=1 and α=30º. The height of the plateaus increases with the ratio a/l.

Altogether, this work enables the use of non-rigid-foldable origami patterns in the design of mechanical metamaterials with theoretically predictive behavior.

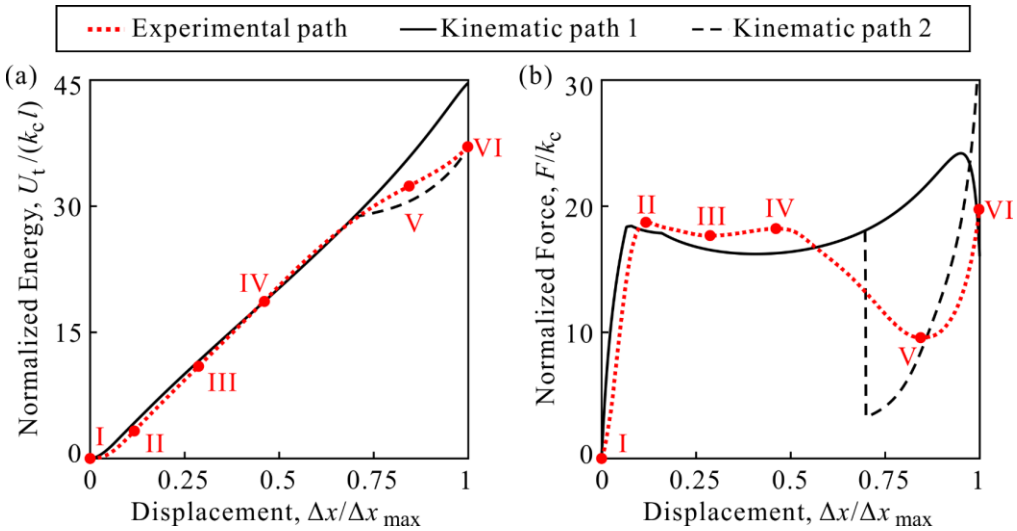

Fig. 2-23 (a) Normalized energy and (b) force vs. normalized displacement, $\Delta x/\Delta x_{max}$, where Δx_{max}=60mm.

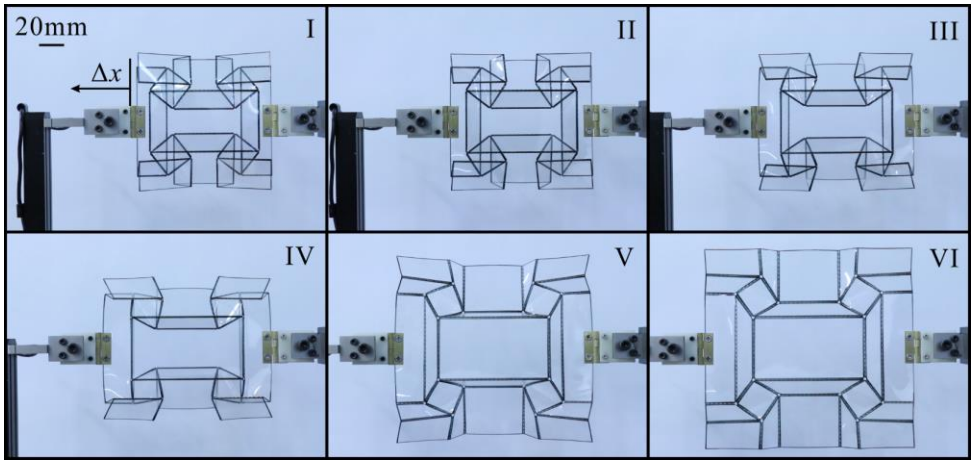

Fig. 2-24 Representative configurations of the tessellation during uniaxial tension experiment.

Chapter 3 The Non-rigid Square-twist Type 1 Unit

3.1 Introduction

The type 1 square-twist pattern in Fig. 3-1(a) or (c) consists of a central square facet, four trapezoidal ones, and four rectangular ones, which is parameterized by two side lengths, l and a, and a twist angle, α. A paper model in the deployed and folded configurations is shown in Fig. 3-1(b) or (d). It can be seen that the crease mountain-valley assignment forms a four-fold rotational symmetry in the pattern. This pattern has great potential in the design of mechanical metamaterials for two reasons. First of all, it has a strong self-locking behavior which is remarkably different from the other three members of the family. Moreover, it is relatively easy to combine it with the other rigid and non-rigid square-twist patterns to form metamaterials with a wide range of tunable properties. However, the quantitative relationship between the mechanical properties of the pattern and the geometric and material design parameters, which is essential for the programmability of the metamaterials, has so far been unclear. According to the previous efforts on mechanical characterization of the pattern, little information is given about the detailed deformation process or validation with experiments. In view of this, characterizing and programing the mechanical properties of the pattern is proposed through a combination of experiments, finite element simulation, and empirical model development.

The outline of this chapter is as follows. In Section 3.2, the biaxial tension experiment of the type 1 origami structure is presented. The kinematic analysis of the modified type 1 pattern is presented in Section 3.3. The numerical simulation and corresponding validation of the type 1 origami structure are studied in Section 3.4. In Section 3.5, the deformation process of the structure, as well as the energy, force, and stiffness responses, are discussed in detail. In Section 3.6, an empirical model is built based on the experimental and numerical analysis to correlate the geometric and material parameters of the structure and its mechanical properties. The empirical model is utilized to program the mechanical properties of the pattern in Section 3.7. Furthermore, a 2×2 type 1 metasheet is tested to demonstrate the feasibility of the proposed theoretical model. Finally, a conclusion is given in Section 3.8.

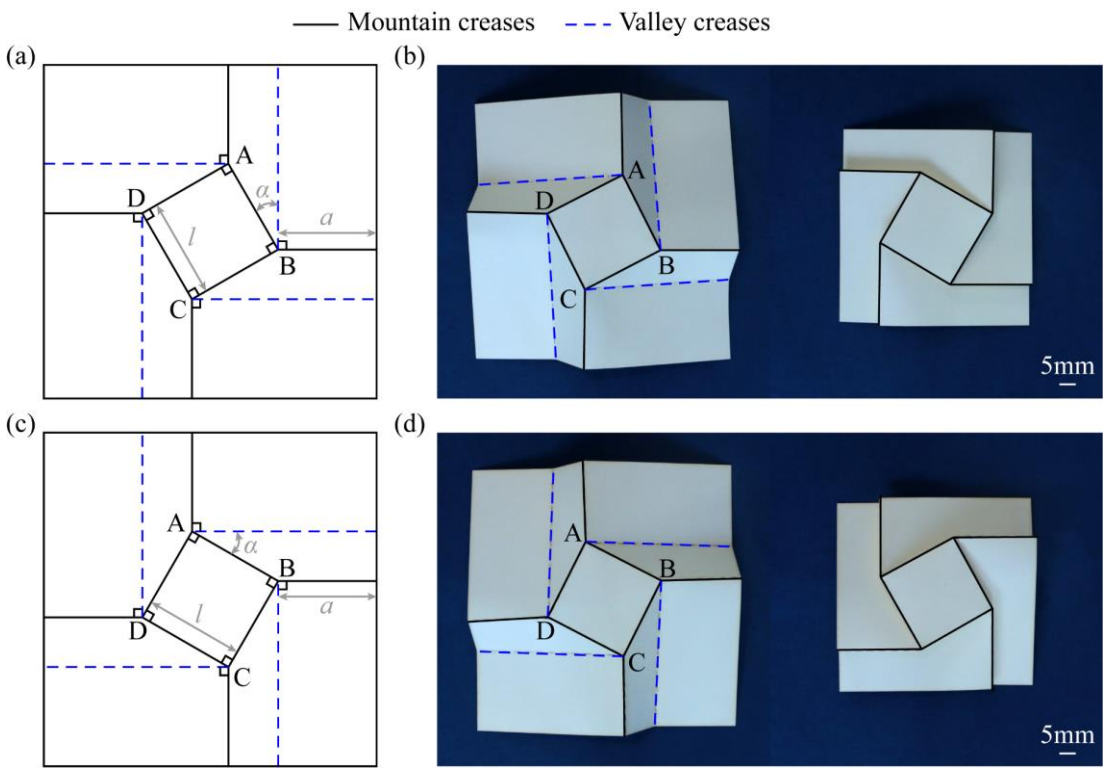

Fig. 3-1 (a and c) Pattern, geometric parameters, and crease mountain-valley assignment of type 1 square-twist pattern with left-handed and right-handed versions, (b and d) unfolded and folded configurations of a paper model with left-handed and right-handed versions.

3.2 Biaxial Tension Experiment

The four-fold rotational symmetry of the pattern results in identical deformation holding on the four corners of the unit in the whole unfolded process. Thus, a biaxial tension experiment, loading at four corners of the structure, was conducted through a specially designed loading mechanism. As shown in Fig. 3-2(a), the square loading mechanism consisted of four sliding units, each of which was composed of a 3D-printed block and a steel linear guide fixed together. The four blocks were used to connect with the four corners of the specimen, respectively. The sliding unit and linear guide on the same block are perpendiculars. There was a channel in each block, where the linear guide from the neighboring sliding unit could pass through with no rotation and forms a prismatic joint. Here, the relative displacement between each sliding unit and its connected linear guide is always identical. Based on this sliding behavior, applying uniaxial loading on two blocks of the mechanism could provide stretching the specimen

equally in the two diagonal directions, which is illustrated through the deformation process of the specimen in Fig. 3-3. Six universal wheel bearings were installed at the bottom of the loading mechanism to minimize the friction between the surface of the machine and the loading mechanism. The loading mechanism was connected to a horizontal testing machine by a stationary and a movable fixture. Using the loading mechanism, only the data in one diagonal direction, i.e., the *x*-direction in Fig. 3-2(a), is tested because the biaxial test is the conversion from uniaxial displacement.

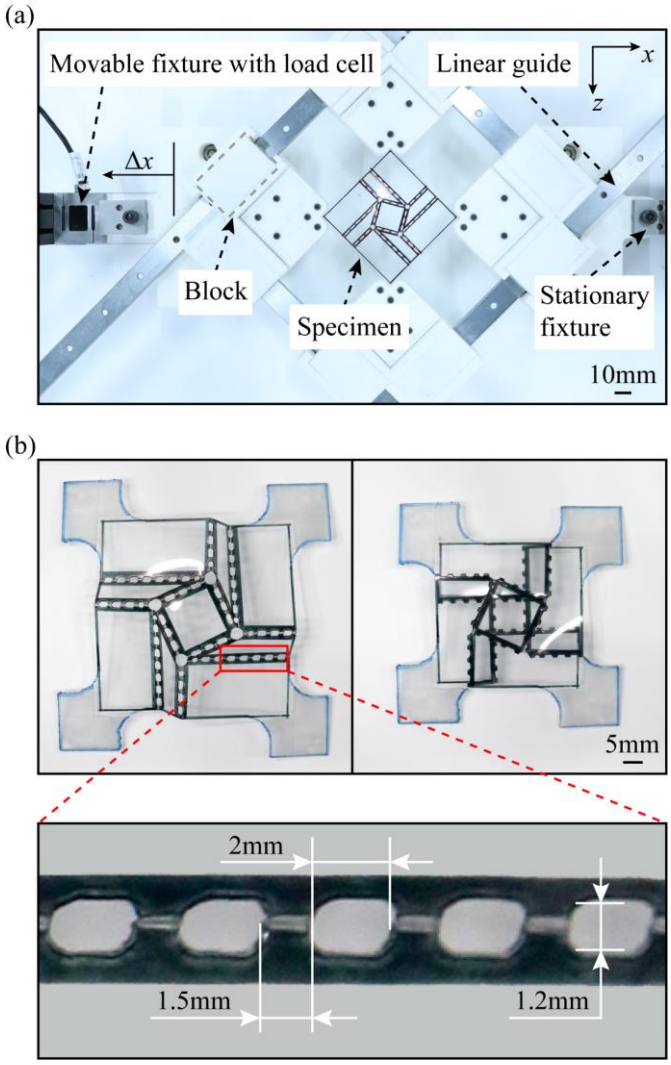

Fig. 3-2 (a) Details of the loading mechanism. (b) Unfolded and folded configurations of the PET specimen, and details of the crease.

The horizontal test machine had a stroke of 800mm and a load cell of 300N with an accuracy of 0.5%. In the experiment, the specimen was tensioned by a displacement

of Δx_{max}=23mm along the diagonal direction at a loading rate of 0.2mm/s to avoid dynamic effects. The exact deformations of the square facet, as well as the portions of the rectangular and trapezoidal ones that were not occluded by others, were captured by the DIC system in Section 2.2. Three specimens were tested to obtain reliable results.

The test specimen was manufactured by PET sheets of thickness t=0.4mm (Fig. 3-2(b)). The geometric parameters were selected as a=l=16.25mm and α=30°. The creases were cut as 1.2-mm-wide dotted lines with 2mm perforations at 1.5mm intervals by a Trotec Speedy 300 laser cutter, and holes with 3.2mm in diameter were cut at the vertices to mitigate stress concentration and fracture. Afterward, the perforated sheet was folded by hand to the fully folded shape.

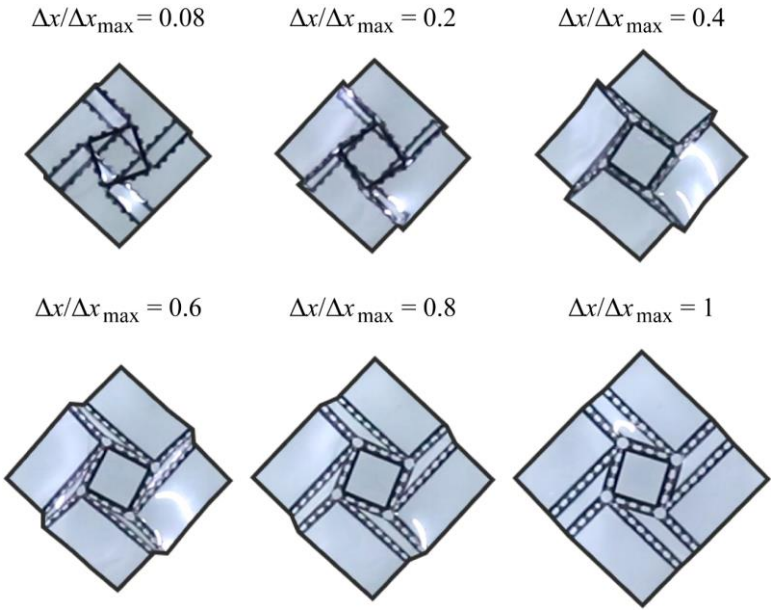

Fig. 3-3 Deformation process of the specimen.

3.3 Kinematic Analysis of Modified Type 1 Unit

Due to the successful work that the foldability of type 2 unit is converted by adding crease on the central square facet, the same research method was used to analyze type 1 unit at the beginning of this chapter. The modified type 1 pattern with an addition crease on the central square facet in Fig. 3-4(a) is similar to the type 2M pattern. Thus, the type 1M unit can also be modeled by two spherical 4R linkages (Fig. 2-5) and two spherical 5R linkages (Fig. 2-8). Because the 5-crease vertices in type 1M pattern (Fig.

3-4(a)) are similar to that in type 2M pattern (Fig. 2-7(a)), the relationship between the rotation variables θ_i^j and θ_{i+1}^j (i=1, 2, 3, 4, 5, and j=b, d) can be solved by Eq. (2-11)-(2-13). Notice that the mountain-valley assignment of vertices A and C in type 1 and 1M patterns causes that θ_1^j and θ_3^j have opposite signs while θ_2^j and θ_4^j have the same (j=a, c). The relationship between the rotation variables θ_i^j and θ_{i+1}^j (i=1, 2, 3, 4, and j=a, c) solving by substituting Eq. (2-5) to Eq. (2-4) can be rewritten as

$$\frac{\tan\frac{\theta_2^j}{2}}{\tan\frac{\theta_1^j}{2}}=\frac{\cos\alpha}{1-\sin\alpha},\ \frac{\tan\frac{\theta_3^j}{2}}{\tan\frac{\theta_2^j}{2}}=\frac{-\cos\alpha}{1+\sin\alpha},$$
$$\frac{\tan\frac{\theta_4^j}{2}}{\tan\frac{\theta_3^j}{2}}=\frac{-\cos\alpha}{1-\sin\alpha},\ \frac{\tan\frac{\theta_1^j}{2}}{\tan\frac{\theta_4^j}{2}}=\frac{\cos\alpha}{1+\sin\alpha}. \tag{3-1}$$

That can be simplified as

$$\tan\frac{\theta_2^j}{2}=\frac{\cos\alpha}{1-\sin\alpha}\tan\frac{\theta_1^j}{2},\ \theta_4^j=\theta_2^j,\ \theta_3^j=-\theta_1^j. \tag{3-2}$$

Since the dihedral angles are influenced by the mountain-valley assignment, a new relationship between rotation variables θ_i^j and dihedral angles ψ_i^j (i=1, 2, 3, 4, j=a, c, and i=1, 2, 3, 4, 5, j=b, d) of type 1M pattern is described as

$$\theta_1^j=\pi-\psi_1^j,\ \theta_2^j=\pi-\psi_2^j,\ \theta_3^j=\psi_3^j-\pi,\ \theta_4^j=\pi-\psi_4^j, \tag{3-3}$$

when j=a, c, and

$$\theta_1^j=\pi-\psi_1^j,\ \theta_2^j=\psi_2^j-\pi,\ \theta_3^j=\pi-\psi_3^j,\ \theta_4^j=\psi_4^j-\pi,\ \theta_5^j=\pi-\psi_5^j, \tag{3-4}$$

when j=b, d. Substituting Eq. (3-3) to Eq. (3-2), the relationship between dihedral angles of vertices A and C is obtained as follows.

$$\tan\frac{\psi_2^j}{2}=\frac{\cos\alpha}{1+\sin\alpha}\tan\frac{\psi_1^j}{2},\ \psi_4^j=\psi_2^j,\ \psi_3^j=\psi_1^j \tag{3-5}$$

where j=a, c. Substituting Eq. (3-4) into Eq. (2-11)-(2-13), the relationship between dihedral angles of vertices B and D can be calculated by

$$\tan\frac{\psi_4^j}{2}=\frac{q_1^j}{q_2^j\mp\sqrt{q_3^j}}, \tag{3-6}$$

$$\tan\frac{\psi_5^j}{2}=\frac{p_1^j}{p_2^j+\sqrt{\left(p_2^j\right)^2-p_1^j\cdot p_3^j}}, \tag{3-7}$$

$$\cos\psi_2^j=2\sin\alpha\cdot\left(-\cos\alpha\cdot\cos\psi_4^j+\cos\alpha\cdot\cos\psi_5^j-\sin\alpha\cdot\sin\psi_4^j\cdot\sin\psi_5^j\right)-1. \tag{3-8}$$

where

$$
\begin{aligned}
q_1^j &= \sin\alpha + \cos\alpha - \sin\alpha \cdot \cos\psi_1^j - \cos\alpha \cdot \cos\psi_3^j \\
q_2^j &= \sin\psi_3^j \\
q_3^j &= \sin^2\alpha \cdot \left(\sin^2\psi_1^j + \sin^2\psi_3^j\right) + 2\sin\alpha \cdot \cos\alpha \cdot \left(\cos\psi_1^j - \cos\psi_3^j\right)
\end{aligned}
\tag{3-9a}
$$

$$
\begin{aligned}
p_1^j &= \left(\cos\alpha \cdot \sin\psi_3^j \cdot \sin\psi_4^j + \cos^2\alpha \cdot \cos\psi_3^j \cdot \cos\psi_4^j - \sin\alpha \cdot \cos\alpha \cdot \cos\psi_4^j - 1\right) \\
&\quad + \left(\sin^2\alpha \cdot \cos\psi_3^j + \sin\alpha \cdot \cos\alpha\right) \\
p_2^j &= \sin\alpha \cdot \sin\psi_3^j \cdot \cos\psi_4^j - \sin\alpha \cdot \cos\alpha \cdot \cos\psi_3^j \cdot \sin\psi_4^j + \sin^2\alpha \cdot \sin\psi_4^j \\
p_3^j &= \left(\cos\alpha \cdot \sin\psi_3^j \cdot \sin\psi_4^j + \cos^2\alpha \cdot \cos\psi_3^j \cdot \cos\psi_4^j - \sin\alpha \cdot \cos\alpha \cdot \cos\psi_4^j - 1\right) \\
&\quad - \left(\sin^2\alpha \cdot \cos\psi_3^j + \sin\alpha \cdot \cos\alpha\right)
\end{aligned}
\tag{3-9b}
$$

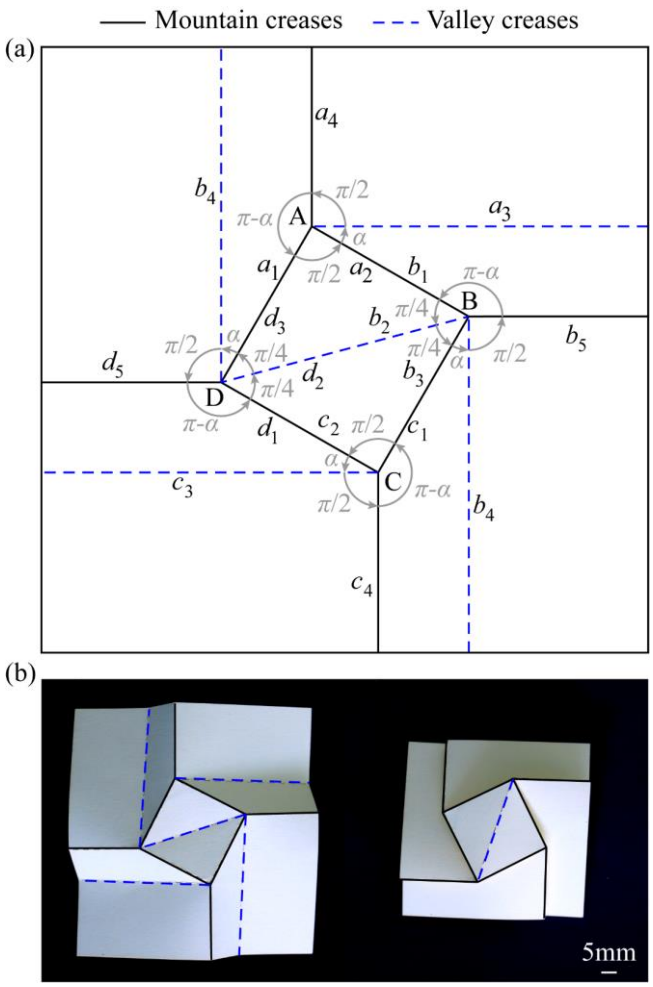

Fig. 3-4 (a) The origami pattern, definition of creases and vertices, (b) unfolding and folding configurations of modified type 1 (1M) unit.

Joining the four vertices together, the relationship of the dihedral angles ψ_i^j on the common creases can be expressed using the same equation as type 2M pattern, see Eq. (2-23). And the compatibility condition to determine the rigid foldability of type

1M pattern is also the same as that of type 2M pattern, see Eq. (2-24). Using the same analysis approach as type 2M pattern, it can be concluded that the whole type 1M system is of only one degree of freedom.

Substituting Eq. (3-5)-(3-9) and (2-23) into Eq. (2-24), two sets of kinematic equations of the type 1M pattern can be obtained, which means there are two folding paths for the pattern. The equations for path 1 are

$$\tan\frac{\psi_2^a}{2}=\frac{\cos\alpha}{1+\sin\alpha}\tan\frac{\psi_1^a}{2}, \tag{3-10a}$$

$$\psi_2^a=\psi_4^a=\psi_2^c=\psi_4^c=\psi_1^b=\psi_1^d, \tag{3-10b}$$

$$\psi_1^a=\psi_3^a=\psi_1^c=\psi_3^c=\psi_3^b=\psi_3^d, \tag{3-10c}$$

$$\tan\frac{\psi_4^d}{2}=\frac{q_1^d}{q_2^d+\sqrt{q_3^d}}, \tag{3-10d}$$

$$\tan\frac{\psi_5^d}{2}=\frac{p_1^d}{p_2^d+\sqrt{\left(p_2^d\right)^2-p_1^d\cdot p_3^d}}, \tag{3-10e}$$

$$\cos\psi_2^d=2\sin\alpha\cdot\left(-\cos\alpha\cdot\cos\psi_4^d+\cos\alpha\cdot\cos\psi_5^d-\sin\alpha\cdot\sin\psi_4^d\cdot\sin\psi_5^d\right)-1, \tag{3-10f}$$

$$\psi_2^b=\psi_2^d, \tag{3-10g}$$

$$\psi_4^b=\psi_4^d, \tag{3-10h}$$

$$\psi_5^b=\psi_5^d, \tag{3-10i}$$

and the equations of path 2 are

$$\tan\frac{\psi_2^a}{2}=\frac{\cos\alpha}{1+\sin\alpha}\tan\frac{\psi_1^a}{2}, \tag{3-11a}$$

$$\psi_2^a=\psi_4^a=\psi_2^c=\psi_4^c=\psi_1^b=\psi_1^d, \tag{3-11b}$$

$$\psi_1^a=\psi_3^a=\psi_1^c=\psi_3^c=\psi_3^b=\psi_3^d, \tag{3-11c}$$

$$\tan\frac{\psi_4^d}{2}=\frac{q_1^d}{q_2^d-\sqrt{q_3^d}}, \tag{3-11d}$$

$$\tan\frac{\psi_5^d}{2}=\frac{p_1^d}{p_2^d+\sqrt{{p_2^d}^2-p_1^d\cdot p_3^d}}, \tag{3-11e}$$

$$\cos\psi_2^d=2\sin\alpha\cdot\left(-\cos\alpha\cdot\cos\psi_4^d+\cos\alpha\cdot\cos\psi_5^d-\sin\alpha\cdot\sin\psi_4^d\cdot\sin\psi_5^d\right)-1, \tag{3-11f}$$

$$\psi_2^b=\psi_2^d, \tag{3-11g}$$

$$\psi_4^b=\psi_4^d, \tag{3-11h}$$

$$\psi_5^b=\psi_5^d, \tag{3-11i}$$

where

$$\begin{aligned} q_1^d&=\sin\alpha+\cos\alpha-\sin\alpha\cdot\cos\psi_1^d-\cos\alpha\cdot\cos\psi_3^d\\ q_2^d&=\sin\psi_3^d\\ q_3^d&=\sin^2\alpha\cdot\left(\sin^2\psi_1^d+\sin^2\psi_3^d\right)+2\sin\alpha\cdot\cos\alpha\cdot\left(\cos\psi_1^d-\cos\psi_3^d\right)\end{aligned}, \tag{3-12a}$$

$$
\begin{aligned}
p_1^d &= \left(\cos\alpha\cdot\sin\psi_3^d\cdot\sin\psi_4^d+\cos^2\alpha\cdot\cos\psi_3^d\cdot\cos\psi_4^d-\sin\alpha\cdot\cos\alpha\cdot\cos\psi_4^d-1\right)\\
&\quad+\left(\sin^2\alpha\cdot\cos\psi_3^d+\sin\alpha\cdot\cos\alpha\right)\\
p_2^d &= \sin\alpha\cdot\sin\psi_3^d\cdot\cos\psi_4^d-\sin\alpha\cdot\cos\alpha\cdot\cos\psi_3^d\cdot\sin\psi_4^d+\sin^2\alpha\cdot\sin\psi_4^d \qquad .(3\text{-}12b)\\
p_3^d &= \left(\cos\alpha\cdot\sin\psi_3^d\cdot\sin\psi_4^d+\cos^2\alpha\cdot\cos\psi_3^d\cdot\cos\psi_4^d-\sin\alpha\cdot\cos\alpha\cdot\cos\psi_4^d-1\right)\\
&\quad-\left(\sin^2\alpha\cdot\cos\psi_3^d+\sin\alpha\cdot\cos\alpha\right)
\end{aligned}
$$

To illustrate the kinematic characteristics, two kinematic paths of the type 1M pattern, which are exemplified by ψ_4^d and ψ_5^d, together with six representative configurations on each path are shown in Fig. 3-5. The configurations (I_1 II_1 III_1 IV_1 V_1 VI_1) represent the unfolding sequence on path 1; (I_2 II_2 III_2 IV_2 V_2 VI_2) represent the unfolding motion on path 2. Rectangular facets in the same colour (dark or light blue) are parallel during motion. In each kinematic path, there are two pairs of parallel rectangular facets. These paths only intersect at two points that correspond to fully folded (I_1 and I_2) and fully deployed (VI_1 and VI_2). Once the motion is underway, the two kinematic paths cannot be switched.

Two phenomena should be noticed here. First, penetration of the facets occurs on kinematic path 1 between $\psi_1^d=0°$ (configuration I_1) and $\psi_1^d=74.46°$ (configuration III_1), i.e. $\psi_5^d<0°$ as shown in Fig. 3-5. Second, crease d_4 is switched from the valley crease, where $\psi_4^d<180°$, to the mountain one, where $\psi_4^d>180°$, at configuration III_1, where $\psi_1^d=74.46°$. Moreover, the critical condition for the two phenomena that $\psi_1^d=74.46°$ in Fig. 3-5 only holds when α=30°. The kinematic curves in Fig. 3-6(c) and (d) indicate that both the facet penetration and switch between valley and mountain creases rely on the geometric parameter α.

Notice that in Eq. (3-10)-(3-12), only five different variables are presented in the type 1M unit. In Fig. 3-6, the curves of relationship between the four dependent variables ψ_2^d, ψ_3^d, ψ_4^d, ψ_5^d and the independent variable ψ_1^d are depicted, where α is varied. The characteristics for ψ_2^d and ψ_3^d of type 1M unit in Fig. 3-6(a) and (b) are similar to those of type 2M unit in Fig. 2-10(a) and (b). From ψ_4^d and ψ_5^d in Fig. 3-6(c) and (d), the facet penetration and crease switch occur only when α≥23.4°. The larger α is, the sooner the crease switch happens and the larger the range of motion is where the penetration happens.

However, the kinematic analysis in this section cannot accurately describe the motion of the type 1 unit, because the additional crease on the central square breaks the four-fold rotational symmetry of this pattern in Fig. 3-1. Thus, a combination of

experiments and finite element model is introduced to investigate the folding motion and mechanical properties of the type 1 unit with retaining symmetric property, and to build an empirical model of this structure.

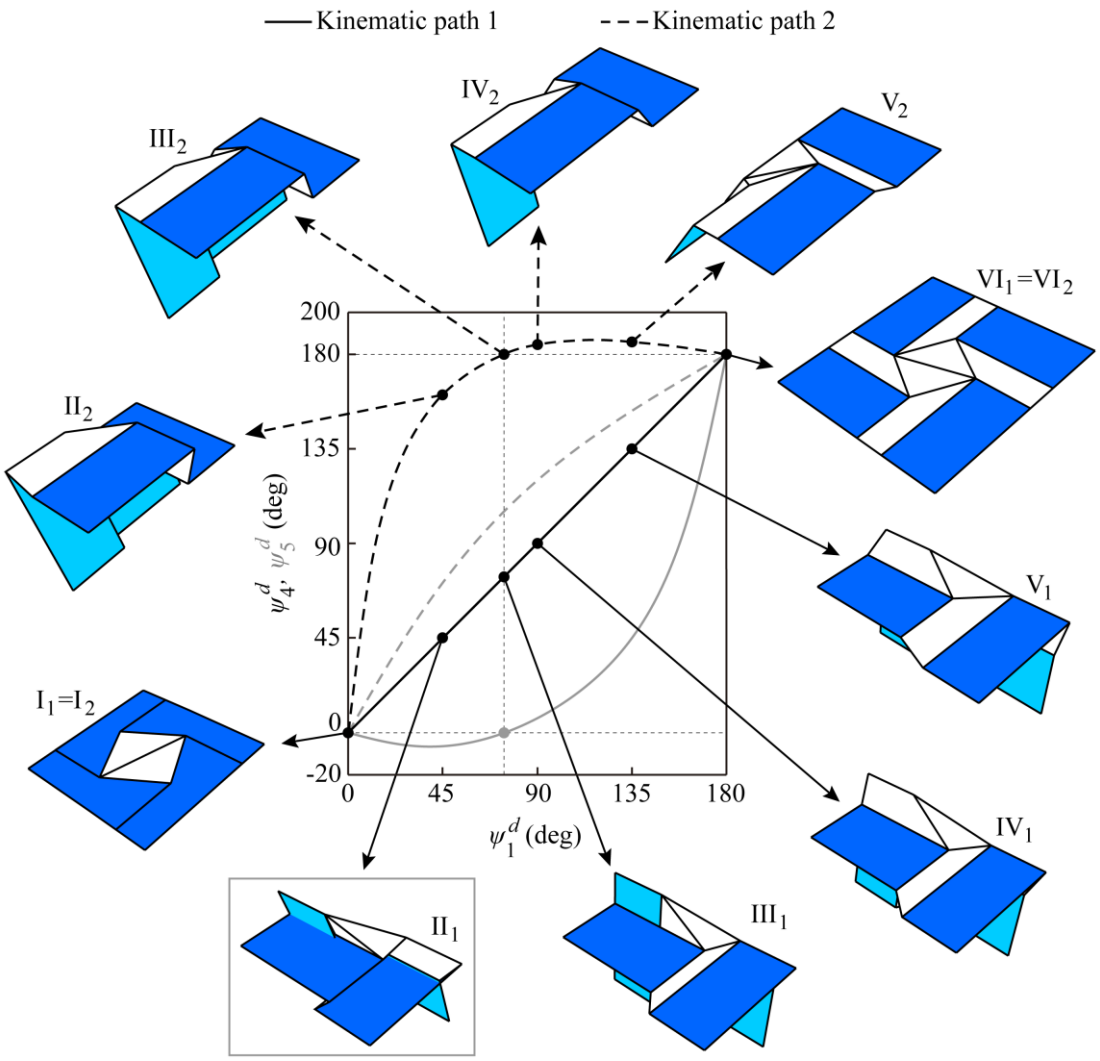

Fig. 3-5 Two different kinematic paths of the type 1M pattern expressed by ψ_4^d and ψ_5^d together with six representative configurations on each path, where α=30°.

3.4 Finite Element Modeling

For the finite element analysis, a simplified definition of creases and vertices in the type 1 pattern is presented in Fig. 3-7. The dihedral angles of the facets at crease i are described by φ_i (i=1, 2, 3, …, 12), and the vertices are defined as P_j (j=1, 2, 3, …,

16). Due to the elastic spring back of the creases, the specimen was not completely flat but had a natural dihedral angle formed by the square and trapezoidal facets $\varphi_{i,0}$=19.58° (i=1, 4, 7, 10), diagonal length L_{D0}=53.30mm, and height H_{D0}=7.80mm.

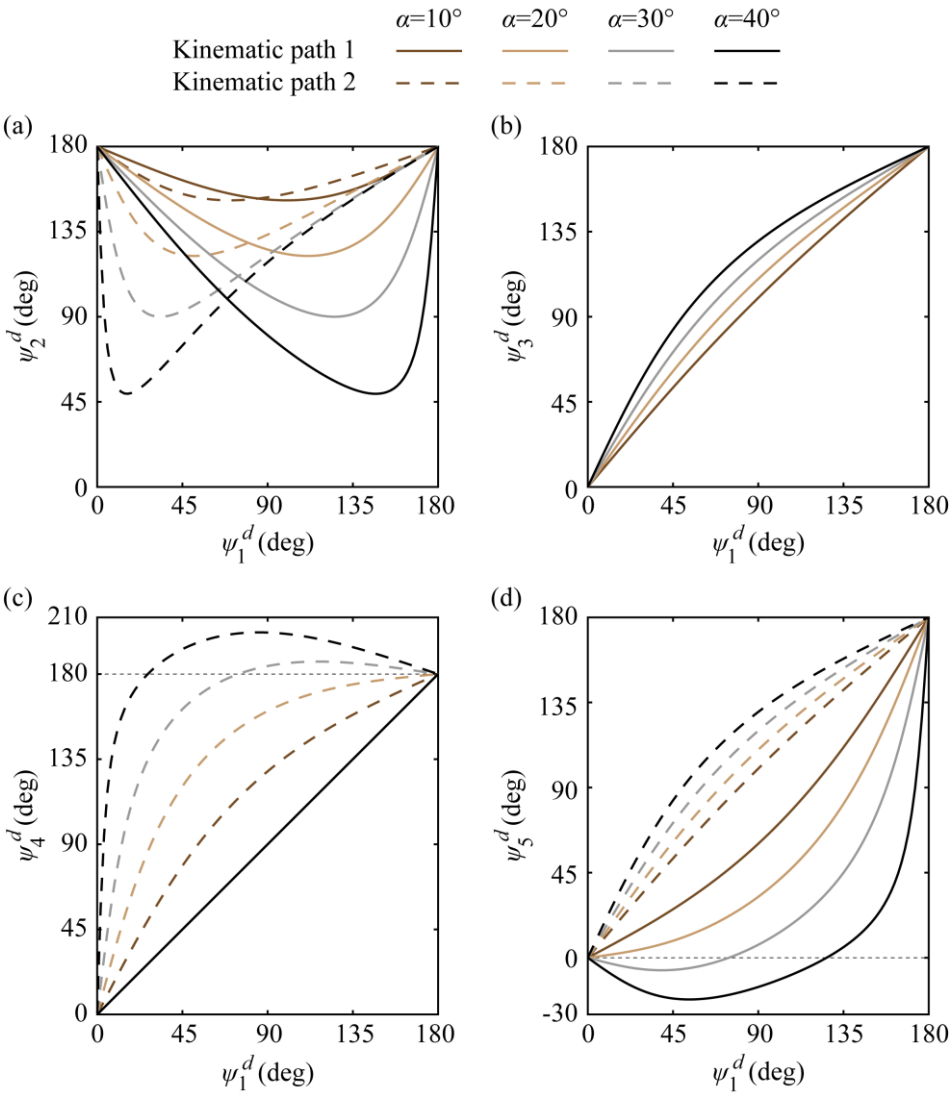

Fig. 3-6 Kinematic curves of the dihedral angles (a) ψ_2^d, (b) ψ_3^d, (c) ψ_4^d, and (d) ψ_5^d vs. ψ_1^d for kinematic paths 1 and 2 of the type 1M unit with varied α.

3.4.1 Finite Element Modeling

In addition to the experiment, a finite element model of type 1 square-twist origami structure using Abaqus/Explicit was also developed, first of all, to obtain detailed deformations of the facet portions that were occluded by other facets during tensioning,

and secondly, to investigate the effects of design parameters on the mechanical properties of the structure. As mentioned in Section 3.2, the non-rigid pattern satisfies the compatibility condition only at the fully folded and fully deployed configurations, where all the facets maintain the original flat shape. Then, for the type 1 specimen with a natural dihedral angle, a major difficulty arises, i.e., how to rationally build its geometry when the planar surface cannot be employed in all of the facets. Here the adopted method was to keep the central square flat and use curved surfaces to replace the rectangular and trapezoid facets. To investigate the influence of curved facets on the mechanical properties of the structure, four different geometric construction schemes were designed, replacing the trapezoidal facets with two planar triangles as shown in Fig. 3-8(a), replacing the rectangular facets with curved surfaces as shown in Fig. 3-8(b), replacing trapezoidal facets with curved surfaces as shown in Fig. 3-8(c), and replacing trapezoidal facets with curved creases and curved surfaces as shown in Fig. 3-8(d).

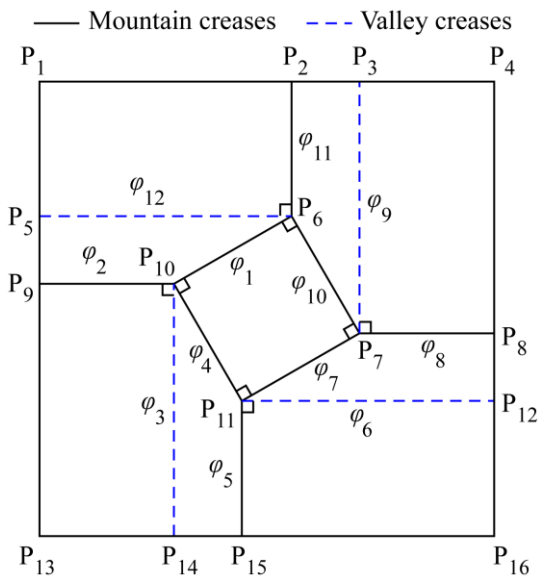

Fig. 3-7 Definition of vertices and creases in type 1 pattern.

All the models have the same diagonal length and height as the physical specimen. The model in Fig. 3-8(b) has curved rectangular facets bounded by four straight sides. The geometric construction starts with the planar square and rectangular facets based on the diagonal length and height. The loading point is also obtained after this. Subsequently, the trapezoidal facet is introduced to connect with the side of the square facet and the long side of the rectangular facet. Afterward, the planar rectangular facet

is removed, and a curved one is defined by the two common sides with the trapezoidal facets and the loading point. Finally, the curved surface of the rectangular facet is generated by the boundary-surface method in Solidworks. For the model in Fig. 3-8(c) which has curved trapezoidal facets bounded by four straight sides, the planar square and rectangular facets are first placed based on the diagonal length and height, which determine the two common sides between the rectangular and trapezoidal facets as well as the one between the square and trapezoidal facets. Then, the fourth side of the trapezoidal facet is a straight line between the two endpoints of the common sides with the rectangular facet. Finally, the curved surface of the trapezoidal facet is again generated by the boundary-surface method. For the model in Fig. 3-8(d), the planar square and rectangular facets are placed in the same manner as the model in Fig. 3-8(c). Then, the long common side of the trapezoidal and rectangular facets is cut by a line parallel to the short common side, generating a new curved common side to replace the original straight one. Subsequently, the fourth side of the trapezoidal facet is obtained by connecting the endpoints of the curved side and the short common side with the rectangular facet. Finally, the curved surface of the trapezoidal facet is created using the boundary-surface method.

The numerical model had an identical natural configuration and facet thickness with the physical specimen. The facets were modeled as thin shells with elastoplastic properties obtained from tension experiments: Young's modulus E=2216.78MPa and yield stress σ_y=24.46MPa. The Poisson's ratio, v, was set to be 0.39[164]. And the density of the material was 1.01g·cm^{-3}. The creases were modeled by revolute connection with tie constraint. The torsional stiffness per unit length of the creases, k_c=0.44N·rad^{-1}, was experimentally determined from a rigid type 3 square-twist structure that had identical geometry and base material with the type 1 specimen. Multiple point constraint (MPC) of a beam type as shown in Fig. 3-9(a) was applied to the four corners of the model to achieve a biaxial loading. Each loading point had only one translational degree of freedom in the x-z plane, i.e., the two points on the diagonal parallel to the x-axis moved along the x-direction and the other two on the diagonal parallel to the z-axis moved along the z-direction. The four-node quadrilateral shell elements with reduced integration, S4R, were used to mesh the model. Self-contact with no friction was established to simulate the contacts among different facets. Mesh convergence in Fig. 3-9(b) was carried out to determine the element size of 1mm. The dynamic explicit

solver was used for its capability of simulating the large deformation of origami structure and complex contact conditions among the facets. An analysis time convergence test was conducted, from which a loading rate of 50mm/s was found to yield a quasi-static deformation process. No mass scaling was used in the simulation.

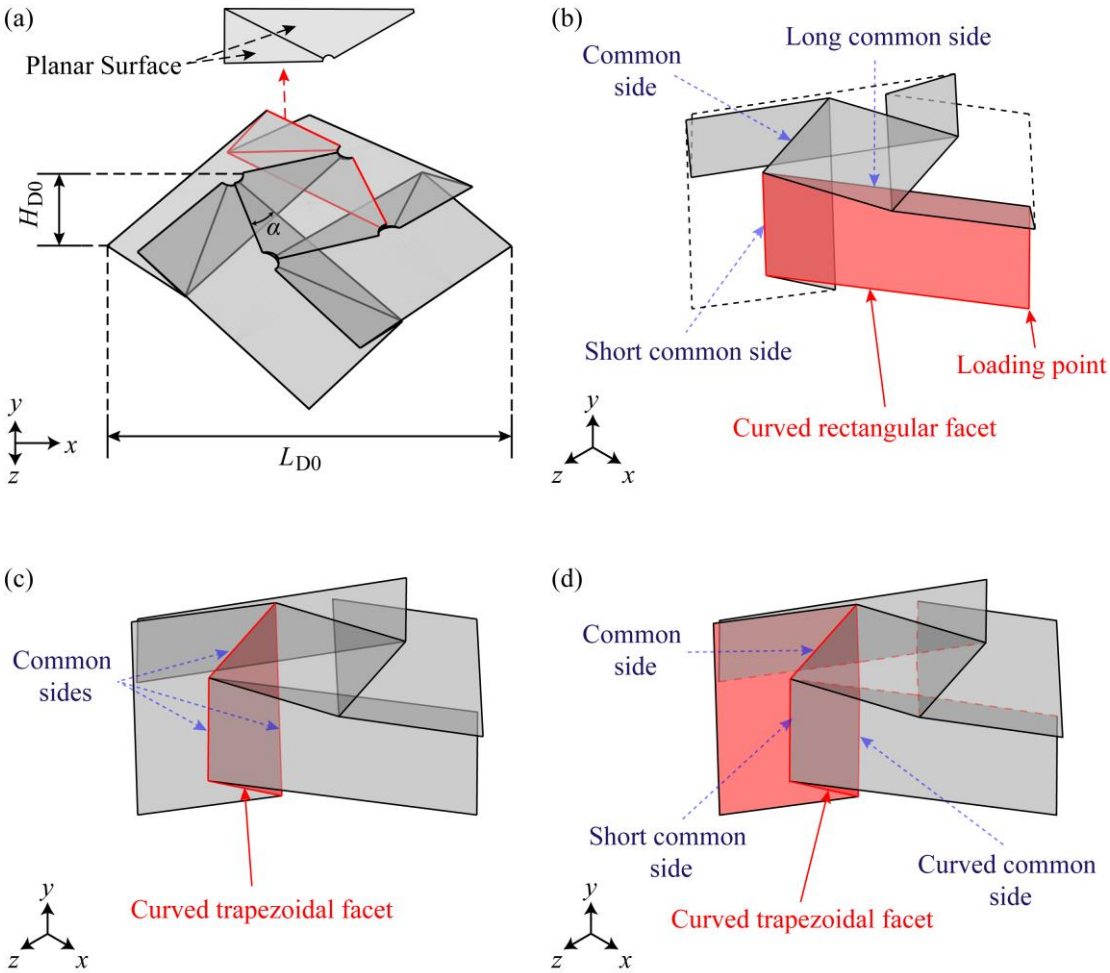

Fig. 3-8 Geometric model of type 1 square-twist structure constructed by (a) replacing the trapezoidal facet with two intersected triangular planar surfaces, (b) replacing the rectangular facets with curved surfaces, (c) replacing trapezoidal facets with curved surfaces, and (d) replacing trapezoidal facets with curved creases and curved surfaces.

The normalized force versus normalized displacement curves of the four models is shown in Fig. 3-10, from which a good agreement is observed. This indicates that the behavior of the structure is not sensitive to the specific type of curved surfaces. The tension simulation results showed that the four models generated nearly identical force

versus displacement curves, implying that the behavior of the structure was not sensitive to the specific type of curved surfaces in the geometric construction. Thus the scheme in Fig. 3-8(a) was adopted in the subsequent simulation.

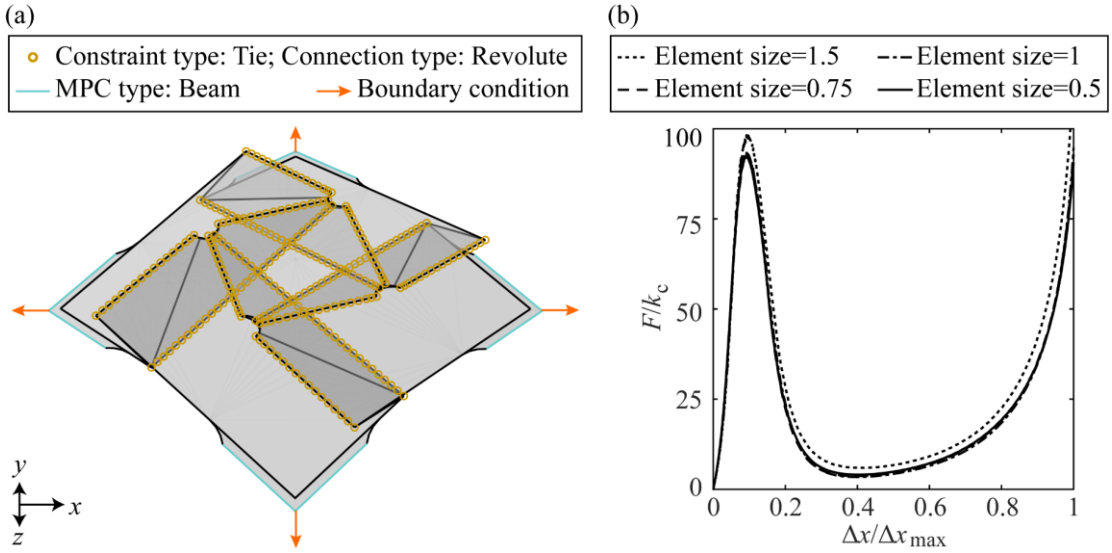

Fig. 3-9 (a) Details of the constraint and boundary condition. (b) The normalized force, F/k_c, against normalized displacement, $\Delta x/\Delta x_{max}$, the convergence analysis results.

3.4.2 Validation of Finite Element Model

The experimentally reconstructed (colored points) and numerically obtained (yellow surfaces) deformed square, rectangular, and trapezoidal facets are compared in Fig. 3-11, Fig. 3-12, and Fig. 3-13 at normalized displacement $\Delta x/\Delta x_{max}$=0.08, 0.2, 0.4, 0.6, and 0.8, respectively. For the reconstructed facets, the DIC test provides the deformed configuration instead of the strain distribution because the large deformation of the origami unit is unfavorable for the strain measurement of the DIC technique. In addition, the missing trapezoid data at $\Delta x/\Delta x_{max}$=0.08 and 0.8 is caused by the overlap and reflection of the specimen. The difference between the experimental and numerical surfaces is measured by the fitting error, which is defined as the closest line distance between the experimental points and the numerical surfaces and calculated as a minimized overall surface error through optimizing the 6-DoF rigid body displacement of the experimental results with respect to the numerical ones[142]. The magnitude of the fitting error is represented by the color of the experimentally reconstructed points, which ranges from -2t to 2t as shown in the color legend. Note t=0.4mm is the material

thickness. Moreover, the pie graphs below the configurations show the fitting error compared with half of the material thickness. The green and yellow areas indicate the error is within 0.5t whereas the red and blue areas mean the error is beyond 0.5t. The diagrams indicate that the fitting error is within half of the material thickness in over 80% of the measured area, suggesting a good match between the experimental and numerical results in the entire unfolding process. Therefore, the numerical model is capable of capturing the main deformation feature of the structure.

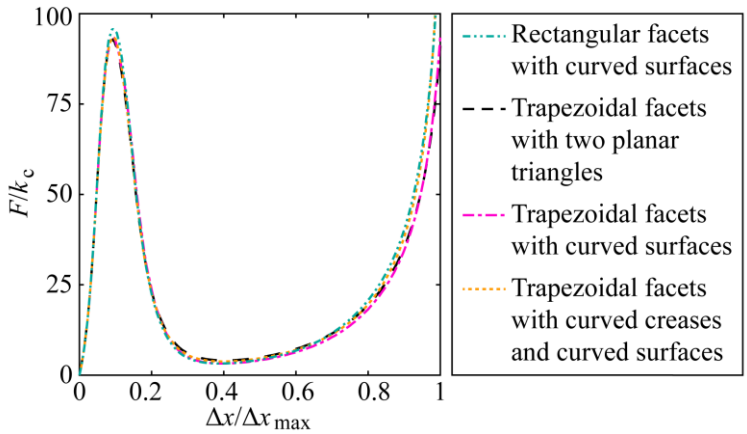

Fig. 3-10 The normalized force, F/k_c, against normalized displacement, $\Delta x/\Delta x_{max}$, of the four models constructed by different methods.

Moreover, the numerical normalized energy, $U/(k_c l)$, normalized force, F/k_c, and normalized stiffness, Kl/k_c, are drawn against normalized displacement, $\Delta x/\Delta x_{max}$, of type 1 square-twist structure together with the experimental ones as shown in Fig. 3-14. The force is directly measured from experiments or exported from the numerical model. Then, it is integrated and differentiated with respect to tension displacement to gain energy and stiffness, respectively. The red shade for the experimental curves represents the repeatability of three specimens. Again a reasonable agreement between numerical and experimental curves is obtained. The small gap between the numerical and experimental forces around configuration V was mainly caused by that the displacement control setup in the experiments could not fully capture the sharply changed force when the specimen quickly snapped open after passing the initial peak force. Thus, it can be concluded that the numerical model can accurately capture the mechanical behaviors of type 1 square-twist structure, which will later be used to unveil the detailed deformation process in the subsequent section.

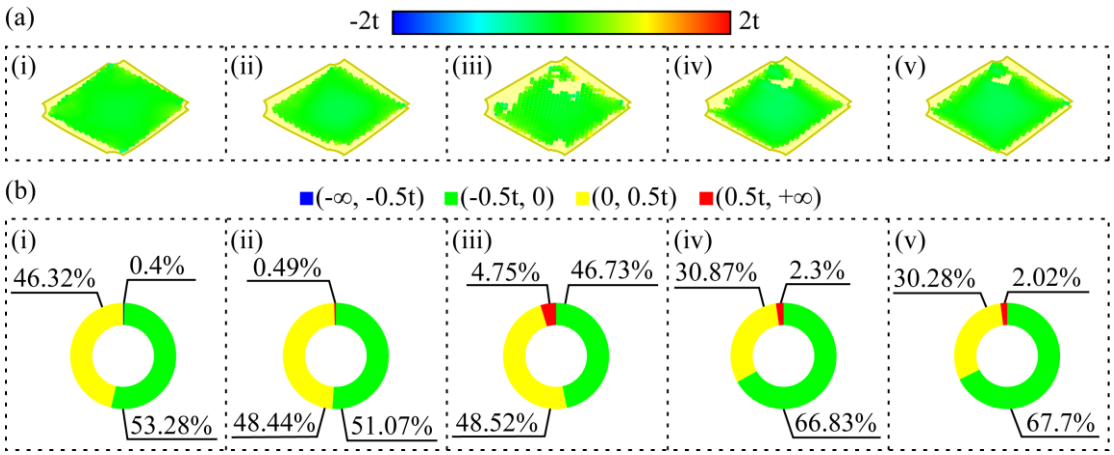

Fig. 3-11 (a) Comparison between experimentally reconstructed and numerically obtained deformed shapes and (b) errors (pie graphs) of the square facet. The normalized displacements of the five representatives, $\Delta x/\Delta x_{max}$, are: (i) 0.08 (initial peak force), (ii) 0.2, (iii) 0.4, (iv) 0.6, and (v) 0.8.

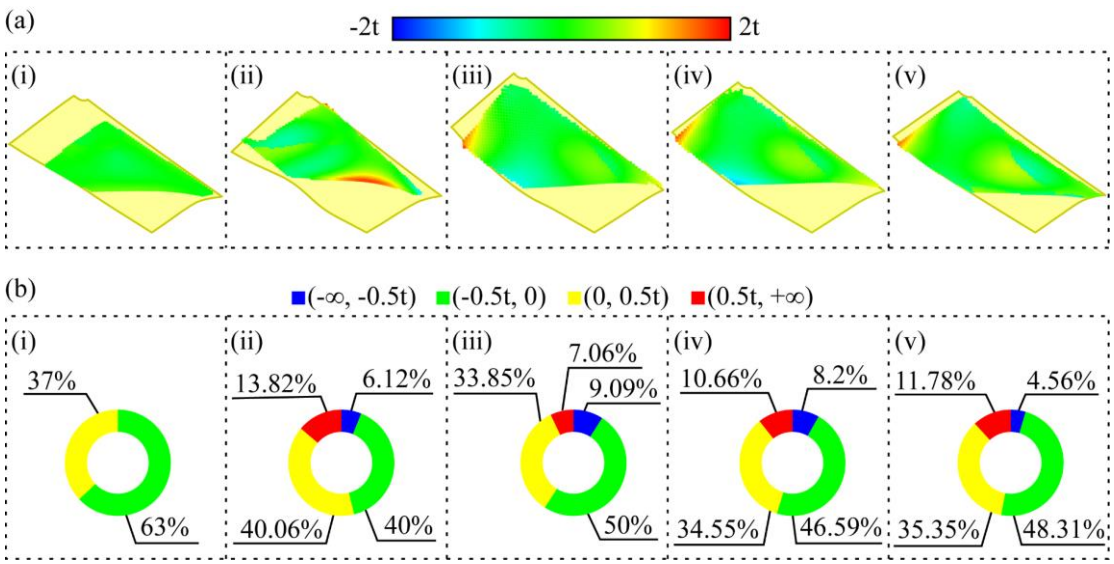

Fig. 3-12 (a) Comparison between experimentally reconstructed and numerically obtained deformed shapes and (b) errors (pie graphs) of the rectangular facet. The normalized displacements of the five representatives, $\Delta x/\Delta x_{max}$, are: (i) 0.08 (initial peak force), (ii) 0.2, (iii) 0.4, (iv) 0.6, and (v) 0.8.

3.5 Deformation Process of Type 1 unit

To demonstrate the deformation process of the origami structure, six key points are selected and marked with I to VI based on the numerical energy, force, and stiffness

curves in Fig. 3-14, where I and VI represent the initial and final configurations, II is the maximum stiffness, III and V are the initial peak and valley forces, and IV describes a transition point in the energy curve. The configurations of the structure corresponding to the six points are presented in front and side views in Fig. 3-15. Moreover, the normalized height, H_D/H_{D0}, and the dihedral angles, φ_i (i=1, 2, 3, …, 12), of the structure, are respectively shown in Fig. 3-16(a) and (b). And the total energy of the facets and that of the creases are drawn in Fig. 3-16(c). In the calculation of crease energy, a narrow strip of 0.6mm on each side of the crease is included so that the width is 1.2mm which is equal to that of the physical specimen. Apart from the global behavior of the structure, the diagonal lengths, energies, as well as the von Mises stress and equivalent plastic strain (PEEQ) contours of the local square, rectangular, and trapezoidal facets are presented in Fig. 3-17 and Fig. 3-18 to depict their deformation evolution in detail.

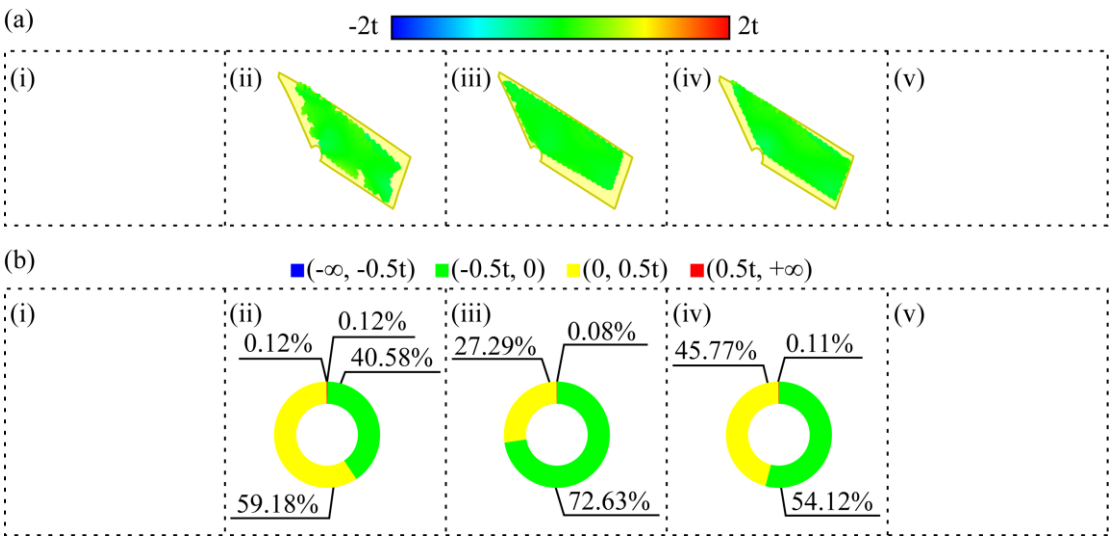

Fig. 3-13 (a) Comparison between experimentally reconstructed and numerically obtained deformed shapes and (b) errors (pie graphs) of trapezoidal facet. The normalized displacements of the five representatives, $\Delta x/\Delta x_{max}$, are: (i) 0.08 (initial peak force), (ii) 0.2, (iii) 0.4, (iv) 0.6, and (v) 0.8.

It can be seen from Fig. 3-16(a) that during the unfolding process, while the diagonal length monotonically increases, the structure height first slightly drops, and then rises quickly followed by another slow drop. Consequently, the deformation process of the structure can be divided into three stages: a tightening stage (configurations I-II), an unlocking stage (configurations II-V), and a flattening stage

(configurations V-VI). First, consider the tightening stage. During this stage, the initially tilted rectangular facets tend to be horizontal, leading to a more compact structure with a slightly reduced height. Theoretically, the fully folded configuration of the structure should have a zero height and a diagonal length of 54.37mm. Due to the natural dihedral angle, nevertheless, the numerical model has a larger height of 7.80mm combined with a smaller diagonal length of 53.30mm. As a result, when stretched, the structure tends to approach its fully folded configuration, although is not able to completely reach that. At configuration II, the structure reaches its smallest height, or the most locked form that can be achieved for the selected material and loading condition. This explains why the maximum stiffness appears here. Both facet distortions and crease rotations are small at this stage.

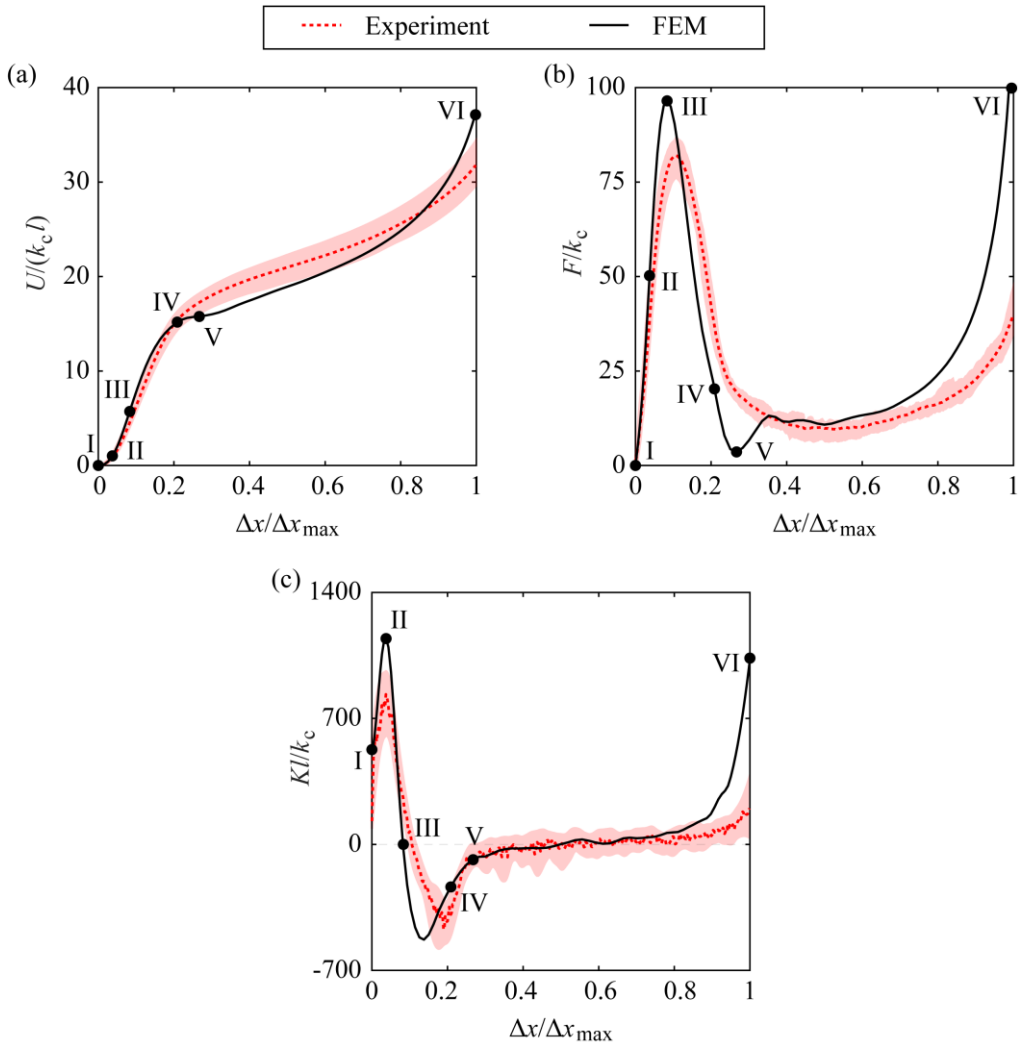

Fig. 3-14 Experimental and numerical normalized (a) energy, $U/(k_c l)$, (b) force, F/k_c, and (c) stiffness, Kl/k_c, of the type 1 structure against normalized displacement, $\Delta x/\Delta x_{max}$.

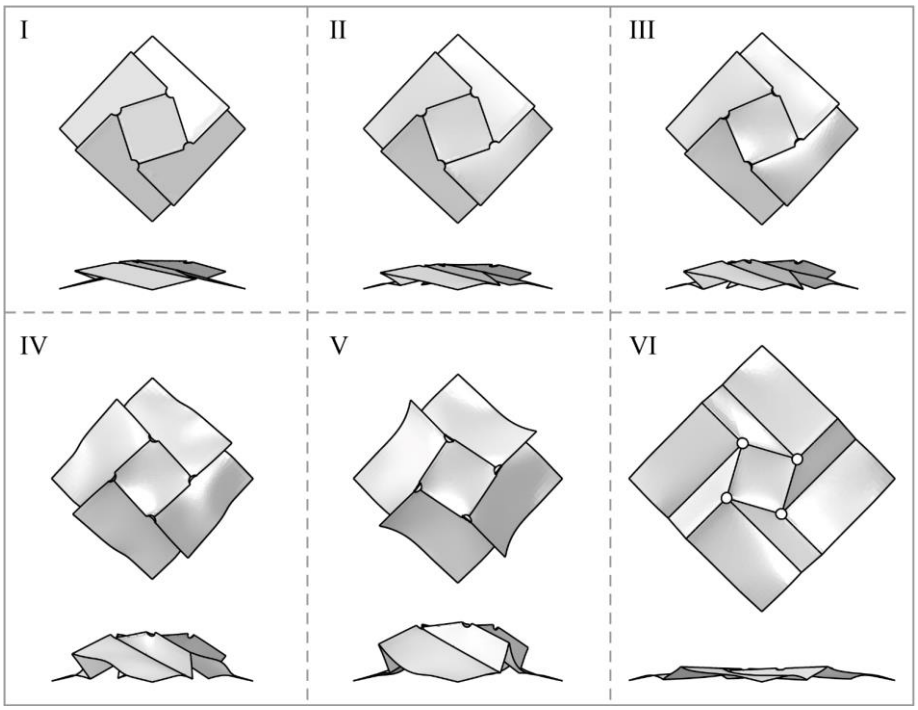

Fig. 3-15 Six typical configurations of the structure in the front and side views.

Upon further tension, the structure starts to open up, entering the unlocking stage between configurations II and V. As can be seen in Fig. 3-15, the rectangular and trapezoidal facets gradually tilt at this stage, thereby raising the central square and the height of the structure. From configuration II to III, the crease rotations are found to be non-synchronized, i.e., the dihedral angles formed along the long sides of the rectangular facets, φ_i (i=3, 6, 9, 12), are almost unchanged whereas all the others increase monotonically, see Fig. 3-16(b). To accommodate this non-synchronization, the facets are further distorted to maintain the internal connectivity of the structure. Specifically, the square facet is squeezed by the neighboring facets and bulges out-of-plane to form a dome-like shape, which is manifested by the shrinkage in diagonal length in Fig. 3-17(a). The corner areas undergo the largest deformation and develop plasticity shown in the PEEQ contour Fig. 3-18(a). Meanwhile, the rectangular and trapezoidal facets are also minorly compressed along the diagonal lengths as shown in Fig. 3-17(c) and (e), but remain elastic in most of the area. The large facet distortions lead to a sharp rise in the reaction force, which reaches its initial peak force at configuration III. From configuration III to IV, creases 3, 6, 9, 12 start to open up along with the others, which in turn mitigate the required facet distortions. As a result, the deformation of the facets continues to develop, but at a gradually reduced rate, which

can be concluded by comparing the energy curves of the three facets between II-III and III-IV in Fig. 3-17(b), (d) and (f). This leads to a reduced reaction force and consequently a negative stiffness. When the unit passes configuration III, large plastic regions start to appear in the three types of facets, especially the rectangular one, see the PEEQ contours in Fig. 3-18. This is echoed in the plastic energy of the facets in Fig. 3-17(b), (d), and (f). The development of plasticity slowers the energy development of the structure, leading to the transition point IV on the energy curve in Fig. 3-14(a). Further stretching the structure to configuration V, the diagonal length of the rectangular facet reaches its minimum, indicating that it reaches its most distorted, also most tilted shape. This marks the closure of the unlocking stage, characterized by the largest structure height.

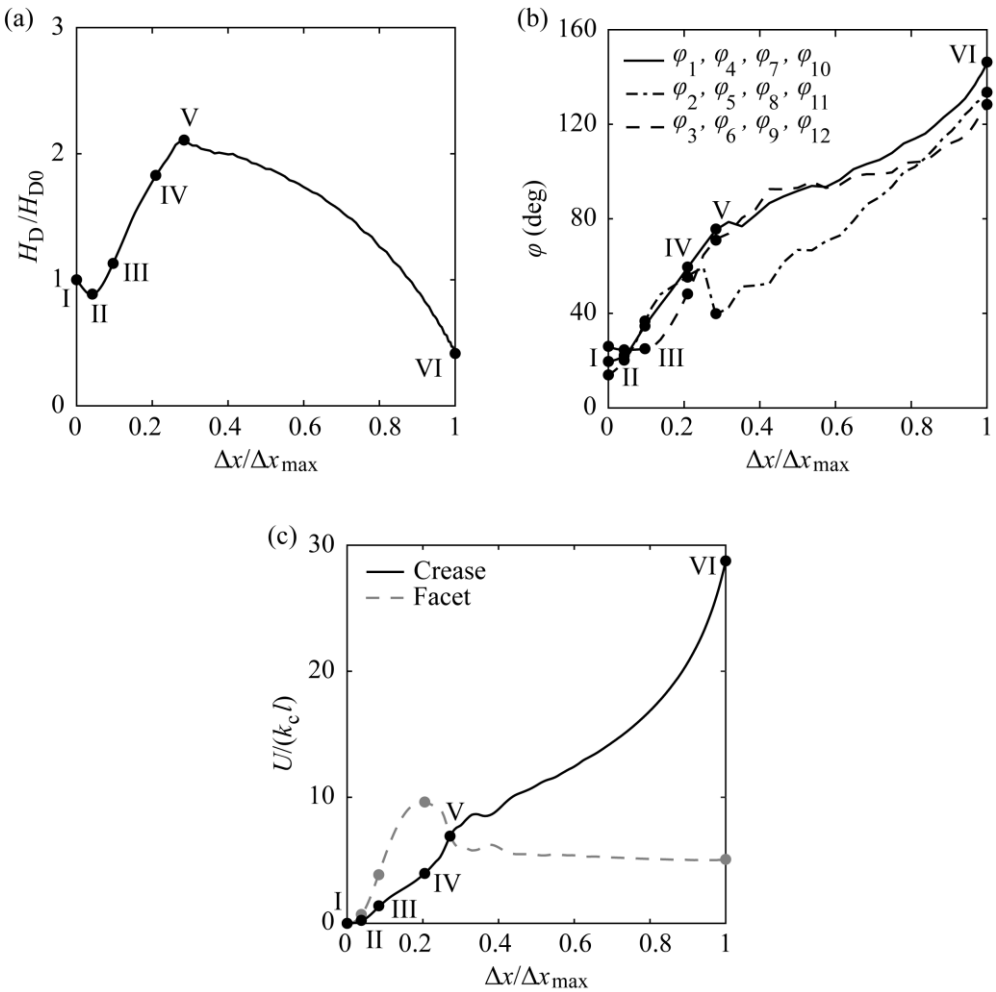

Fig. 3-16 (a) Numerical normalized height, H_D/H_{D0}, (b) dihedral angles, φ_i (i=1, 2, …, 12), and (c) facet and crease energies of the structure versus normalized displacement, $\Delta x/\Delta x_{max}$.

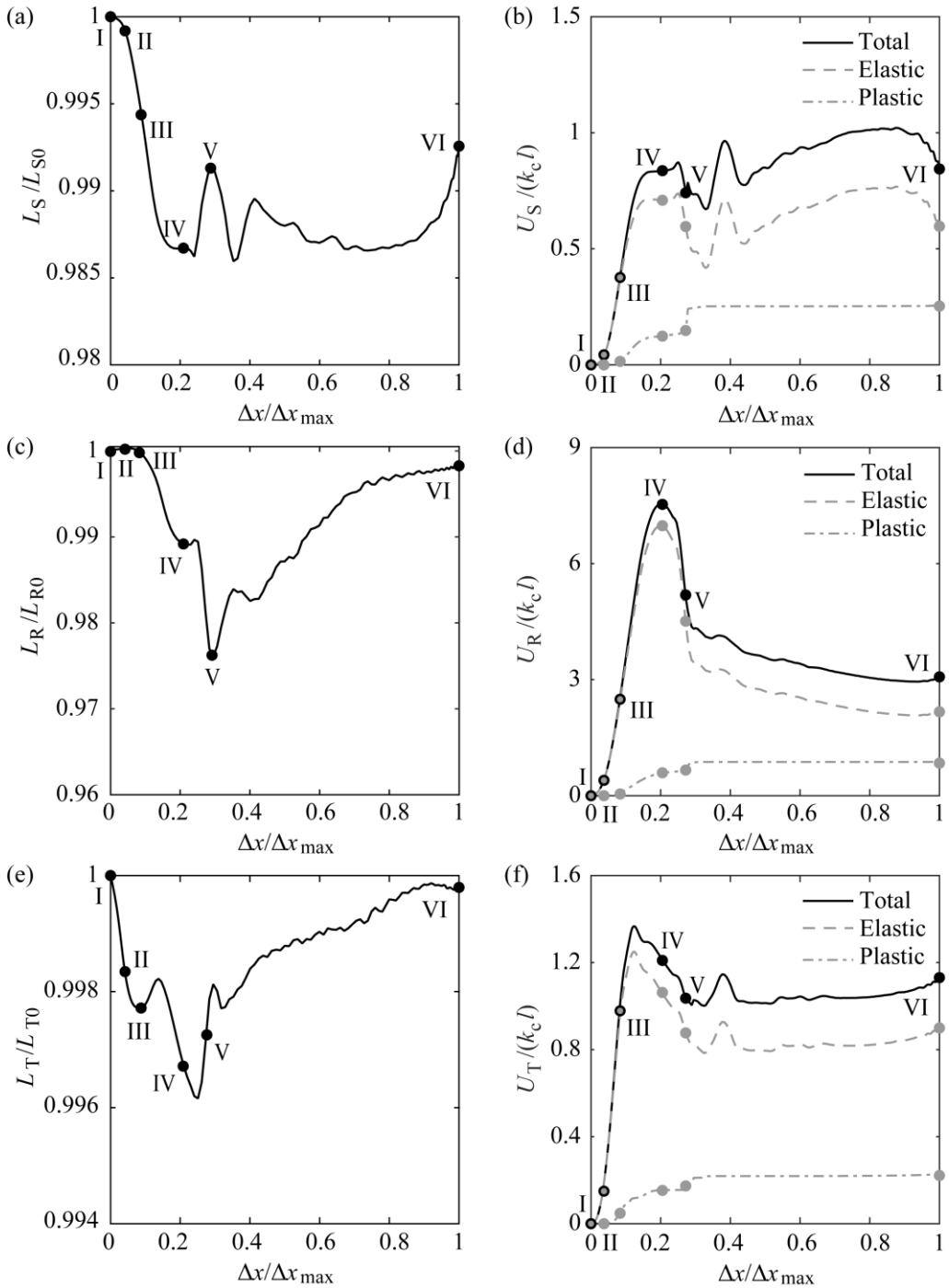

Fig. 3-17 Illustration of the deformed square, rectangular, and trapezoidal facets. (a and b) Normalized diagonal length and energy of the square facet, L_S/L_{S0} and $U_S/(k_c l)$, (c and d) that of the rectangular facet, L_R/L_{R0} and $U_R/(k_c l)$, and (e and f) that of the trapezoidal facet, L_T/L_{T0} and $U_T/(k_c l)$ versus normalized displacement, $\Delta x/\Delta x_{max}$.

After configuration V, the structure enters the final flattening stage. At this stage, the tilted rectangular and trapezoidal facets rotate along the crease to level again, which

causes a further unfolding of the structure accompanied by a reduction in height. The energy curves in Fig. 3-18 indicate that all the facets tend to recover by partially releasing their elastic energy. The rectangular facet which is mostly deformed releases more than half of its elastic energy, whereas its plastic energy keeps steady. All the creases, on the other hand, continuously open up till the end as shown in Fig. 3-16(b), resulting in a roughly linearly increasing crease energy curve in Fig. 3-16(c). Since the reaction force is mainly used to overcome the stiffness of the creases, a relatively low force in comparison with the previous two stages is generated until when the structure is nearly flat at the end.

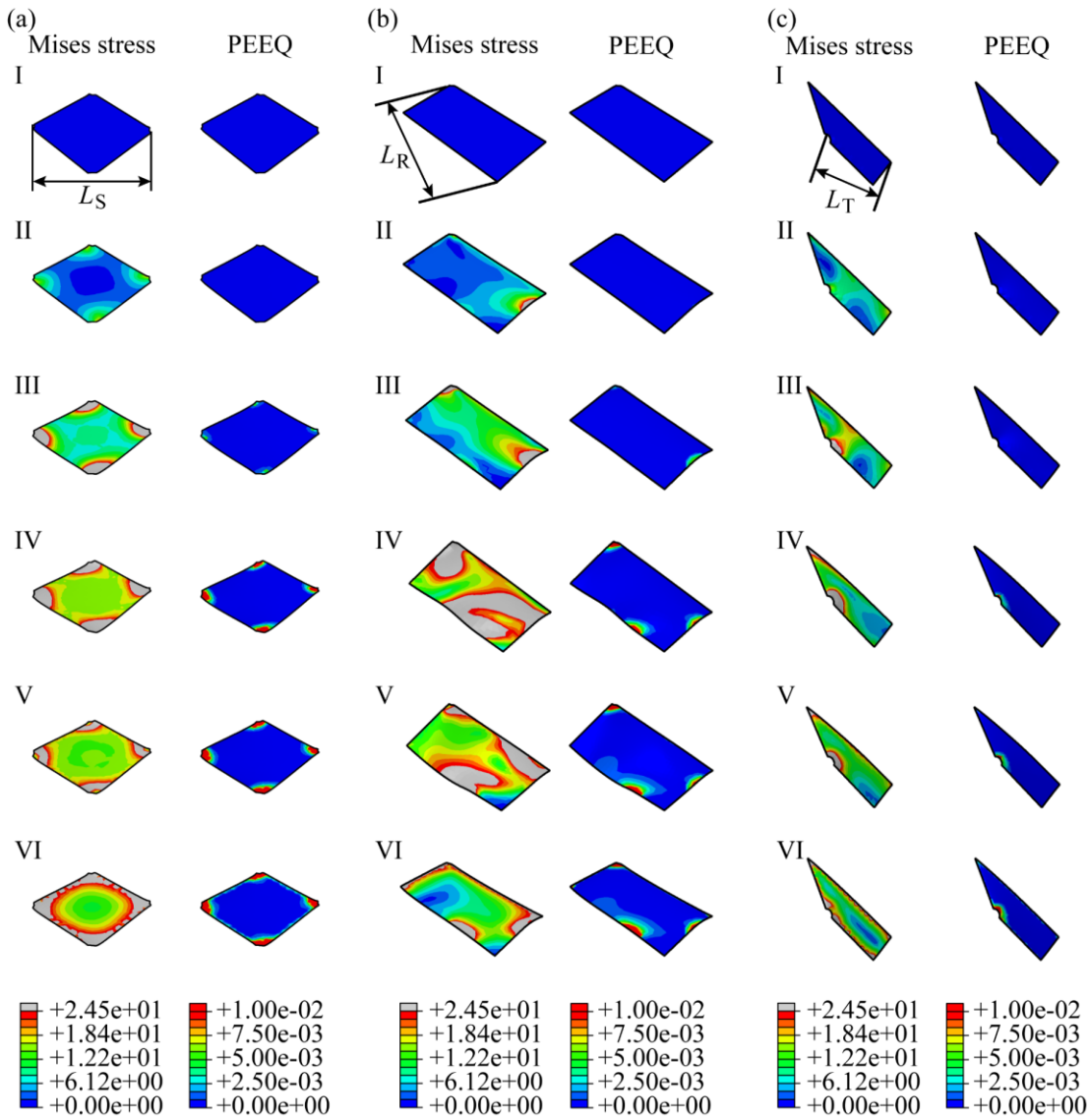

Fig. 3-18 The Mises stress and PEEQ contours of the (a) square, (b) rectangular, and (c) trapezoidal facets.

Overall, the total crease energy in Fig. 3-16(c) tends to increase approximately during tension, whereas the total facet energy shows a local peak associated with the unlocking process. Moreover, the crease energy is much larger than the facet energy in the end. This result indicates that facet deformation is mainly responsible for the high initial peak, while crease rotation is still the main source of structure energy absorption.

3.6 Empirical Model of Type 1 unit

From the viewpoint of programmability, it is crucial to develop a mathematical model to predict the mechanical properties of type 1 square-twist structure. However, it has been shown in Section 3.5 that very complicated deformation modes are generated on the facets of the structure during the unfolding process. As a result, it is difficult to build an elegant theoretical model for the structure by previous methods such as adding virtual creases to create an equivalent rigid structure. Instead, an empirical model is developed based on the numerical results to provide a practical prediction approach. Here, three key mechanical properties are focused on, i.e. the energy at the end of deformation corresponding to configuration VI, initial peak force corresponding to configuration III, and maximum stiffness corresponding to configuration II in Fig. 3-14.

I start by analyzing the energy of the structure which is the summation of the total crease energy and the total facet energy. The energy of a crease is dependent on its length, torsional stiffness per unit length, as well as the amount of rotation. As a result, the total crease energy is assumed to be in the form of

$$U_{\mathrm{c}} = \sum_{i=1}^{12} u_{\mathrm{c}i} \cdot k_{\mathrm{c}i} \cdot L_{\mathrm{c}i} \cdot f_{\mathrm{c}i}(\varphi) \tag{3-13}$$

where u_{ci}, k_{ci}, L_{ci}, and $f_{ci}(\varphi)$ are respectively a constant energy coefficient, torsional stiffness per unit length, crease length, and rotation function with a variable φ. The crease deformed behavior of the type 1 unit is the same as that of the type 2 unit, which implies the relationship between the moment and rotation angle is described by a nonlinear elastic model with two stages. Thus, when the crease deformation is within the first-stage nonlinear elastic response, the rotation function is expressed as $f_{ci}(\varphi) \propto (\varphi - \varphi_0)^2$. And the second-stage nonlinear deformation causes the expression to be revised as $f_{ci}(\varphi) \propto \Delta\varphi_y{}^2 + \Delta\varphi_y \cdot (\varphi_i - \varphi_{i,0} - \Delta\varphi_y)$, where $\Delta\varphi_y$ is the angle at the end of the first stage of the nonlinear relationship. Since the type 1 square twist structure has a four-fold rotational symmetry and all the creases have identical stiffness, all the

12 creases fall into three groups with length l represented by φ_i (i=1, 4, 7, 10), a represented by φ_i (i=2, 5, 8, 11), and $l\cdot\cos\alpha+a$ represented by φ_i (i=3, 6, 9, 12). Thus Eq. (3-13) can be rewritten as

$$U_{\mathrm{c}} = 4k_{\mathrm{c}}\left[u_{\mathrm{c1}}\cdot l\cdot f_{\mathrm{c1}}(\varphi)+u_{\mathrm{c2}}\cdot a\cdot f_{\mathrm{c2}}(\varphi)+u_{\mathrm{c3}}\cdot(l\cdot\cos\alpha+a)\cdot f_{\mathrm{c3}}(\varphi)\right] \tag{3-14}$$

Notice that there are three deformation functions in the equation because the three groups of creases do not open up at the same rate, which can be seen in Fig. 3-16(b).

Similar to Eq. (3-13), the energy of facet deformation can be given by

$$U_{\mathrm{f}} = u_{\mathrm{f}}\cdot k_{\mathrm{f}}\cdot L_{\mathrm{f}}\cdot f_{\mathrm{f}}(\varphi) \tag{3-15}$$

where u_{f} and k_{f} are the energy coefficients and bending stiffness of facet, while L_{f} and $f_{\mathrm{f}}(\varphi)$ are the length and function of facet deformation. The parameter L_{f} relies on the deformed area of the facet, S_{f}, which can be expressed as $L_{\mathrm{f}} \propto S_{\mathrm{f}}/l$. Thus, Eq. (3-15) can be rewritten as

$$U_{\mathrm{f}} = u_{\mathrm{f}}\cdot k_{\mathrm{f}}\cdot\frac{S_{\mathrm{f}}}{l}\cdot f_{\mathrm{f}}(\varphi) = u_{\mathrm{f}}\cdot k_{\mathrm{f}}\cdot\frac{1}{l}\cdot S_{\mathrm{f}}\cdot f_{\mathrm{f}}(\varphi) \tag{3-16}$$

It has been shown from the numerical simulation that both elastic and plastic regions could develop in the facets during loading. The plastic regions exist because the large deformation of the structure leads to the material of the facet reaching the yield point. Therefore, the deformed area of facet, S_{f}, consists of the plastic region, S_{p}, and the elastic one, S_{e}. The plastic regions of the square, rectangular, and trapezoidal facets, which depend on the geometric and material parameters, are first assumed as follows

$$S_{\text{S-p}} = \gamma_{\mathrm{S1}}\cdot l^2\cdot\tan\alpha+\gamma_{\mathrm{S2}}\cdot a^2+\gamma_{\mathrm{S3}}\cdot l^2\cdot\frac{k_{\mathrm{c}}}{k_{\mathrm{f}}} \tag{3-17}$$

$$S_{\text{R-p}} = \gamma_{\mathrm{R1}}\cdot l^2\cdot\tan\alpha+\gamma_{\mathrm{R2}}\cdot a^2+\gamma_{\mathrm{R3}}\cdot l^2\cdot\frac{k_{\mathrm{c}}}{k_{\mathrm{f}}} \tag{3-18}$$

$$S_{\text{T-p}} = \gamma_{\mathrm{T1}}\cdot l^2\cdot\tan\alpha+\gamma_{\mathrm{T2}}\cdot a^2+\gamma_{\mathrm{T3}}\cdot l^2\cdot\frac{k_{\mathrm{c}}}{k_{\mathrm{f}}} \tag{3-19}$$

in which γ_{i1}, γ_{i2}, γ_{i3} (i=S, R, T) are constant coefficients. Then the elastic regions of the three types of facets are

$$S_{\text{S-e}} = l^2-\gamma_{\mathrm{S1}}\cdot l^2\cdot\tan\alpha-\gamma_{\mathrm{S2}}\cdot a^2-\gamma_{\mathrm{S3}}\cdot l^2\cdot\frac{k_{\mathrm{c}}}{k_{\mathrm{f}}} \tag{3-20}$$

$$S_{\text{R-e}} = a\cdot(l\cdot\cos\alpha+a)-\gamma_{\mathrm{R1}}\cdot l^2\cdot\tan\alpha-\gamma_{\mathrm{R2}}\cdot a^2-\gamma_{\mathrm{R3}}\cdot l^2\cdot\frac{k_{\mathrm{c}}}{k_{\mathrm{f}}} \tag{3-21}$$

$$S_{\text{T-e}} = l\cdot\sin\alpha\cdot(l\cdot\cos\alpha+2a)-\gamma_{\mathrm{T1}}\cdot l^2\cdot\tan\alpha-\gamma_{\mathrm{T2}}\cdot a^2-\gamma_{\mathrm{T3}}\cdot l^2\cdot\frac{k_{\mathrm{c}}}{k_{\mathrm{f}}} \tag{3-22}$$

With the plastic and elastic regions, the total facet energy is assumed to be calculated by the following equation

$$\begin{aligned}
U_{\mathrm{f}} = {} & u_{\text{S-e}} \cdot k_{\mathrm{f}} \cdot \frac{1}{l} \cdot \left(l^2 - \gamma_{\mathrm{S1}} \cdot l^2 \cdot \tan\alpha - \gamma_{\mathrm{S2}} \cdot a^2 - \gamma_{\mathrm{S3}} \cdot l^2 \cdot \frac{k_{\mathrm{c}}}{k_{\mathrm{f}}} \right) \cdot f_{\text{S-e}}(\varphi) \\
& + u_{\text{S-p}} \cdot k_{\mathrm{f}} \cdot \frac{1}{l} \cdot \left(\gamma_{\mathrm{S1}} \cdot l^2 \cdot \tan\alpha + \gamma_{\mathrm{S2}} \cdot a^2 + \gamma_{\mathrm{S3}} \cdot l^2 \cdot \frac{k_{\mathrm{c}}}{k_{\mathrm{f}}} \right) \cdot f_{\text{S-p}}(\varphi) \\
& + 4u_{\text{R-e}} \cdot k_{\mathrm{f}} \cdot \frac{1}{l} \cdot \left[a \cdot (l \cdot \cos\alpha + a) - \gamma_{\mathrm{R1}} \cdot l^2 \cdot \tan\alpha - \gamma_{\mathrm{R2}} \cdot a^2 - \gamma_{\mathrm{R3}} \cdot l^2 \cdot \frac{k_{\mathrm{c}}}{k_{\mathrm{f}}} \right] \cdot f_{\text{R-e}}(\varphi) \\
& + 4u_{\text{R-p}} \cdot k_{\mathrm{f}} \cdot \frac{1}{l} \cdot \left(\gamma_{\mathrm{R1}} \cdot l^2 \cdot \tan\alpha + \gamma_{\mathrm{R2}} \cdot a^2 + \gamma_{\mathrm{R3}} \cdot l^2 \cdot \frac{k_{\mathrm{c}}}{k_{\mathrm{f}}} \right) \cdot f_{\text{R-p}}(\varphi) \\
& + 4u_{\text{T-e}} \cdot k_{\mathrm{f}} \cdot \frac{1}{l} \cdot \left[\begin{array}{l} l \cdot \sin\alpha \cdot (l \cdot \cos\alpha + 2a) - \gamma_{\mathrm{T1}} \cdot l^2 \cdot \tan\alpha - \gamma_{\mathrm{T2}} \cdot a^2 \\ - \gamma_{\mathrm{T3}} \cdot l^2 \cdot \dfrac{k_{\mathrm{c}}}{k_{\mathrm{f}}} \end{array} \right] \cdot f_{\text{T-e}}(\varphi) \\
& + 4u_{\text{T-p}} \cdot k_{\mathrm{f}} \cdot \frac{1}{l} \cdot \left(\gamma_{\mathrm{T1}} \cdot l^2 \cdot \tan\alpha + \gamma_{\mathrm{T2}} \cdot a^2 + \gamma_{\mathrm{T3}} \cdot l^2 \cdot \frac{k_{\mathrm{c}}}{k_{\mathrm{f}}} \right) \cdot f_{\text{T-p}}(\varphi)
\end{aligned} \tag{3-23}$$

where $u_{\text{S-}j}$, $u_{\text{R-}j}$, $u_{\text{T-}j}$ (j=e, p) are the elastic and plastic energy coefficients of the square, rectangular, and trapezoidal facets, respectively. And $f_{\text{S-}j}(\varphi)$, $f_{\text{R-}j}(\varphi)$, $f_{\text{T-}j}(\varphi)$ (j=e, p) are the deformation functions of elastic and plastic energy, respectively. Here, $f_{i\text{-e}}(\varphi)$ (i=S, R, T) is related to dihedral angle, φ, and natural dihedral angle, φ_0, while the $f_{i\text{-p}}(\varphi)$ (i=S, R, T) is affected by yield angle, $\Delta\varphi$, besides parameters φ and φ_0.

Then, since the force and stiffness equations rely on the displacement parameter, a calculation is established to describe the diagonal length of the structure in the loading direction. The length is assumed to be related to the side lengths and crease rotations through the following equation.

$$D_{\mathrm{D}} = \sqrt{2}\left[d_1 \cdot l \cdot \sin\alpha \cdot f_{\mathrm{d1}}(\varphi) + d_2 \cdot a \cdot f_{\mathrm{d2}}(\varphi) + d_3 \cdot (l \cdot \cos\alpha + a) \cdot f_{\mathrm{d3}}(\varphi) \right]. \tag{3-24}$$

where d_1, d_2, and d_3 are length coefficients, $f_{\mathrm{d1}}(\varphi)$, $f_{\mathrm{d2}}(\varphi)$, and $f_{\mathrm{d3}}(\varphi)$ are deformation functions of creases 1, 2, and 3, respectively. Notice that the rotation of crease 2 does not affect the diagonal length, and therefore $f_{\mathrm{d2}}(\varphi)$=1, and then Eq. (3-24) can be simplified to

$$D_{\mathrm{D}} = \sqrt{2}\left[d_1 \cdot l \cdot \sin\alpha \cdot f_{\mathrm{d1}}(\varphi) + d_2 \cdot a + d_3 \cdot (l \cdot \cos\alpha + a) \cdot f_{\mathrm{d3}}(\varphi) \right]. \tag{3-25}$$

Here, the function, $f_{\mathrm{d}i}(\varphi)$ (i=1, 2, 3), is expressed as $f_{\mathrm{d}i}(\varphi) \propto \cos\varphi$.

With all the above equations, the energy, force, and stiffness of the structure can be obtained as

$$
\begin{aligned}
U &= U_{\mathrm{f-S}} + U_{\mathrm{f-R}} + U_{\mathrm{f-T}} + U_{\mathrm{c}} \\
&= u_{\text{S-e}} \cdot k_{\mathrm{f}} \cdot \frac{1}{l} \cdot \left(l^2 - \gamma_{\mathrm{S1}} \cdot l^2 \cdot \tan\alpha - \gamma_{\mathrm{S2}} \cdot a^2 - \gamma_{\mathrm{S3}} \cdot l^2 \cdot \frac{k_{\mathrm{c}}}{k_{\mathrm{f}}} \right) \cdot f_{\text{S-e}}(\varphi) \\
&\quad + u_{\text{S-p}} \cdot k_{\mathrm{f}} \cdot \frac{1}{l} \cdot \left(\gamma_{\mathrm{S1}} \cdot l^2 \cdot \tan\alpha + \gamma_{\mathrm{S2}} \cdot a^2 + \gamma_{\mathrm{S3}} \cdot l^2 \cdot \frac{k_{\mathrm{c}}}{k_{\mathrm{f}}} \right) \cdot f_{\text{S-p}}(\varphi) \\
&\quad + 4u_{\text{R-e}} \cdot k_{\mathrm{f}} \cdot \frac{1}{l} \cdot \left[a \cdot (l \cdot \cos\alpha + a) - \gamma_{\mathrm{R1}} \cdot l^2 \cdot \tan\alpha - \gamma_{\mathrm{R2}} \cdot a^2 - \gamma_{\mathrm{R3}} \cdot l^2 \cdot \frac{k_{\mathrm{c}}}{k_{\mathrm{f}}} \right] \cdot f_{\text{R-e}}(\varphi) \\
&\quad + 4u_{\text{R-p}} \cdot k_{\mathrm{f}} \cdot \frac{1}{l} \cdot \left(\gamma_{\mathrm{R1}} \cdot l^2 \cdot \tan\alpha + \gamma_{\mathrm{R2}} \cdot a^2 + \gamma_{\mathrm{R3}} \cdot l^2 \cdot \frac{k_{\mathrm{c}}}{k_{\mathrm{f}}} \right) \cdot f_{\text{R-p}}(\varphi) \\
&\quad + 4u_{\text{T-e}} \cdot k_{\mathrm{f}} \cdot \frac{1}{l} \cdot \begin{bmatrix} l \cdot \sin\alpha \cdot (l \cdot \cos\alpha + 2a) - \gamma_{\mathrm{T1}} \cdot l^2 \cdot \tan\alpha \\ - \gamma_{\mathrm{T2}} \cdot a^2 - \gamma_{\mathrm{T3}} \cdot l^2 \cdot \dfrac{k_{\mathrm{c}}}{k_{\mathrm{f}}} \end{bmatrix} \cdot f_{\text{T-e}}(\varphi) \\
&\quad + 4u_{\text{T-p}} \cdot k_{\mathrm{f}} \cdot \frac{1}{l} \cdot \left(\gamma_{\mathrm{T1}} \cdot l^2 \cdot \tan\alpha + \gamma_{\mathrm{T2}} \cdot a^2 + \gamma_{\mathrm{T3}} \cdot l^2 \cdot \frac{k_{\mathrm{c}}}{k_{\mathrm{f}}} \right) \cdot f_{\text{T-p}}(\varphi) \\
&\quad + 4u_{\mathrm{c1}} \cdot k_{\mathrm{c}} \cdot a \cdot f_{\mathrm{c1}}(\varphi) + 4u_{\mathrm{c2}} \cdot k_{\mathrm{c}} \cdot l \cdot f_{\mathrm{c2}}(\varphi) + 4u_{\mathrm{c3}} \cdot k_{\mathrm{c}} \cdot (l \cdot \cos\alpha + a) \cdot f_{\mathrm{c3}}(\varphi)
\end{aligned}
\tag{3-26}
$$

$$
\begin{aligned}
F &= \frac{dU/d\varphi}{dD_{\mathrm{D}}/d\varphi} \\
&= \frac{\left\{ \begin{aligned}
& u_{\text{S-e}} \cdot k_{\mathrm{f}} \cdot \frac{1}{l} \cdot \left(l^2 - \gamma_{\mathrm{S1}} \cdot l^2 \cdot \tan\alpha - \gamma_{\mathrm{S2}} \cdot a^2 - \gamma_{\mathrm{S3}} \cdot l^2 \cdot \frac{k_{\mathrm{c}}}{k_{\mathrm{f}}} \right) \cdot f'_{\text{S-e}}(\varphi) \\
& + u_{\text{S-p}} \cdot k_{\mathrm{f}} \cdot \frac{1}{l} \cdot \left(\gamma_{\mathrm{S1}} \cdot l^2 \cdot \tan\alpha + \gamma_{\mathrm{S2}} \cdot a^2 + \gamma_{\mathrm{S3}} \cdot l^2 \cdot \frac{k_{\mathrm{c}}}{k_{\mathrm{f}}} \right) \cdot f'_{\text{S-p}}(\varphi) \\
& + 4u_{\text{R-e}} \cdot k_{\mathrm{f}} \cdot \frac{1}{l} \cdot \left[a \cdot (l \cdot \cos\alpha + a) - \gamma_{\mathrm{R1}} \cdot l^2 \cdot \tan\alpha - \gamma_{\mathrm{R2}} \cdot a^2 - \gamma_{\mathrm{R3}} \cdot l^2 \cdot \frac{k_{\mathrm{c}}}{k_{\mathrm{f}}} \right] \cdot f'_{\text{R-e}}(\varphi) \\
& + 4u_{\text{R-p}} \cdot k_{\mathrm{f}} \cdot \frac{1}{l} \cdot \left(\gamma_{\mathrm{R1}} \cdot l^2 \cdot \tan\alpha + \gamma_{\mathrm{R2}} \cdot a^2 + \gamma_{\mathrm{R3}} \cdot l^2 \cdot \frac{k_{\mathrm{c}}}{k_{\mathrm{f}}} \right) \cdot f'_{\text{R-p}}(\varphi) \\
& + 4u_{\text{T-e}} \cdot k_{\mathrm{f}} \cdot \frac{1}{l} \cdot \begin{bmatrix} l \cdot \sin\alpha \cdot (l \cdot \cos\alpha + 2a) - \gamma_{\mathrm{T1}} \cdot l^2 \cdot \tan\alpha \\ - \gamma_{\mathrm{T2}} \cdot a^2 - \gamma_{\mathrm{T3}} \cdot l^2 \cdot \dfrac{k_{\mathrm{c}}}{k_{\mathrm{f}}} \end{bmatrix} \cdot f'_{\text{T-e}}(\varphi) \\
& + 4u_{\text{T-p}} \cdot k_{\mathrm{f}} \cdot \frac{1}{l} \cdot \left(\gamma_{\mathrm{T1}} \cdot l^2 \cdot \tan\alpha + \gamma_{\mathrm{T2}} \cdot a^2 + \gamma_{\mathrm{T3}} \cdot l^2 \cdot \frac{k_{\mathrm{c}}}{k_{\mathrm{f}}} \right) \cdot f'_{\text{T-p}}(\varphi) \\
& + 4u_{\mathrm{c1}} \cdot k_{\mathrm{c}} \cdot a \cdot f'_{\mathrm{c1}}(\varphi) + 4u_{\mathrm{c2}} \cdot k_{\mathrm{c}} \cdot l \cdot f'_{\mathrm{c2}}(\varphi) + 4u_{\mathrm{c3}} \cdot k_{\mathrm{c}} \cdot (l \cdot \cos\alpha + a) \cdot f'_{\mathrm{c3}}(\varphi)
\end{aligned} \right\}}{d_1 \cdot l \cdot \sin\alpha \cdot f'_{\mathrm{d1}}(\varphi) + d_3 \cdot (l \cdot \cos\alpha + a) \cdot f'_{\mathrm{d3}}(\varphi)}
\end{aligned}
\tag{3-27}
$$

$$K=\frac{dF/d\varphi}{dD_{\mathrm{D}}/d\varphi}=\frac{\begin{bmatrix}\tilde{K}_1\cdot\left(d_1\cdot l\cdot\sin\alpha\cdot f'_{\mathrm{d1}}(\varphi)+d_3\cdot\left(l\cdot\cos\alpha+a\right)\cdot f'_{\mathrm{d3}}(\varphi)\right)\\-\tilde{K}_2\cdot\left(d'_1\cdot l\cdot\sin\alpha\cdot f''_{\mathrm{d1}}(\varphi)+d'_3\cdot\left(l\cdot\cos\alpha+a\right)\cdot f''_{\mathrm{d3}}(\varphi)\right)\end{bmatrix}}{\left[d_1\cdot l\cdot\sin\alpha\cdot f'_{\mathrm{d1}}(\varphi)+d_3\cdot\left(l\cdot\cos\alpha+a\right)\cdot f'_{\mathrm{d3}}(\varphi)\right]^3} \tag{3-28}$$

where

$$\begin{aligned}\tilde{K}_1=&\,u_{\text{S-e}}\cdot k_{\mathrm{f}}\cdot\frac{1}{l}\cdot\left(l^2-\gamma_{\mathrm{S1}}\cdot l^2\cdot\tan\alpha-\gamma_{\mathrm{S2}}\cdot a^2-\gamma_{\mathrm{S3}}\cdot l^2\cdot\frac{k_{\mathrm{c}}}{k_{\mathrm{f}}}\right)\cdot f''_{\text{S-e}}(\varphi)\\&+u_{\text{S-p}}\cdot k_{\mathrm{f}}\cdot\frac{1}{l}\cdot\left(\gamma_{\mathrm{S1}}\cdot l^2\cdot\tan\alpha+\gamma_{\mathrm{S2}}\cdot a^2+\gamma_{\mathrm{S3}}\cdot l^2\cdot\frac{k_{\mathrm{c}}}{k_{\mathrm{f}}}\right)\cdot f''_{\text{S-p}}(\varphi)\\&+4u_{\text{R-e}}\cdot k_{\mathrm{f}}\cdot\frac{1}{l}\cdot\left[a\cdot\left(l\cdot\cos\alpha+a\right)-\gamma_{\mathrm{R1}}\cdot l^2\cdot\tan\alpha-\gamma_{\mathrm{R2}}\cdot a^2-\gamma_{\mathrm{R3}}\cdot l^2\cdot\frac{k_{\mathrm{c}}}{k_{\mathrm{f}}}\right]\cdot f''_{\text{R-e}}(\varphi)\\&+4u_{\text{R-p}}\cdot k_{\mathrm{f}}\cdot\frac{1}{l}\cdot\left(\gamma_{\mathrm{R1}}\cdot l^2\cdot\tan\alpha+\gamma_{\mathrm{R2}}\cdot a^2+\gamma_{\mathrm{R3}}\cdot l^2\cdot\frac{k_{\mathrm{c}}}{k_{\mathrm{f}}}\right)\cdot f''_{\text{R-p}}(\varphi)\\&+4u_{\text{T-e}}\cdot k_{\mathrm{f}}\cdot\frac{1}{l}\cdot\begin{bmatrix}l\cdot\sin\alpha\cdot\left(l\cdot\cos\alpha+2a\right)-\gamma_{\mathrm{T1}}\cdot l^2\cdot\tan\alpha\\-\gamma_{\mathrm{T2}}\cdot a^2-\gamma_{\mathrm{T3}}\cdot l^2\cdot\frac{k_{\mathrm{c}}}{k_{\mathrm{f}}}\end{bmatrix}\cdot f''_{\text{T-e}}(\varphi)\\&+4u_{\text{T-p}}\cdot k_{\mathrm{f}}\cdot\frac{1}{l}\cdot\left(\gamma_{\mathrm{T1}}\cdot l^2\cdot\tan\alpha+\gamma_{\mathrm{T2}}\cdot a^2+\gamma_{\mathrm{T3}}\cdot l^2\cdot\frac{k_{\mathrm{c}}}{k_{\mathrm{f}}}\right)\cdot f''_{\text{T-p}}(\varphi)\\&+4u_{\mathrm{c1}}\cdot k_{\mathrm{c}}\cdot a\cdot f''_{\mathrm{c1}}(\varphi)+4u_{\mathrm{c2}}\cdot k_{\mathrm{c}}\cdot l\cdot f''_{\mathrm{c2}}(\varphi)+4u_{\mathrm{c3}}\cdot k_{\mathrm{c}}\cdot\left(l\cdot\cos\alpha+a\right)\cdot f''_{\mathrm{c3}}(\varphi)\end{aligned} \tag{3-29}$$

$$\begin{aligned}\tilde{K}_2=&\,u_{\text{S-e}}\cdot k_{\mathrm{f}}\cdot\frac{1}{l}\cdot\left(l^2-\gamma_{\mathrm{S1}}\cdot l^2\cdot\tan\alpha-\gamma_{\mathrm{S2}}\cdot a^2-\gamma_{\mathrm{S3}}\cdot l^2\cdot\frac{k_{\mathrm{c}}}{k_{\mathrm{f}}}\right)\cdot f'_{\text{S-e}}(\varphi)\\&+u_{\text{S-p}}\cdot k_{\mathrm{f}}\cdot\frac{1}{l}\cdot\left(\gamma_{\mathrm{S1}}\cdot l^2\cdot\tan\alpha+\gamma_{\mathrm{S2}}\cdot a^2+\gamma_{\mathrm{S3}}\cdot l^2\cdot\frac{k_{\mathrm{c}}}{k_{\mathrm{f}}}\right)\cdot f'_{\text{S-p}}(\varphi)\\&+4u_{\text{R-e}}\cdot k_{\mathrm{f}}\cdot\frac{1}{l}\cdot\left[a\cdot\left(l\cdot\cos\alpha+a\right)-\gamma_{\mathrm{R1}}\cdot l^2\cdot\tan\alpha-\gamma_{\mathrm{R2}}\cdot a^2-\gamma_{\mathrm{R3}}\cdot l^2\cdot\frac{k_{\mathrm{c}}}{k_{\mathrm{f}}}\right]\cdot f'_{\text{R-e}}(\varphi)\\&+4u_{\text{R-p}}\cdot k_{\mathrm{f}}\cdot\frac{1}{l}\cdot\left(\gamma_{\mathrm{R1}}\cdot l^2\cdot\tan\alpha+\gamma_{\mathrm{R2}}\cdot a^2+\gamma_{\mathrm{R3}}\cdot l^2\cdot\frac{k_{\mathrm{c}}}{k_{\mathrm{f}}}\right)\cdot f'_{\text{R-p}}(\varphi)\\&+4u_{\text{T-e}}\cdot k_{\mathrm{f}}\cdot\frac{1}{l}\cdot\begin{bmatrix}l\cdot\sin\alpha\cdot\left(l\cdot\cos\alpha+2a\right)-\gamma_{\mathrm{T1}}\cdot l^2\cdot\tan\alpha\\-\gamma_{\mathrm{T2}}\cdot a^2-\gamma_{\mathrm{T3}}\cdot l^2\cdot\frac{k_{\mathrm{c}}}{k_{\mathrm{f}}}\end{bmatrix}\cdot f'_{\text{T-e}}(\varphi)\\&+4u_{\text{T-p}}\cdot k_{\mathrm{f}}\cdot\frac{1}{l}\cdot\left(\gamma_{\mathrm{T1}}\cdot l^2\cdot\tan\alpha+\gamma_{\mathrm{T2}}\cdot a^2+\gamma_{\mathrm{T3}}\cdot l^2\cdot\frac{k_{\mathrm{c}}}{k_{\mathrm{f}}}\right)\cdot f'_{\text{T-p}}(\varphi)\\&+4u_{\mathrm{c1}}\cdot k_{\mathrm{c}}\cdot a\cdot f'_{\mathrm{c1}}(\varphi)+4u_{\mathrm{c2}}\cdot k_{\mathrm{c}}\cdot l\cdot f'_{\mathrm{c2}}(\varphi)+4u_{\mathrm{c3}}\cdot k_{\mathrm{c}}\cdot\left(l\cdot\cos\alpha+a\right)\cdot f'_{\mathrm{c3}}(\varphi)\end{aligned} \tag{3-30}$$

Assuming the variable φ corresponding to the energy at the end of loading, initial peak force, and maximum stiffness is φ_U, φ_F, and φ_K, respectively, the three properties can be calculated from Eq. (3-26)-(3-30),

$$\begin{aligned}
U = {} & u_{U1} \cdot k_f \cdot \frac{1}{l} \cdot \left(l^2 - \gamma_{S1} \cdot l^2 \cdot \tan\alpha - \gamma_{S2} \cdot a^2 - \gamma_{S3} \cdot l^2 \cdot \frac{k_c}{k_f} \right) \\
& + u_{U2} \cdot k_f \cdot \frac{1}{l} \cdot \left(\gamma_{S1} \cdot l^2 \cdot \tan\alpha + \gamma_{S2} \cdot a^2 + \gamma_{S3} \cdot l^2 \cdot \frac{k_c}{k_f} \right) \\
& + u_{U3} \cdot k_f \cdot \frac{1}{l} \cdot \left[a \cdot (l \cdot \cos\alpha + a) - \gamma_{R1} \cdot l^2 \cdot \tan\alpha - \gamma_{R2} \cdot a^2 - \gamma_{R3} \cdot l^2 \cdot \frac{k_c}{k_f} \right] \\
& + u_{U4} \cdot k_f \cdot \frac{1}{l} \cdot \left(\gamma_{R1} \cdot l^2 \cdot \tan\alpha + \gamma_{R2} \cdot a^2 + \gamma_{R3} \cdot l^2 \cdot \frac{k_c}{k_f} \right) \\
& + u_{U5} \cdot k_f \cdot \frac{1}{l} \cdot \left[l \cdot \sin\alpha \cdot (l \cdot \cos\alpha + 2a) - \gamma_{T1} \cdot l^2 \cdot \tan\alpha - \gamma_{T2} \cdot a^2 - \gamma_{T3} \cdot l^2 \cdot \frac{k_c}{k_f} \right] \\
& + u_{U6} \cdot k_f \cdot \frac{1}{l} \cdot \left(\gamma_{T1} \cdot l^2 \cdot \tan\alpha + \gamma_{T2} \cdot a^2 + \gamma_{T3} \cdot l^2 \cdot \frac{k_c}{k_f} \right) \\
& + u_{U7} \cdot k_c \cdot a + u_{U8} \cdot k_c \cdot l + u_{U9} \cdot k_c \cdot (l \cdot \cos\alpha + a)
\end{aligned} \tag{3-31}$$

$$F_{max} = \frac{\left[\begin{array}{l}
u_{F1} \cdot k_f \cdot \frac{1}{l} \cdot \left(l^2 - \gamma_{S1} \cdot l^2 \cdot \tan\alpha - \gamma_{S2} \cdot a^2 - \gamma_{S3} \cdot l^2 \cdot \frac{k_c}{k_f} \right) \\
+ u_{F2} \cdot k_f \cdot \frac{1}{l} \cdot \left(\gamma_{S1} \cdot l^2 \cdot \tan\alpha + \gamma_{S2} \cdot a^2 + \gamma_{S3} \cdot l^2 \cdot \frac{k_c}{k_f} \right) \\
+ u_{F3} \cdot k_f \cdot \frac{1}{l} \cdot \left(a \cdot (l \cdot \cos\alpha + a) - \gamma_{R1} \cdot l^2 \cdot \tan\alpha - \gamma_{R2} \cdot a^2 - \gamma_{R3} \cdot l^2 \cdot \frac{k_c}{k_f} \right) \\
+ u_{F4} \cdot k_f \cdot \frac{1}{l} \cdot \left(\gamma_{R1} \cdot l^2 \cdot \tan\alpha + \gamma_{R2} \cdot a^2 + \gamma_{R3} \cdot l^2 \cdot \frac{k_c}{k_f} \right) \\
+ u_{F5} \cdot k_f \cdot \frac{1}{l} \cdot \left(\begin{array}{l} l \cdot \sin\alpha \cdot (l \cdot \cos\alpha + 2a) - \gamma_{T1} \cdot l^2 \cdot \tan\alpha \\ - \gamma_{T2} \cdot a^2 - \gamma_{T3} \cdot l^2 \cdot \frac{k_c}{k_f} \end{array} \right) \\
+ u_{F6} \cdot k_f \cdot \frac{1}{l} \cdot \left(\gamma_{T1} \cdot l^2 \cdot \tan\alpha + \gamma_{T2} \cdot a^2 + \gamma_{T3} \cdot l^2 \cdot \frac{k_c}{k_f} \right) \\
+ u_{F7} \cdot k_c \cdot a + u_{F8} \cdot k_c \cdot l + u_{F9} \cdot k_c \cdot (l \cdot \cos\alpha + a)
\end{array} \right]}{d_{F1} \cdot l \cdot \sin\alpha + d_{F3} \cdot (l \cdot \cos\alpha + a)} \tag{3-32}$$

$$K_{max} = \frac{\tilde{K}_1 \cdot \left[d_{K1} \cdot l \cdot \sin\alpha + d_{K3} \cdot (l \cdot \cos\alpha + a) \right] - \tilde{K}_2 \cdot \left[d'_{K1} \cdot l \cdot \sin\alpha + d'_{K3} \cdot (l \cdot \cos\alpha + a) \right]}{\left[d_{K1} \cdot l \cdot \sin\alpha + d_{K3} \cdot (l \cdot \cos\alpha + a) \right]^3} \tag{3-33}$$

where

$$\begin{aligned}\tilde{K}_1 &= u_{\mathrm{K1}} \cdot k_{\mathrm{f}} \cdot \frac{1}{l} \cdot l^2 + u_{\mathrm{K2}} \cdot k_{\mathrm{f}} \cdot \frac{1}{l} \cdot a \cdot (l \cdot \cos\alpha + a) \\ &+ u_{\mathrm{K3}} \cdot k_{\mathrm{f}} \cdot \frac{1}{l} \cdot l \cdot \sin\alpha \cdot (l \cdot \cos\alpha + 2a) \\ &+ u_{\mathrm{K4}} \cdot k_{\mathrm{c}} \cdot a + u_{\mathrm{K5}} \cdot k_{\mathrm{c}} \cdot l + u_{\mathrm{K6}} \cdot k_{\mathrm{c}} \cdot (l \cdot \cos\alpha + a)\end{aligned} \tag{3-34}$$

$$\begin{aligned}\tilde{K}_2 &= u_{\mathrm{K7}} \cdot k_{\mathrm{f}} \cdot \frac{1}{l} \cdot l^2 + u_{\mathrm{K8}} \cdot k_{\mathrm{f}} \cdot \frac{1}{l} \cdot a \cdot (l \cdot \cos\alpha + a) \\ &+ u_{\mathrm{K9}} \cdot k_{\mathrm{f}} \cdot \frac{1}{l} \cdot l \cdot \sin\alpha \cdot (l \cdot \cos\alpha + 2a) \\ &+ u_{\mathrm{K10}} \cdot k_{\mathrm{c}} \cdot a + u_{\mathrm{K11}} \cdot k_{\mathrm{c}} \cdot l + u_{\mathrm{K12}} \cdot k_{\mathrm{c}} \cdot (l \cdot \cos\alpha + a)\end{aligned} \tag{3-35}$$

$$\begin{aligned}&u_{\mathrm{U1}} = u_{\mathrm{S\text{-}e}} \cdot f_{\mathrm{S\text{-}e}}(\varphi)\big|_{\varphi_{\mathrm{U}}}, u_{\mathrm{U2}} = u_{\mathrm{S\text{-}p}} \cdot f_{\mathrm{S\text{-}p}}(\varphi)\big|_{\varphi_{\mathrm{U}}}, u_{\mathrm{U3}} = 4u_{\mathrm{R\text{-}e}} \cdot f_{\mathrm{R\text{-}e}}(\varphi)\big|_{\varphi_{\mathrm{U}}}, \\ &u_{\mathrm{U4}} = 4u_{\mathrm{R\text{-}p}} \cdot f_{\mathrm{R\text{-}p}}(\varphi)\big|_{\varphi_{\mathrm{U}}}, u_{\mathrm{U5}} = 4u_{\mathrm{T\text{-}e}} \cdot f_{\mathrm{T\text{-}e}}(\varphi)\big|_{\varphi_{\mathrm{U}}}, u_{\mathrm{U6}} = 4u_{\mathrm{T\text{-}p}} \cdot f_{\mathrm{T\text{-}p}}(\varphi)\big|_{\varphi_{\mathrm{U}}}, \\ &u_{\mathrm{U7}} = 4u_{\mathrm{c1}} \cdot f_{\mathrm{c1}}(\varphi)\big|_{\varphi_{\mathrm{U}}}, u_{\mathrm{U8}} = 4u_{\mathrm{c2}} \cdot f_{\mathrm{c2}}(\varphi)\big|_{\varphi_{\mathrm{U}}}, u_{\mathrm{U9}} = 4u_{\mathrm{c3}} \cdot f_{\mathrm{c3}}(\varphi)\big|_{\varphi_{\mathrm{U}}};\end{aligned} \tag{3-36}$$

$$\begin{aligned}&u_{\mathrm{F1}} = u_{\mathrm{S\text{-}e}} \cdot f'_{\mathrm{S\text{-}e}}(\varphi)\big|_{\varphi_{\mathrm{F}}}, u_{\mathrm{F2}} = u_{\mathrm{S\text{-}p}} \cdot f'_{\mathrm{S\text{-}p}}(\varphi)\big|_{\varphi_{\mathrm{F}}}, u_{\mathrm{F3}} = 4u_{\mathrm{R\text{-}e}} \cdot f'_{\mathrm{R\text{-}e}}(\varphi)\big|_{\varphi_{\mathrm{F}}}, \\ &u_{\mathrm{F4}} = 4u_{\mathrm{R\text{-}p}} \cdot f'_{\mathrm{R\text{-}p}}(\varphi)\big|_{\varphi_{\mathrm{F}}}, u_{\mathrm{F5}} = 4u_{\mathrm{T\text{-}e}} \cdot f'_{\mathrm{T\text{-}e}}(\varphi)\big|_{\varphi_{\mathrm{F}}}, u_{\mathrm{F6}} = 4u_{\mathrm{T\text{-}p}} \cdot f'_{\mathrm{T\text{-}p}}(\varphi)\big|_{\varphi_{\mathrm{F}}}, \\ &u_{\mathrm{F7}} = 4u_{\mathrm{c1}} \cdot f'_{\mathrm{c1}}(\varphi)\big|_{\varphi_{\mathrm{F}}}, u_{\mathrm{F8}} = 4u_{\mathrm{c2}} \cdot f'_{\mathrm{c2}}(\varphi)\big|_{\varphi_{\mathrm{F}}}, u_{\mathrm{F9}} = 4u_{\mathrm{c3}} \cdot f'_{\mathrm{c3}}(\varphi)\big|_{\varphi_{\mathrm{F}}}, \\ &d_{\mathrm{F1}} = d_1 \cdot f'_{\mathrm{d1}}(\varphi)\big|_{\varphi_{\mathrm{F}}}, d_{\mathrm{F3}} = d_3 \cdot f'_{\mathrm{d3}}(\varphi)\big|_{\varphi_{\mathrm{F}}};\end{aligned} \tag{3-37}$$

$$\begin{aligned}&u_{\mathrm{K1}} = u_{\mathrm{S\text{-}e}} \cdot f''_{\mathrm{S\text{-}e}}(\varphi)\big|_{\varphi_{\mathrm{K}}}, u_{\mathrm{K2}} = 4u_{\mathrm{R\text{-}e}} \cdot f''_{\mathrm{R\text{-}e}}(\varphi)\big|_{\varphi_{\mathrm{K}}}, u_{\mathrm{K3}} = 4u_{\mathrm{T\text{-}e}} \cdot f''_{\mathrm{T\text{-}e}}(\varphi)\big|_{\varphi_{\mathrm{K}}}, \\ &u_{\mathrm{K4}} = 4u_{\mathrm{c1}} \cdot f''_{\mathrm{c1}}(\varphi)\big|_{\varphi_{\mathrm{K}}}, u_{\mathrm{K5}} = 4u_{\mathrm{c2}} \cdot f''_{\mathrm{c2}}(\varphi)\big|_{\varphi_{\mathrm{K}}}, u_{\mathrm{K6}} = 4u_{\mathrm{c3}} \cdot f''_{\mathrm{c3}}(\varphi)\big|_{\varphi_{\mathrm{K}}}, \\ &u_{\mathrm{K7}} = u_{\mathrm{S\text{-}e}} \cdot f'_{\mathrm{S\text{-}e}}(\varphi)\big|_{\varphi_{\mathrm{K}}}, u_{\mathrm{K8}} = 4u_{\mathrm{R\text{-}e}} \cdot f'_{\mathrm{R\text{-}e}}(\varphi)\big|_{\varphi_{\mathrm{K}}}, u_{\mathrm{K9}} = 4u_{\mathrm{T\text{-}e}} \cdot f'_{\mathrm{T\text{-}e}}(\varphi)\big|_{\varphi_{\mathrm{K}}}, \\ &u_{\mathrm{K10}} = 4u_{\mathrm{c1}} \cdot f'_{\mathrm{c1}}(\varphi)\big|_{\varphi_{\mathrm{K}}}, u_{\mathrm{K11}} = 4u_{\mathrm{c2}} \cdot f'_{\mathrm{c2}}(\varphi)\big|_{\varphi_{\mathrm{K}}}, u_{\mathrm{K12}} = 4u_{\mathrm{c3}} \cdot f'_{\mathrm{c3}}(\varphi)\big|_{\varphi_{\mathrm{K}}}, \\ &d_{\mathrm{K1}} = d_1 \cdot f'_{\mathrm{d1}}(\varphi)\big|_{\varphi_{\mathrm{K}}}, d_{\mathrm{K3}} = d_3 \cdot f'_{\mathrm{d3}}(\varphi)\big|_{\varphi_{\mathrm{K}}}, \\ &d'_{\mathrm{K1}} = d'_1 \cdot f''_{\mathrm{d1}}(\varphi)\big|_{\varphi_{\mathrm{K}}}, d'_{\mathrm{K3}} = d'_3 \cdot f''_{\mathrm{d3}}(\varphi)\big|_{\varphi_{\mathrm{K}}}.\end{aligned} \tag{3-38}$$

Notice that in Eq. (3-33) for the maximum stiffness, the terms associated with the plastic regions are ignored because the PEEQ contours in Fig. 3-18 indicate that all the facets remain elastic at configuration II where the maximum stiffness is achieved.

To determine the unknown coefficients in Eq. (3-31)-(3-35), a series of 20 numerical models with varying side length, a, twist angle, α, and crease torsional stiffness, k_{c}, as listed in Table 3-1 were built and analyzed. The side length, l, was fixed to 16.25mm for all the models, and the sheet thickness and material parameters were the same as that in Section 3.2. Based on the results also listed in Table 3-1, the coefficients can be obtained as follows using the nonlinear regression.

Table 3-1 Geometric and material parameters of the numerical models and results.

Model	a [mm]	α [deg]	k_c [N·rad^{-1}]	Δx_{max} [mm]	$U/(k_c l)$	F_{max}/k_c	$K_{max}l/k_c$
1	16.25	30	0.68×10^{-2}	23.00	202.18	4643.79	64760.59
2	16.25	30	0.43×10^{-1}	23.00	69.57	750.27	10422.74
3	16.25	30	0.85×10^{-1}	23.00	51.16	378.97	5252.42
4	16.25	30	0.11	23.00	46.80	285.42	3951.94
5	16.25	30	0.17	23.00	41.60	192.87	2653.91
6	16.25	30	0.34	23.00	32.07	98.62	1330.74
7	16.25	30	0.51	23.00	27.26	67.15	899.22
8	16.25	30	0.68	23.00	23.85	51.15	679.44
9	8.13	30	0.44	22.39	23.04	53.46	995.56
10	12.19	30	0.44	22.70	26.08	66.20	1011.09
11	16.25	30	0.44	23.00	28.77	77.57	1050.77
12	24.38	30	0.44	23.63	36.52	99.98	1223.23
13	32.50	30	0.44	24.25	46.34	115.33	1300.21
14	48.75	30	0.44	25.49	63.86	142.80	1614.16
15	65.00	30	0.44	26.73	72.17	145.37	1631.23
16	16.25	20	0.44	15.70	24.76	22.41	249.98
17	16.25	25	0.44	19.46	27.04	41.76	544.72
18	16.25	35	0.44	26.20	34.72	137.75	2063.27
19	16.25	40	0.44	29.51	50.45	201.23	3398.61
20	16.25	45	0.44	32.45	68.27	267.75	5055.34

$$\begin{aligned}
&u_{U1}=-21.35, u_{U2}=1.35\times10^{-3}, u_{U3}=4.88, u_{U4}=-409.96, u_{U5}=-9.05,\\
&u_{U6}=271.38, u_{U7}=6.73, u_{U8}=5.57\times10^{-2}, u_{U9}=8.54,\\
&\gamma_{S1}=0.32, \gamma_{S2}=0.06\times10^{-4}, \gamma_{S3}=0.19,\\
&\gamma_{R1}=0.42\times10^{-5}, \gamma_{R2}=9.26\times10^{-3}, \gamma_{R3}=0.84\times10^{-1},\\
&\gamma_{T1}=0.18, \gamma_{T2}=0.81\times10^{-5}, \gamma_{T3}=0.12;
\end{aligned} \tag{3-39}$$

$$\begin{aligned}
&u_{F1}=-50.61, u_{F2}=294.82, u_{F3}=6.73, u_{F4}=313.16, u_{F5}=33.43, u_{F6}=225.41,\\
&u_{F7}=7.60, u_{F8}=8.74\times10^{-2}, u_{F9}=2.02\times10^{-2}, d_{F1}=-1.52, d_{F3}=0.90,\\
&\gamma_{S1}=0.33\times10^{-1}, \gamma_{S2}=0.65\times10^{-2}, \gamma_{S3}=0.63\times10^{-8},\\
&\gamma_{R1}=0.65\times10^{-1}, \gamma_{R2}=0.42\times10^{-2}, \gamma_{R3}=0.11\times10^{-8},\\
&\gamma_{T1}=0.83\times10^{-1}, \gamma_{T2}=0.81\times10^{-2}, \gamma_{T3}=0.41\times10^{-9};
\end{aligned} \tag{3-40}$$

$$u_{K1}=-165.75, u_{K2}=79.86, u_{K3}=44.80, u_{K4}=9.67, u_{K5}=5.72\times10^{-4},$$
$$u_{K6}=1.19, u_{K7}=-59.66, u_{K8}=-63.14, u_{K9}=407.88, u_{K10}=0.16\times10^{-1}, \quad (3\text{-}41)$$
$$u_{K11}=4.51, u_{K12}=2.04\times10^{-3}, d_{K1}=-0.11, d_{K3}=0.25, d'_{K1}=-0.56, d'_{K3}=0.11.$$

Substituting Eq. (3-39)-(3-41) to Eq. (3-31)-(3-35), the energy, initial peak force, and maximum stiffness of the structure can be obtained.

In addition, the deformation process of the numerical model with k_f/k_c=1 is studied. The parameter implies that the stiffness of the creases is identical to that of the facets, which is different from the ordinary origami structures with weakened creases. The numerical results in Fig. 3-19(a) and (b) show that the structure still follows the same three-stage process. And comparing with Fig. 3-18, the Mises stress and PEEQ contours in Fig. 3-19(c) and (d) indicate that the plastically deformed regions increase with the crease stiffness. Thus the empirical model applies.

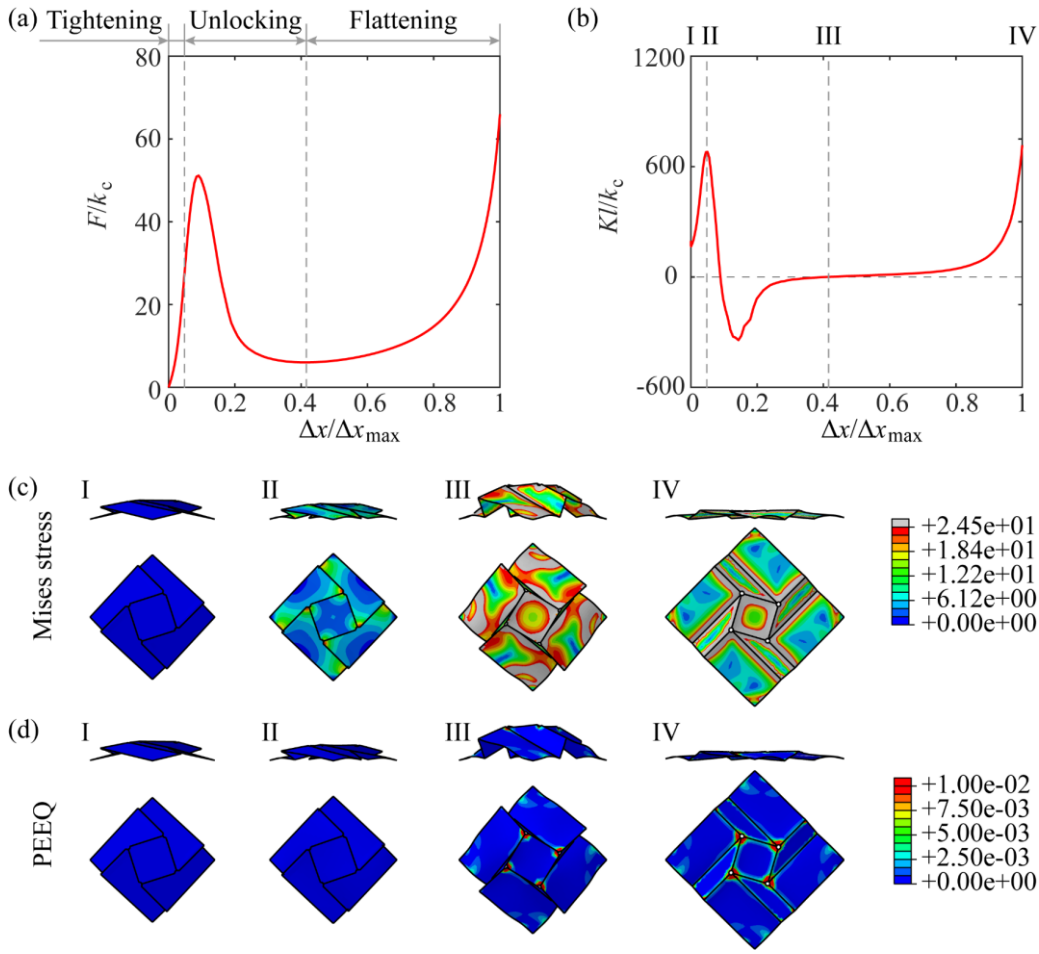

Fig. 3-19 (a) Normalized force, F/k_c, and (b) normalized stiffness, Kl/k_c, versus normalized displacement, $\Delta x/\Delta x_{max}$, of the numerical model with k_f/k_c=1. (c) The Mises stress and (d) PEEQ contours of the numerical model with k_f/k_c=1.

3.7 Programmability and Prediction of Mechanical Properties

3.7.1 Programmable Properties

The predicted curves of normalized energy, initial peak force, and maximum stiffness of the structure based on the empirical equations (3-31)-(3-35) are respectively drawn in Fig. 3-20, Fig. 3-21, and Fig. 3-22 together with the numerical results (black triangles) and experimental results (red circles) in Section 3.2, from which a good match is obtained for all the three properties.

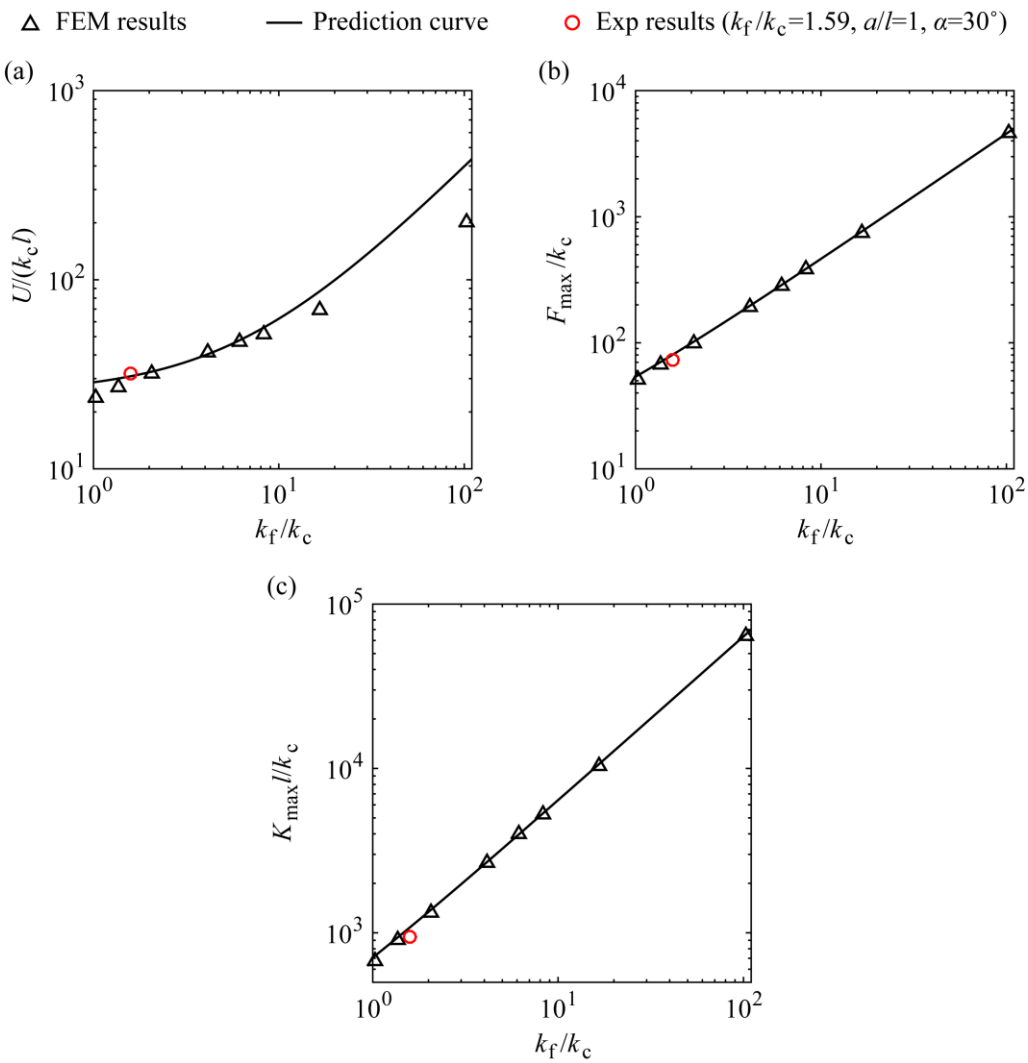

Fig. 3-20 Predicted (a) normalized energy, $U/(k_c l)$, (b) initial peak force, F_{max}/k_c, and (c) maximum stiffness $K_{max}l/k_c$, of type 1 square-twist structure with normalized crease stiffness k_f/k_c from 1 to 110. The experimental and numerical results are also shown in the figure.

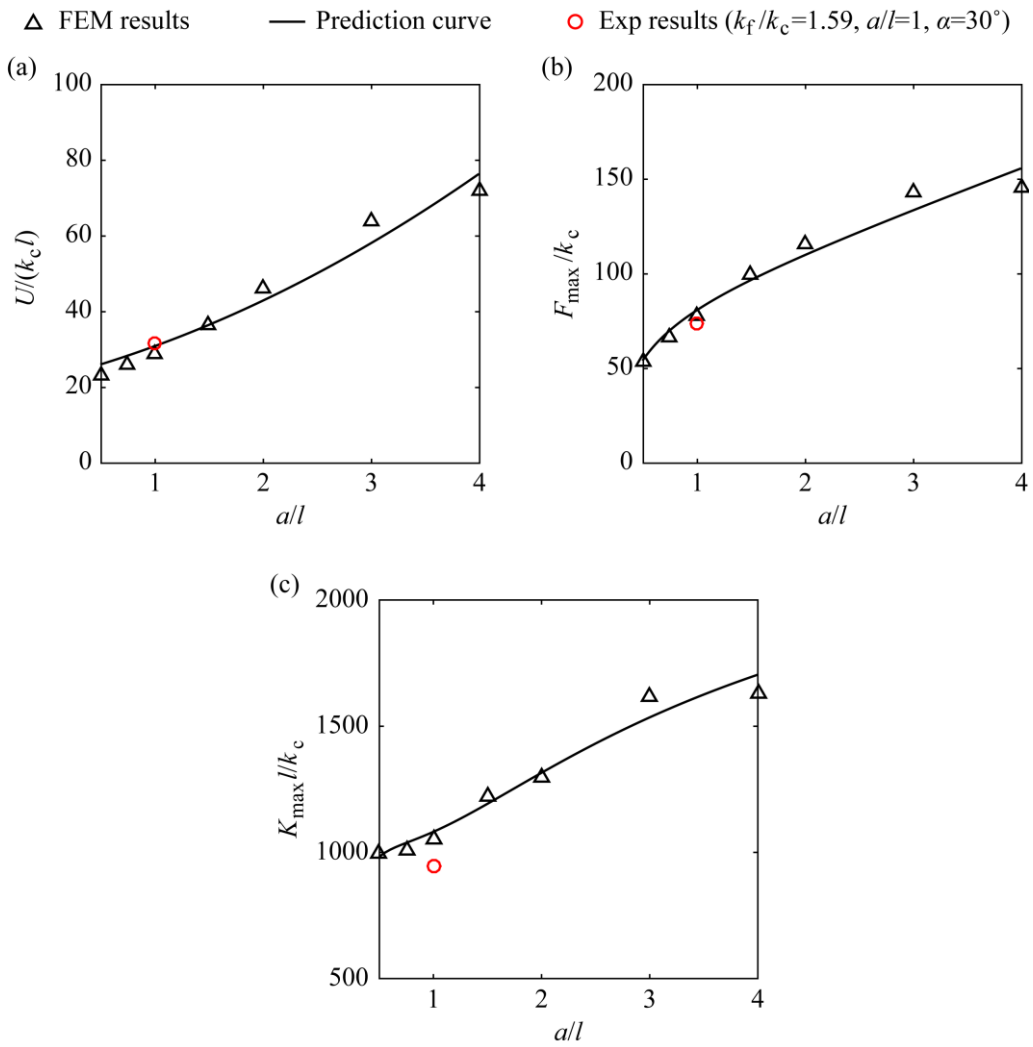

Fig. 3-21 Predicted (a) normalized energy, $U/(k_c l)$, (b) initial peak force, F_{max}/k_c, and (c) maximum stiffness $K_{max}l/k_c$, of type 1 square-twist structure with side length ratio a/l from 0.5 to 4. The experimental and numerical results are also shown in the figure.

The empirical equations enable us to program the mechanical properties of the structure based on material and geometric parameters. Figure 3-20 shows the results with fixed geometric parameters a/l=1 and α=30°, and varying ratio of facet bending stiffness to crease rotational stiffness k_f/k_c, in which k_f is experimentally determined to be 0.70N·rad^{-1} based on the method in Chapter 2. It can be seen that when k_f/k_c is relatively small, the energy increases at a low rate with k_f/k_c, which implies that the contribution from crease rotations is dominant in the energy of the structure. As k_f/k_c becomes larger, the role played by facet distortions is more prominent, and consequently, the energy rises at a higher rate. The initial peak force and maximum stiffness, on the

other hand, increase nearly linearly with k_f/k_c in the entire range, indicating that these two properties are dominated by the facets of the structure.

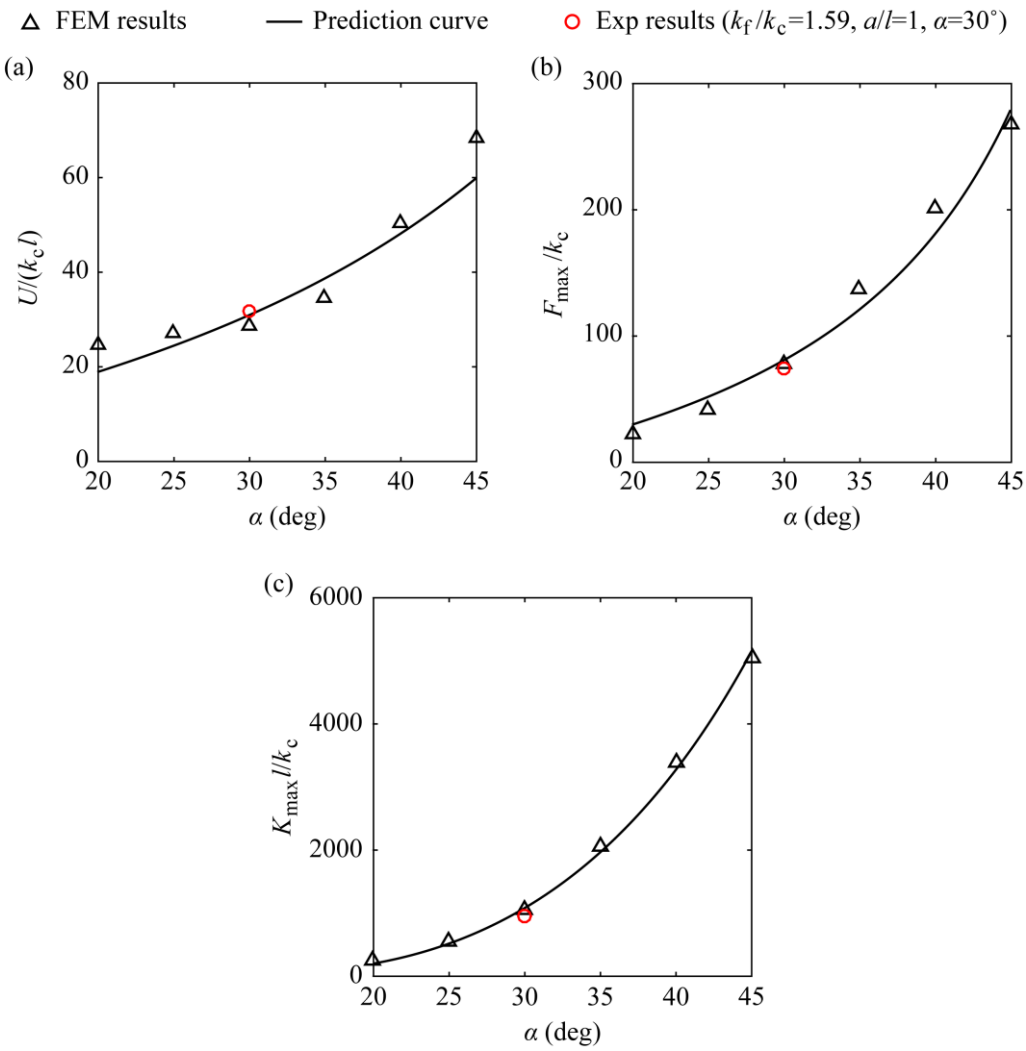

Fig. 3-22 Predicted normalized (a) energy, $U/(k_c l)$, (b) initial peak force, F_{max}/k_c, and (c) maximum stiffness $K_{max}l/k_c$, of the type 1 square-twist structure with twist angle α from 20° to 45°. The experimental and numerical results are also shown in the figure.

Furthermore, if normalized crease stiffness k_f/k_c=1.59 and twist angle α=30° are kept, while side length ratio a/l is varied from 0.5 to 4, it can be found from Fig. 3-21 that the energy, initial peak force, and maximum stiffness increase with a/l since it enlarges the rectangular and trapezoidal facets while keeping the size of the square constant. Finally, the results of the models with identical k_f/k_c=1.59 and a/l=1, and different twist angle α ranging from 20° to 45°, are shown in Fig. 3-22. Increasing α

raises all three mechanical properties especially the maximum stiffness since a larger twist angle leads to a more twisted and consequently stiffer structure. When α is less than 20°, the structure behaves like a rigid origami structure with no obvious initial peak force but a long plateau force as in the case of the type 3 origami structure[65].

To further validate the accuracy of the empirical equations, another structure with a=24.375mm, l=16.25mm, α=35°, and k_c=0.24N·rad^{-1} was fabricated and tested following the same procedure in Section 2. The experimentally obtained energy, initial peak force, and maximum stiffness were 234.93J, 43.77N, and 44.11N·mm^{-1}, whereas the predicted values were 202.57J, 54.02N, and 43.73N·mm^{-1}. The experimental and predicted normalized mechanical responses are shown in Fig. 3-23, where the predictions are very close to the corresponding experimental results. Thus, it can be safely concluded that the empirical equations developed here are capable of predicting the mechanical properties of type 1 square-twist structure.

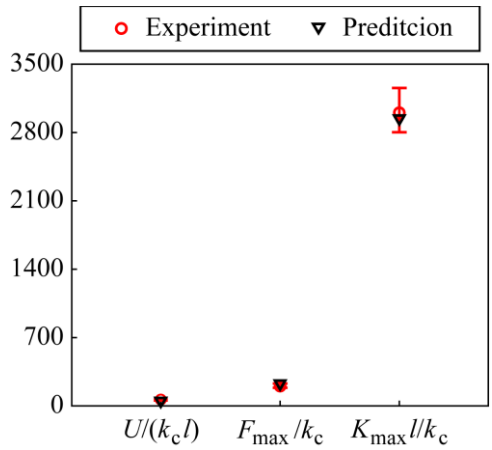

Fig. 3-23 Experimental and predicted normalized energy, $U/(k_c l)$, initial peak force, F_{max}/k_c, and maximum stiffness $K_{max}l/k_c$, of the validated model with k_f/k_c=2.92, a/l=1.5, and α=35°.

3.7.2 Predicted Properties

The prediction of mechanical properties of type 1 metasheet by the empirical model of the corresponding unit is presented in this section. A 2×2 tessellation of the type 1 unit (Fig. 3-24(a)) was designed, manufactured using the same material and technique for the type 1 unit as mentioned in Section 3.2, and tested to demonstrate the feasibility of the proposed design approach. Therefore, the same torsional stiffness for

the original and virtual creases was also utilized to calculate the predicted energy, initial peak force, and maximum stiffness. Here, the same geometric parameters as the experimental specimen in Section 3.2 were chosen for the tessellation so that the prediction results of tessellation can be calculated by the prediction of a unit in Fig. 3-22. The predicted energy, initial peak force, and maximum stiffness calculated from Eq. (3-31)-(3-35) are drawn together with the experimental results in Fig. 3-24(c).

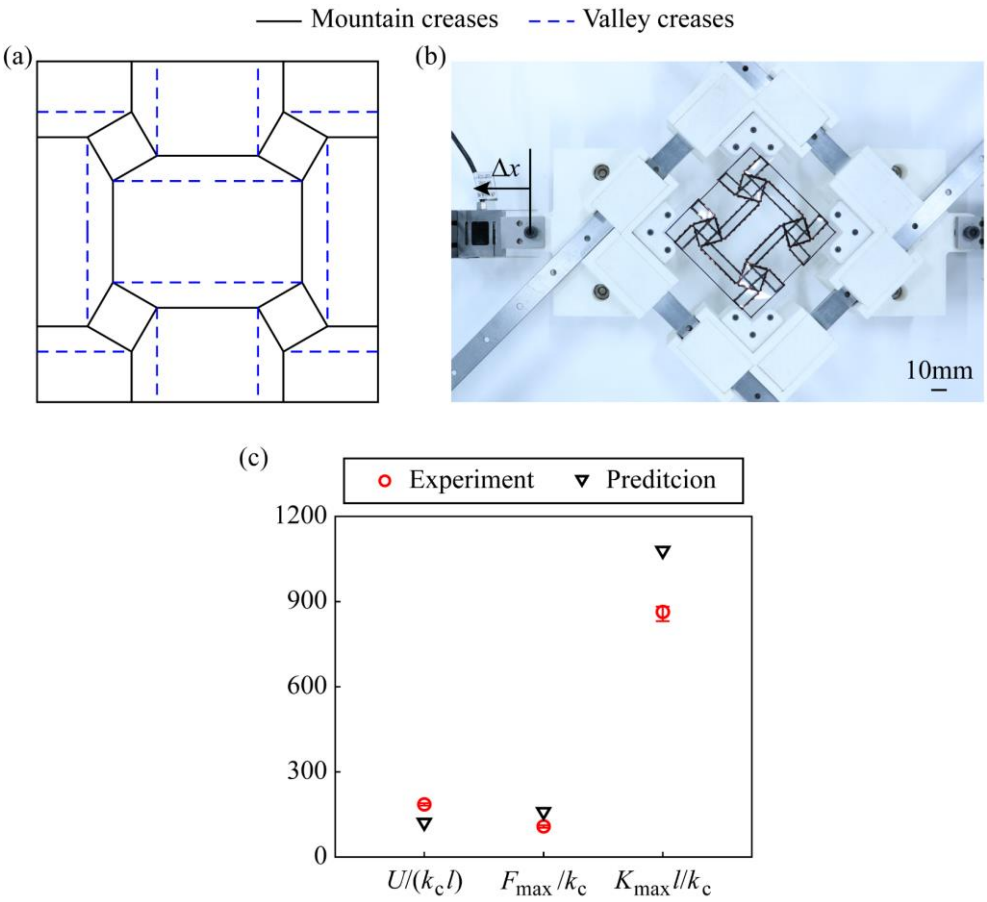

Fig. 3-24 (a) Pattern, (b) experimental system, (c) predicted normalized energy, $U/(k_c l)$, initial peak force, F_{max}/k_c, and maximum stiffness $K_{max}l/k_c$, of the 2×2 type 1 metasheet (k_f/k_c=1.59, a/l=1, and α=30°). The experimental results are also shown in the figure.

As shown in Fig. 3-24(b), the loading system, as well as the connection between specimen and fixtures of the 2×2 tessellation, are identical to those of the unit, which implies that each unit in the tessellation structure is controlled by one fixture and two neighbour units. Then, the units can be considered as nonlinear springs and the metasheet as an assembly of springs connected in series and parallel. Thus, the

predicted energy of the metasheet is calculated by the total energy of four units, i.e. $U_{2\times2}=4U$. The predicted initial peak force and maximum stiffness of the metasheet are obtained by adding up those of the units and then dividing them by 2 and 2^2, i.e. $F_{2\times2\text{-max}}=2F_{\max}$ and $K_{2\times2\text{-max}}=K_{\max}$. Again the predictions are very close to the corresponding experimental results, see Fig. 3-24(c). Notice that the difference between experimental and predicted stiffness exists in the 2×2 metasheet. To explain this phenomenon, a characteristic of the type 1 structure is proposed that the maximum stiffness happens in the tightening stage of the unfolded process (see Section 3.5 and Section 3.6). The deformation of tightening status performs differently between a single unit and a 2×2 metasheet because the fixture is identical on the four corners of a single unit but the unit in a 2×2 metasheet has only one corner supported by the fixture while three corners supported by the other units. Therefore, the different deformation of the structures leads to an error between the experimental and predicted results of the 2×2 type 1 metasheet. In general, the results in Fig. 3-24 indicate that the empirical equations can be used in predicting the mechanical properties of the square-twist metasheet.

The three validated models in Section 3.7 have different material parameters (k_f/k_c=1.59, 2.92), various geometric parameters (a/l=1, 1.5 and α=30°, 35°), and diverse numbers of units (single unit, 2×2 metasheet). But all of them show a reasonably good match between predicted and experimental results. Thus, the conclusion can be presented that the predicted method proposed in this work is available for type 1 units with arbitrary parameters.

3.8 Conclusions

To conclude this chapter, the deformation characteristics and mechanical properties of a rotationally symmetric square-twist origami structure, referred to as the type 1 square-twist structure, have been analyzed experimentally and numerically. This work unveiled the three-stage deformation process of the structure, including the tightening stage, unlocking stage, and flattening stage, and analyzed the evolution of facet distortions together with the key features in the energy, force, and stiffness curves in detail. This result thus enables an exact understanding of the deformation and mechanics of the structure, which cannot be achieved by the previous facet triangulation approaches[65, 149, 160] due to that they can only capture facets bending, or equivalent

compliant mechanism method[153] because it ignores the facet distortions. Based on the deformation analysis of the structure, a series of empirical equations have been for the first time established to quantitively correlate the geometric parameters and base materials with the energy, initial peak force, and maximum stiffness of the structure, which are validated by quasi-static tension experiments. The empirical model offers an approach to accurately programming the mechanical properties of the non-rigid origami structure as well as guidance for its applications in various engineering fields.

Only the mechanical properties of an individual square-twist structure have been investigated in this paper. When forming metamaterials, how those properties will be related to the bulk materials warrants further research. Next, I will study the design principle and property programmability of mechanical metamaterials composed of a single type of square-twist structure or a mixture of them, aiming to develop a series of origami-inspired metamaterials with a wide bandwidth of programmability and tunability.

Chapter 4 Metasheets Built with a Mixture of Rigid and Non-rigid Square-twist Units

4.1 Introduction

The reported metamaterial designs are usually formed by periodic tessellation of a single type of either rigid or non-rigid pattern and thus are not able to cover the wide range of mechanical properties provided by a possible mixture of rigid and non-rigid patterns. Here, a potential design approach that combines rigid and non-rigid origami units in a single metamaterial is proposed to overcome such a problem. By varying the proportion of each type of unit, the mechanical properties can be tuned between the upper limit posed by the non-rigid pattern and the lower limit set by the rigid one. It should be noted that incorporating origami units of different types is in general not a trivial task because they commonly have different crease numbers and mountain-valley assignments and may not match each other. In this chapter, I take advantage of this unique feature of origami and propose a new kind of metasheets based on the square-twist pattern, see Fig. 4-1(a). Previous work[149] indicated that there are four possible assignments of mountain and valley creases as shown in Fig. 4-1(b-d), leading to two non-rigid units named types 1 and 2, and two rigid ones denoted types 3 and 4. Each square-twist unit has distinct folding behavior and mechanical properties, which have been thoroughly studied at the unit level in Chapter 2 and 3. In this Chapter, combining these different units in a single metasheet is proposed, aiming for programming its mechanical properties in terms of energy, load bearing capability, and stiffness within an elevated landscape by varying the type and proportion of different patterns.

The outline of this chapter is as follows. The tessellation rule of the metasheets composed of different types of units with different geometric parameters is set up in Section 4.2. In section 4.3, a series of metasheets are designed and fabricated, and quasi-static tension experiments are conducted to obtain the deformation process and force versus displacement response. The experimental results of different types of metasheet and varied boundary conditions are also presented and discussed in this section. In Section 4.4, the relationship between the global mechanical properties of the metasheets

and the constitutional unit behaviors, and the property programming strategy are also studied. Finally, the conclusion is given in Section 4.5, which summarizes the main findings in this Chapter.

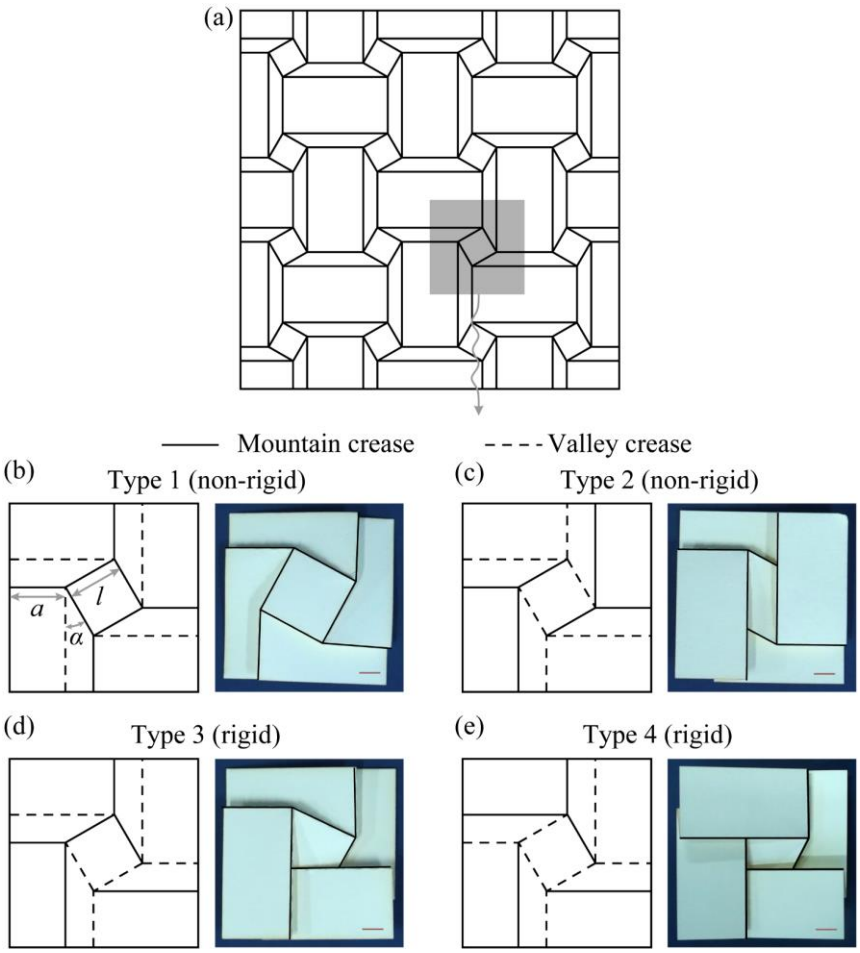

Fig. 4-1 (a) Pattern of a 4×4 metasheet tessellated by square-twist units. Crease mountain-valley assignments of (b) type 1, (c) type 2, (d) type 3, and (e) type 4 square-twist origami units and their folded configurations. (Scale bar: 5mm) The mountain and valley creases are described by solid and dashed lines, respectively.

4.2 Tessellation Rule

4.2.1 Compatible Mountain-valley Assignment

To build the tessellation rule of the metasheets based on the square-twist units, first consider tessellating units with identical geometric parameters, i.e., side lengths l and

a, and twist angle α as shown in Fig. 4-1(b). Here only three types of units, the non-rigid types 1 and 2 and the rigid type 3, are included in the tessellation. The rigid type 4 unit is excluded since it has a similar mechanical response to type 3. When building the tessellation, the three types of units can either be in the form as shown in Fig. 4-1(b-d) or their flip-overs, i.e., units with reversed mountain-valley crease assignments. Note that the flip-overs of type 2 and 3 units are equivalent rotating each of them by 90° and 180°, respectively, whereas the reversed type 1 is not. Hence, the reversed type 1 unit, denoted as type 1R, is treated as an independent building unit in the tessellation. As a result, four building units are shown as enclosed in the upper box of Fig. 4-2. Furthermore, since the units have rotational symmetry, if those in the upper box of Fig. 4-2 are defined as left-handed units, their right-handed counterparts enclosed in the lower box can also be generated. And the left-handed and right-handed versions of the same unit cannot match each other by rotation either. Therefore, a total of eight building units can be derived from the three types of units, named T_i^j (i=1, 1R, 2, 3, and j=L, R for left- and right-handed units).

Having obtained the building units, next the compatibility condition for neighboring units is set up in the flat state. As also seen in Fig. 4-2, each edge of the unit has a long and a short crease perpendicular to and intersecting with it. When two units are connected by a common edge, the two short creases intersecting with the common edge must have the same mountain-valley assignment and be colinear in order to be merged to form a new crease, and so should the two long creases. To visualize the connectivity of the units, a schematic representation is introduced as shown in color in Fig. 4-2. Such schematic representation was first used in a study of origami patterns formed by degree-4 vertices[165]. Each edge of the unit is represented as a colored serrated line. The arrow-shaped protrusions in the left-handed units and the notches in the right-handed ones indicate the position of the pair of long and short creases. In addition, the yellow color is applied when the short crease is a mountain and the long one is a valley, and the green color when the assignment is opposite. Following this schematic representation, the geometrical compatibility condition dictates that units can be joined only when the connecting edges have identical color and complementary serrated shapes.

Utilizing the eight building units and the tessellation rule, the metasheets can be designed like playing a jigsaw puzzle. Start from square metasheets with 2×2 units. It

can be seen in Fig. 4-3(a) that left-handed units must be surrounded by right-handed ones, but the selection of each quarter is not unique. There are four shared edges in the 2×2 tessellation, and each one can be either yellow or green, leading to 16 (2^4) possible combinations (Fig. 4-3(b)). And in each combination, there are two units to choose from for each piece, resulting in 16 (2^4) possible tessellations (Fig. 4-3(b)). Therefore, the number of all possible 2×2 tessellations is 256 ($2^4 \times 2^4$). Excluding those that can be obtained by rotating the others, 136 tessellations are left, which are arranged by the numbers of type 1 and 2 based units in Table 4-1 (details shown in Appendix A). Note that the number of type 3 based units can be worked out by 4 minus the total of the other two types of units. Since a 2×2 tessellation contains four units, the lines in Table 4-1 indicate that the sum of the number of type 1 and 2 based units is more than four. As in the case of creating a single unit, the tessellations fall into two groups which are mirror-symmetric to each other. Another important feature is that all the tessellations share the same crease layout shown in Fig. 4-3(a), and they differentiate from each other only by the mountain-valley assignments. This indicates that all the designs can be obtained using the same pre-creased sheet material, and even transform the metasheet from one design to another by unfolding and refolding. In fact, this feature can be generalized to any *m*×*m* pattern, in which *m* is a positive integer.

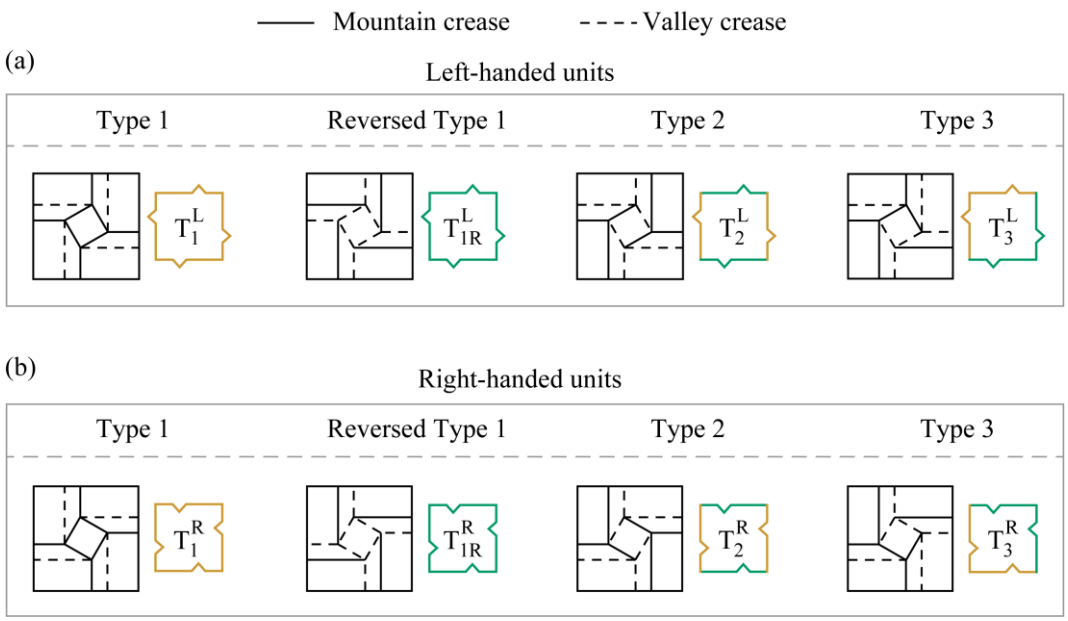

Fig. 4-2 The mountain-valley assignments and jigsaw puzzle representations of (a) left-handed and (b) right-handed type 1, reversed type 1, type 2, and type 3 units.

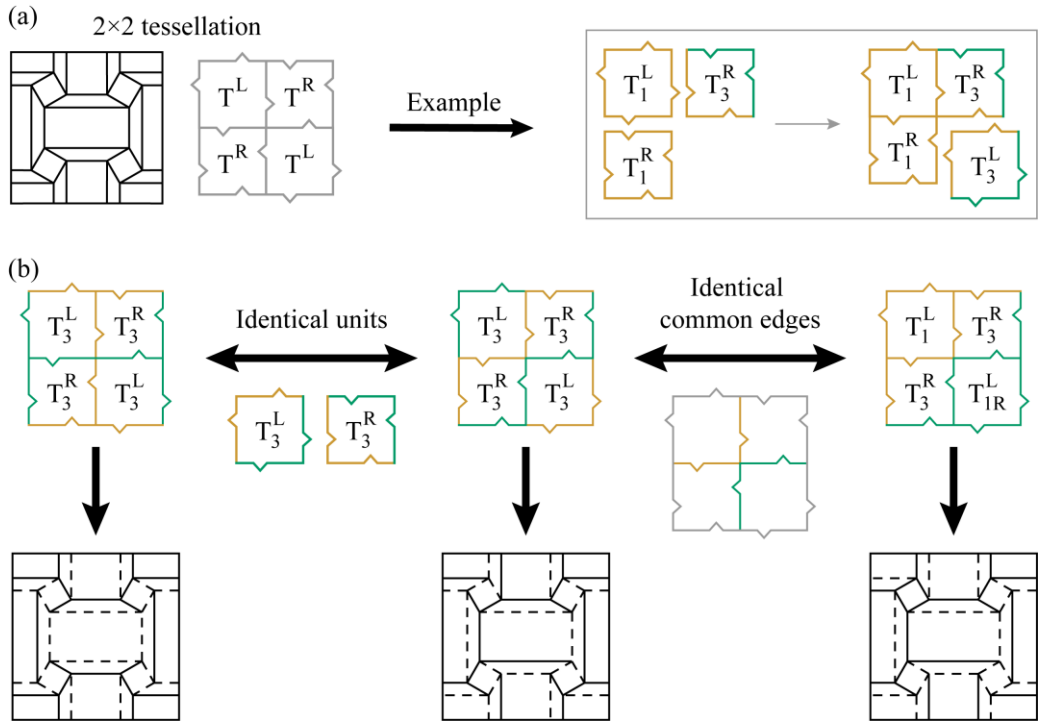

Fig. 4-3 Tessellation rule of the square-twist units with identical geometric parameters. (a) A 2×2 tessellation defined by left- and right-handed units. (b) Different 2×2 tessellations modelled by identical units or identical common edges.

Table 4-1 The number of 2×2 tessellations excluding those obtained by rotating the others.

	0 type 1 unit	1 type 1 unit	2 type 1 units	3 type 1 units	4 type 1 units
0 type 2 unit	10	16	14	4	2
1 type 2 unit	16	24	12	0	—
2 type 2 units	14	12	6	—	—
3 type 2 units	4	0	—	—	—
4 type 2 units	2	—	—	—	—

Starting from 2×2 tessellations, the larger metasheets can be built using either of two methods. A straightforward one is adding one unit at a time based on the established tessellation rule. Alternatively, the 136 2×2 tessellations can be used as second-order building units to create larger tessellations, which is more efficient without missing any design. Theoretically, the number of tessellations increases exponentially with the number of units; $m\times m$ units could produce $2^{m(m+2)}$ square tessellations (details shown in Section 4.2.2). While this enables great diversity in the metasheets, it also makes the

design process quite complicated. From the viewpoint of mechanical property, nevertheless, not all the possibilities are needed in the exploration. This is because the units out of the same type can be treated as identical because flipping over a unit or changing it from left-handed to right-handed does not affect its folding behavior. Therefore, the eight units can be categorized into three groups, the type 1 units including T_1^L, T_1^R, T_{1R}^L and T_{1R}^R, the type 2 units including T_2^L and T_2^R, and the type 3 units including T_3^L and T_3^R, and consider only the number of each group in the study of metasheet mechanical properties. Consequently, only a small fraction of the vast pool of tessellations with varying unit combinations is required to program the properties of the metasheets. For instance, only 15 second-order units are required to design nine 4×4 tessellations with varying proportions of type 1 units from 100% to 0% at an interval of 25%, which are shown in Fig. 4-4. In addition to the tessellations with 0, 4, 8, 12, and 16 type 1 units shown in Fig. 4-4, those with other numbers of type 1 units are shown in Fig. 4-5. It implies that the number of type 1 units can continuously vary from 0 to 16 in a 4×4 tessellation. As in the case of 2×2 tessellations, all patterns shown in Fig. 4-4 and Fig. 4-5 have the same crease layout, though the mountain valley assignments differ, i.e., one crease is mountain in one pattern whereas it may become valley in another.

4.2.2 The Number of Possible *m*×*m* Tessellations

The procedure of calculating the number of possible tessellations for an *m*×*m* metasheet, N_m, is illustrated in Fig. 4-6. When *m* is an odd integer, the procedure is started from one unit as shown in Fig. 4-6(a), which has $N_1=2^3$ possibilities. Extending it to 3×3, the inner unit is surrounded by 8 outer units with 8 common edges (the gray dotted lines) that are located on two rows and two columns, which means a single row or column has 3-1=2 common edges. As demonstrated in Section 4.2.1, each common edge has two options, yellow or green, and therefore the possible combinations of the common edges between the outer units are $2^{4(3-1)}$. When the inner unit is determined, the units that share a common edge with it are also determined. The four units at the corners, which have two common edges with other units, have two selections for each, leading to 2^4 possible combinations. Therefore, the number of possible 3×3 metasheet is $N_3=\left(2^4\cdot 2^{4(3-1)}\right)\cdot N_1$. Using the same approach, the number of possible 5×5 tessellations is $N_5=\left(2^4\cdot 2^{4(5-1)}\right)\cdot N_3$, and that of 7×7 tessellations is

$N_7 = \left(2^4 \cdot 2^{4(7-1)}\right) \cdot N_5$ in Fig. 4-6(a). Thus, the number of possible $m \times m$ square-twist tessellations with an odd m can be given as

$$N_m = \left(2^4 \cdot 2^{4(m-1)}\right) \cdot N_{m-2}. \tag{4-1}$$

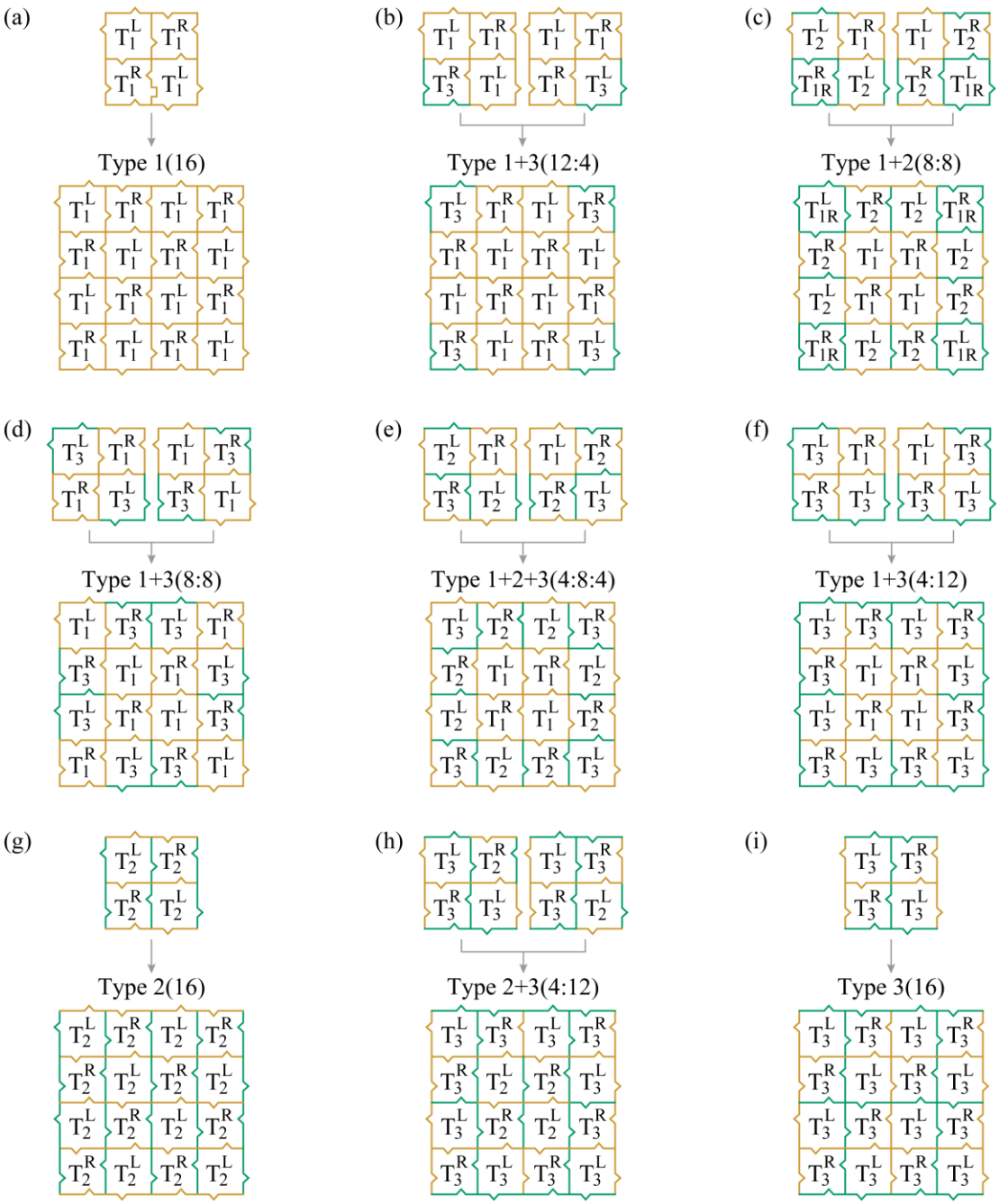

Fig. 4-4 Nine 4×4 tessellations with varying number of type 1 units. (a) 16 type 1 units, (b) 12 type 1 and 4 type 3 units, (c) 8 type 1 and 8 type 2 units, (d) 8 type 1 and 8 type 3 units, (e) 4 type 1, 8 type 2, and 4 type 3 units, (f) 4 type 1 and 12 type 3 units, (g) 16 type 2 units, (h) 4 type 2 and 12 type 3 units, (i) 16 type 3 units.

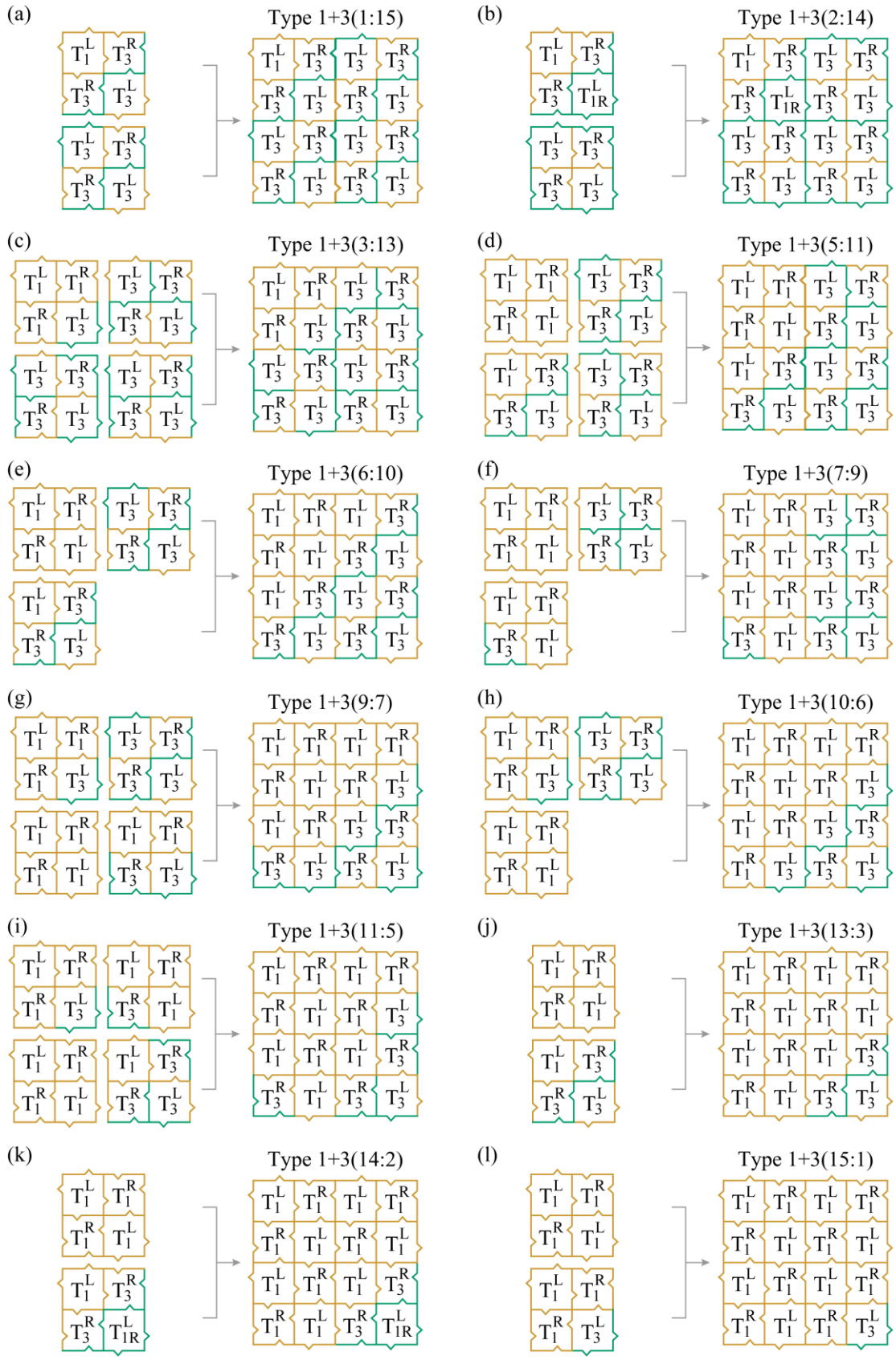

Fig. 4-5 4×4 tessellations with (a) 1, (b) 2, (c) 3, (d) 5, (e) 6, (f) 7, (g) 9, (h) 10, (i) 11, (j) 13, (k) 14, (l) 15 type 1 units that are supplemented by type 3 units.

When m is an even integer, the center is a 2×2 tessellation with $N_2 = 2^4 \cdot 2^{4(2-1)}$ possible combinations as shown in Fig. 4-6(b). Using the same method as for the odd m, the number of possible 4×4 tessellations in Fig. 4-6(b) is determined by the number of inner 2×2 tessellations, the possible combinations of the common edges of the outer units, and the possible combinations of the four corner units, from which $N_4 = \left(2^4 \cdot 2^{4(4-1)}\right) \cdot N_2$ can be obtained. Similarly, the number of possible 6×6 tessellations in Fig. 4-6(b) is $N_6 = \left(2^4 \cdot 2^{4(6-1)}\right) \cdot N_4$. Thus, the number of possible m×m square-twist tessellations with an even m is also given by Eq. (4-1).

For odd m, Eq. (4-1) can be written as

$$\begin{aligned} N_m &= \left(2^4 \cdot 2^{4(m-1)}\right) \cdot N_{m-2} \\ &= \left(2^4 \cdot 2^{4(m-1)}\right) \cdot \left(2^4 \cdot 2^{4((m-2)-1)}\right) \cdot N_{m-4} \\ &\vdots \\ &= \left(2^4 \cdot 2^{4(m-1)}\right) \cdot \left(2^4 \cdot 2^{4((m-2)-1)}\right) \cdots \left(2^4 \cdot 2^{4(3-1)}\right) \cdot 2^3 \end{aligned} \tag{4-2}$$

Substituting m=2q-1 (q=1, 2, 3, ...) to Eq. (4-2), it can be simplified as

$$\begin{aligned} N_m &= \left(2^4 \cdot 2^{4((2q-1)-1)}\right) \cdot \left(2^4 \cdot 2^{4((2(q-1)-1)-1)}\right) \cdots \left(2^4 \cdot 2^{4(3-1)}\right) \cdot 2^3 \\ &= 2^{4(q-1)} \cdot 2^{4\sum_{g=1}^{q}(2g-1)-1} \cdot 2^3 \\ &= 2^{4q-1+4q(q-1)} \\ &= 2^{2(m+1)-1+2(m+1)\left(\frac{m+1}{2}-1\right)} \\ &= 2^{m(m+2)} \end{aligned} \tag{4-3}$$

For even m, Eq. (4-1) can be written as

$$\begin{aligned} N_m &= \left(2^4 \cdot 2^{4(m-1)}\right) \cdot N_{m-2} \\ &= \left(2^4 \cdot 2^{4(m-1)}\right) \cdot \left(2^4 \cdot 2^{4((m-2)-1)}\right) \cdot N_{m-4} \\ &\vdots \\ &= \left(2^4 \cdot 2^{4(m-1)}\right) \cdot \left(2^4 \cdot 2^{4((m-2)-1)}\right) \cdots \left(2^4 \cdot 2^{4(4-1)}\right) \cdot \left(2^4 \cdot 2^{4(2-1)}\right) \end{aligned} \tag{4-4}$$

Substituting m=2q (q=1, 2, 3, ...) to Eq. (4-4), it can be simplified as

$$\begin{aligned} N_m &= \left(2^4 \cdot 2^{4(2q-1)}\right) \cdot \left(2^4 \cdot 2^{4((2(q-1))-1)}\right) \cdots \left(2^4 \cdot 2^{4(4-1)}\right) \cdot \left(2^4 \cdot 2^{4(2-1)}\right) \\ &= 2^{4q} \cdot 2^{4\sum_{g=1}^{q}(2g-1)} \\ &= 2^{4q} \cdot 2^{4 \cdot \frac{(1+(2q-1))q}{2}} \\ &= 2^{2q(2q+2)} \\ &= 2^{m(m+2)} \end{aligned} \tag{4-5}$$

Comparing Eq. (4-3) and (4-5), it can be concluded that the number of possible $m\times m$ square-twist tessellations designed by the method presented in this paper is $2^{m(m+2)}$ for an arbitrary m. Finally, it should be mentioned that some tessellations obtained this way may match others by rotating a certain angle, but they are not excluded from the calculation of the total number of possible tessellations.

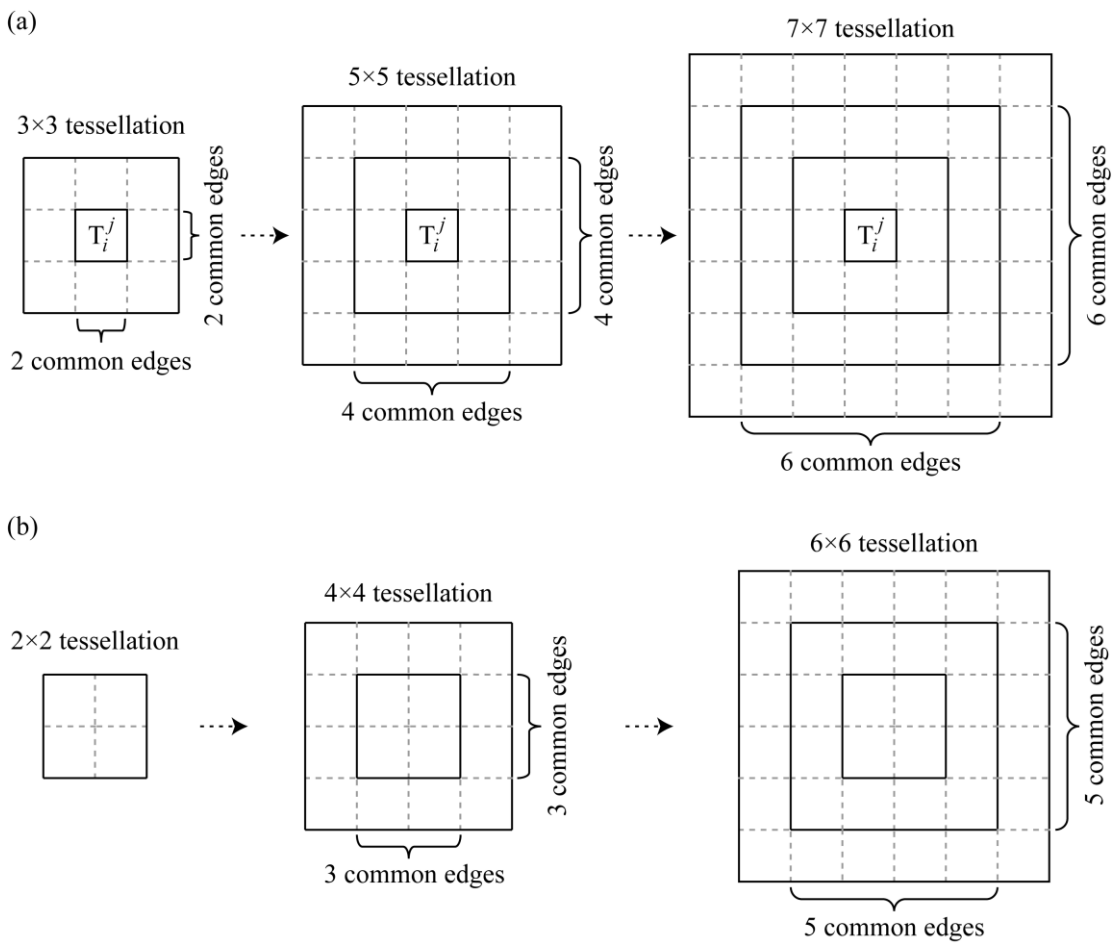

Fig. 4-6 Illustrations of calculating the number of possible $m\times m$ tessellations for (a) an odd m and (b) an even m.

4.2.3 Compatible Geometric Parameters

In addition to tessellating units with identical geometric parameters, it is also possible to introduce geometric gradients in a tessellation. Still consider a 2×2 tessellation as an instance. In the general case, all the four units can have different side lengths l_i and twist angles α_i (i=1, 2, 3, 4). To satisfy compatibility conditions on the

common edges, the geometric parameters of the units in Fig. 4-7 should satisfy the following equations

$$\begin{aligned}
&l_1 \cdot \sin\alpha_1 = l_2 \cdot \sin\alpha_2 = l_3 \cdot \sin\alpha_3 = l_4 \cdot \sin\alpha_4, \\
&a_1^1 = a_3^1, a_1^3 + l_1 \cdot \cos\alpha_1 = a_3^3 + l_3 \cdot \cos\alpha_3, \\
&a_1^2 = a_2^2, a_1^4 + l_1 \cdot \cos\alpha_1 = a_2^4 + l_2 \cdot \cos\alpha_2, \\
&a_2^3 = a_4^3, a_2^1 + l_2 \cdot \cos\alpha_2 = a_4^1 + l_4 \cdot \cos\alpha_4, \\
&a_3^4 = a_4^4, a_3^2 + l_3 \cdot \cos\alpha_3 = a_4^2 + l_4 \cdot \cos\alpha_4,
\end{aligned} \tag{4-6}$$

It is important to note that in the graded tessellation, the four side lengths a_i^1, a_i^2, a_i^3, a_i^4 (i=1, 2, 3, 4) in a unit are no longer identical, and they have to be defined individually. Metasheets with more units can be designed following the same principle.

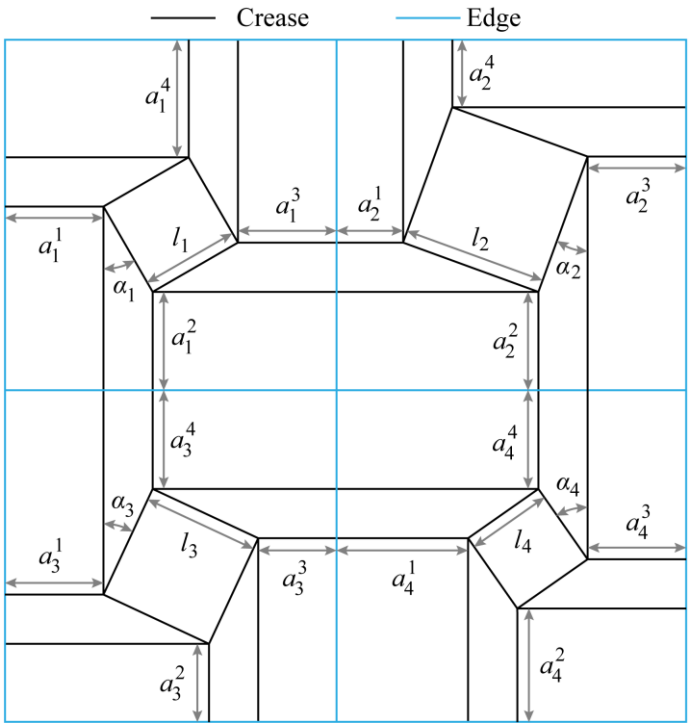

Fig. 4-7 A 2×2 tessellation with geometric gradients.

4.3 Mechanical Properties of Tessellated Metasheets

4.3.1 Fabrication and Experiment

To investigate the mechanical properties of the metasheets, physical specimens of the nine 4×4 designs with different unit combinations, as shown in Fig. 4-4, were

fabricated and tested. The geometric parameters were set as l=a=16.25mm and α=30º. The specimens were fabricated from a 0.4mm-thick PET sheet. The creases were cut as 0.8mm×3mm perforations at 1.5mm intervals and holes were cut at the vertices to mitigate stress concentration and fracture, shown in Fig. 4-8(a), using a Trotec Speedy 300 laser cutting machine and then manually folded to their fully folded states.

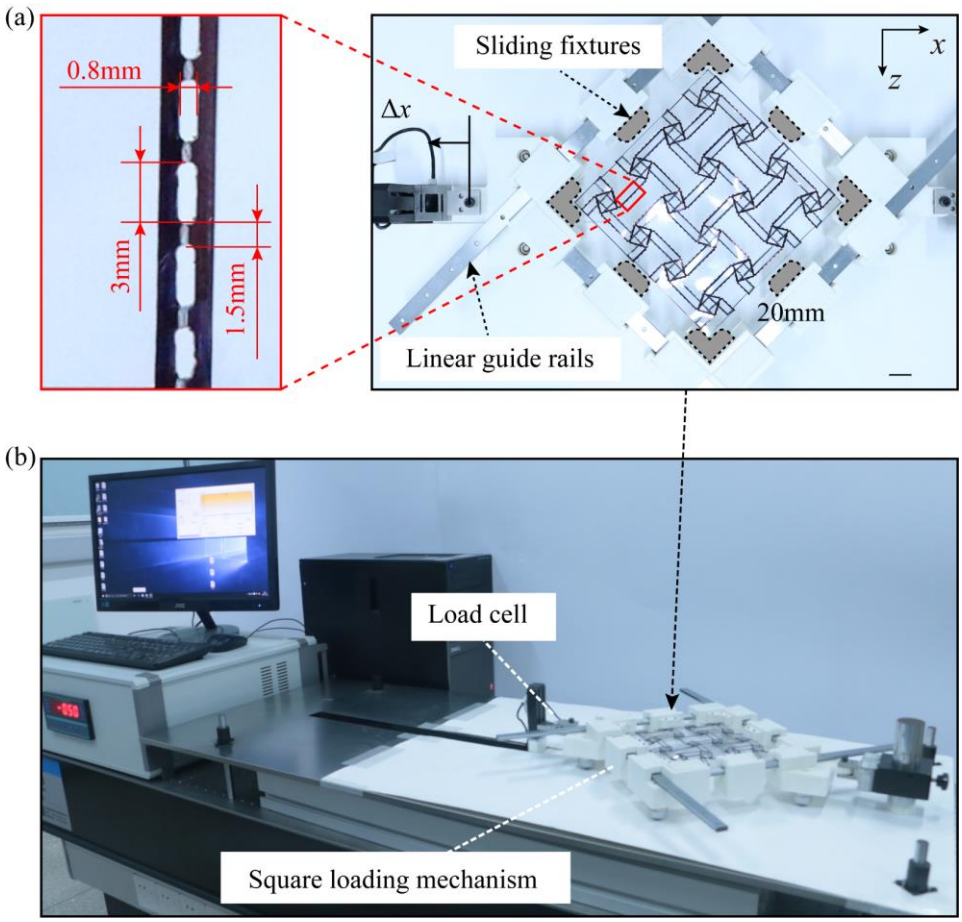

Fig. 4-8 Tension experiment of the metasheets. (a) Crease design of the specimen and square loading mechanism. (b) Experimental setup.

Quasi-static tension experiments were conducted on the specimens with the same horizontal testing machine in Section 2.2. The machine had a stroke of 800mm and a load cell of 300N. To achieve a uniform deformation, a square loading mechanism composed of four linear guide rails and eight sliding fixtures was designed to load the specimen at four corners and four middle points of the sides as shown in Fig. 4-8(b). For eliminating dynamic effects, the specimen was stretched at a loading rate of 0.2mm/s until the diagonal length reached 306mm. The entire deformation process of

the specimen and the force versus displacement curve were recorded using the same method in Section 2.2. In addition, three key mechanical properties of the unit, the energy, U, initial peak force, F_{max}, and maximum stiffness, K_{max}, were also calculated from the curve. The energy was defined as the work done by the force during the loading process, and the maximum stiffness was the largest tangent slope of the force versus displacement curve prior to the initial peak as mentioned in Chapter 3. To obtain reliable results, three specimens were tested for each design.

4.3.2 Mechanical Properties of Used Units in the Metasheet

Before researching the metasheets, the three types of units were also characterized experimentally following the methods provided in Chapter 2 and 3. The unit samples adopted the same geometric parameters and fabrication process as the metasheets. The facet bending stiffness and crease rotational stiffness of the units were determined as k_f=0.70N·rad^{-1} and k_c=0.44N·rad^{-1}, and the yield rotation angle $\Delta\varphi_y$=22.92º. The experimental normalized force, F/k_f, versus normalized displacement, $\Delta x/\Delta x_{max}$, curves of the three units are drawn in Fig. 4-9(a), and the normalized energy, $U/(k_f l)$, initial peak force, F_{max}/k_f, and maximum stiffness, $K_{max}l/k_f$, are presented in Fig. 4-9(b-d).

For each curve in Fig. 4-9(a), the solid line is the averaged result of three tests, and the shaded band is the standard deviation. The natural dihedral angles formed by the square and trapezoidal facets of type 1, 2, and 3 units are experimentally obtained as 19.58°, 25.20°, and 28.30°. It can be seen that all the three properties of the type 1 unit are remarkably larger than those of type 2 and 3 units. Moreover, the three properties of the type 1 unit are predicted using the empirical formulas in Chapter 3, and those of the types 2 and 3 units using the theoretical formulas in Chapter 2. As shown in Fig. 4-9(b-d), these predictions match reasonably well with the experimental data, which will later be utilized to program the properties of the metasheets.

4.3.3 Mechanical Properties of Uniform Metasheets

The deformation processes and normalized force, F/k_f, versus normalized displacement, $\Delta x/\Delta x_{max}$, curves of the three metasheets composed of a single type of units are presented in Fig. 4-10(a-c). First, the performance of the one formed by the rigid type 3 units is investigated. It can be seen from Fig. 4-10(a) that a simultaneous unfolding of all the units is obtained, leading to a slowly rising force followed by a long

plateau. Similarly, the metasheet comprising solely of the non-rigid type 2 units shows a synchronized unfolding process among the units which is shown in Fig. 4-10(b). As result, a smooth force curve as in the case of a single type 2 unit is also generated.

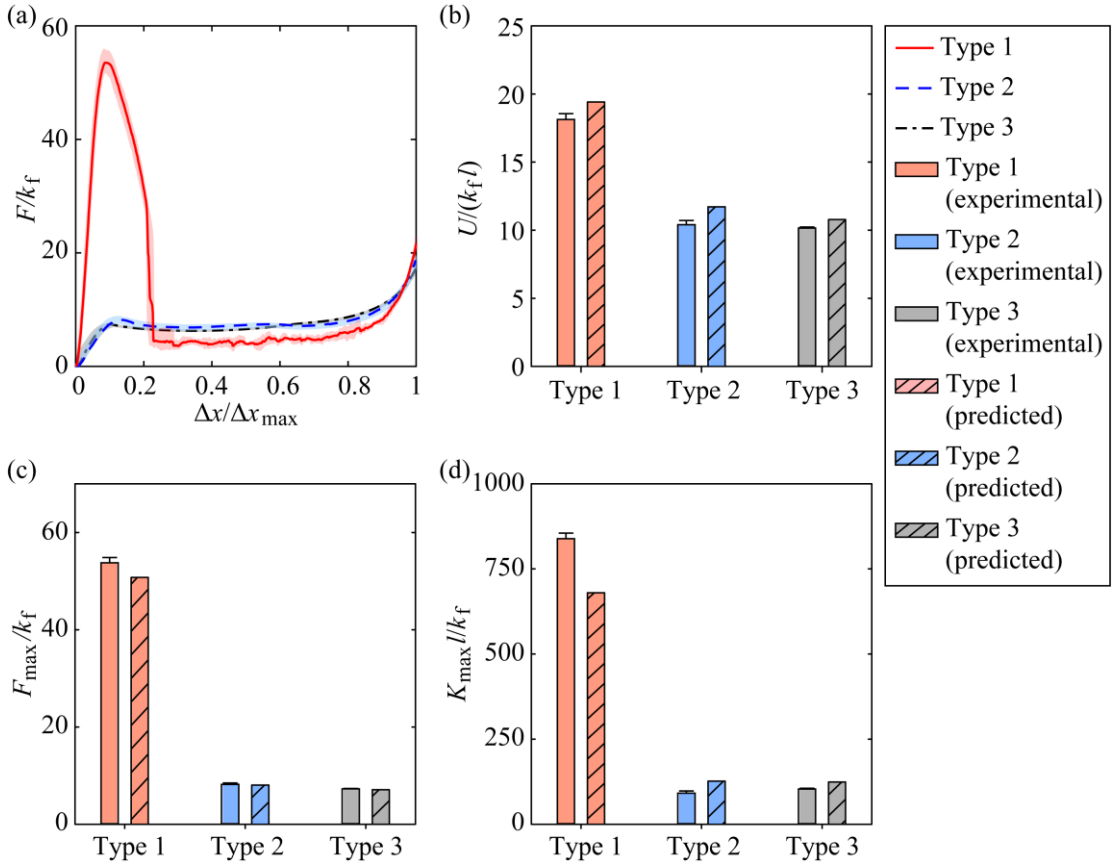

Fig. 4-9 Mechanical properties of the three types of units. (a) The normalized force, F/k_f, vs. displacement, $\Delta x/\Delta x_{max}$, curves. The experimental and predicted normalized (b) energy, $U/(k_f l)$, (c) initial peak force, F_{max}/k_f, and (d) maximum stiffness, $K_{max}l/k_f$.

Subsequently, the metasheet formed by sixteen type 1 units is examined, as shown in Fig. 4-10(c). Overall, the metasheet still demonstrates a response similar to that of the individual unit in Fig. 4-9(a), which is characterized by a high initial peak force and a sharp force drop due to unlocking of the units, followed by a short plateau mainly contributed by rotation of the creases. Nevertheless, the units show a noticeable trend of sequential rather than synchronized deformation. To explain this in detail, the units are classified into four groups based on their locations in the tessellation. $T_{1\text{-i}}$ units are in the four corners enclosed in the purple boxes, which have two edges joined with surrounding units and two free edges. $T_{1\text{-ii}}$ units are on the top and bottom sides of the

metasheet enclosed in the yellow boxes, which have three edges joined with those of the neighboring units and are loaded at the long side of the rectangular facets. $T_{1\text{-iii}}$ units are on the left and right sides enclosed in the blue boxes, which also have three edges joined with neighboring units but are loaded at the short side of the rectangular facets. And $T_{1\text{-iv}}$ units are in the middle enclosed in the red box, which is characterized by four common edges with neighboring units.

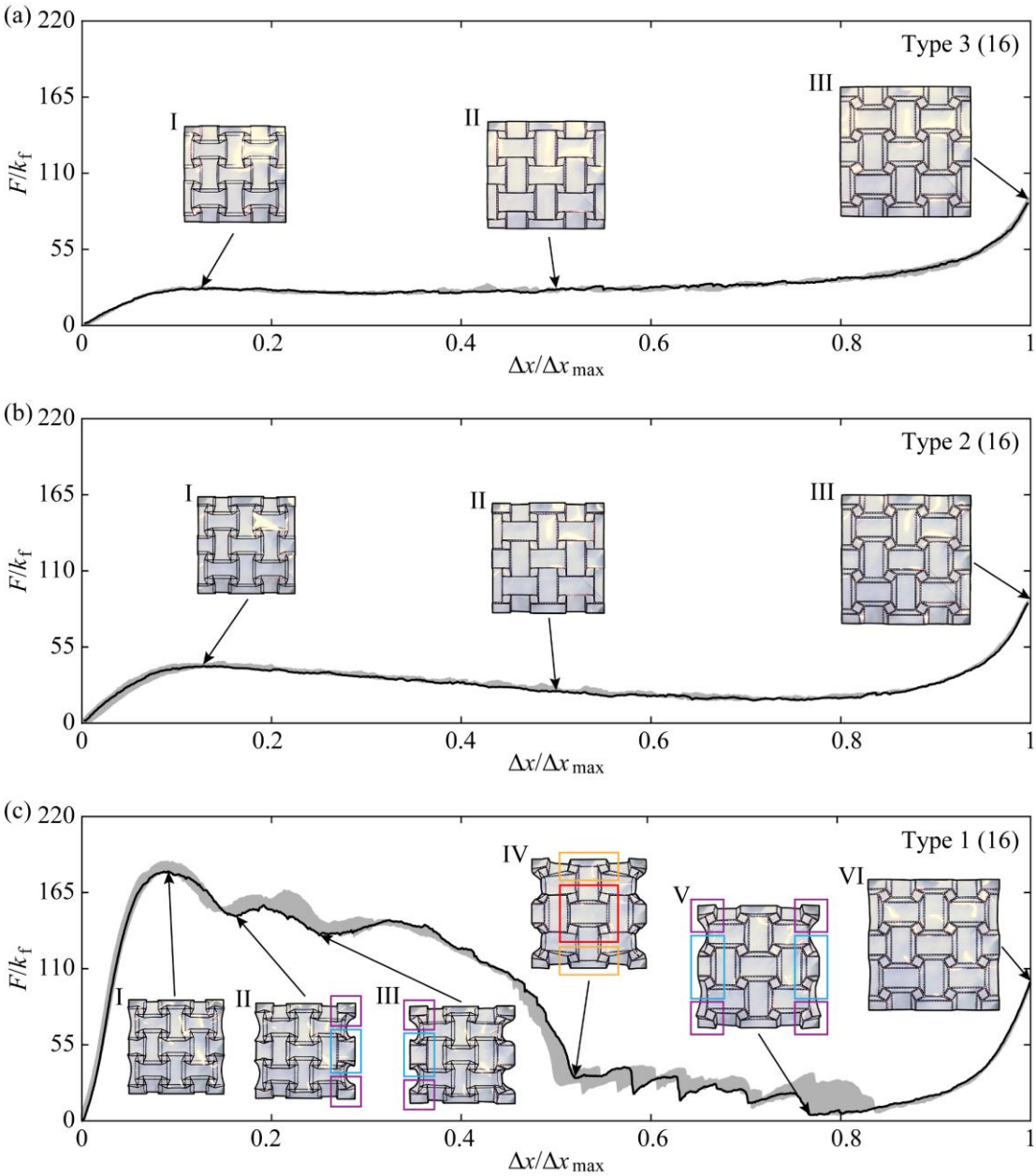

Fig. 4-10 Deformation processes and mechanical properties of the uniform metasheets. The normalized force vs. displacement curves and key configurations of the uniform metasheets composed solely of (a) type 3, (b) type 2, and (c) type 1 units, respectively.

The deformation of the 4×4 type 1 metasheet can be divided into five stages, see Fig. 4-10(c). At stage 1 from beginning to configuration I, all the units are stretched simultaneously until the force reaches its initial peak. Subsequently, at stage 2 between configurations I and III, the long rectangle facets formed by the neighboring $T_{1\text{-i}}$ and $T_{1\text{-iii}}$ units on the left and right sides of the metasheet, start to bend inward (configurations II and III), leading to a slight drop in force. Notice that the rectangular facets on the right side bend slightly ahead of those on the left side, probably due to the small geometric imperfection during fabrication. At this stage, all the units are still locked. Upon further loading, the metasheet enters stage 3 bounded by configurations III and IV, where the eight $T_{1\text{-ii}}$ and $T_{1\text{-iv}}$ units first open up (configuration IV), corresponding to another small peak followed by a sharp drop in force. Afterward at stage 4 between configurations IV and V, the eight $T_{1\text{-i}}$ and $T_{1\text{-iii}}$ units (configuration V) pop open, and the force is further reduced. Finally, all the unlocked units are further stretched to flat at stage 5 bounded by configurations V and VI, and the force rises again.

4.3.4 Mechanical Properties of Mixed Metasheets

Having studied the performance of uniform metasheets, I examine the behavior of those formed by a mixture of different units in this section. First consider the design with twelve type 1 and four type 3 units in the corners as shown in Fig. 4-4(b). It can be seen from Fig. 4-11(a) that a sequential deformation process similar to that of the uniform one with type 1 units is generated. After the initial uniform deformation, the rectangular facets on the left and right sides bend inward, then the eight $T_{1\text{-ii}}$ and $T_{1\text{-iv}}$ units open up, followed by the four $T_{1\text{-iii}}$ units. In addition, the type 1 units from the same groups as those in the uniform metasheet also tend to deform in the same manner, implying that the behavior of the type 1 unit is mainly determined by the location in the metasheet or boundary condition. The type 3 units, on the other hand, are roughly unfolded continuously. Due to the similar deformation process, the force curve is also close in shape to that of the uniform one, but the magnitude is reduced because of the presence of four type 3 units. For a metasheet of the design shown in Fig. 4-4(d), where the number of type 1 units is further reduced to eight while the number type 3 units becomes eight, Fig. 4-11(b) shows its deformation process. The four $T_{1\text{-i}}$ units at the corners, which have fewer constrained edges, pop open in advance of the four $T_{1\text{-iv}}$ units in the middle, leading to two comparable local peaks on the force curves. A small local

peak force occurs between configurations I and II because the four $T_{1\text{-}i}$ units do not open simultaneously. Besides, inward bending of the long rectangular facets is no longer evident. For a metasheet consisting of only four type 1 units in the middle surrounded by twelve type 3 units, whose design is given by Fig. 4-4(f), the type 1 units tend to pop open at the same time, leading to a force curve similar to that of a single type 1 unit as shown in Fig. 4-11(c).

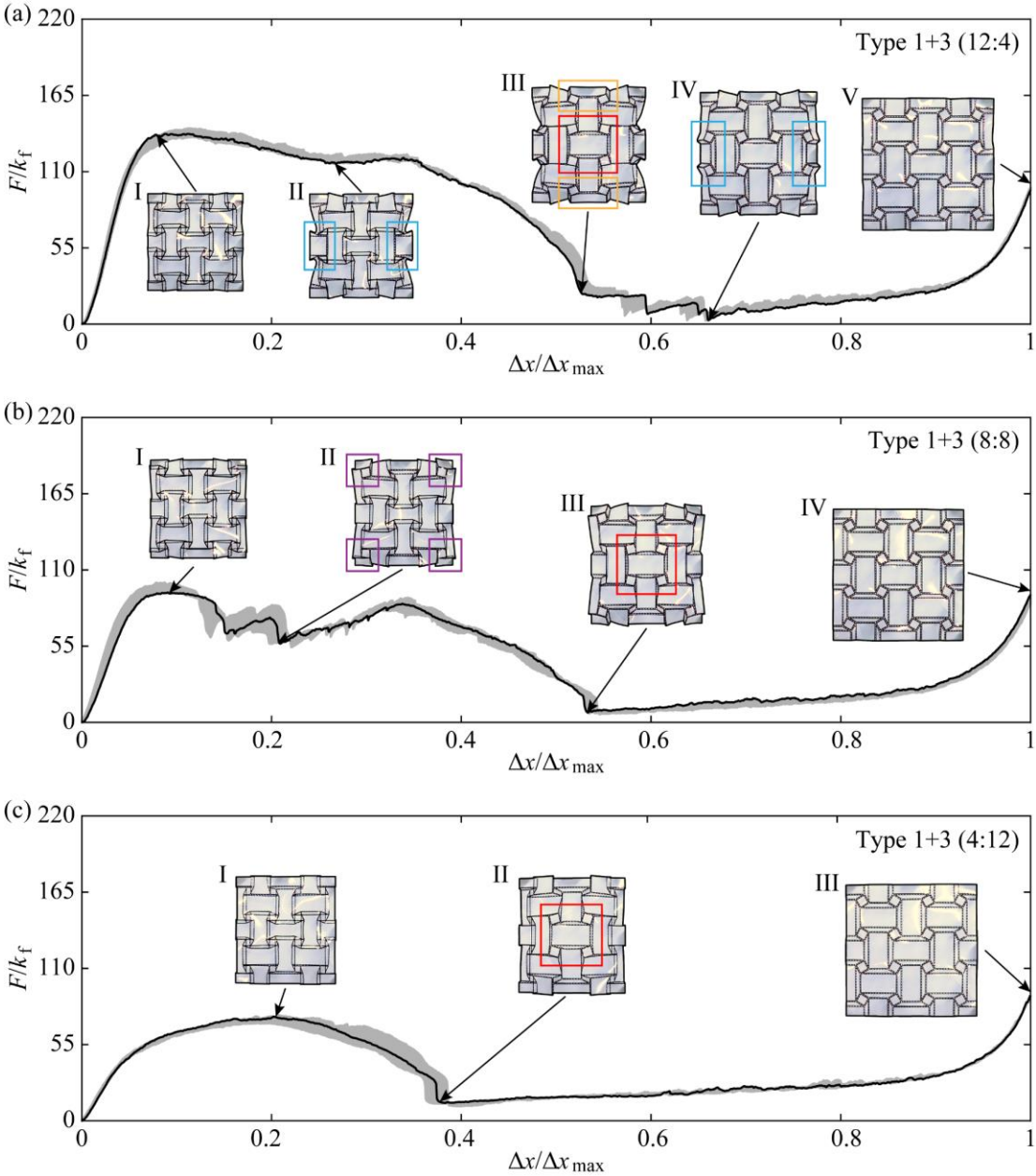

Fig. 4-11 Deformation processes and mechanical properties of the mixed metasheets. The normalized force vs. displacement curves and key configurations of the mixed metasheets consisting of (a) twelve, (b) eight, and (c) four type 1 units that are supplemented by type 3 units.

4.4 Programmability and Prediction of Tessellated Metasheets

4.4.1 Predicted Properties

Before predicting the energy, initial peak force, and maximum stiffness of the metasheets, a relationship between the prediction of units and metasheets is established using the example of a 4×4 metasheet. First, the predicted energy of the metasheet, $U_{4\times4}$, is the simple summation of unit energy, U_{t}^{i} (i=1, 2, …, 16 represents the i-th unit), which is expressed as

$$U_{4\times4} = \sum_{i=1}^{16} U_{\mathrm{t}}^{i} . \tag{4-7}$$

Second, the force is the derivative of energy versus displacement, which is given by

$$F_{4\times4} = \frac{dU_{4\times4}}{dD_{4\times4}} . \tag{4-8}$$

As shown in Fig. 4-8, the 4×4 metasheet specimen shows that only four units lay in the loading direction (diagonal of the metasheet). In the experiment, the square loading mechanism introduces identical unfolded deformation to each unit. Thus, the displacement of the 4×4 metasheet is calculated by $D_{4\times4} = 4 \cdot D_{\mathrm{t}}$, where D_{t} is that of the unit. Then, equation (4-8) can be rewritten as

$$F_{4\times4} = \frac{d\sum_{i=1}^{16} U_{\mathrm{t}}^{i}}{4 \cdot dD_{\mathrm{t}}} = \frac{1}{4} \cdot \sum_{i=1}^{16} F_{\mathrm{t}}^{i} , \tag{4-9}$$

where F_{t}^{i} is the external force of the i-th unit. Finally, the stiffness is the derivative of force versus displacement, which is expressed as

$$K_{4\times4} = \frac{dF_{4\times4}}{dD_{4\times4}} = \frac{\frac{1}{4} \cdot d\sum_{i=1}^{16} F_{\mathrm{t}}^{i}}{4 \cdot dD_{\mathrm{t}}} = \frac{d\sum_{i=1}^{16} F_{\mathrm{t}}^{i}}{16 \cdot dD_{\mathrm{t}}} = \frac{1}{16} \cdot \sum_{i=1}^{16} K_{\mathrm{t}}^{i} , \tag{4-10}$$

where K_{t}^{i} is the stiffness of the i-th unit. With the predicted unit behaviors in Fig. 4-9(b-d), the bar charts in Fig. 4-12 compare the experimental and predicted results of the three uniform and six mixed metasheets illustrated in Fig. 4-4.

In the predicted models, the natural dihedral angles formed by the square and trapezoidal facets of type 1, 2, and 3 units used in the prediction are experimentally obtained as 19.58°, 20.50°, and 24.30°. It can be seen that in general a reasonably good match between the experimental data and predictions is achieved. For the one composed of type 1 units, the predictions tend to underestimate the energy. This is mainly caused

by the extra bending of the rectangular facets on the left and right sides which is not observed at the unit level. Thus, it can be safely concluded that the properties of the metasheets can be well predicted by the unit results.

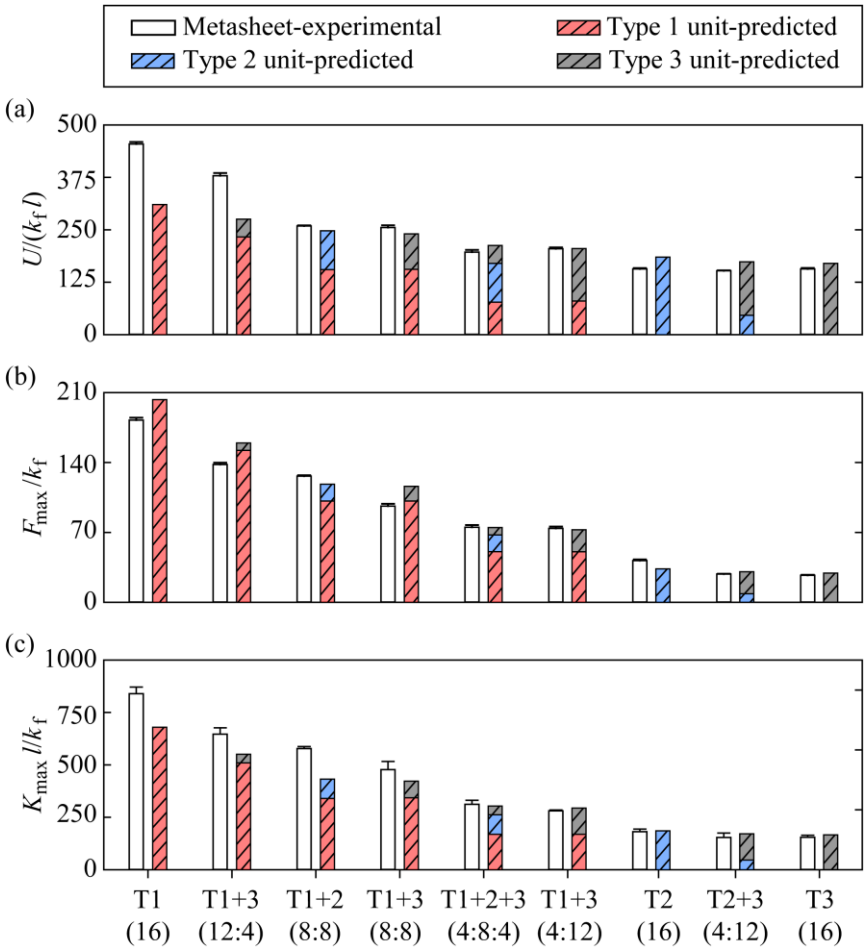

Fig. 4-12 Comparison of (a) normalized energy, (b) initial peak force, and (c) maximum stiffness between the experimental results and predictions.

4.4.2 Programmable Properties

Having demonstrated that the energy, initial peak force, and maximum stiffness of the metasheets can be obtained by adding up the corresponding unit properties that are predictable theoretically or empirically, I can now program the material properties of the metasheets through a coarse stepped tuning by the proportions of different units and fine continuous tuning by geometric and material parameters. To demonstrate this, consider a series of 4×4 metasheets composed of type 1 and type 3 units, which have

identical geometric and material parameters as those in Sections 4.3. The number of type 1 units that play a major role in determining the properties changes from 0 to 16, where some of the possible patterns are shown in Fig. 4-4 and Fig. 4-5. Figure 4-13 shows the variation of normalized energy, initial peak force, and maximum stiffness of the metasheets. As expected, all three properties increase linearly with the number of type 1 units in a stepped manner. Additionally, since all these 4×4 metasheets can be fabricated out of the same crease layout, as proven in Section 4.3.1, the metasheets can be even reprogrammed in response to specific needs, i.e., it is first folded to the design with only type 3 units to achieve a low force, and then unfolded and refolded to the design with only type 1 units to obtain a high initial peak. A similar reprogramming/reconfiguring strategy has been used at the unit level to design frequency reconfigurable antennas[154]. But with the proposed tessellation designs, the variety and tunable range can be greatly expanded.

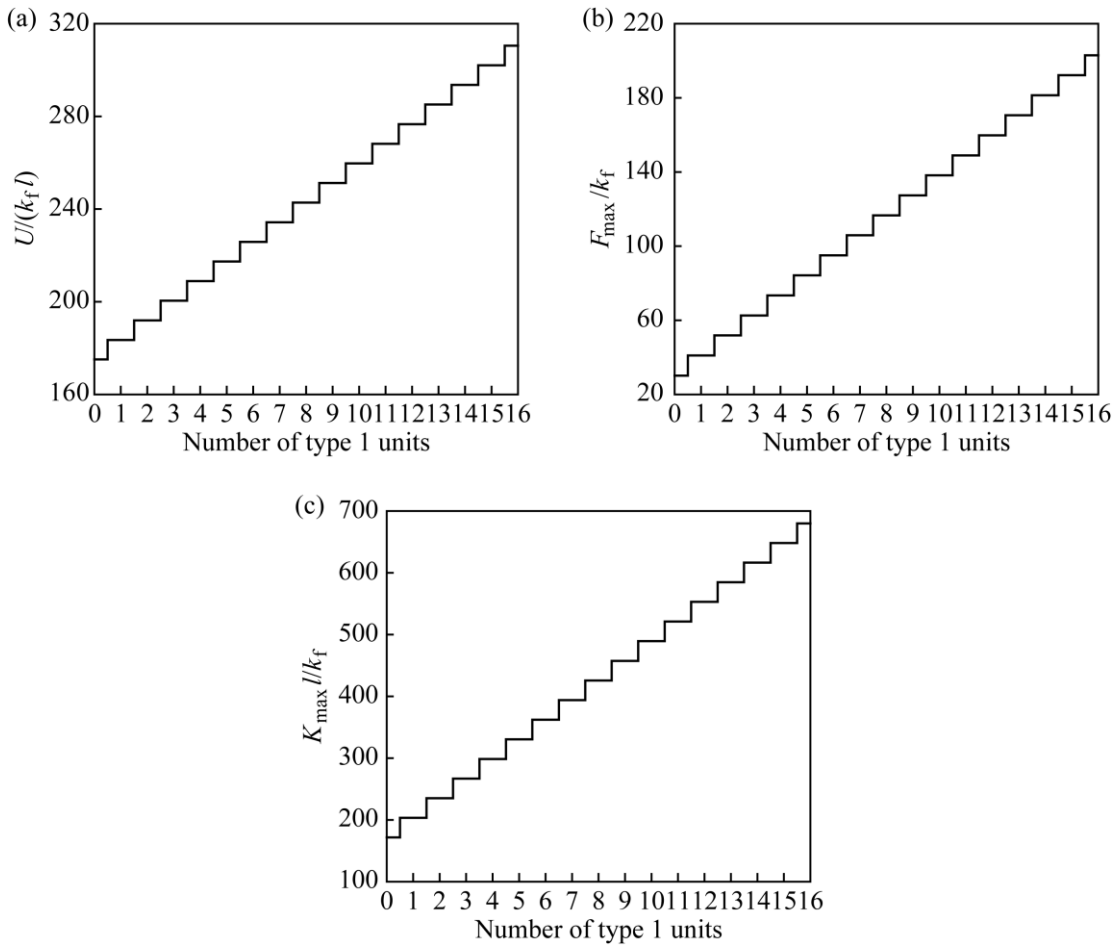

Fig. 4-13 Programmability of the normalized (a) energy, (b) initial peak force, and (c) maximum stiffness of 4×4 metasheets with varying numbers of type 1 units from 0 to 16.

By further incorporating unit geometric and material properties, continuous fine-tuning over a wide bandwidth can be achieved. The geometric parameters discussed in this section contain the side lengths ratio, a/l, and the twist angle, α. The effects of a/l in combination with the number of type 1 units in the 4×4 metasheets are first presented in Fig. 4-14(a), (c), and (e). It can be seen that within the range of 0.5 to 4, a/l tends to increase all three mechanical properties, regardless of the number of type 1 units. Moreover, any value between the two adjacent steps in Fig. 4-13 can be obtained by selecting a/l appropriately. It can be obtained from Fig. 4-13(a) that the normalized energy $U/(k_f l)$ is 223.60 when there are 8 type 1 units in the metasheet and becomes 234.44 when there are 9. If a $U/(k_f l)$=229.00, which is the average of the previous two, is wanted to be obtained, the solution can be given by keeping 8 type 1 units and increasing a/l from 1 to 1.06, or preserving the number of type 1 units as 9 and reducing a/l from 1 to 0.94.

The effect of the other geometrical parameter, α, is presented in Fig. 4-14(b), (d), and (f) where α changes from 20° to 45°. Similar to a/l, an increase in the twist angle leads to improvement of all three properties. However, the effect of increasing type 1 units on the initial peak force and maximum stiffness is prominent only when α is relatively large beyond about 30°. This is because when α is small, the unit is less twisted, leading to sharply reduced initial peak force and maximum stiffness for the type 1 unit.

Finally, the effect of varying k_c/k_f, the ratio of crease-rotation stiffness to facet-bending stiffness, between 0.25 and 0.75 is presented in Fig. 4-15. Changing k_c/k_f primarily alters the total energy of the metamaterial, and is less effective on tuning either initial peak force or maximum stiffness. And again this parameter can be used to obtain any value between the two neighboring steps in Fig. 4-13 as in the case of a/l and α.

Notice that in the discussion here, all the units in a metasheet have identical geometry and stiffness. Using unit types, design parameters, or a combination of both, the properties of the metasheet can be tailored to meet specific requirements. For example, to design an impact energy absorption device, which requires a low initial peak force but high energy absorption, the number of type 1 units should be lowered because it leads to a high peak, while large values of a/l, α, and k_c/k_f should be selected to maximize the energy absorption.

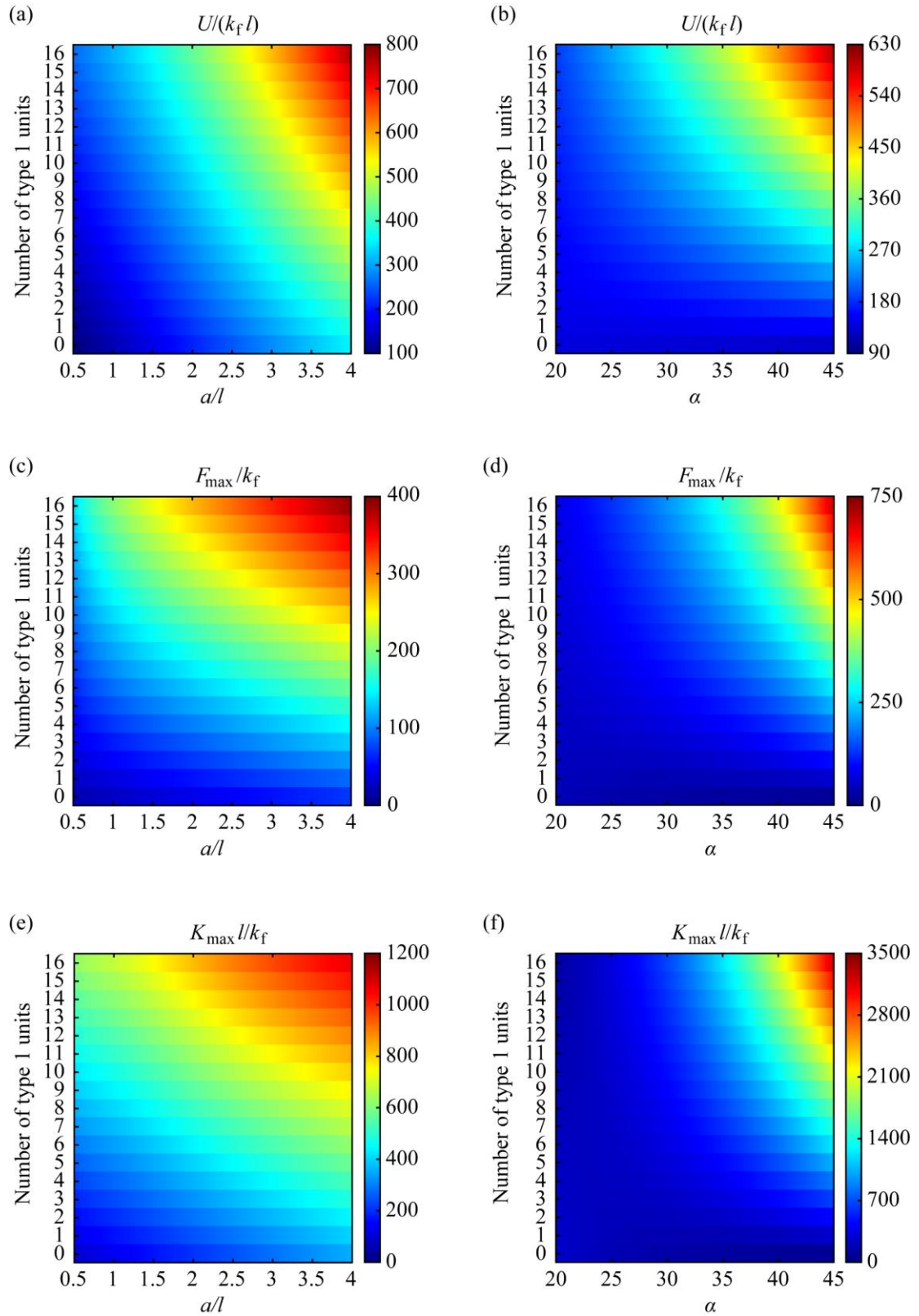

Fig. 4-14 Programmability of the normalized energy, initial peak force, and maximum stiffness of 4×4 metasheets with varying geometric parameters. Specifically, in (a, c, and e) a/l varies from 0.5 to 4, while α=30º, k_c/k_f=0.63, in (b, d, and f) α varies 20° to 45°, while a/l=1, k_c/k_f=0.63.

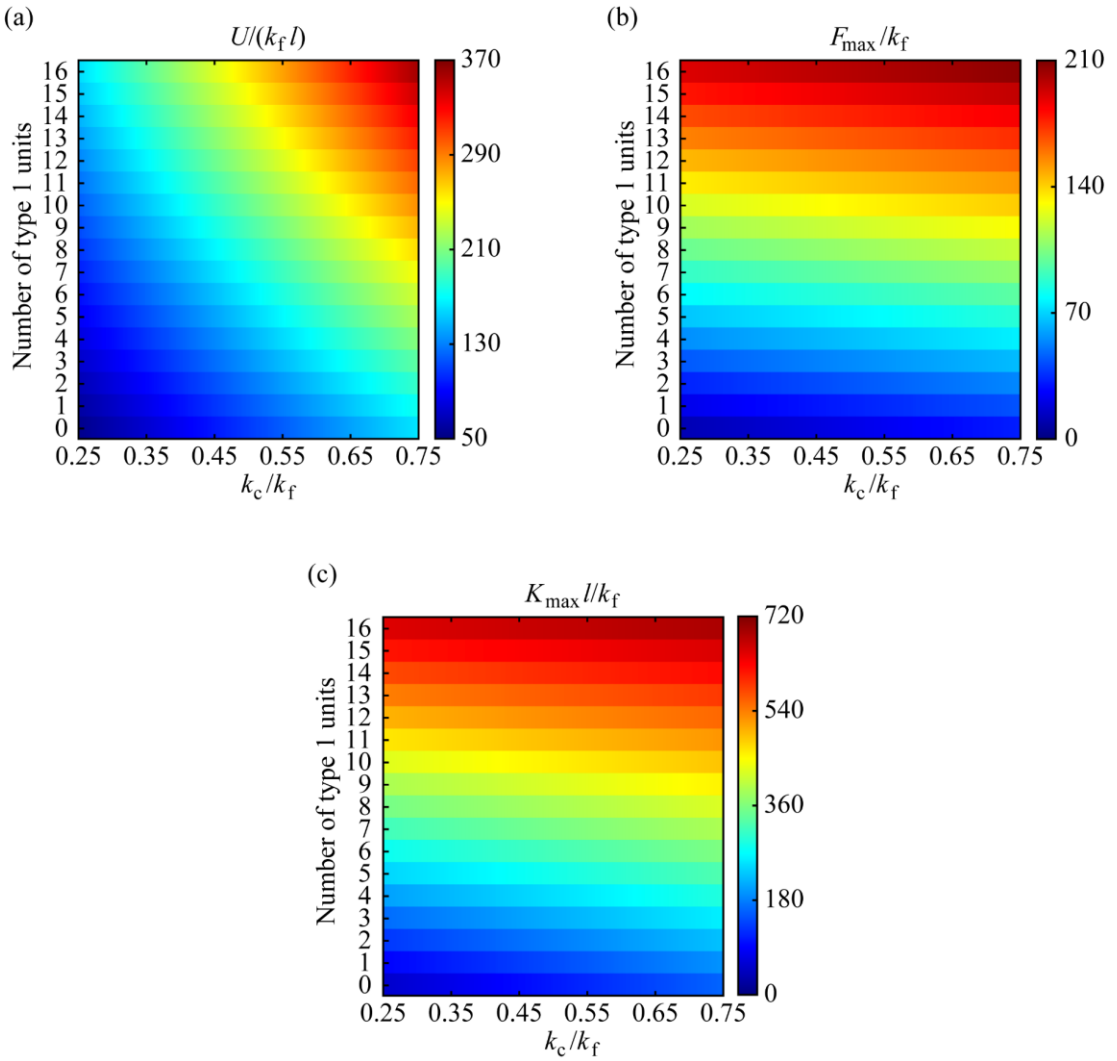

Fig. 4-15 Programmability of the normalized energy, initial peak force, and maximum stiffness of the metasheets with k_c/k_f varying from 0.25 to 0.75, while a/l=1, α=30º.

4.4.3 Graded Property

Unit grading can also be introduced to further enhance the performance of a metasheet. In certain engineering applications, e.g., non-lethal projectiles for peacekeeping operations, a graded stiffness could enhance the functionality of the structures or materials[166]. By purposely introducing a geometric gradient in a metasheet, a sequential deformation mode and a graded response can be engineered. To demonstrate this, a graded 4×4 metasheet with type 1 units as shown in Fig. 4-16(a) was designed, fabricated, and tested following the procedure in Section 4.3. It can be seen from Fig. 4-16(b) that the eight units along the left and right sides, which have a

smaller twist angle and correspondingly a lower initial peak force, first open up, followed by the eight middle ones with a larger twist angle. As a result, a graded force with two consecutive local peaks is obtained. More local peaks can be triggered by increasing the number of units, and the position and magnitude of each peak can be programmed based on the properties of the units.

Table 4-2 The parameters of the graded 4×4 metasheet in Fig. 4-16.

Location of unit	α [deg]	l [mm]	a_1 [mm]	a_2 [mm]	a_3 [mm]	a_4 [mm]
Middle columns	40	13.15	20	20	24.02	28.05
Left and right sides	25	20	24.03	20	20	20

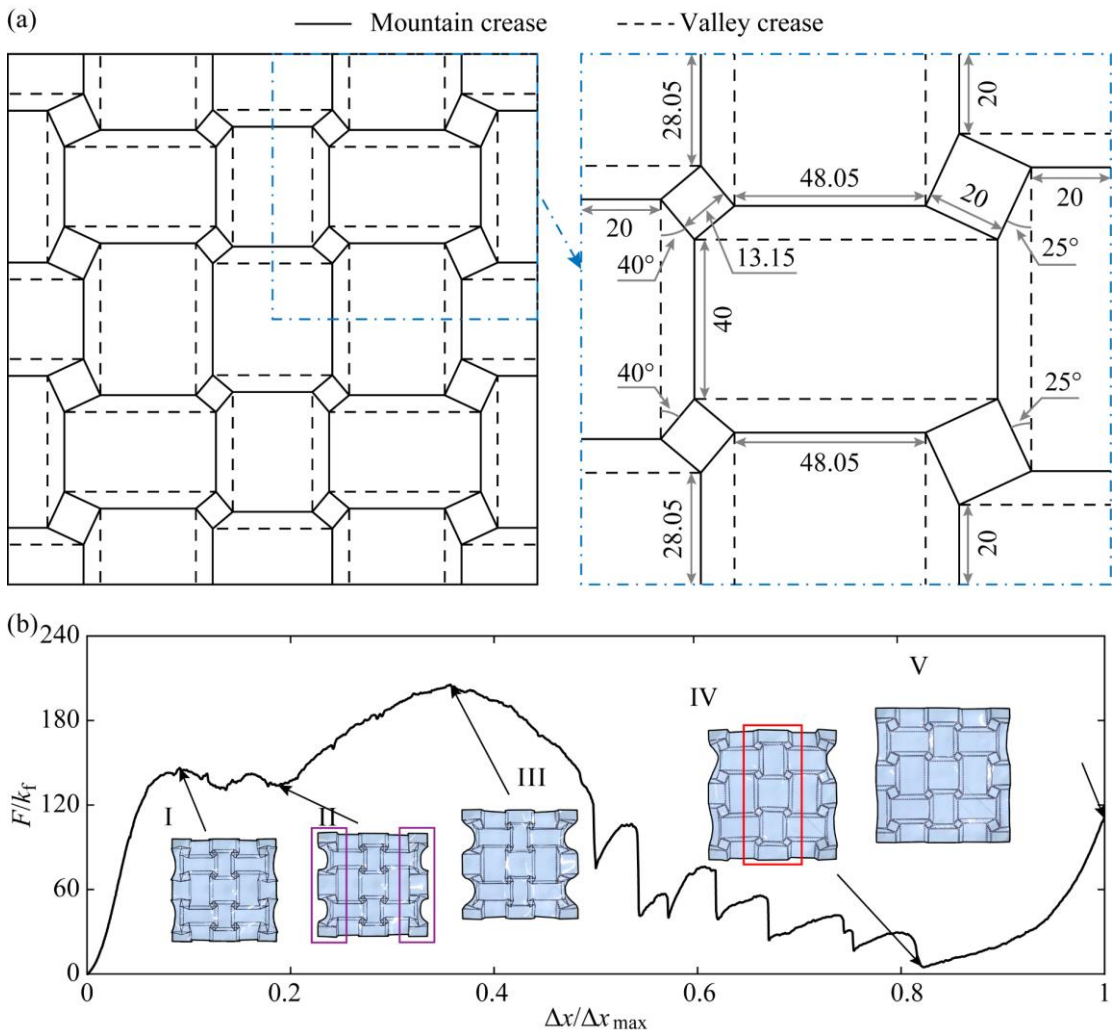

Fig. 4-16 Graded 4×4 metasheet with type 1 units. (a) Pattern and geometric parameters. (b) The normalized force versus displacement curve and key configurations.

4.5 Effects of Different Boundary Conditions

In addition, the effects of different boundary conditions are discussed in this work. As mentioned in Section 4.3.3 and Section 4.3.4, the units in a tessellation metasheet can be separated into four groups. Each group has a particular boundary condition that can be modeled using the tension experiment on 2×2 metasheets, $T_{2\times2}$. The $T_{2\times2\text{-i}}$ metasheet in Fig. 4-17 (a) shows the same boundary condition of T_i unit, which has two edges fixed and one point loaded. The $T_{2\times2\text{-ii}}$ metasheet in Fig. 4-17 (b) shows the same boundary condition of T_{ii} unit, which has three edges fixed and the long side of the rectangular facet loaded. The $T_{2\times2\text{-iii}}$ metasheet in Fig. 4-17 (c) shows the same boundary condition of T_{iii} unit, which has three edges fixed and the short side of the rectangular facet loaded. The $T_{2\times2\text{-iv}}$ metasheet in Fig. 4-17 (c) shows the same boundary condition of T_{iv} unit, whose all four edges are fixed.

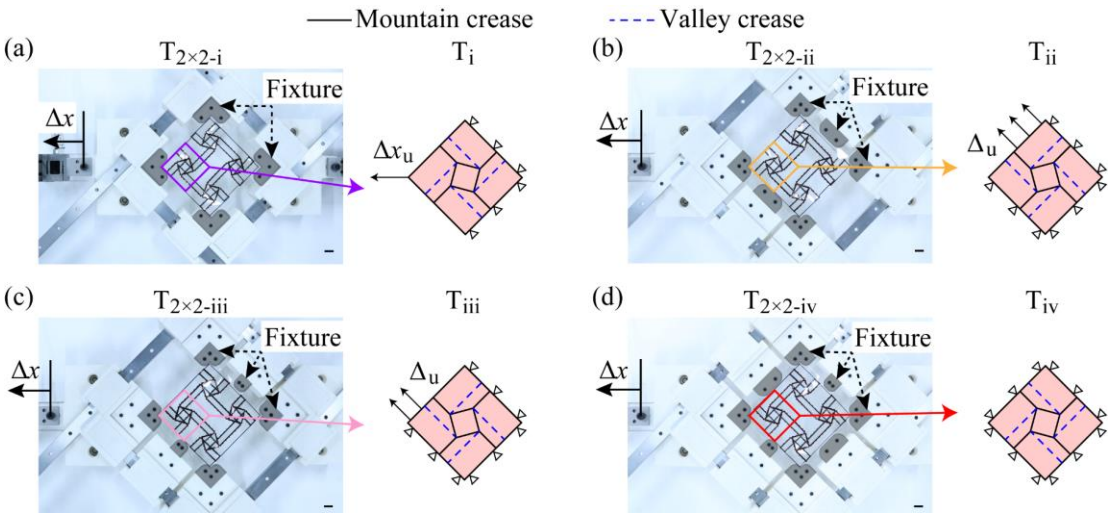

Fig. 4-17 The boundary condition of (a) $T_{2\times2\text{-i}}$ metasheet and T_i unit, (b) $T_{2\times2\text{-ii}}$ metasheet and T_{ii} unit, (c) $T_{2\times2\text{-iii}}$ metasheet and T_{iii} unit, and (d) $T_{2\times2\text{-iv}}$ metasheet and T_{iv} unit. (Scale bar: 10mm)

Based on the same experimental method, the mechanical properties of four 2×2 metasheets are shown in Fig. 4-18 and compared with predicted results. A good match between experimental data and prediction is found in 2×2 type 2 and type 3 metasheets, which implies that boundary conditions hardly influence the mechanical properties of type 2 and 3 units. However, a distinction between experimental and predicted results is discovered in the 2×2 type 1 metasheets with all four boundary conditions, which means the type 1 unit is sensitive to the boundary condition. As shown in Fig. 4-18(c)-

(e), except for the significant difference found in the comparing results of the normalized energy of $T1_{2\times2\text{-iii}}$ metasheet, only a subtle distinction exists in other mechanical results of the metasheets with different boundary conditions. Fortunately, the proportion of T_{iii} units in an $m\times m$ metasheet is small. Thus, predicting the mechanical behavior of metasheets can be achieved by using the results of the type 1 unit shown in Section 4.3.2, which is illustrated by nine 4×4 tessellation specimens in Section 4.3.3 and Section 4.3.4.

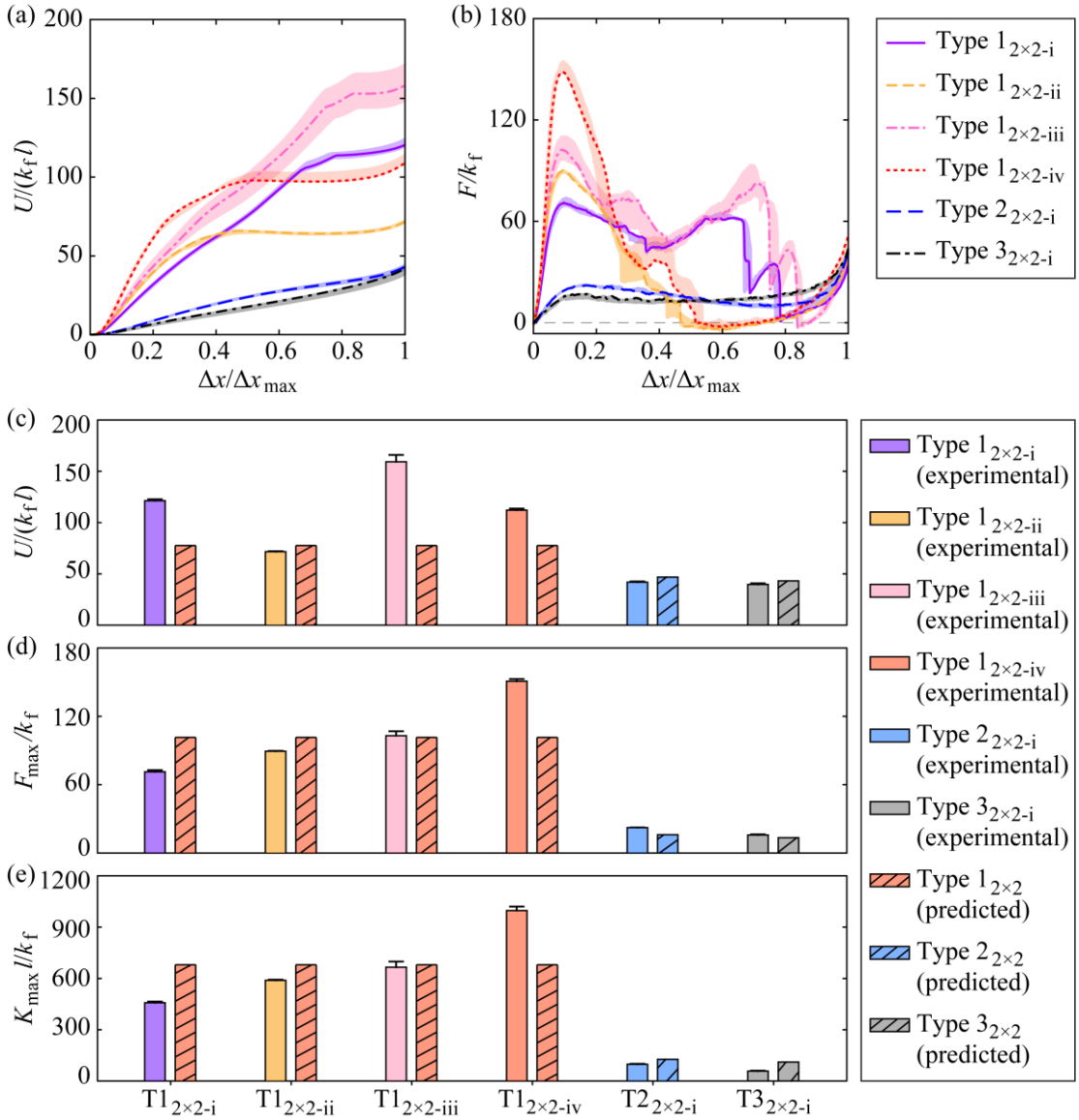

Fig. 4-18 Mechanical properties of 2×2 metasheets with different boundary conditions. (a and b) The normalized energy, $U/(k_f l)$, and force, F/k_f, vs. displacement, $\Delta x/\Delta x_{max}$, curves. (c-e) The experimental and predicted normalized energy, $U/(k_f l)$, initial peak force, F_{max}/k_f, and maximum stiffness, $K_{max} l/k_f$.

4.6 Conclusions

The theoretical and experimental results in Section 2.6, Section 3.7, Section 4.3, and Section 4.4 show the potential of the programmable process of square-twist metasheets in practical application. For example, to design an ideal impact energy absorption device, which requires a long and flat plateau, the type 2 unit should be used in creating metasheets, where smaller values of k_f/k_c and α, and a larger value of a/l should be selected to minimize the force drop at the bifurcation point and provide an increase in the whole force curve. Moreover, to create a graded stiffness metasheet, various groups of type 1 units should be selected with different geometric parameters, where a larger value of α should be coupled with a larger value of a/l to produce larger stiffness.

I have designed a new group of origami metasheets by amalgamating rigid and non-rigid square-twist origami units in a single metasheet and analyzed their energy, load bearing capability, and stiffness. The tessellation rule for the metasheets has been established to satisfy the compatibility conditions among neighboring units of different types and geometric parameters. A series of metasheets with varying unit combinations have been designed, fabricated, and tested. The experimental results indicate that the three types of units can in general maintain their specific deformation modes and corresponding mechanical properties. A metasheet can be treated as an assembly of nonlinear springs connected in series and in parallel for the purpose of predicting its energy, initial peak force, and maximum stiffness. The mechanical properties of the metasheet can be obtained simply by summing up the properties of its constitutive units. A good agreement between experimental data and predictions are obtained. Based on this, the mechanical properties of the metasheets can be continuously programmed over a wide range by tuning the proportions of different units within a sheet and the geometric and material parameters of the units. And all the metasheets with the same layout can be folded out from the same pre-creased sheet, thus enabling re-programmability by simply folding the sheet following different crease mountain-valley assignments.

This work expands the design scope of origami-inspired metamaterials with a wide range of property programmability and re-programmability to meet practical engineering demands in various fields. The finding has opened doors to many

interesting future research directions. For instance, in order to achieve an automatic and efficient property programming process, a machine learning algorithm could be incorporated into what has been discovered in this paper to more efficiently search for the desired tessellation and design parameters to meet a specific requirement.

Chapter 5 Achievements and Future Works

This dissertation aimed to propose a design method of origami-inspired mechanical metamaterials by combining the rigid-foldable origami pattern with the non-rigid-foldable one and present validated study methods for their mechanical properties. This chapter summarizes the main achievements and the highlighted future work.

5.1 Main Achievements

- **The non-rigid square-twist type 2 unit**

First, a theoretical model for the non-rigid-foldable type 2 square-twist pattern has been developed by modeling the deformation of the central square facet as the rotation of a virtual crease on its diagonal of it. The kinematic analysis of the modified type 2 unit with additional crease has been generated by modeling the four-/five-crease vertices as a closed loop of spherical 4R/5R linkages. The type 2M unit has been proved rigid-foldable according to the relationship between dihedral angles. A bifurcation during tension has been found and validated by experiment. Based on the kinematic results, the mechanical properties, such as elastic energy, of both type 2 and type 2M units have been calculated and proved to rely on the geometric parameters of the pattern and the material parameter of the facet and creases. Moreover, the mechanical behavior of the type 2 unit has been programmed by tuning geometry or material properties.

The kinematic model and experimental investigation of non-rigid-foldable type 2 unit have been presented in Chapter 2. The mechanical properties programmed and predicted by geometric and material parameters using the theoretical model expand the design of mechanical metamaterials using non-rigid-foldable origami patterns. The work of kinematic analysis has been published in a journal paper named “Rigid foldability and mountain-valley crease assignments of square-twist origami pattern” on Mechanism and Machine Theory. The prediction and programmability of mechanical behavior based on the experimental study have been published as a journal paper titled “Theoretical characterization of a non-rigid-foldable square-twist origami for property programmability” on International Journal of Mechanical Sciences.

- **The non-rigid square-twist type 1 unit**

Second, an empirical model of the non-rigid-foldable type 1 square-twist pattern has been established by a combination of experimental and numerical analyses. The kinematic analysis of the modified unit with an additional crease on the central square has been proved unavailable for the four-fold rotational symmetry of the type 1 unit. Thus, a finite element model has been presented for accurate deformation analysis and validated by a biaxial tension experiment result. The finite element model of the type 1 unit shows a three-stage deformation process, divided by the tightening, unlocking, and flattening stages. The key features in the energy, force, and stiffness curves of the type 1 unit have been analyzed in detail. Validated by experiment, the empirical model is available for predicting and programming the mechanical behaviors by geometric and material parameters.

The invalidated kinematic analysis, experimental and numerical investigation, and validated empirical model of non-rigid-foldable type 1 unit have been presented in Chapter 3. The programmable and predicted behaviors studied by the empirical model enable metamaterial design by combining square-twist type 1 units with other rigid or non-rigid units. The study of kinematic analysis has been published by a journal paper named “Rigid foldability and mountain-valley crease assignments of square-twist origami pattern” on Mechanism and Machine Theory. The research on mechanical behavior has been submitted as a journal paper titled “Deformation characteristics and mechanical properties programming of a non-rigid square-twist origami structure with rotational symmetry” on Thin-walled Structures.

- **Metasheets built with a mixture of rigid and non-rigid square-twist units**

Finally, a tessellation rule has been proposed to design metasheets using non-rigid type 1 and 2 and rigid type 3 square-twist units. Both the compatible mountain-valley assignment and geometric parameters have been discussed. The number of possible $m\times m$ tessellations is calculated as an equation of the variable m. To explain the design principle, the 2×2 tessellations excluding those obtained by rotating the others have been illustrated as a jigsaw puzzle.

The mechanical performances of metasheets fabricated by uniform units are different from those of metasheets designed by mixture units. The deformation characteristics of metasheet in the biaxial tension experiment have been explained by uniform and mixture specimens that the proportion of type 1 unit ranges from 0% to

100%. Considering the units as nonlinear springs and the metasheet as an assembly of springs connected in series and parallel, the predicted energy of the metasheet is the simple summation of unit energy. Thus, mechanical behaviors of the metasheet have been programmed by the proportion and property of units. Since the three types of units can be fabricated by identical geometric and material parameters, the reprogrammability of square-twist metasheets has been presented.

The mechanical metasheets designed by a combination of rigid and non-rigid origami patterns in Chapter 4 widen the range of property programmability. The reprogrammability in configuration paves a way to produce origami metasheets meeting practical engineering demands in various fields. The work has been accepted by Engineering and named “Tessellation rule and properties programming of origami metasheets built with a mixture of rigid and non-rigid square-twist patterns”.

5.2 Future Works

The research reported in this dissertation establishes a rational design principle of origami metamaterials using the unit patterns with different rigidities and presents the corresponding prediction and programing approaches of mechanical behaviors. In this design method, the compatible principle of both mountain-valley assignment and geometric parameters is universal in the metamaterial design based on origami structures. Thus, the findings of this work can be used for reference in similar studies. To enhance the practical usage of this type of metamaterial, several potential topics can be further explored:

First, further study can focus on the structural design method of multi-layer square-twist origami metamaterials based on the one-layer metasheet presented in this dissertation. In a one-layer metasheet configuration, only the mountain-valley assignment and the geometric parameters in the adjacent units are needed to consider. But for a multi-layer metamaterial, the connecting facets or creases between neighboring layers request more attention. For example, the square-twist metasheet always has several rectangular facets on the upper or lower surface. Then, a two-layer metamaterial can be formed by connecting the identical rectangular facets of different one-layer metasheets. When a stacked multi-layer structure of square-twist origami pattern is established, the programming on an individual unit, a layer, or the whole

configuration will be explored to tune both in- and out-of-layer units in one metamaterial. The multi-layer metamaterial with arbitrary programmability may widen the range of mechanical behaviors.

Second, because of the square-twist origami pattern obtained by multiple four-crease vertices, the combination of different origami patterns designed by four-crease vertices, such as Miura-ori and double corrugated, can be furtherly researched. It would be a novel discovery whether the physical properties of the combined metamaterial are the sum of those of different structural components or not. The new combined metamaterial may generate a wide range of exotic behaviors in mechanical, thermal, electromagnetic fields, etc.

Third, the tunable configuration of coupled rigid/non-rigid tessellation structure can be either associated with shape memory material controlled by magnetic/temperature field or fabricated by flexible materials driven by magnetic actuators or motor-driven tendons. It achieves an active or passive reconfiguration performance to design soft robots that are tunable and adaptive to various environments in the future.

Finally, a characteristic of the square-twist origami pattern is that an identical crease layout with different mountain-valley assignments can result in different types of units and various mechanical properties. In other words, the same patterned material sheet can form multiple metasheets with different proportions of type 1 units using different folding paths. It indicates that a folded metasheet can be reprogramed/reconfigured by unfolding to the initial state and switching the folded path. Thus, future studies can focus on designing and analyzing reprogrammable/reconfigurable metamaterials that may satisfy more complex requirements. Moreover, the reprogrammability/reconfigurability can be autonomically tuned when the metamaterial is manufactured by shape memory material.

References

[1] Shelby R A, Smith D R, Schultz S. Experimental Verification of a Negative Index of Refraction[J]. Science, 2001, 292(5514): 77-79.

[2] Mei J, Ma G, Yang M, et al. Dark Acoustic Metamaterials as Super Absorbers for Low-frequency Sound[J]. Nature Communications, 2012, 3: 756.

[3] Bertoldi K, Reis P M, Willshaw S, et al. Negative Poisson's Ratio Behavior Induced by an Elastic Instability[J]. Advanced Materials, 2010, 22(3): 361-366.

[4] Lee J-H, Wang L, Boyce M C, et al. Periodic Bicontinuous Composites for High Specific Energy Absorption[J]. Nano Letters, 2012, 12(8): 4392-4396.

[5] Zheng X, Lee H, Weisgraber Todd H, et al. Ultralight, Ultrastiff Mechanical Metamaterials[J]. Science, 2014, 344(6190): 1373-1377.

[6] Zhang W, Zhao S, Sun R, et al. In-Plane Mechanical Behavior of a New Star-re-entrant Hierarchical Metamaterial[J]. Polymers (Basel), 2019, 11(7): 1132.

[7] Morris C, Bekker L, Spadaccini C, et al. Tunable Mechanical Metamaterial with Constrained Negative Stiffness for Improved Quasi-static and Dynamic Energy Dissipation[J]. Advanced Engineering Materials, 2019, 21(7): 1900163.

[8] Chen Y, Li T, Scarpa F, et al. Lattice Metamaterials with Mechanically Tunable Poisson’s Ratio for Vibration Control[J]. Physical Review Applied, 2017, 7(2): 024012.

[9] Pan F, Li Y, Li Z, et al. 3D Pixel Mechanical Metamaterials[J]. Advanced Materials, 2019, 31(25): e1900548.

[10] Meng H, Huang X, Chen Y, et al. Structural Vibration Absorption in Multilayered Sandwich Structures Using Negative Stiffness Nonlinear Oscillators[J]. Applied Acoustics, 2021, 182: 108240.

[11] Liu B, Silverberg J L, Evans A A, et al. Topological Kinematics of Origami Metamaterials[J]. Nature Physics, 2018, 14(8): 811-815.

[12] Coulais C, Kettenis C, van Hecke M. A Characteristic Length Scale Causes Anomalous Size Effects and Boundary Programmability in Mechanical Metamaterials[J]. Nature Physics, 2018, 14(1): 40-44.

[13] Coulais C, Sounas D, Alu A. Static Non-reciprocity in Mechanical Metamaterials[J]. Nature, 2017, 542(7642): 461-464.

[14] Wang H, Zhang Y, Lin W, et al. A Novel Two-dimensional Mechanical Metamaterial with Negative Poisson’s Ratio[J]. Computational Materials Science, 2020, 171: 109232.

[15] Shaw L A, Sun F, Portela C M, et al. Computationally Efficient Design of Directionally Compliant Metamaterials[J]. Nature Communications, 2019, 10(1): 291.

[16] Coulais C, Sabbadini A, Vink F, et al. Multi-step Self-guided Pathways for Shape-changing Metamaterials[J]. Nature, 2018, 561(7724): 512-515.

[17] Tang Y, Lin G, Han L, et al. Design of Hierarchically Cut Hinges for Highly Stretchable and Reconfigurable Metamaterials with Enhanced Strength[J]. Advanced Materials, 2015, 27(44): 7181-7190.

[18] Tang Y, Yin J. Design of Cut Unit Geometry in Hierarchical Kirigami-based Auxetic Metamaterials for High Stretchability and Compressibility[J]. Extreme Mechanics Letters, 2017, 12: 77-85.

[19] Tang Y, Li Y, Hong Y, et al. Programmable Active Kirigami Metasheets with More Freedom of Actuation[J]. Proceedings of the National Academy of Sciences of the United States of America, 2019, 116(52): 26407-26413.

[20] Choi G P T, Dudte L H, Mahadevan L. Programming Shape Using Kirigami Tessellations[J]. Nature Materials, 2019, 18(9): 999-1004.

[21] An N, Domel A G, Zhou J, et al. Programmable Hierarchical Kirigami[J]. Advanced Functional Materials, 2019, 30(6): 1906711.

[22] Tang Y, Lin G, Yang S, et al. Programmable Kiri-Kirigami Metamaterials[J]. Advanced Materials, 2017, 29(10): 1604262.

[23] Zhong R, Fu M, Chen X, et al. A Novel Three-dimensional Mechanical Metamaterial with Compression-torsion Properties[J]. Composite Structures, 2019, 226: 111232.

[24] Wang Y-B, Liu H-T, Zhang D-Q. Compression-torsion Conversion Behavior of a Cylindrical Mechanical Metamaterial Based on Askew Re-Entrant Cells[J]. Materials Letters, 2021, 303: 130572.

[25] Frenzel T, Kadic M, Wegener M. Three-dimensional Mechanical Metamaterials with a Twist[J]. Science, 2017, 358: 1072–1074.

[26] Kadic M, Diatta A, Frenzel T, et al. Static Chiral Willis Continuum Mechanics for Three-dimensional Chiral Mechanical Metamaterials[J]. Physical Review B, 2019, 99(21): 214101.

[27] Goswami D, Zhang Y, Liu S, et al. Mechanical Metamaterials with Programmable Compression-twist Coupling[J]. Smart Materials and Structures, 2020, 30(1): 015005.

[28] Lin G, Li J, Chen P, et al. Buckling of Lattice Columns Made from Three-dimensional Chiral Mechanical Metamaterials[J]. International Journal of Mechanical Sciences, 2021, 194: 106208.

[29] Cheng L, Tang T, Yang H, et al. The Twisting of Dome-like Metamaterial from Brittle to Ductile[J]. Advanced Science, 2021, 8(13): 2002701.

[30] Ion A, Frohnhofen J, Wall L, et al. Metamaterial Mechanisms[C]. Symposium on User Interface Software & Technology,

[31] Wu K, Sigmund O, Du J. Design of Metamaterial Mechanisms Using Robust Topology Optimization and Variable Linking Scheme[J]. Structural and Multidisciplinary Optimization, 2021, 63(4): 1975-1988.

[32] Ion A, Lindlbauer D, Herholz P, et al. Understanding Metamaterial Mechanisms. Proceedings of the 2019 Chi Conference on Human Factors in Computing Systems[C], Association for Computing Machinery, 2019: 647.

[33] Ou J, Ma Z, Peters J, et al. Kinetix - Designing Auxetic-inspired Deformable Material Structures[J]. Computers & Graphics, 2018, 75: 72-81.

[34] Rafsanjani A, Pasini D. Bistable Auxetic Mechanical Metamaterials Inspired by Ancient Geometric Motifs[J]. Extreme Mechanics Letters, 2016, 9: 291-296.

[35] Jin L, Khajehtourian R, Mueller J, et al. Guided Transition Waves in Multistable Mechanical Metamaterials[J]. Proceedings of the National Academy of Sciences of the United States of America, 2020, 117(5): 2319-2325.

[36] Hu W, Ren Z, Wan Z, et al. Deformation Behavior and Band Gap Switching Function of 4D Printed Multi-stable Metamaterials[J]. Materials & Design, 2021, 200: 109481.

[37] Ren Z, Ji L, Tao R, et al. Smp-based Multi-stable Mechanical Metamaterials: From Bandgap Tuning to Wave Logic Gates[J]. Extreme Mechanics Letters, 2021, 42: 101077.

[38] Yang H, Ma L. 1d to 3d Multi-stable Architected Materials with Zero Poisson's Ratio and Controllable Thermal Expansion[J]. Materials & Design, 2020, 188: 108430.

[39] Chen T, Panetta J, Schnaubelt M, et al. Bistable Auxetic Surface Structures[J]. ACM Transactions on Graphics, 2021, 40(4): a39.

[40] Zhang Y, Wang Y, Chen C Q. Ordered Deformation Localization in Cellular Mechanical Metamaterials[J]. Journal of the Mechanics and Physics of Solids, 2019, 123: 28-40.

[41] Wu Y, Chaunsali R, Yasuda H, et al. Dial-in Topological Metamaterials Based on Bistable Stewart Platform[J]. Scientific Reports, 2018, 8(1): 112.

[42] Liu Y, Lei M, Lu H, et al. Sequentially Tunable Buckling in 3d Printing Auxetic Metamaterial Undergoing Twofold Viscoelastic Resonances[J]. Smart Materials and Structures, 2021, 30(10): 105018.

[43] Yang Y, Dias M A, Holmes D P. Multistable Kirigami for Tunable Architected Materials[J]. Physical Review Materials, 2018, 2(11): 110601.

[44] Rafsanjani A, Bertoldi K. Buckling-induced Kirigami[J]. Physical Review Letters, 2017, 118(8): 084301.

[45] Castle T, Cho Y, Gong X, et al. Making the Cut: Lattice Kirigami Rules[J]. Physical Review Letters, 2014, 113(24): 245502.

[46] Schenk M, Guest S D. Geometry of Miura-folded Metamaterials[J]. Proceedings of the National Academy of Sciences of the United States of America, 2013, 110(9): 3276-3281.

[47] Kidambi N, Wang K W. Dynamics of Kresling Origami Deployment[J]. Physical Review E, 2020, 101(6-1): 063003.

[48] Kamrava S, Ghosh R, Yang Y, et al. Slender Origami with Complex 3d Folding Shapes[J]. EPL (Europhysics Letters), 2018, 124(5): 58001.

[49] Boatti E, Vasios N, Bertoldi K. Origami Metamaterials for Tunable Thermal Expansion[J]. Advanced Materials, 2017, 29(26): 1700360.

[50] Nauroze S A, Novelino L S, Tentzeris M M, et al. Continuous-range Tunable Multilayer Frequency-selective Surfaces Using Origami and Inkjet Printing[J]. Proceedings of the National Academy of Sciences of the United States of America, 2018, 115(52): 13210.

[51] Wang Z, Jing L, Yao K, et al. Origami-based Reconfigurable Metamaterials for Tunable Chirality[J]. Advanced Materials, 2017, 29(27): 1700412.

[52] Zhang J, Karagiozova D, You Z, et al. Quasi-static Large Deformation Compressive Behaviour of Origami-based Metamaterials[J]. International Journal of Mechanical Sciences, 2019, 153-154: 194-207.

[53] Lv C, Krishnaraju D, Konjevod G, et al. Origami Based Mechanical Metamaterials[J]. Scientific Reports, 2014, 4(1): 5979.

[54] Wei Z Y, Guo Z V, Dudte L, et al. Geometric Mechanics of Periodic Pleated Origami[J]. Physical Review Letters, 2013, 110(21): 325-329.

[55] Zhou X, Zang S, You Z. Origami Mechanical Metamaterials Based on the Miura-Derivative Fold Patterns[J]. Proceedings of the Royal Society A: Mathematical, Physical and Engineering Sciences, 2016, 472(2191): 20160361.

[56] Ma J, Song J, Chen Y. An Origami-Inspired Structure with Graded Stiffness[J]. International Journal of Mechanical Sciences, 2018, 136: 134-142.

[57] Yuan L, Dai H, Song J, et al. The Behavior of a Functionally Graded Origami Structure Subjected to Quasi-static Compression[J]. Materials & Design, 2020, 189: 108494.

[58] Fang H, Chu S A, Xia Y, et al. Programmable Self-locking Origami Mechanical Metamaterials[J]. Advanced Materials, 2018, 30(15): e1706311.

[59] Eidini M, Paulino Glaucio H. Unraveling Metamaterial Properties in Zigzag-Base Folded Sheets[J]. Science Advances, 2015, 1(8): e1500224.

[60] Eidini M. Zigzag-Base Folded Sheet Cellular Mechanical Metamaterials[J]. Extreme Mechanics Letters, 2016, 6: 96-102.

[61] Bhovad P, Kaufmann J, Li S. Peristaltic Locomotion without Digital Controllers: Exploiting Multi-stability in Origami to Coordinate Robotic Motion[J]. Extreme Mechanics Letters, 2019, 32: 100552.

[62] Kresling B. The Fifth Fold: Complex Symmetries in Kresling-origami Patterns[J]. Symmetry: Culture and Science, 2020, 31(4): 403-416.

[63] Cai J, Liu Y, Ma R, et al. Nonrigidly Foldability Analysis of Kresling Cylindrical Origami[J]. Journal of Mechanisms and Robotics, 2017, 9(4): 041018.

[64] Cai J, Ma R, Feng J, et al. Foldability Analysis of Cylindrical Origami Structures[C]. Advances in Reconfigurable Mechanisms and Robots II, Cham: Springer International Publishing, 143-151.

[65] Silverberg J L, Na J H, Evans A A, et al. Origami Structures with a Critical Transition to Bistability Arising from Hidden Degrees of Freedom[J]. NATURE MATERIALS, 2015, 14(4): 389-393.

[66] Kawasaki T, Yoshida M. Crystallographic Flat Origamis[J]. Memoirs of the Faculty of Science, Kyushu University. Series A, Mathematics, 1988, 42(2): 153-157.

[67] Zhang Y, Li B, Zheng Q S, et al. Programmable and Robust Static Topological Solitons in Mechanical Metamaterials[J]. Nature Communications, 2019, 10(1): 5605.

[68] Liu K, Zegard T, Pratapa P P, et al. Unraveling Tensegrity Tessellations for Metamaterials with Tunable Stiffness and Bandgaps[J]. Journal of the Mechanics and Physics of Solids, 2019, 131: 147-166.

[69] Bossart A, Dykstra D M J, van der Laan J, et al. Oligomodal Metamaterials with Multifunctional Mechanics[J]. Proceedings of the National Academy of Sciences of the United States of America, 2021, 118(21): e2018610118.

[70] Ho D T, Park H S, Kim S Y, et al. Graphene Origami with Highly Tunable Coefficient of Thermal Expansion[J]. ACS Nano, 2020, 14(7): 8969-8974.

[71] Kaufmann J, Bhovad P, Li S. Harnessing the Multistability of Kresling Origami for Reconfigurable Articulation in Soft Robotic Arms[J]. Soft Robotics, 2021, ahead of print: FEB 2021.

[72] Yasuda H, Chong C, Charalampidis E G, et al. Formation of Rarefaction Waves in Origami-based Metamaterials[J]. Physical Review E, 2016, 93(4): 043004.

[73] Filipov E T, Tachi T, Paulino G H. Origami Tubes Assembled into Stiff, yet Reconfigurable Structures and Metamaterials[J]. Proceedings of the National Academy of Sciences of the United States of America, 2015, 112(40): 12321-12326.

[74] Zhao Z, Kuang X, Wu J, et al. 3d Printing of Complex Origami Assemblages for Reconfigurable Structures[J]. Soft Matter, 2018, 14(39): 8051-8059.

[75] Lin Z, Novelino L S, Wei H, et al. Folding at the Microscale: Enabling Multifunctional 3d Origami-architected Metamaterials[J]. Small, 2020, 16(35): e2002229.

[76] Ma J, Feng H, Chen Y, et al. Folding of Tubular Waterbomb[J]. Research, 2020, 2020(1): 1-8.

[77] Feng H, Ma J, Chen Y, et al. Twist of Tubular Mechanical Metamaterials Based on Waterbomb Origami[J]. Scientific Reports, 2018, 8(1): 9522.

[78] Mukhopadhyay T, Ma J, Feng H, et al. Programmable Stiffness and Shape Modulation in Origami Materials: Emergence of a Distant Actuation Feature[J]. Applied Materials Today, 2020, 19: 100537.

[79] Treml B, Gillman A, Buskohl P, et al. Origami Mechanologic[J]. Proceedings of the National Academy of Sciences of the United States of America, 2018, 115(27): 6916.

[80] Lee D, Kim J, Kim S, et al. Design of Deformable-wheeled Robot Based on Origami Structure with Shape Memory Alloy Coil Spring[C]. 2013 10th International Conference on Ubiquitous Robots and Ambient Intelligence (URAI), 120-120.

[81] Jiang W, Ma H, Feng M, et al. Origami-Inspired Building Block and Parametric Design for Mechanical Metamaterials[J]. Journal of Physics D: Applied Physics, 2016, 49(31): 315302.

[82] Lee D-Y, Kim S-R, Kim J-S, et al. Origami Wheel Transformer: A Variable-diameter Wheel Drive Robot Using an Origami Structure[J]. Soft Robotics, 2017, 4(2): 163-180.

[83] Watanabe N, Kawaguchi K I. The Method for Judging Rigid Foldability. Origami4[C], New York: A K Peters/CRC Press, 2009: 14.

[84] Tachi T. Generalization of Rigid Foldable Quadrilateral Mesh Origami[J]. Journal of the International Association for Shell & Spatial Structures, 2009, 50(3): 173-179.

[85] Stachel H. A Kinematic Approach to Kokotsakis Meshes[J]. Computer Aided Geometric Design, 2010, 27(6): 428-437.

[86] Dai J S, Jones J R. Mobility in Metamorphic Mechanisms of Foldable/Erectable Kinds[J]. Journal of Mechanical Design, 1999, 121(3): 375-382.

[87] Feng H, Peng R, Ma J, et al. Rigid Foldability of Generalized Triangle Twist Origami Pattern and Its Derived 6r Linkages[J]. Journal of Mechanisms and Robotics, 2018, 10(5): 051003.

[88] Peng R, Ma J, Chen Y. The Effect of Mountain-Valley Folds on the Rigid Foldability of Double Corrugated Pattern[J]. Mechanism and Machine Theory, 2018, 128: 461-474.

[89] Wu W, You Z. Modelling Rigid Origami with Quaternions and Dual Quaternions[J]. Proceedings of the Royal Society A: Mathematical, Physical and Engineering Sciences, 2010, 466(2119): 2155-2174.

[90] Waitukaitis S, Menaut R, Chen B G, et al. Origami Multistability: From Single Vertices to Metasheets[J]. Physical Review Letters, 2015, 114(5): 055503.

[91] Brunck V, Lechenault F, Reid A, et al. Elastic Theory of Origami-based Metamaterials[J]. Physical Review E, 2016, 93(3): 033005.

[92] Karagiozova D, Zhang J, Lu G, et al. Dynamic in-plane Compression of Miura-ori Patterned Metamaterials[J]. International Journal of Impact Engineering, 2019, 129: 80-100.

[93] Wickeler A L, Naguib H E. Novel Origami-inspired Metamaterials: Design, Mechanical Testing and Finite Element Modelling[J]. Materials & Design, 2020, 186: 108242.

[94] Chen S, Mahadevan L. Rigidity Percolation and Geometric Information in Floppy Origami[J]. Proceedings of the National Academy of Sciences of the United States of America, 2019, 116(17): 8119-8124.

[95] Silverberg J L, Evans A A, McLeod L, et al. Using Origami Design Principles to Fold Reprogrammable Mechanical Metamaterials[J]. Science, 2014, 345(6197): 647-650.

[96] Liu K, Novelino L S, Gardoni P, et al. Big Influence of Small Random Imperfections in Origami-based Metamaterials[J]. Proceedings of the Royal Society A: Mathematical, Physical and Engineering Sciences, 2020, 476(2241): 20200236.

[97] Pratapa P P, Liu K, Paulino G H. Geometric Mechanics of Origami Patterns Exhibiting Poisson's Ratio Switch by Breaking Mountain and Valley Assignment[J]. Physical Review Letters, 2019, 122(15): 155501.

[98] Sengupta S, Li S. Harnessing the Anisotropic Multistability of Stacked-origami Mechanical Metamaterials for Effective Modulus Programming[J]. Journal of Intelligent Material Systems and Structures, 2018, 29(14): 2933-2945.

[99] Li S, Wang K W. Fluidic Origami with Embedded Pressure Dependent Multi-stability: A Plant Inspired Innovation[J]. Journal of The Royal Society Interface, 2015, 12(111): 20150639.

[100] Wu H, Fang H, Chen L, et al. Transient Dynamics of a Miura-origami Tube During Free Deployment[J]. Physical Review Applied, 2020, 14(3): 034068.

[101] Fang H, Chang T-S, Wang K W. Magneto-origami Structures: Engineering Multi-stability and Dynamics via Magnetic-elastic Coupling[J]. Smart Materials and Structures, 2020, 29(1): 015026.

[102] Li Z, Yang Q, Fang R, et al. Origami Metamaterial with Two-stage Programmable Compressive Strength under Quasi-Static Loading[J]. International Journal of Mechanical Sciences, 2021, 189: 105987.

[103] He Y L, Zhang P W, You Z, et al. Programming Mechanical Metamaterials Using Origami Tessellations[J]. Composites Science and Technology, 2020, 189: 108015.

[104] Wang H, Zhao D, Jin Y, et al. Modulation of Multi-directional Auxeticity in Hybrid Origami Metamaterials[J]. Applied Materials Today, 2020, 20: 100715.

[105] Yang N, Silverberg J L. Decoupling Local Mechanics from Large-scale Structure in Modular Metamaterials[J]. Proceedings of the National Academy of Sciences of the United States of America, 2017, 114(14): 3590-3595.

[106] Yang N, Chen C-W, Yang J, et al. Emergent Reconfigurable Mechanical Metamaterial Tessellations with an Exponentially Large Number of Discrete Configurations[J]. Materials & Design, 2020, 196: 109143.

[107] Kamrava S, Mousanezhad D, Ebrahimi H, et al. Origami-based Cellular Metamaterial with Auxetic, Bistable, and Self-locking Properties[J]. Scientific Reports, 2017, 7: 46046.

[108] Kamrava S, Ghosh R, Wang Z, et al. Origami-inspired Cellular Metamaterial with Anisotropic Multi-stability[J]. Advanced Engineering Materials, 2019, 21(2): 1800895.

[109] Yang N, Zhang M, Zhu R, et al. Modular Metamaterials Composed of Foldable Obelisk-Like Units with Reprogrammable Mechanical Behaviors Based on Multistability[J]. Scientific Reports, 2019, 9(1): 18812.

[110] Overvelde J T B, de Jong T A, Shevchenko Y, et al. A Three-dimensional Actuated Origami-inspired Transformable Metamaterial with Multiple Degrees of Freedom[J]. Nature Communications, 2016, 7(1): 10929.

[111] Overvelde J T B, Weaver J C, Hoberman C, et al. Rational Design of Reconfigurable Prismatic Architected Materials[J]. Nature, 2017, 541(7637): 347-352.

[112] Babaee S, Overvelde Johannes T B, Chen Elizabeth R, et al. Reconfigurable Origami-inspired Acoustic Waveguides[J]. Science Advances, 2016, 2(11): e1601019.

[113] Chen Z, Wu T, Nian G, et al. Ron Resch Origami Pattern Inspired Energy Absorption Structures[J]. Journal of Applied Mechanics, 2018, 86(1): 011005.

[114] Reid A, Lechenault F, Rica S, et al. Geometry and Design of Origami Bellows with Tunable Response[J]. Physical Review E, 2017, 95(1-1): 013002.

[115] Li Z, Kidambi N, Wang L, et al. Uncovering Rotational Multifunctionalities of Coupled Kresling Modular Structures[J]. Extreme Mechanics Letters, 2020, 39: 100795.

[116] Liu X, Yao S, Georgakopoulos S V. Mode Reconfigurable Bistable Spiral Antenna Based on Kresling Origami[C]. 2017 IEEE International Symposium on Antennas and Propagation & USNC/URSI National Radio Science Meeting, 413-414.

[117] Rubio A J, Kaddour A S, Georgakopolous S V. Circularly Polarized Wideband Yagi-Uda Array on a Kresling Origami Structure[C]. 2020 IEEE International Symposium on Antennas and Propagation and North American Radio Science Meeting, 1805-1806.

[118] Ishida S, Uchida H, Shimosaka H, et al. Design and Numerical Analysis of Vibration Isolators with Quasi-zero-stiffness Characteristics Using Bistable Foldable Structures[J]. Journal of Vibration and Acoustics, 2017, 139(3): 031015.

[119] Zhai Z, Wang Y, Jiang H. Origami-inspired, on-demand Deployable and Collapsible Mechanical Metamaterials with Tunable Stiffness[J]. Proceedings of the National Academy of Sciences of the United States of America, 2018, 115(9): 2032-2037.

[120] Yasuda H, Miyazawa Y, Charalampidis E G, et al. Origami-based Impact Mitigation Via Rarefaction Solitary Wave Creation[J]. Science Advances, 2019, 5(5): eaau2835.

[121] Li J, Chen Y, Feng X, et al. Computational Modeling and Energy Absorption Behavior of Thin-walled Tubes with the Kresling Origami Pattern[J]. Journal of the International Association for Shell and Spatial Structures, 2021, 62(2): 71-81.

[122] Masana R, Daqaq M F. Equilibria and Bifurcations of a Foldable Paper-based Spring Inspired by Kresling-pattern Origami[J]. Physical Review E, 2019, 100(6): 063001.

[123] Yasuda H, Yamaguchi K, Miyazawa Y, et al. Data-driven Prediction and Analysis of Chaotic Origami Dynamics[J]. Communications Physics, 2020, 3(1): 168.

[124] Masana R, Khazaaleh S, Alhussein H, et al. An Origami-inspired Dynamically Actuated Binary Switch[J]. Applied Physics Letters, 2020, 117(8): 081901.

[125] Wu S, Ze Q, Dai J, et al. Stretchable Origami Robotic Arm with Omnidirectional Bending and Twisting[J]. Proceedings of the National Academy of Sciences of the United States of America, 2021, 118(36): e2110023118.

[126] Novelino L S, Ze Q, Wu S, et al. Untethered Control of Functional Origami Microrobots with Distributed Actuation[J]. Proceedings of the National Academy of Sciences of the United States of America, 2020, 117(39): 24096.

[127] Yang X, Keten S. Multi-stability Property of Magneto-Kresling Truss Structures[J]. Journal of Applied Mechanics, 2021, 88(9): 091009.

[128] Pagano A, Yan T, Chien B, et al. A Crawling Robot Driven by Multi-stable Origami[J]. Smart Materials and Structures, 2017, 26(9): 094007.

[129] Gustafson K, Angatkina O, Wissa A. Model-Based Design of a Multistable Origami-enabled Crawling Robot[J]. Smart Materials and Structures, 2019, 29(1): 015013.

[130] Xu Z-L, Wang Y-Q, Zhu R, et al. Torsional Bandgap Switching in Metamaterials with Compression-torsion Interacted Origami Resonators[J]. Journal of Applied Physics, 2021, 130(4): 045105.

[131] Tao R, Ji L, Li Y, et al. 4D Printed Origami Metamaterials with Tunable Compression Twist Behavior and Stress-strain Curves[J]. Composites Part B: Engineering, 2020, 201: 108344.

[132] Min C C S, H. Geometrical Properties of Paper Spring[M]. Manufacturing Systems and Technologies for the New Frontier, London: Springer, 2008:

[133]Hu F, Wang W, Cheng J, et al. Origami Spring-inspired Metamaterials and Robots: An Attempt at Fully Programmable Robotics[J]. Science Progress, 2020, 103(3): 0036850420946162.

[134] Ye H, Ma J, Zhou X, et al. Energy Absorption Behaviors of Pre-folded Composite Tubes with the Full-diamond Origami Patterns[J]. Composite Structures, 2019, 221: 110904.

[135] Zhai Z, Wang Y, Lin K, et al. In Situ Stiffness Manipulation Using Elegant Curved Origami[J]. Science Advances, 2020, 6(47): eabe2000.

[136] Du Y, Keller T, Song C, et al. Origami-inspired Carbon Fiber-reinforced Composite Sandwich Materials – Fabrication and Mechanical Behavior[J]. Composites Science and Technology, 2021, 205: 108667.

[137] Woodruff S R, Filipov E T. A Bar and Hinge Model Formulation for Structural Analysis of Curved-crease Origami[J]. International Journal of Solids and Structures, 2020, 204-205: 114-127.

[138] Woodruff S R, Filipov E T. Curved Creases Redistribute Global Bending Stiffness in Corrugations: Theory and Experimentation[J]. Meccanica, 2021, 56(6): 1613-1634.

[139] Baek S-M, Yim S, Chae S-H, et al. Ladybird Beetle-inspired Compliant Origami[J]. Science Robotics, 2020, 5(41): eaaz6262.

[140] Lee T-U, Yang X, Ma J, et al. Elastic Buckling Shape Control of Thin-walled Cylinder Using Pre-embedded Curved-crease Origami Patterns[J]. International Journal of Mechanical Sciences, 2019, 151: 322-330.

[141] Bende N P, Evans A A, Innes-Gold S, et al. Geometrically Controlled Snapping Transitions in Shells with Curved Creases[J]. Proceedings of the National Academy of Sciences of the United States of America, 2015, 112(36): 11175.

[142] Lee T-U, You Z, Gattas J M. Elastica Surface Generation of Curved-crease Origami[J]. International Journal of Solids and Structures, 2018, 136-137: 13-27.

[143] Bukauskas A, Koronaki A, Lee T U, et al. Curved-crease Origami Face Shields for Infection Control[J]. PLoS One, 2021, 16(2): e0245737.

[144] Ying Y, Xin-zhuo X, Yao-zhi L. Programmable Instability of Spatial Structures Based on Kresling Origami[J]. Engineering Mechanics, 2021, 38(8): 75.

[145] Jianguo C, Xiaowei D, Yuting Z, et al. Folding Behavior of a Foldable Prismatic Mast with Kresling Origami Pattern[J]. Journal of Mechanisms and Robotics, 2016, 8(3): 031004.

[146] Zhang Q, Wang X, Cai J, et al. Motion Paths and Mechanical Behavior of Origami-inspired Tunable Structures[J]. Materials Today Communications, 2021, 26: 101872.

[147] Hwang H-Y. Effects of Perforated Crease Line Design on Mechanical Behaviors of Origami Structures[J]. International Journal of Solids and Structures, 2021, 230-231: 111158.

[148] Liu K, Tachi T, Paulino G H. Bio-Inspired Origami Metamaterials with Metastable Phases through Mechanical Phase Transitions[J]. Journal of Applied Mechanics, 2021: 1-13.

[149] Feng H, Peng R, Zang S, et al. Rigid Foldability and Mountain-valley Crease Assignments of Square-twist Origami Pattern[J]. Mechanism and Machine Theory, 2020, 152: 103947.

[150] Liu K, Tachi T, Paulino G H. Invariant and Smooth Limit of Discrete Geometry Folded from Bistable Origami Leading to Multistable Metasurfaces[J]. Nature Communications, 2019, 10(1): 4238.

[151] Liu K, Paulino G H. Nonlinear Mechanics of Non-rigid Origami: An Efficient Computational Approach[J]. Proceedings of the Royal Society A: Mathematical, Physical and Engineering Sciences, 2017, 473(2206): 20170348.

[152] Schenk M, Guest S D. Origami Folding: A Structural Engineering Approach. Origami5[C], New York: A K Peters/CRC Press, 2011: 291-303.

[153] Kamrava S, Ghosh R, Xiong J, et al. Origami-equivalent Compliant Mechanism[J]. Applied Physics Letters, 2019, 115(17): 171904.

[154] Wang L C, Song W L, Zhang Y J, et al. Active Reconfigurable Tristable Square-twist Origami[J]. Advanced Functional Materials, 2020, 30(13): 1909087.

[155] Hull T C. Counting Mountain-valley Assignments for Flat Folds[J]. Ars Combinatoria, 2003, 67: 175-188.

[156] Hull T C. Project Origami: Activities for Exploring Mathematics[M]. New York: A K Peters/CRC Press, 2013.

[157] Evans T A, Lang R J, Magleby S P, et al. Rigidly Foldable Origami Twists. Origami^6[C], 2015: 119-130.

[158] Wang L C, Song W L, Fang D. Twistable Origami and Kirigami: From Structure-guided Smartness to Mechanical Energy Storage[J]. ACS Applied Materials & Interfaces, 2019, 11(3): 3450-3458.

[159] Edmondson B J, Lang R J, Morgan M R, et al. Thick Rigidly Foldable Structures Realized by an Offset Panel Technique. Origami^6[C], 2015: 149-161.

[160] Hull T C, Urbanski M T. Rigid Foldability of the Augmented Square Twist. Origami7[C], New York: A K Peters/CRC Press, 2018: 533-544.

[161] Wang L-C, Song W-L, Fang H, et al. Reconfigurable Force-displacement Profiles of the Square-twist Origami[J]. International Journal of Solids and Structures, 2022, 241: 111471.

[162] Denavit J, Hartenberg R S. A Kinematic Notation for Lower-pair Mechanisms[J]. Trans.of the Asme.journal of Applied Mechanics, 1955, 23: 215-221.

[163] Lu G, Yu T X. Energy Absorption of Structures and Materials[M]. Cambridge, UK: CRC-Woodhead, 2003.

[164] Zang S, Zhou X, Wang H, et al. Foldcores Made of Thermoplastic Materials: Experimental Study and Finite Element Analysis[J]. Thin-Walled Structures, 2016, 100: 170-179.

[165] Dieleman P, Vasmel N, Waitukaitis S, et al. Jigsaw Puzzle Design of Pluripotent Origami[Nature Physics, 2020, 16(1): 63-68.

[166] Jha D K, Kant T, Singh R K. A Critical Review of Recent Research on Functionally Graded Plates[J]. Composite Structures, 2013, 96: 833-849.

Appendix

A. The 2×2 tessellations excluding those that can be obtained by rotating the others. (Section 4.2)

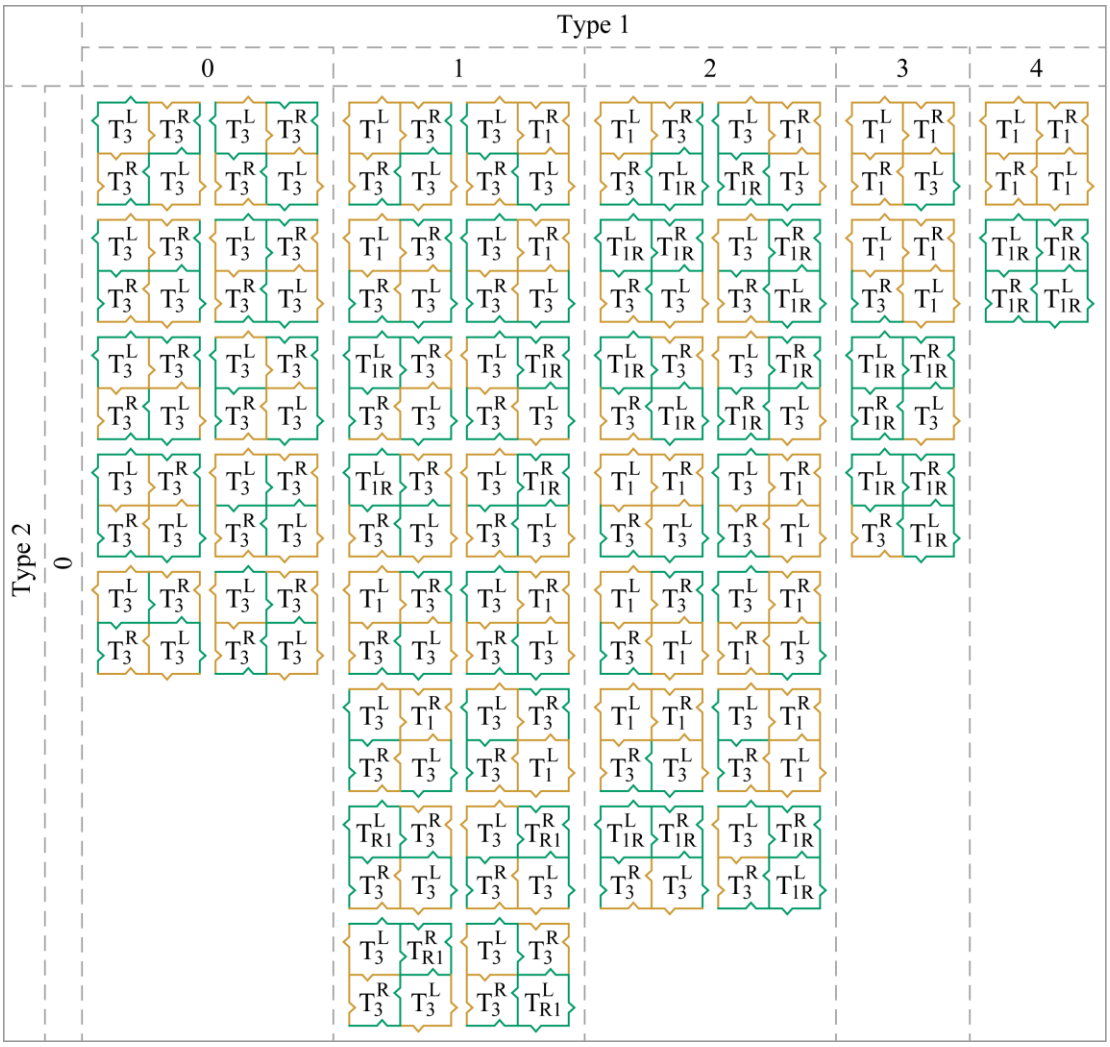

Fig. A1 The 2×2 tessellations arranged by the numbers of type 1 and 2 units.

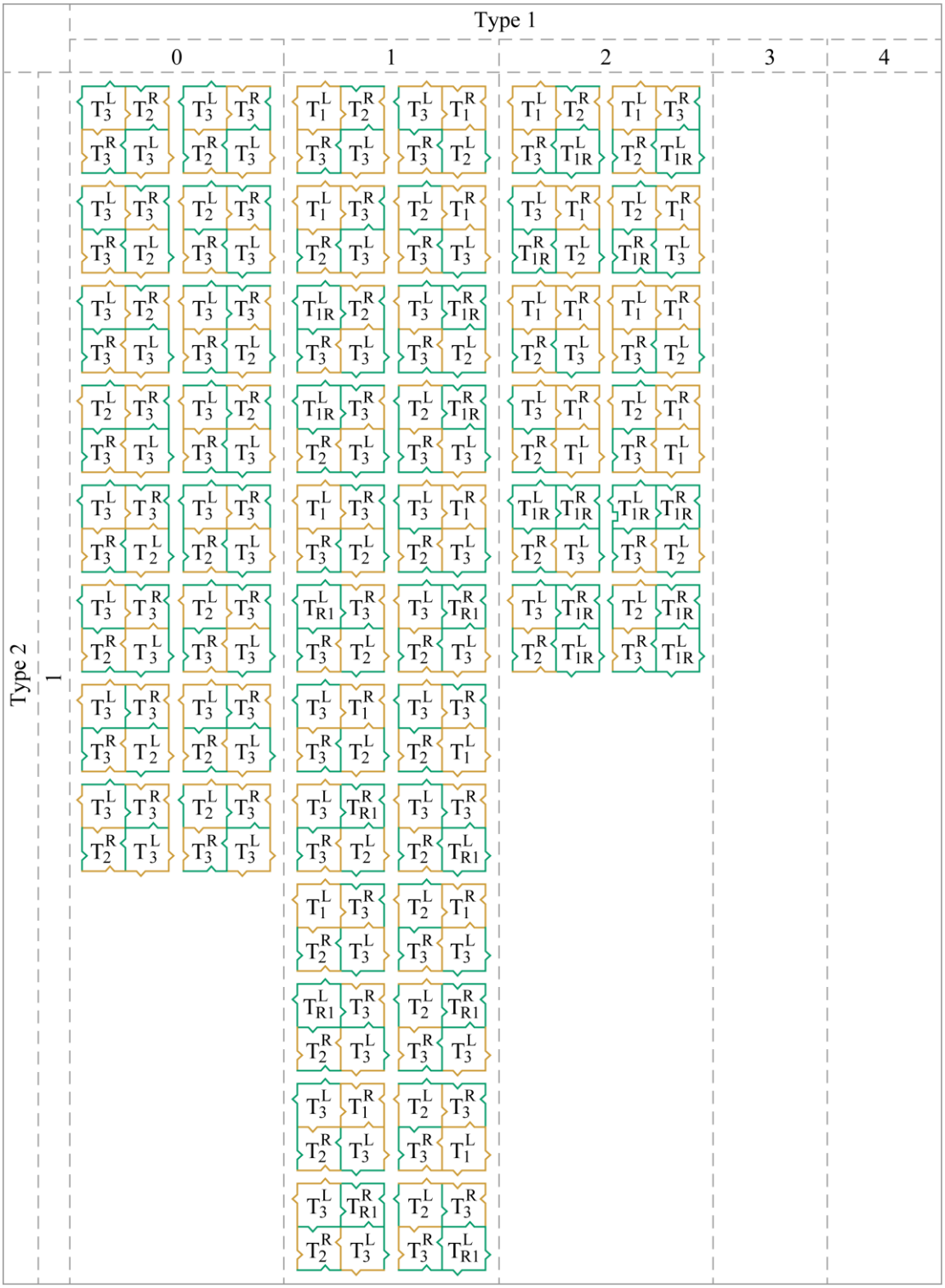

Fig. A1 The 2×2 tessellations arranged by the numbers of type 1 and 2 units. (Continued)

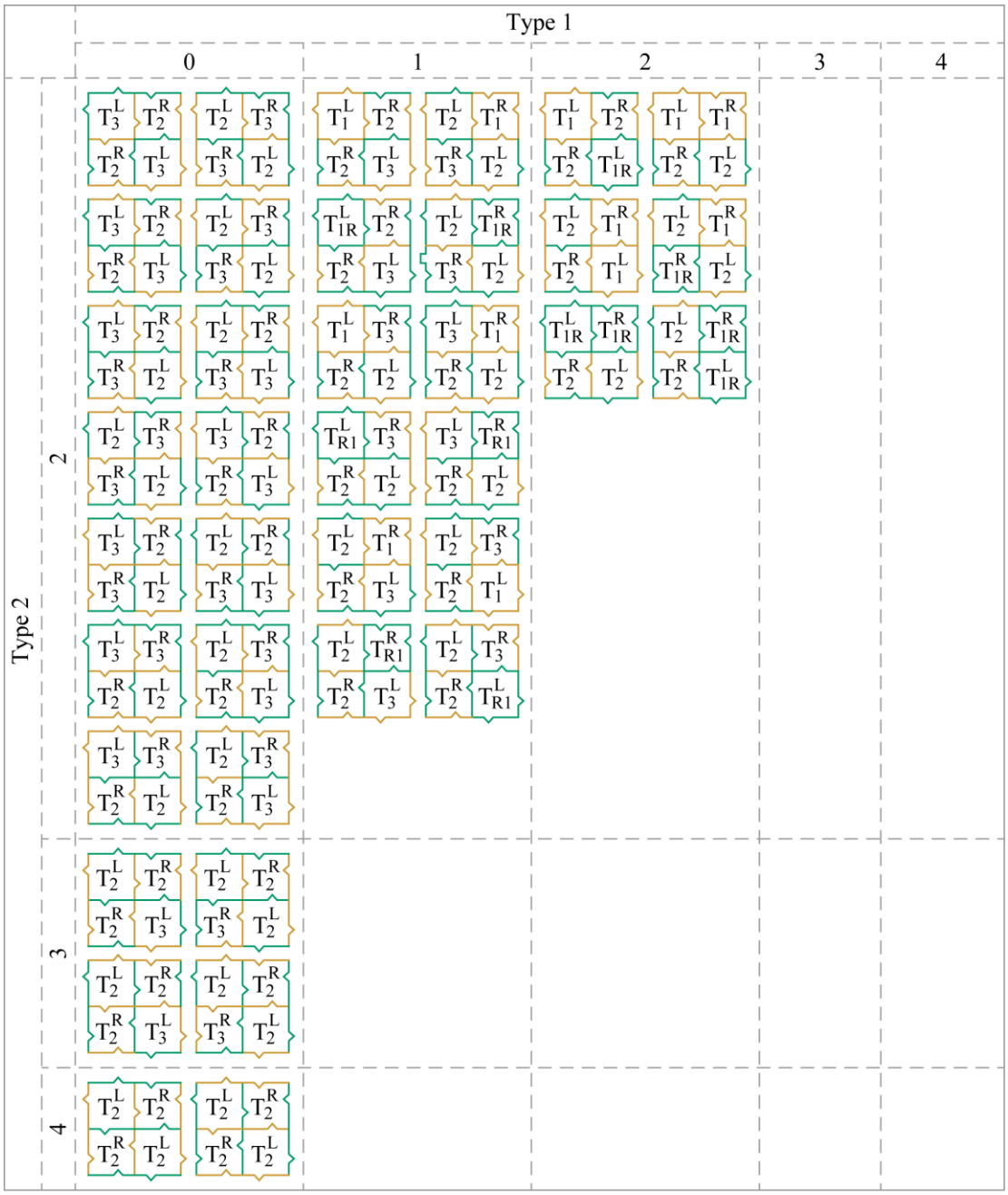

Fig. A1 The 2×2 tessellations arranged by the numbers of type 1 and 2 units. (Continued)

中文大摘要

超材料是一种新型的人造材料，其制造方法是按照一定的设计准则在普通材料中构造出具有重复性的微观结构，从而产生传统材料无法实现的独特的物理性能，例如机械领域的负泊松比等。这些特性使超材料受到了广泛的关注，并且已经在地震监测和航空航天等多个工程领域取得了优异的表现，有着广阔的应用前景。已有研究证明，超材料的独特性能受到其重复性微观结构（单元）以及材料组分的双重影响，表明了其性能可以通过选取不同的几何设计参数或多种材料参数进行调控和编程。根据设计和制造方法的不同，超材料的性能编程有两种方式：（1）在不改变三维结构的情况下，用性能（如弹性模量等）完全不同的材料制造结构中的不同部分，实现在应对相同的外部激励时，不同材料制造的结构部位产生不同的变形，从而在整体结构中表现出多种物理性能；（2）在材料组分不变的情况下，可以改变整体结构或一部分单元的几何参数，也可以将具有同样几何参数但是处于不同稳定状态的单元进行组合，实现预期的物理性能。由此可见，合理的可动结构或可变形结构的设计方法，是实现超材料的多种可编程和反直觉物理性能的前提。

在现有的结构设计方法中，折纸结构设计理论因其设计参数丰富，可以创造出各种复杂程度不同的可动结构，已经获得了广泛的关注和研究。折纸结构的制造方法是，在二维片材上生成特定的折痕图案，之后将其按照计划的变形路径折叠成复杂的三维结构。这一独特的设计制造方式，使折纸结构为超材料的设计和编程提供了全新的思路，展现出了较强的实用性。按照不同的变形模式，可以将折纸超材料分为两类：刚性折纸超材料和非刚性折纸超材料。在刚性折纸超材料中，其结构的运动和变形通过折痕转动实现，在折叠过程中不发生面板变形。因此，如果将刚性折纸结构的面板视为连杆，而折痕视为转动副，就可以将整个结构等效为一个球面机构网格，从而应用机构运动学方法确定折痕的转角关系，进一步结合力学方法构建分析模型，为后续机械性能的预测和编程提供理论依据。但是刚性折纸超材料存在一个缺点：由于其变形过程只由折痕转动控制，其性能可以视为折痕性能的简单叠加，因此其性能通常表现出相对单一和调控范围小的特点。在非刚性折纸超材料中，其结构运动和变形需要依靠折痕转动和面板变形的共同作用才能实现，其中的面板变形在丰富超材料的性能以及提高其调控范围等方面做出了很大贡献。然而，非刚性折纸超材料也存在一个缺点：因其具有复杂的结构运动和变形，在分析过程中难以获得有效的理论建模方法，进而较难实

现对其性能的预测和编程。所以，对于非刚性折纸超材料，如何构造合理有效的分析模型成为了研究工作的重点和难点。

此外，在以往的研究中，人们通常只考虑通过单一类型的折纸结构设计超材料，没有将刚性折纸与非刚性折纸进行组合的设计准则。虽然用刚性和非刚性折纸结构混合的方式，可以构造出具有更为多样的机械性能和更先进的超材料，但是在这个设计过程中有两个问题亟待解决。第一，如何将两种或两种以上不同类型的折纸结构组合在一起。因为折纸单元的组合都是通过图案镶嵌的方法得到的，所以为了保证组合后的折纸结构依然可动且可变形，需要满足的基础设计准则是：不同单元的山谷折痕排布相互协调，不同单元的几何设计参数相匹配。第二，如何实现混合折纸超材料的性能预测和编程。由于不同类型的折纸单元具有不同的性能，因此，除了调节几何和材料参数外，混合折纸超材料的性能编程还可以通过改变不同类型单元的比例来实现。综上所述，为了获得混合刚性和非刚性折纸超材料，需要完成的工作包括：（1）构造刚性和非刚性折纸单元的的分析模型，得到其设计参数与机械性能之间的关系；（2）建立合理的拼接准则，使混合超材料中的不同单元可以协调运动和变形；（3）确定单元数量、几何参数和基础材料与超材料性能之间的关系，实现对混合折纸超材料能的预测和编程。

本文选择了 Square-twist 折纸结构，旨在建立合理有效的非刚性 Square-twist 折纸结构的分析模型，探寻刚性和非刚性 Square-twist 单元混合的折纸超材料的设计方法，实现对混合折纸超材料的机械性能的预测和编程。传统的 Square-twist 折纸图案，是由一个中心正方形面、四个梯形面和四个矩形面组成。根据山谷折痕排布的不同，可以获得 4 种 Square-twist 折纸单元，分别定义为 Type 1、Type 2、Type 3 和 Type 4。通过机构运动学分析可以确定，其中两种为刚性折纸单元（Type 3 和 Type 4 单元），而另外两种为非刚性折纸单元（Type 1 和 Type 2 单元）。对于刚性折纸单元，可以通过运动学分析直接获得各个折痕的转角关系，进而建立机械性能的理论模型。但是对于非刚性折纸单元，其机械性能的研究更复杂，需要根据不同单元的变形特征，使用不同的建模方法构造分析模型。因此，本文首先研究了非刚性 Type 2 单元，通过增加虚拟折痕的方法构建了其等效的刚性折纸单元，从而将非刚性折纸转化为刚性折纸，通过运动学分析推导出其折痕转角关系，进一步根据力学分析方法获得了机械性能的理论表达式。其次，对于非刚性 Type 1 单元，由于其变形行为复杂，无法用等效刚性单元的方法进行分析，因此本文采用了实验和数值相结合的分析方法，得到了面板与折痕的变形发展规律，进而建立了单元设计参数与机械性能关系的经验公式。这两个非刚性折纸单元的分析模型表明，其机械性能可以通过几何参数（边长 a 和 l 以及扭转

角度 α）和材料参数（折痕转动刚度和面板弯曲刚度）进行编程。再次，在分析清楚单元行为的基础上，本文研究了拓扑构型不同、几何参数不同的 Square-twist 折纸单元的空间排布和拼接方式，提出了混合与渐变折纸超材料的设计准则。最后，基于刚性和非刚性折纸单元的分析模型，建立了超材料的单元类型、几何参数、基础材料与其整体机械性能的定量关系，得到了混合折纸超材料的机械性能的预测和编程方法。本文主要工作包括以下三部分：

- **非刚性 Square-twist Type 2 折纸单元的分析**

本文第二章介绍了对非刚性 Square-twist Type 2 单元的机械性能的研究。在分析非刚性 Type 2 单元时，第一步就是建立有效的理论模型。通过观察 Type 2 单元的纸板模型的运动过程，以及用 PET 材料制造试件并进行数字图像相关（DIC）实验，发现在其折叠和展开过程中，除了初始折痕的旋转外，中心正方形面板呈现出比较明显的弯曲现象，而其他面板基本上仍然保持平面状态。

在针对单元变形的分析中，本文选择在 Type 2 单元的中心正方形面板上，沿对角线方向添加一条虚拟折痕。通过将正方形面板弯曲变形转换为两个三角形面板的相对转动，得到了一个等效折纸单元，其在运动过程中仅出现折痕转动变形。根据运动学分析方法，将该等效折纸单元中的两个四折痕顶点模拟为球面四杆机构，而两个五折痕顶点模拟为球面五杆机构。通过求解球面机构对应的闭环方程，得到了其内部各个铰链之间的转角关系，进一步根据对应的山谷折痕推导了二面角之间的关系。本文的分析证明了这些折痕的二面角之间满足变形协调条件，确定了该等效单元为刚性折纸单元。因此，本文通过添加虚拟折痕的方式，将非刚性 Type 2 单元转化为等效刚性折纸单元，得到了其折痕转角关系。

Type 2 单元的运动计算结果表明，单元的变形展开过程存在两条运动路径，且交于一点。随后，本文从结构力学出发，选择用单元的变形能确定 Type 2 单元的实际变形运动路径。由于面板上添加的是虚拟折痕，Type 2 变形能分为折痕和面板两部分。折痕的变形能通过折痕转角关系和折痕转动刚度计算，其中转角关系由等效刚性折纸单元的运动学分析得到，而折痕转动刚度则用非线性弹性的本构关系进行计算。而面板变形能通过虚拟折痕转角与面板等效弯曲刚度计算，由于面板弯曲角度小，因此其弯曲刚度用线弹性模型计算。通过叠加折痕转动能量和面板等效变形能，建立了 Type 2 单元的理论分析模型。理论模型的能量计算结果表明，Type 2 单元在展开过程中并不是沿单一路径运动，而是在两条路径的交点处发生分岔现象，且该现象在后续的对比实验中得到了验证。

根据 Type 2 单元的理论模型，本文得到了几何和材料参数与其机械性能的对应关系。文中结果表明，当面板弯曲刚度与折痕刚度的比值增加时，由于面板

弯曲的贡献增加，折纸单元的整体能量与反力均会提高。同时，由于面板在展开过程中弯曲角度先变大后变小，因此单元反力在分叉点会显著下降。在刚度比超过临界数值以后，单元反力降到零以下，出现双稳态现象。此外，随着角度参数的增加，面板的最大弯曲角度增大，导致变形能与反力的增加。当折痕长度比增大时，力曲线中平台阶段的数值会整体升高，即能量吸收效率更高。

基于以上结论，本文提出了对 Type 2 折纸单元的机械性能进行预测和编程的方法，为其实现各种工程应用提供了理论基础。例如，在设计理想的冲击吸能装置时，需要在力-位移曲线中产生一个较长且平坦的平台阶段，根据本文的研究结果，应选择较小的面板与折痕的刚度比和角度参数，并且选择较大的折痕长度比，此时对应的力曲线中分叉点处的力下降程度最小，即平台阶段更平缓。基于本章的研究结果，非刚性 Type 2 单元可以被用于设计折纸超材料，并且获得可以预测和编程的机械性能。

- **非刚性 Square-twist Type 1 折纸单元的分析**

本文第三章着重分析了非刚性 Square-twist Type 1 折纸单元的变形与机械性能。从单元的折纸图案中可以看出，其山谷折痕的排布展现了四重旋转对称性，因此，本文对 Type 1 单元进行了双轴拉伸实验。该实验通过独特设计的夹具，实现了在 Type 1 单元的整个展开过程中，其两个对角线方向上的位移一致。从实验结果中观察到，非刚性 Type 1 单元具有显著的双稳态与自锁特性。此外，DIC 测量结果显示，与其他 Square-twist 折纸单元不同，Type 1 单元在展开过程中，所有面板上均产生显著变形，而且其中心正方形面板呈现出中间下凹四周上翘的复杂变形。

在建立有效的非刚性 Type 1 单元的分析模型时，本文首先使用了在中心正方形面板上添加虚拟折痕，构造等效折纸单元的研究方法。通过对等效单元进行运动学分析，证明了其是刚性折纸单元，且存在两条运动路径。但是在运动过程中，该等效折纸单元不再表现出四重旋转对称性，其各个面板也产生了与实验中 Type 1 单元完全不一样的变形。以上研究结果说明，构造等效刚性折纸单元的方法不适用于建立非刚性 Type 1 单元的分析模型。

针对这一问题，本文提出使用力学分析中的有限元方法对 Type 1 单元的变形模式进行研究。由于 Type 1 折纸单元的非刚性折叠特性，只有在整个单元完全折死或者完全展开的状态下才能构造理想模型，然而这两种情况下的模型无法成为有限元分析时的初始状态。因此，本文选择了用两个交叉的三角形平面代替梯形面板的方法，建立了一个含有微小缺陷的 Type 1 有限元模型。此外，在有限元结果与 DIC 实验中得到的变形特性和机械性能进行的对比中，得到了较好的

吻合结果，证明了该有限元模型可以用于对 Type 1 单元的变形特性进行分析。从该分析模型的计算结果曲线和构型中可以观察到，非刚性 Type 1 单元的变形过程分为三个阶段：（1）第一阶段是模型从初始状态向折死状态运动的拉紧阶段，在最终锁紧状态下，模型处于最难被拉开的位置，导致结构刚度达到最大值；（2）第二阶段是模型通过增大面的变形来克服自身锁定状态的解锁阶段，此时总能量和反力均显著提升，随后 Type 1 单元的双稳态特性导致大部分的面变形能被释放，造成反力的下降；（3）第三阶段是以折痕转动变形为主的模型展平阶段，此时面板上的弹性变形能均被释放，反力呈现平缓上升状态。

根据以上变形特点，本文建立了非刚性 Type 1 单元的经验模型，并提出了四个假设。第一，由于 Type 1 单元变形复杂，此经验模型只考虑三个重要的性能：完全展开时的能量、峰值力以及最大刚度。第二，单元的总能量由每个面板以及每条折痕的能量叠加得到。第三，折痕能量为转动变形能，并使用了非线性弹性的本构关系。第四，由于有限元中的材料设定为弹塑性材料，面板的变形能分为弹性和塑性两部分。在获得了 Type 1 单元的经验模型后，本文用多组不同参数的实验结果验证了该模型的有效性。

基于 Type 1 单元的经验模型，本文确定了单元的几何和材料参数与其机械性能之间的定量关系。分析结果表明，当模型的边长比增大时，矩形和梯形部分面积增大，导致单元的变形能增大，进而造成了能量、力和刚度的增大。当面板与折痕的刚度比增大时，面板变形能的贡献增加，同样造成了三个性能参数的增大。此外，当角度参数增大时，Type 1 单元的双稳态更明显，导致其更难被拉开，进而造成三个性能参数的增大。基于本章的研究结果，可以实现对非刚性 Type 1 单元的机械性能进行预测和编程，为后续折纸超材料的设计与分析究奠定了基础。

- **刚性与非刚性混合 Square-twist 折纸超材料的设计与分析**

本文在第四章中提出了 Square-twist 折纸超材料的设计准则，建立了其性能的编程方法。因为研究证明了非刚性折纸单元可以实现更广泛的机械性能和功能，所以本文在超材料设计中使用了不同的刚性与非刚性 Square-twist 折纸单元。第二、三章的研究内容已经给出了非刚性折纸单元的性能分析模型，确定了几何和材料参数与其机械性能的关系。因此，本章工作内容的重点在于：（1）提出单元拼接时对应的山谷折痕排布和几何参数的匹配准则，使具有不同刚性可折叠性的单元可以拼接在一起；（2）分析由不同单元混合模式制造的折纸超材料的机械性能，找出其特点和变化规律，确定不同单元对超材料整体性能的影响；（3）研究影响 Square-twist 折纸超材料机械性能的几何和材料等参数，实现对其性能的预测和编程。

首先，在设计 Square-twist 折纸超材料时，本文使用了拼图原理，共选取了三种单元并将其定义为不同的拼图块，包括非刚性 Type 1 和 Type 2 单元以及刚性 Type 3 单元。从 Square-twist 折纸单元的拼接过程中发现：（1）非刚性 Type 1 单元在翻转后表现为完全不同的折痕排布，因此在拼接准则中被定义为单独的单元拼图块；（2）相邻单元的中心正方形面板扭转方向不同，在文中被分别定义为左手和右手单元，并用不同形状的拼图块加以区分。基于以上单元图案的特点，在分析 Square-twist 折纸超材料的设计准则时，本文共定义 8 个单元拼图块。因此，不同单元的拼接即为将对应的拼图块组合在一起。在拼接过程中，本文提出了单元匹配准则：左手单元与右手单元相接，长边与长边相接，山折痕与山折痕相接。基于此设计准则，本文给出了 Square-twist 超材料的数量计算公式：对于含有 $m\times m$ 个单元的超材料，共有 $2^{m(m+2)}$种可能的拼接形式。文中针对该计算公式进行了进一步分析，以 2×2 个单元的 Square-twist 超材料为例，其中一些超材料的设计图案可由其他图案旋转得到，在排除这些情况之后，可能的拼接形式的总数由 $2^{2(2+2)}$=256 个降为 136 个。此外，本文也给出了几何参数的单元之间的拼接准则，并以此为基础设计了渐变 Square-twist 折纸超材料。

其次，本文设计、制作和测试了多种单元组合的 Square-twist 超材料，其中各个单元的占比在 0%~100%之间变化，单元的翻转或者左右旋转换均不影响其机械性能。在分析内部单元一致的超材料模型时，本文发现了模型的整体变形过程跟单个单元的表现很类似，唯一的差别是：只含有 Type 2 和 Type 3 单元的超材料中，所有单元基本同步展开；而在只含有 Type 1 单元的超材料中，由于边界条件的影响，各个单元的展开并没有完全同步，造成了该超材料的反力曲线出现局部波动。本文基于以上实验结果提出，位于超材料内部的单元仍然保持了单个单元的变形模式和机械性能。因此，超材料的机械性能可以用单元的性能进行预测。以 4×4 个单元的 Square-twist 超材料为例，其能量可以认为是全部 16 个单元的能量之和。文中的实验加载装置保证了超材料中各个单元可以同步展开，因此，超材料的总位移为实验加载方向上全部单元位移的总和，在此模型中为 4 倍的单元位移。之后，因为力是能量对位移求导，所以可以推导出，超材料所受的外力是各个单元所受外力之和的四分之一。同理，刚度是力对位移求导，因此，超材料的刚度是单元刚度之和的十六分之一。通过与实验结果进行对比，本文证明了用单元性能能够有效预测超材料的整体性能。

最后，综合以上研究结果，本文基于第二、三章建立的非刚性单元的性能分析模型，提出了 Square-twist 折纸超材料的机械性能编程方法。因为本文前几章的分析已经证明，Type 1 单元的机械性能远大于其他两个单元，所以其数量可以

显著改善超材料的性能。但是由于 Type 1 单元只能逐个增加，因此这种提升呈现出阶梯状的有级变化。此外，超材料性能的叠加预测理论表明，影响单元性能的几何和材料参数均可用于编程超材料的整体机械性能，且分析结果证明了该方式可以实现连续编程。例如，折痕和面板的刚度比的增加造成了折痕转动能量增大，进而导致总能量显著提升。此外，角度参数的增大使超材料中的非刚性单元更难被展开，而边长比的增加则导致了非刚性单元中面变形能的增加，这两个参数均造成了三个机械性能参数的显著增长。通过以上两种编程方法的对比证明了，在单元比例调控的基础上改变几何或材料参数，可以实现更大范围的机械性能的编程。本章中对刚性和非刚性混合折纸超材料的研究，拓展了折纸超材料的设计方法，拓宽了其机械性能的可编程范围，为生产满足各领域实际工程需求的折纸超材料提供了理论依据。

- **结论与展望**

本文建立了非刚性 Square-twist Type 2 单元的理论模型以及 Type 1 单元的经验模型，给出了两个非刚性单元的性能编程方法。在此基础上，提出了新型折纸超材料的设计准则，确定了不同单元拼接时需要协调的山谷折痕分布以及几何参数，实现了通过改变单元比例以及调整几何和材料参数对折纸超材料的性能进行编程。本文中提出的设计准则和性能编程方法，普遍适用于其他折纸结构设计的超材料。因此，本研究结果对同类型研究具有一定的指导意义。为了提高这类折纸超材料的实际应用，可以在如下几个方面进行深入研究：

（1）基于本文提出的单层 Square-twist 超材料设计方法，未来工作可以进一步研究多层折纸超材料的设计原则。在单层超材料结构设计中，只需要考虑山谷折痕分布和相邻单元中的几何参数，但是对于多层超材料而言，相邻层之间的连接面或折痕也是重要的影响参数。例如，当两个单层 Square-twist 超材料模型中，对应位置的矩形平面均位于其外表面上时，可以将这两个单层超材料在矩形面处进行拼接，形成多层超材料。这种多层超材料可以实现更大范围的机械性能编程。

（2）本文研究的 Square-twist 折纸图案是由多个四折痕顶点组合而成，因此，未来可以进一步研究其它四折痕顶点图案（如 Miura-ori 和 double corrugated 图案）是否可以与 Square-twist 折纸图案进行组合。每一类折痕图案所形成的折纸结构都有独特的物理性质，因此，创造出的新型组合超材料可能产生更为广泛的特性。

（3）刚性和非刚性混合折纸结构可以与其它可变形材料（如磁/温场控制的形状记忆材料）相结合，制造出可进行主动或被动调谐的结构。这种可控的重构性能可用于设计适应各种复杂环境的软体机器人。

（4）Square-twist 折纸图案的一个特点是，相同的折痕分布在不同的山谷线排布情况下，会创造不同类型的单元，从而产生不同的机械性能。也就是说，相同的片状超材料，即可以折叠为全部由 Type 1 单元组成的超材料，也可以折叠为全部由 Type 3 单元组成的超材料。这两种不同的超材料具有截然不同的机械性能，却可以通过中间的平面状态进行转化，这一特性即为超材料的重编程/重构。因此，未来的研究可以聚焦于 Square-twist 折纸结构的重编程/重构特性。此外，当折纸超材料由形状记忆材料制造时，其重编程/重构特性可以实现自主调节。

关键词：运动学，非刚性折纸，山谷折痕排布，图案镶嵌，机械超材料，可编程性，可预测性

Publications and Research Projects

Papers:

[1] Ma J, Zang S, Feng H, Chen Y, and You Z. Theoretical characterization of a non-rigid-foldable square-twist origami for property programmability[J]. International Journal of Mechanical Sciences, 2020, 189: 105981. (导师一作，共同一作)

[2] Feng H, Peng R, Zang S, Ma J, and Chen Y. Rigid foldability and mountain-valley crease assignments of square-twist origami pattern[J]. Mechanism and Machine Theory, 2020, 152: 103947.

[3] Yang X, Zang S, Ma J, and Chen Y, Elastic buckling of thin-walled cylinders with pre-embedded diamond patterns[C]. 7OSME, The Seventh International Meeting of Origami Science, Mathematics and Education, Oxford, UK, September 5-7, 2018.

[4] Ma J, Zang S, Chen Y, and You Z. Tessellation rule and properties programming of origami metasheets built with a mixture of rigid and non-rigid square-twist patterns[J]. Engineering, Accepted, 2022. (导师一作，共同一作)

[5] Zang S, Ma J, You Z, and Chen Y. Deformation characteristics and mechanical properties programming of a non-rigid square-twist origami structure with rotational symmetry[J]. Thin-walled Structures, Under Revision.

Acknowledgments

First and foremost, I would like to express my deepest sense of gratitude to my supervisors, Prof. Yan Chen and Prof. Jiayao Ma, for their constant encouragement and patient guidance throughout my PhD's study. I am extremely grateful to Prof. Yan Chen for sharing her expertise and providing me with numerous exchange opportunities. Her requirements of being proficient, professional, and perfect in doing research inspired me a lot. I am also greatly thankful to Prof. Jiayao Ma for his constructive suggestions and valuable guidance in my work. All the things I've learned from these supervisors will continue to influence my future work and life.

I am also grateful to Prof. Zhong You for his advice and help in my research. Appreciation also goes to Dr. Huijuan Feng, Dr. Rui Peng, Dr. Xiao Zhang, Dr. Jeff Lee, Dr. Ying Zhang, and Miss Xiaochen Yang. Discussions with them deepen my understanding of the research. Meanwhile, I would like to thank my colleagues in Motion Structure Laboratory, in particular Miss Miao Zhang, Miss Xiaoyi Jiang, Mr. Zufeng Shang, Mr. Weilin Lv, Mr. Degao Hou, Mr. Huaping Dai, and Mr. Xuesong Chen, for their friendly help. Moreover, special gratitude goes to my friends, in particular Ms. Ying Yu, Mr. Shaozhe Pan, Mr. Yilong Zhu, and teachers, Mr. Yue Liu and Ms. Gengyun Tan, for helping me to go through many hard times in my study life.

Finally, I would like to express my sincerest thanks to my family, in particular my parents, Ms. Yajie Zheng and Mr. Yongyun Zang. Their support, encouragement, and love provide me with the courage and belief to overcome any difficulty during my study and life.